Delft University of Technology

Quantum transport in hybrid semiconductor-superconductor nanostructures

Levajac, V.

DOI
10.4233/uuid:faf12bf9-8dc5-42ae-8025-b22b6d88e97e

Publication date
2023

Document Version
Final published version

Citation (APA)
Levajac, V. (2023). *Quantum transport in hybrid semiconductor-superconductor nanostructures*. [Dissertation (TU Delft), Delft University of Technology]. https://doi.org/10.4233/uuid:faf12bf9-8dc5-42ae-8025-b22b6d88e97e

Important note
To cite this publication, please use the final published version (if applicable).
Please check the document version above.

Copyright
Other than for strictly personal use, it is not permitted to download, forward or distribute the text or part of it, without the consent of the author(s) and/or copyright holder(s), unless the work is under an open content license such as Creative Commons.

Takedown policy
Please contact us and provide details if you believe this document breaches copyrights.
We will remove access to the work immediately and investigate your claim.

This work is downloaded from Delft University of Technology.
For technical reasons the number of authors shown on this cover page is limited to a maximum of 10.

QUANTUM TRANSPORT IN HYBRID SEMICONDUCTOR-SUPERCONDUCTOR NANOSTRUCTURES

QUANTUM TRANSPORT IN HYBRID SEMICONDUCTOR-SUPERCONDUCTOR NANOSTRUCTURES

Dissertation

for the purpose of obtaining the degree of doctor
at Delft University of Technology
by the authority of the Rector Magnificus, prof. dr. ir. T.H.J.J. van der Hagen,
chair of the Board for Doctorates
to be defended publicly on
Monday 20 November 2023 at 10:00 o'clock

by

Vukan LEVAJAC

Master of Science in Nanoscience and Nanotechnology
KU Leuven, Belgium
born in Kragujevac, Serbia

This dissertation has been approved by the promotors.

Composition of the doctoral committee:

Rector Magnificus	chairperson
Prof. dr. ir. L.P. Kouwenhoven	Delft University of Technology, promotor
Dr. M.T. Wimmer	Delft University of Technology, copromotor
Independent members:	
Prof. dr. Y.V. Nazarov	Delft University of Technology
Dr. S. De Franceschi	CEA Grenoble, France
Dr. E. Prada	Materials Science Institute Madrid, Spain
Dr. ir. M. Veldhorst	Delft University of Technology
Prof. dr. ir. L.M.K. Vandersypen	Delft University of Technology, reserve member

Printed by: Gildeprint

Cover by: Vukan Levajac

Copyright © 2023 by V. Levajac

ISBN 000-00-0000-000-0

An electronic copy of this dissertation is available at
https://repository.tudelft.nl/.

Contents

Summary ix

Samenvatting xi

1 Introduction 1

1.1 Quantum technology . . . 2
1.2 Topological quantum computing . . . 4
1.3 Thesis outline . . . 5

2 Theory 9

2.1 Semiconducting nanostructures . . . 10
2.1.1 General concepts . . . 10
2.1.2 Rashba nanaowires . . . 11
2.1.3 Planar Ge . . . 12
2.2 Superconductivity . . . 14
2.2.1 BCS theory . . . 14
2.2.2 Density of states in superconductors . . . 15
2.3 Transport between a normal metal and a superconductor . . . 17
2.4 Josephson junctions . . . 19
2.4.1 SNS Josephson junctions . . . 20
2.4.2 Magnetic field effects . . . 22
2.4.3 dc-SQUID . . . 26
2.5 Topological superconductivity . . . 27
2.5.1 Majorana nanowire model . . . 27
2.5.2 Considerations beyond the minimal model . . . 29
2.6 Hybrid nanowire island . . . 32

3 Supercurrent parity meter in a nanowire Cooper pair transistor 39

3.1 Introduction . . . 40
3.2 Results . . . 40
3.3 Conclusion . . . 47
3.4 Supplementary Material . . . 48
3.4.1 Methods . . . 48
3.4.2 Supplementary figures . . . 49
3.4.3 Effective Hamiltonian for the nanowire Cooper-pair transistor . . . 53

4 Impact of junction length on supercurrent resilience against magnetic field in InSb-Al nanowire Josephson junctions 63

4.1 Introduction . . . 64

4.2 Results . . . 65
4.3 Discussion . . . 70
4.4 Conclusion . . . 73
4.5 Supporting Information . . . 73
4.5.1 Methods . . . 73
4.5.2 Effects of junction length and global back gate on induced superconducting gap . . . 78
4.5.3 Effects of local gates on supercurrent resilience . . . 79
4.5.4 Supporting figures . . . 81

5 Supercurrent in the presence of direct transmission and a resonant localized state 95
5.1 Introduction . . . 96
5.2 Results . . . 97
5.3 Discussion . . . 105
5.4 Conclusion . . . 105
5.5 Theoretical model . . . 105
5.5.1 Hamiltonians . . . 106
5.5.2 Normal transport for many dots . . . 107
5.5.3 Normal transport for two dots . . . 109
5.5.4 Normal transport examples . . . 113
5.5.5 Superconducting transport . . . 116
5.5.6 Numerical details . . . 119
5.5.7 Superconducting transport examples . . . 120
5.5.8 Conclusions theory part . . . 125
5.6 Methods . . . 126
5.6.1 Data selection . . . 126
5.6.2 Measurement setup . . . 127

6 Subgap spectroscopy along hybrid nanowires by nm-thick tunnel barriers 135
6.1 Introduction . . . 136
6.2 Results . . . 137
6.3 Discussion . . . 146
6.4 Conclusion . . . 147
6.5 Supplementary Materials . . . 148
6.5.1 Device fabrication . . . 148
6.5.2 Measurement setups . . . 150
6.5.3 Extended data . . . 155

7 Hard superconducting gap in germanium 169
7.1 Introduction . . . 170
7.2 Results . . . 171
7.2.1 Material properties . . . 171
7.2.2 Highly transparent Josephson junction . . . 173
7.2.3 Hard induced superconducting gap . . . 175
7.2.4 Superconducting quantum interference devices . . . 177

7.2.5 Scalable junctions . . . 177
7.3 Conclusion and future prospectives . . . 180
7.4 Supplementary Information . . . 181
7.4.1 Methods . . . 181
7.4.2 Key metrics . . . 182
7.4.3 Supplementary figures . . . 183

8 Conclusions & Outlook **199**
8.1 Conclusions . . . 200
8.2 Outlook . . . 201
8.2.1 Magnetic field resilient Cooper-pair transistor . . . 201
8.2.2 Nanometer-thick tunnel barriers on three-facet hybrid nanowires . . . 202
8.2.3 Non-local spectroscopy of a hybrid nanowire with a superconductor-free bulk . . . 204

Acknowledgements **209**

Curriculum Vitæ **213**

List of Publications **215**

SUMMARY

Quantum technology is a developing field of science where devices possess novel and superior functionalities thanks to their quantum-mechanical behaviour at the nanometer scale. A typical example is a quantum computer, where information is stored in quantum states of its quantum bits. By manipulating entangled and superposition states of these qubits, quantum computers can achieve exponential speed-ups in calculation and therefore solve currently unsolvable problems within polynomial computational times. This powerful advantage of quantum computers is particularly difficult to achieve in practice, due to decoherence - a tendency of quantum objects to lose their quantum-mechanical properties when interacting with their environment. Obviously, qubit decoherence cannot be avoided because the control of a quantum computer inevitably causes couplings to the environment. To mitigate decoherence, fault-tolerant implementations of quantum computing need to be developed.

Topological quantum computing has been proposed to achieve fault-tolerance since its significant robustness to decoherence is inherent in the quantum-mechanical nature of topological qubits. Building units of a topological qubit are Majorana zero modes (MZMs) – zero-energy quasiparticles that possess the non-Abelian anyonic exchange statistics and are localized at the boundaries of a topological superconductor. In sufficiently large topological superconductors, MZMs exhibit no overlap and therefore can in pairs host non-local fermions. By braiding non-overlapping MZMs, the information stored in the non-local fermions is manipulated while being insensitive to local noise. In this way one can perform computation that is topologically protected against local sources of decoherence.

In 2010, III-V semiconductor nanowires proximitized by s-wave superconductors were proposed as a suitable candidate platform for the realization of topological superconductors. Topological superconducting phase occurs in such a hybrid nanowire due to an interplay among the large spin-orbit interaction, s-wave superconductivity, controllable electron density and large Zeeman energy introduced by an external magnetic field. Consequently, the nanowire bulk undergoes a band inversion and two MZMs appear at the two nanowire ends. First signatures of MZMs were reported in 2012 and since then a lot of effort has been put in fully demonstrating them. Despite huge improvements in the materials and measurement techniques, conclusive evidence of MZMs in hybrid nanowires is still missing. This is because disorder in hybrid nanowires can also cause the observed signatures of MZMs and make the topological scenario indistinguishable from the trivial ones. Therefore, further improvements and more detailed studies are needed and this thesis shows some recent examples of these.

We begin by presenting fundamental concepts of semiconductors, superconductors and the quantum transport in hybrid devices that combine them. We also elaborate on the physics of hybrid devices - such as hybrid Josephson junctions, Majorana nanowires and hybrid islands (Chapter 2).

The first experimental chapter (Chapter 3) studies the supercurrent transport through a hybrid InSb-Al nanowire island. It is shown that the current-phase relation (CPR) can have a parity-dependent phase shift when subgap states in the island mediate the supercurrent. This demonstrates that CPR measurements can be used to measure the island parity even in the $1e$-regime where conductance measurements cannot distinguish between the two parities.

We proceed by studying the impact of the length of a Josephson junction (JJ) on its supercurrent resilience against magnetic field. We use the shadow-wall lithography to create hybrid InSb-Al nanowire JJs of various lengths and find that reducing the junction length improves its magnetic field resilience. We reproducibly detect supercurrent at parallel magnetic fields of ~ 1.3 T in ~ 40 nm-long JJs (Chapter 4).

Next, we embed two ~ 40 nm-long InSb-Al nanowire JJs into a superconducting loop and study the CPR up to parallel magnetic fields of ~ 700 mT. We find that a localized resonant state in the JJ can modulate the supercurrent asymmetrically in a narrow range of the electro-chemical potential. Moreover, in this range the junction becomes a π-junction at high magnetic fields. These observations have been reproduced by a theoretical model that considers the interference between a localized state and direct transmission inside a single JJ (Chapter 5).

We move from studying supercurrent and proceed by developing hybrid InSb-Al nanowire devices with multiple nm-thick AlOx tunnel probes. We obtain these probes by combining the shadow-wall lithography and controlled oxidation of the Al film on the nanowires. By comparing tunneling spectroscopy obtained by neighbouring tunnel probes, Andreev bound states (ABSs) localized over ~ 200 nm are observed at the ends and inside the bulks of multiple hybrids. (Chapter 6)

In the last study (Chapter 7), we explore how superconductivity can be induced in high-mobility Ge two-dimensional hole gases (2DHGs). We demonstrate for the first time a hard superconducting gap in Ge induced by PtSiGe. The superconducting PtSiGe is obtained by depositing Pt on top of a Ge/SiGe quantum well and thermally diffusing it into the SiGe. This platform may be in future considered a suitable candidate for topological superconductivity since it combines low disorder and hard superconducting gap.

Finally, we comment on our results and propose several new experiments (Chapter 8) that represent follow-up studies in various directions that have been taken throughout this thesis.

SAMENVATTING

Kwantumtechnologie is een ontwikkelend gebied van de wetenschap waarbij apparaten nieuwe en superieure functionaliteiten bezitten dankzij hun kwantummechanische gedrag op nanometerschaal. Een typisch voorbeeld is een kwantumcomputer, waar informatie wordt opgeslagen in kwantumtoestanden van kwantumbits. Door het manipuleren van verstrengelde en superpositie-toestanden van qubits, kunnen kwantumcomputers exponentiële versnellingen in de berekeningen bereiken en daardoor tegenwoordig onoplosbare problemen binnen polynomiale rekentijden oplossen. Dit krachtige voordeel van kwantumcomputers is in de praktijk bijzonder moeilijk te verwezenlijken vanwege decoherentie - de neiging van kwantumobjecten om hun kwantummechanische eigenschappen te verliezen vanwege interactie met hun omgeving. Het is duidelijk dat decoherentie van qubits niet kan worden vermeden, omdat de besturing van een kwantumcomputer onvermijdelijk koppelingen met de omgeving veroorzaakt. Om decoherentie te verminderen moeten fout-tolerante implementaties van kwantumcomputers worden ontwikkeld.

Topologische kwantumcomputers zijn voorgesteld om fout-tolerantie te bereiken, aangezien de aanzienlijke robuustheid ervan tegen decoherentie inherent is aan de kwantummechanische aard van topologische qubits. De bouweenheden van een topologische qubit zijn Majorana zero modes (MZM's) - nul-energie quasideeltjes die de niet-Abelse anyonische uitwisselingsstatistiek bezitten en gelokaliseerd zijn aan de grenzen van een topologische supergeleider. In voldoend grote topologische supergeleiders vertonen MZM's geen overlap en kunnen daarom in paren niet-lokale fermionen hosten. Door niet-overlappende MZM's te vlechten, wordt de informatie die is opgeslagen in de niet-lokale fermionen gemanipuleerd terwijl deze ongevoelig is voor lokale ruis. Op deze manier kan men berekeningen uitvoeren die topologisch beschermd zijn tegen lokale bronnen van decoherentie.

In 2010 werden III-V-halfgeleidernanodraden, geproximiteerd door s-wave supergeleiders, voorgesteld als een geschikt kandidaatplatform voor de realisatie van topologische supergeleiders. Topologische supergeleidende fase treedt op in zo'n hybride nanodraad als gevolg van een samenspel tussen de grote spin-orbitinteractie, s-wave supergeleiding, regelbare elektronendichtheid en grote Zeeman-energie geïntroduceerd door een extern magnetisch veld. Als gevolg daarvan ondergaat de bulk van de nanodraden een bandinversie en verschijnen er twee MZM's aan de twee uiteinden van de nanodraden. De eerste signaturen van MZM's werden gerapporteerd in 2012 en sindsdien is er veel moeite gestoken in het volledig aantonen ervan. Ondanks enorme verbeteringen in de materialen en meettechnieken ontbreekt er nog steeds sluitend bewijs voor MZM's in hybride nanodraden. Dit komt omdat wanorde in hybride nanodraden ook de waargenomen signaturen van MZM's kan veroorzaken en het topologische scenario niet te onderscheiden is van de triviale scenario's. Daarom zijn verdere verbeteringen en meer gedetailleerd onderzoek nodig en dit proefschrift laat enkele recente voorbeelden hiervan zien.

We beginnen met het presenteren van fundamentele concepten van halfgeleiders, supergeleiders en het kwantumtransport in hybride apparaten die deze combineren. We gaan ook dieper in op de fysica van hybride apparaten, zoals hybride Josephson juncties, Majorana nanodraden en hybride eilanden (Hoofdstuk 2).

Het eerste experimentele hoofdstuk (Hoofdstuk 3) bestudeert het superstroomtransport door een hybride InSb-Al nanodraadeiland. Er wordt aangetoond dat de stroomfaserelatie (*eng.* current-phase relation) (CPR) een pariteitsafhankelijke faseverschuiving kan hebben wanneer subgap-toestanden op het eiland de superstroom bemiddelen. Dit toont aan dat CPR-metingen kunnen worden gebruikt om de eilandpariteit te meten, zelfs in het $1e$-regime waar geleidingsmetingen geen onderscheid kunnen maken tussen de twee pariteiten.

We gaan verder met het bestuderen van de impact van de lengte van een Josephson junctie (JJ) op zijn superstroombestendigheid tegen magnetisch veld. We gebruiken de schaduw-muur lithografie om hybride InSb-Al nanodraad JJ's van verschillende lengtes te maken en ontdekken dat het verkleinen van de junctielengte de bestendigheid tegen het magnetische veld verbetert. We detecteren op reproduceerbare wijze superstroom bij parallelle magnetische velden van $\sim 1.3\,\mathrm{T}$ in $\sim 40\,\mathrm{nm}$-lange JJs (Hoofdstuk 4).

Vervolgens hebben we twee $\sim 40\,\mathrm{nm}$-lange InSb-Al nanodraad JJ's in een supergeleidende lus ingebed en bestuderen we de CPR bij parallelle magnetische velden tot $\sim 700\,\mathrm{nT}$. We ontdekken dat een gelokaliseerde resonante toestand in de JJ de superstroom asymmetrisch kan moduleren in een smal interval van het elektrochemische potentieel. Bovendien wordt de junctie in dit interval een π-junctie bij hoge magnetische velden. Deze waarnemingen zijn gereproduceerd door een theoretisch model dat rekening houdt met de interferentie tussen een gelokaliseerde toestand en directe transmissie binnen een enkele JJ (hoofdstuk 5).

We gaan over van het bestuderen van superstroom en gaan verder met het ontwikkelen van hybride InSb-Al nanodraad-devices met meerdere nm-dikke AlOx-tunnelcontacten. We verkrijgen deze contacten door de schaduw-muur lithografie en gecontroleerde oxidatie van de Al-film op de nanodraden te combineren. Door tunnelspectroscopie verkregen door naburige tunnelcontacten te vergelijken, worden Andreev-gebonden toestanden (*eng.* Andreev bound states) (ABS's) gelokaliseerd over $\sim 200\,\mathrm{nm}$ waargenomen aan de uiteinden en in de bulk van meerdere hybriden. (Hoofdstuk 6)

In de laatste studie (hoofdstuk 7) onderzoeken we hoe supergeleiding kan worden geïnduceerd in Ge tweedimensionale elektronengat-gassen (*eng.* hole-gases) (2DHG's) met hoge mobiliteit. We demonstreren voor het eerst een harde supergeleidende gap in Ge veroorzaakt door PtSiGe. Het supergeleidende PtSiGe wordt verkregen door Pt op een Ge/SiGe kwantumstip af te zetten en het thermisch in het SiGe te diffunderen. Dit platform kan in de toekomst worden beschouwd als een geschikte kandidaat voor topologische supergeleiding, omdat het lage wanorde en een harde supergeleidende gap combineert.

Ten slotte geven we commentaar op onze resultaten en stellen we verschillende nieuwe experimenten voor (hoofdstuk 8) die vervolgstudies vertegenwoordigen in verschillende richtingen die in dit proefschrift zijn gevolgd.

1

Introduction

1

1.1. QUANTUM TECHNOLOGY

The turn between the nineteenth and twentieth century was marked by newly observed physical phenomena - such as the black-body radiation [1] and the photoelectric effect [2, 3] - that could not be explained by the then-existing theory of matter. This inspired physicists to come up with a new theory with fundamentally different concepts which would manage to explain the new phenomena. These counterintuitive concepts, for example, allowed particles to be localized in and transmitted through energy barriers, or assumed that a single particle can be simultaneously in multiple states characterized by different values of a same observable. Two central concepts in the new theory were the particle-wave duality of matter and the discretization of energy in the form of *quanta*. Therefore, the new theory was called *the quantum theory* and its establishment is known as the first quantum revolution.

Quantum theory did not only manage to create a consistent set of laws that govern the behaviour of particles at the nanometer scale, but also played an important role in various technological developments of the twentieth century. For example, basic components - such as lasers and transistors - could only be invented and miniaturized thanks to understandings how electrons and photons behave and interact - which directly followed from the quantum theory. Due to rapid miniaturization of technology taking place over the past several decades, electronic devices nowadays consist of nanocomponents which require a fully quantum approach. In addition, quantum theory has also been used to design devices that exploit the laws of quantum theory to gain fundamentally different and superior functionalities. Applying quantum theory to create such superior and novel, *quantum technology* has led to the second quantum revolution [4].

The field of quantum technology can be divided into four subfields depending on purposes the technology serves – quantum communication, quantum sensing, quantum simulation and quantum computing. In quantum communication, secure communication is achieved thanks to the fundamental property of the quantum entanglement between quantum states of two quantum objects (photons, for example). Any interception of the information flow via a quantum-communication link is detected by entangling the exchanged quantum state (photon) with another precisely prepared state (photon) at each end of the link. This represents the basic principle of the quantum key distribution (QKD) protocol for secure communication [5]. Quantum sensing relies on the high sensitivity of quantum objects to electric and magnetic fields, which is reached via quantum entanglement, quantum interference or quantum phase squeezing [6]. Since extremely small values of electric and magnetic fields can be detected with great precision, quantum sensors beat sensors based on classical principles. Quantum simulations are performed by mapping a real quantum many-body system onto an artificially made quantum many-body system - a quantum simulator. The quantum simulator is then controlled and let to evolve by following the laws of quantum mechanics - simulating the real system [7]. In this way, quantum materials or chemicals can be modelled and their properties can be studied by quantum simulators realized on different platforms - with some examples being superconducting qubits, trapped ions and quantum dots [8]. In quantum simulators, complete control of all components is not required and they are, thus, easier to realize in comparison to the most challenging quantum-technology systems – quantum computers.

Quantum computing relies on encoding information into quantum states of two-level systems known as *quantum bits* or *qubits*. As each qubit can be a quantum superposition of the 0-state and the 1-state, both classical bits 0 and 1 can be manipulated in parallel by single-qubit operations. If multiple qubits are entangled, the number of states that can be manipulated in parallel exponentially grows with the number of qubits. Consequently, exponential speed-ups of calculations can be achieved by quantum computers. This advantage could be used to solve complex problems within reasonably long time frames, which is not feasible by classical computers. An example is the factorization of large numbers by the Shor's algorithm [9].

The idea of a powerful quantum computer is in practice considerably complicated by decoherence - a tendency of quantum objects to lose their quantum properties due to interactions with their environment. The noise from the environment leads to the mechanisms of energy relaxation and dephasing. In the first one, a qubit in the excited state (1-state) decays into the ground state (0-state), while in the second one a coherent superposition of the two states evolves into their statistical mixture [9]. Decoherence is inevitable as qubits have to be manipulated and therefore cannot be isolated from their environment. In order to deal with decoherence, error-correction protocols have been proposed [10]. However, these protocols make use of additional qubits, which increase the total number of qubits and impose the challenge of making a scalable quantum computer.

Achieving high qubit coherence on a scalable qubit platform has been an extremely challenging scientific and engineering task over the past two decades. Various platforms have been extensively studied by many scientists in academia and industry. These qubit platforms include superconducting quantum circuits [11], semiconducting quantum dots [12], trapped ions [13], NV centers in diamond [14] and topological superconductors [15]. Quantum processors have been experimentally realized in most of qubit platform - with an exception for topological superconductors, where no single topological qubit has been demonstrated yet. However, the route of topological quantum computation is still being actively investigated as the topological qubits have been predicted to exhibit significantly improved coherence in comparison to the currently used qubits. Their robustness to decoherence stems from the inherent properties of topological superconductors rather than from specific advancements in the qubit design or operation. Therefore, topological qubits are not only promising candidates for quantum computation, but also form a hot topic in condensed matter physics. In the following section, we introduce the fundamental properties of topological superconductors and show how they are exploited in topological quantum computing.

1

1.2. TOPOLOGICAL QUANTUM COMPUTING

In the three-dimensional world, all quantum particles can be divided in two classes based on their exchange statistics. Upon exchanging the positions of two indistinguishable particles, the wavefunction Ψ describing the system of particles can either remain unchanged or flip its sign. The first class of particles, where $\Psi \to \Psi$, are bosons, which typical representatives are photons. The second class, where $\Psi \to -\Psi$ are fermions, with electrons as common examples. Upon exchanging the same pair of fermions or bosons twice, the system wavefunction remains the same as before the exchanges, as $\Psi \to \pm\Psi \to \Psi$ [16]. The mathematical property that the wavefunction remains unchanged has a physical consequence that the system observables do not change their values.

If one considers a system of indistinguishable particles confined in two dimensions, a third class of particles arises. In this class, exchanging the positions of two particles twice does not bring the system into its initial state, but, instead, changes the phase factor in its wavefunction [17]. This means that a single exchange of two particles gives $\Psi \to e^{\pm i\alpha}\Psi$, where the two signs correspond to the clockwise and anti-clockwise exchange direction. These particles are known as *anyons* since the global phase factor can take *any* value [18]. Typical representatives of anyons are edge states in the quantum spin-Hall system [19, 20].

A system of anyons becomes even more interesting if its ground state is degenerate. In this case, exchanging a pair of anyons can move the system from one to another quantum state within the same ground-state degeneracy manifold. This means that exchanging two anyons corresponds to multiplying the system wavefunction by a matrix, and, therefore, an interesting consequence of it is that exchange operations do not commute in general. These anyons are known as *non-Abelian* anyons [21] and typical representatives are Majorana zero modes (MZMs). The paths of exchanging MZMs in the three-dimensional time-space (one temporal axis + two spatial axis) can be visualized as braids and their manipulation is therefore referred as *braiding* [22].

Majorana zero modes are quasiparticles that are an equal superposition of an electron and a hole. They are in condensed matter mathematically analogous to the Majorana fermions originally established by Ettore Majorana as zero-energy solutions of the Dirac equation [23]. By being half-electron and half-hole, MZMs can in pairs host single electrons. Furthermore, due to the zero- energy of MZMs an electron can occupy a pair of MZMs with no energy cost and lead to a double parity-degeneracy of the ground state of the system containing the MZMs. If the number of pairs of MZMs is increased (N), the size of the degeneracy manifold exponentially increases 2^N. MZMs obey the non-Abelian exchange statistics and by moving them one can realize braiding operations [24]. These operations move the system through different ground states in which the total electron parity remains fixed, but the occupancy of MZMs can change. Importantly, the outcome of braiding depends only on the initial state of the system and the pair of MZMs being exchanged, but not on particular details, such as the microscopic path along which the MZMs move. If during braiding MZMs do not overlap, these operations are protected against local perturbations because the electron states encoded in the MZMs are non-local. Such robustness to local disturbances is analogous to the preservation of properties of geometrical objects studied in topology. For example, an orange can be smoothly transformed into a cup without a handle by only stretching and twisting and without caring about particular (local) details of these transformations. However, making a cup with a handle would require a non-smooth transformation of creating a hole in the orange by cutting and gluing. Analogously, braiding moves the system with MZMs through its degeneracy manifold and the system remains in it as long as non-smooth perturbations of its Hamiltonian do not take place. This robustness to smooth perturbations in the Hamiltonian make the braiding of MZMs *topologically* protected against local noise and represent the ultimate advantage to be used in the *topological quantum computing*. In contrast to other quantum computing platforms, the qubit states here belong to the same degeneracy manifold and have thus the same energy. Furthermore, the qubit states are manipulated through braiding which is in its nature fault-tolerant. Finally, the qubit is read-out by the process of fusion [25], where two MZMs are brought close to each other and annihilated by giving either an electron or a hole.

So far, MZMs have not been found to spontaneously occur in nature like, for example, spins do in semiconductors and are used for spin qubits. Therefore, MZMs have to be engineered first before a topological qubit could be realized. However, engineering MZMs is itself already a great challenge and one could argue that topological quantum computing is therefore practically inferior to other quantum computing platforms. Nevertheless, the theoretically envisioned advantages from the fault-tolerance of topological qubits have still made topological quantum computing a hot topic in both the academic and industrial community. This has resulted in significant advancements in fabrication, control and understanding of condensed matter systems in which scientists have been trying to engineer MZMs. This thesis also tackles some of the challenges that have recently been taken towards improving and better understanding various hybrid semiconductor-superconductor quantum devices that could host MZMs.

1.3. THESIS OUTLINE

The main body of this thesis involves five chapters (Chapter 3-7) that correspond to five experimental studies that we have conducted over the past five years. Although these studies have been done on various material platforms and quantum devices, studying the quantum transport in hybrid semiconductor-superconductor nanostructures is their common element. Some of these experiments have inspired our collaborators to develop theoretical models that have given possible interpretations of the experiments and have become integral parts of the studies.

Before presenting our work, we first give a theoretical background in **Chapter 2**, where we introduce fundamental concepts of semiconductors, superconductors and the quantum transport in hybrid devices that combine them. Particularly, the physics of semiconducting Josephson junctions (JJs) and hybrid islands is described. We also explain how a topological superconducting phase with Majorana zero modes (MZMs) arises in hybrid devices and by which experimental signatures it is accompanied.

In **Chapter 3**, we study the current-phase relation (CPR) of an InSb-Al nanowire Cooper pair transistor (CPT). The supercurrent through the CPT is measured as a function of the electro-chemical potential in the nanowire and an axial magnetic field reaching ~ 200 mT. We also develop a theoretical model of the supercurrent transport mediated by subgap states in a hybrid island.

In order to improve the compatibility of nanowire JJs with high magnetic fields, we examine in **Chapter 4** the impact of junction length on the supercurrent resilience against magnetic field. We use the shadow-wall lithography technique to obtain InSb-Al nanowire JJs with lengths varying from 30 nm to 160 nm, and we examine how their supercurrents vanish when high magnetic fields are applied.

By implementing the design developed in Chapter 4, we embed a 40 nm-long InSb-Al nanowire JJ into a superconducting loop with another identical JJ. In **Chapter 5**, we perform the CPR measurements while varying the junction electro-chemical potential and increasing axial magnetic fields up to ~ 700 mT. Here, we also develop a theoretical model of the supercurrent through a JJ in the presence of interference between a localized state and direct transmission.

Moving from the supercurrent experiments, in **Chapter 6** we present tunneling spectroscopy measurements in hybrid InSb-Al nanowires that use nm-thick tunnel barriers. The novel tunnel probes are realized by combining the shadow-wall lithography and controlled oxidation of the Al film on the nanowires. Since these probes can be positioned at any point along a hybrid nanowire, we use multiple tunnel probes along single hybrids to examine the longitudinal evolution of their subgap states.

Next, we induce superconductivity in the two-dimensional hole gas (2DHG) platform with high-mobility Ge. In **Chapter 7**, we thermally diffuse Pt into Ge/SiGe quantum wells to obtain superconducting PtSiGe and proximity-induce superconudctivity in Ge. We characterize the induced superconductivity by realizing common hybrid device architectures, while particularly assessing the hardness of the induced superconducting gap.

Finally, in the closing **Chapter 8** we give our main conclusions and propose future experiments that are inspired by the previous chapters.

REFERENCES

[1] M. Planck. “Ueber das Gesetz der Energieverteilung im Normalspectrum”. In: *Annalen der Physik* 4 (3 1901), pp. 553–653.

[2] H. Hertz. “Ueber einen Einfluss des ultravioletten Lichtes auf die electrische Entladung”. In: *Annalen der Physik* 267 (8 1887), pp. 983–1000.

[3] A. Einstein. “On a Heuristic Viewpoint Concerning the Emission and Transformation of Light”. In: *Annalen der Physik* 17 (1905).

[4] J. P. Dowling and M. G. “Quantum technology: the second quantum revolution”. In: *Philosophical Transactions of the Royal Society* (2003).

[5] A. K. Ekert. “Quantum cryptography based on Bell’s theorem”. In: *Phys. Rev. Lett.* 67 (6 1991), pp. 661–663.

[6] S. Pirandola, B. R. Bardhan, T. Gehring, C. Weedbrook, and S. Lloyd. “Advances in photonic quantum sensing”. In: *Nature Photon.* 12 (2018), pp. 724–733.

[7] R. Feynman. “Simulating Physics with Computers”. In: *International Journal of Theor. Phys.* 21 (1982), pp. 467–488.

[8] “Nature Physics Insight - Quantum Simulation”. In: *Nat. Phys.* 8.4 (2012).

[9] M. A. Nielsen and I. A. Chuang. *Quantum Computation and Quantum Information.* University Press, 2000.

[10] B. M. Terhal. “Quantum error correction for quantum memories”. In: *Rev. Mod. Phys.* 87 (2 2015), pp. 307–346.

[11] P. Krantz, M. Kjaergaard, F. Yan, T. P. Orlando, S. Gustavsson, and W. D. Oliver. “A quantum engineer’s guide to superconducting qubits”. In: *Appl. Phys. Rev.* (6 2019), p. 021318.

[12] G. Burkard, T. D. Ladd, A. Pan, J. M. Nichol, and J. R. Petta. “Semiconductor spin qubits”. In: *Rev. Mod. Phys.* 95 (2 2023), p. 025003.

[13] R. M. C. D. Bruzewicz J. Chiaverini and J. M. Sage. “Trapped-ion quantum computing: Progress and challenges”. In: *Appl. Phys. Rev.* (6 2019), p. 021314.

[14] S. Pezzagna and J. Meijer. “Quantum computer based on color centers in diamond”. In: *Appl. Phys. Rev.* (8 2021), p. 011308.

[15] C. Nayak, S. H. Simon, A. Stern, M. Freedman, and S. Das Sarma. “Non-Abelian anyons and topological quantum computation”. In: *Rev. Mod. Phys.* 80 (3 2008), pp. 1083–1159.

[16] V. B. Berestetskii, E. M. Lifshitz, and L. P. Pitaevskii. *Quantum Electrodynamics.* Butterworth-Heinemann, 1971.

[17] F. Wilczek. “Quantum Mechanics of Fractional-Spin Particles”. In: *Phys. Rev. Lett.* 49 (14 1982), pp. 957–959.

[18] F. Wilczek. “Magnetic Flux, Angular Momentum, and Statistics”. In: *Phys. Rev. Lett.* 48 (17 1982), pp. 1144–1146.

[19] B. I. Halperin. “Statistics of Quasiparticles and the Hierarchy of Fractional Quantized Hall States”. In: *Phys. Rev. Lett.* 52 (18 1984), pp. 1583–1586.

[20] H. Bartolomei, M. Kumar, R. Bisognin, A. Marguerritte, J.-M. Berroir, E. Bocquillon, B. Placais, A. Cavanna, Q. Dong, U. Gennser, Y. Jin, and G. Féve. “Fractional statistics in anyon collisions”. In: *Science* 368 (2020), pp. 173–177.

[21] N. Read and D. Green. “Paired states of fermions in two dimensions with breaking of parity and time-reversal symmetries and the fractional quantum Hall effect”. In: *Phys. Rev. B* 61 (15 2000), pp. 10267–10297.

[22] D. A. Ivanov. “Non-Abelian Statistics of Half-Quantum Vortices in *p*-Wave Superconductors”. In: *Phys. Rev. Lett.* 86 (2 2001), pp. 268–271.

[23] E. Majorana. “Teoria simmetrica dell’elettrone e del positrone”. In: *Il Nuovo Cimento* 14 (1937), pp. 171–184.

[24] R. Aguado. “Majorana quasiparticles in condensed matter”. In: *La Riv. del Nuovo Cim.* 40 (2017), p. 523.

[25] J. Alicea, Y. Oreg, G. Refael, F. von Oppen, and M. P. A. Fisher. “Non-Abelian statistics and topological quantum information processing in 1D wire networks”. In: *Nat. Phys.* 7 (2011), pp. 412–417.

2

THEORY

Hybrid nanostructures combining semiconductors and superconductors are experimentally and theoretically studied in this thesis. Here, we give a fundamental theoretical background relevant for the phenomena studied in the following chapters. We start with semiconducting nanostructures and BCS superconductivity. Then, we explain the transport mechanisms between a normal metal and a superconductor. We continue by introducing hybrid Josephson junctions and relevant transport phenomena inside magnetic fields. We also explain how topological superconductivity is predicted to arise in hybrid nanowires, and we give a brief overview of different trivial examples mimicking the topological scenario. Finally, we explain the transport through a Cooper pair transistor based on the hybrid nanowire platform, and we give a brief summary of the Fano resonant effect.

2

2.1. SEMICONDUCTING NANOSTRUCTURES

2.1.1. GENERAL CONCEPTS

Electrons in bulk solids occupy states which energies are grouped in continuous intervals of energy bands. This is the direct consequence of the periodic potential that is set by the crystal lattice of solids. Depending on the lattice atomic properties, the energy bands can overlap or be separated by forbidden intervals of energy gaps [1]. In semiconductors, the highest occupied (valence) band and the lowest unoccupied (conduction) band are separated by an energy gap over which electrons can be thermally excited into the conduction band and take part in transport. The states that are so left unoccupied in the valence band are equivalent to positively charged holes that also take part in transport.

Dispersive relation $E(\mathbf{k})$ between the energy and the wave vector for electrons (holes) in the conduction (valence) band is well approximated by the parabolic dispersive relation for free electrons $E(\mathbf{k}) = \hbar^2 k^2/2m^*$ - with an important correction that m^* is an effective mass that reflects the effect of the crystal lattice potential on the electron (hole) motion. With a confinement along any (x, y, z) direction, the wave vector projection along that direction becomes quantized and the continuous energy bands split into discrete subbands that are associated with the discrete projection values. The spacing between the subbands increases with the confinement strength. This is how parabolic subbands emerge for the in-plane motion in quantum wells and for longitudinal motion in nanowires [1].

An important consequence of one dimensional confinement and parabollic subbands in nanowires is that the ballistic transport is quantized [2]. The conductance G at zero temperature and zero magnetic field is a multiple of the number of subbands N crossing the Fermi level and the conductance quantum $G_0 = 2e^2/h$ (e is the elememtary charge and h is the Planck constant). Essentially, this is the direct consequence of the one dimensional density of states $D(E) \propto \frac{1}{\sqrt{E}}$ and the electron momentum $\hbar k_x \propto \sqrt{E}$ - which results in an energy-independent contribution of the electrons at energy E $dI(E) \propto k_x D(E) dE \propto \text{const.} dE$ to the total current I. If the transport is not ballistic and scatterings are prominent, the diffusive transport occurs and it is described by the Drude model [3]. The conductance then depends on the electron mobility $\mu_n = e\tau/m^*$ as $G = \mu_n n e$, where τ is the time between two scattering events and n is the electron concentration.

Semiconducting nanostructures have more complex energy dispersion when two important interactions between an electron spin and local fields are considered. We briefly introduce these effects in the two following paragraphs.

The interaction between the magnetic moment of an electron and a magnetic field manifests through the Zeeman effect [4]. The Zeeman Hamiltonian for spin $\hbar\boldsymbol{\sigma}/2$ inside the field $\mathbf{B}$ is:

$$H_Z = \frac{1}{2}\mu_B g \boldsymbol{\sigma} \cdot \mathbf{B} \tag{2.1}$$

where $\mu_B = e\hbar/2m_0 = 5.788 \times 10^{-6}\,\mathrm{eVT^{-1}}$ is the Bohr magneton and g is the Landé factor. The magnetic field symmetrically splits the spin-degenerate electron eigenstates into a pair of states where the spin and the field are either parallel or antiparallel. These states are separated in energy by $\mu_B g B$.

The coupling of an electric field **E** to the spin $\boldsymbol{\sigma}$ of an electron with a momentum **p** leads to the spin-orbit interaction effect. In the non-relativistic limit, this effect is described by the Hamiltonian [5]:

$$H_{SO} = -\frac{\hbar}{4m_0^2c^2}\boldsymbol{\sigma}\cdot\mathbf{p}\times\mathbf{E} \tag{2.2}$$

where c is the speed of light. The effect can be intuitively and roughly understood as an effective Zeeman effect for the spin in its rest frame – where the electric field is Lorentz-transformed into a magnetic field [6]. Spin-orbit interaction is present when spatial inversion symmetry is broken. This happens via the bulk inversion asymmetry (BIA) - that is intrinsic to some crystal lattices, or via the structural inversion asymmetry (SIA) – that is caused by confinements and externally applied electric fields. The BIA mechanism is referred as the Dresselhaus spin-orbit interaction [7], while the SIA mechanism is known as the Rashba spin-orbit interaction [8].

2.1.2. RASHBA NANAOWIRES

Electron energy spectrum in semiconducting nanowires consists of different subbands for the longitudinal motion of an electron along the nanowire. In Fig. 2.1(a), we show a schematic of a semiconducting nanowire placed along the x-axis on top of an electrostatic gate that sets an electro-chemical potential μ in the nanowire. The nanowire has a hexagonal cross-section - as representative Rashba nanowires made of III-V semiconductors (InAs and InSb). The dispersive relation of the first subband is then $E(k_x) = \hbar^2k_x^2/2m^* - \mu$ and the Fermi wave vector is $k_{F0} = \sqrt{2m^*(E_F+\mu)}/\hbar$, as shown in Fig. 2.1(b) on the left.

An electric field **E** set by the gate is in the (y,z)-plane (due to the symmetry constraints) and, therefore, it is perpendicular to the electron wave vector **k** along the x-axis. The Rashba spin-orbit field $\mathbf{B_{SO}} \propto \mathbf{k}\times\mathbf{E}$ then lays in the (x,y)-plane. For the simplicity, let us assume that **E** is along the z-axis and $\mathbf{B_{SO}}$ is along the y-axis, as depicted in Fig. 2.1(a). If an external magnetic field **B** is applied along the nanowire, with α and g being the Rashba spin-orbit coefficient and Landé g-factor, the nanowire Hamiltonian in the basis $\Psi = \left(c_\uparrow, c_\downarrow\right)^T$ reads:

$$H_0 = \left(\frac{\hbar^2k_x^2}{2m^*} - \mu\right)\sigma_0 + \alpha k_x\sigma_y + E_Z\sigma_z \tag{2.3}$$

where the Zeeman term is $E_Z = \frac{1}{2}g\mu_B B$.

If the external field is zero ($E_Z = 0$) and the spin-orbit interaction is finite, the single band splits along the k_x-axis by $\pm k_{SO} = m^*\alpha/\hbar^2$ into two bands and both bands move down in energy by $E_{SO} = m^*\alpha^2/2\hbar^2$ (Fig.2.1(b) in the middle). The new Fermi wave vector is $k_F = k_{SO} + \sqrt{k_{F0}^2 + k_{SO}^2}$ The electron states corresponding to these two bands have spins that are parallel and antiparallel to the $\mathbf{B_{SO}}$ field. Note that the degeneracy at $k_x = 0$ remains, as $B_{SO} = 0$ there.

A finite external field ($E_Z > 0$) removes the degeneracy at $k_x = 0$ by introducing a splitting of $2E_Z$ (Fig. 2.1(b) on the right). As $\mathbf{B}\perp\mathbf{B_{SO}}$, the pairs of eigenstates have

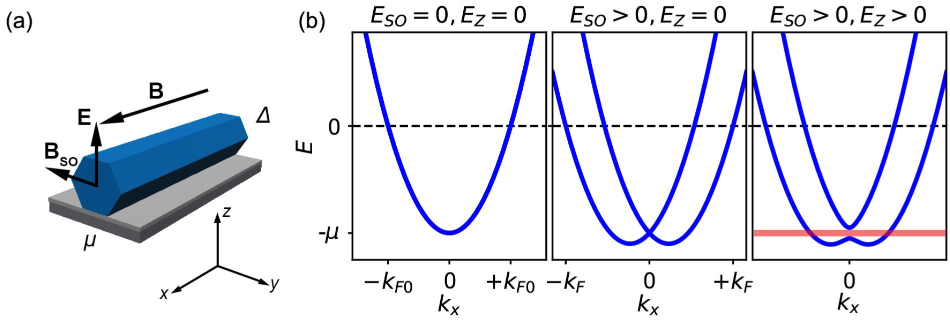

Figure 2.1: **(a)** Schematic of a Rashba nanowire (blue) on top of a gate (grey) that sets the electro-chemical potential μ in the nanowire. An external magnetic field **B** is parallel to the nanowire and perpendicular to the electric field **E** set by the gate and the spin-orbit field $\mathbf{B_{SO}}$. **(b)** Dispersive relation of a single subband without spin-orbit interaction and magnetic field (left), with finite spin-orbit interaction only (middle) and with both finite spin-orbit interaction and magnetic field (right).

opposite spins, which axis ranges from the x-axis at $k_x = 0$ to the z-axis at large k_x. Removing the degeneracy at $k_x = 0$ has an important consequence that there is an energy range (shaded in red in Fig. 2.1(b) on the right) where the electron spin and the electron momentum are interlocked. This interval is called a helical gap.

In InSb Rashba nanowires, the physics described above is quantified by the following parameters: $m^* = 0.014\, m_0$, $\alpha = [0.2-1]\,\mathrm{eV{\cdot}Å}$, $E_{SO} = [0.05-1]\,\mathrm{meV}$ and $g = [40-50]$ [9].

2.1.3. PLANAR GE

Bulk germanium has diamond cubic structure with p-orbitals forming covalent bonds. Three-fold degeneracy of p-orbitals with the angular momentum quantum number $l = 1$ (magnetic quantum numbers $m_l = -1, 0, +1$) and the two-fold spin degeneracy (with spin quantum numbers $m_s = -1/2, +1/2$) are expected to give rise to a six-fold degeneracy in the valence band. However, due to the spin-orbit interaction, the angular momentum **L** and spin **S** are coupled, and the total angular momentum $\mathbf{J} = \mathbf{L} + \mathbf{S}$ characterizes electron states with corresponding total angular momentum quantum numbers $j = |l \pm s|$ and $m_j = m_l + m_s$. At the Γ point ($k = 0$), the six-fold degeneracy of the valence band splits into a four-fold degeneracy of states where **L** and **S** are parallel and $j = 3/2$, and two-fold degeneracy where **L** and **S** are antiparallel and $j = 1/2$ [5]. Around the Γ point, the top of the valence band further splits depending on the projection of **J** on **k** – into a heavy hole (HH) band with projections $m_j = \pm 3/2$, and a light hole (LH) band with projections $m_j = \pm 1/2$ (see Fig. 2.2(a)) [10]. The effective masses corresponding to these bands $m_{HH} \approx 0.33 m_0$ and $m_{LH} \approx 0.04 m_0$ (m_0 is the free electron mass) are derived from the Luttinger parmeters for bulk germanium and differ by approximately one order of magnitude [11]. The splitting due to the spin-orbit interaction in bulk germanium

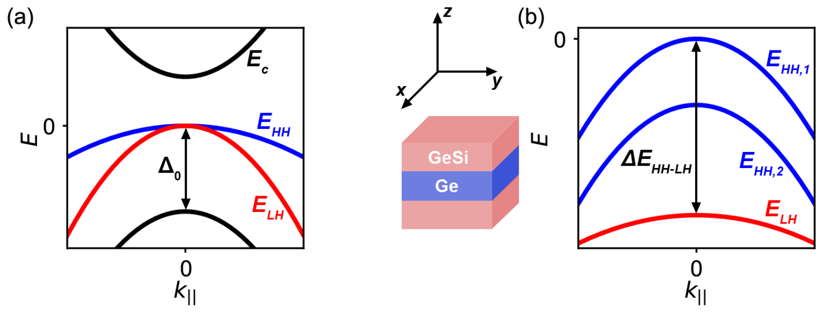

Figure 2.2: **(a)** Band structure of bulk germanium. The top of the valence band is four-fold degenerate, with heavy holes (HH,blue) and light holes (LH, red) bands. The spin-split band is separated from the rest of the valence band by Δ_{SO}. E_C is the conduction band. **(b)** The top of the valence band for planar germanium. The HH-like subbands (blue) and LH-like subbands (red) are splitted by ΔE_{HH-LH} due to the confinement and strain. HH-like subbands exhibit smaller effective mass.

is $\Delta_0 = 0.3\,\text{eV}$ [5].

When pure germanium is confined between two SiGe buffer layers, a Ge quantum well with a two-dimensional hole gas (2DHG) is formed - due to the valence band offset. The strong confinement along the growth direction (z-axis in Fig. 2.2) leads to large values of the perpendicular wave vector projections (k_z). Consequently, the eigenstates of the confined structure are closely described by the states of heavy holes and light holes in the bulk [5]. Such heavy hole-like (HH-like) and light hole-like (LH-like) states in planar Ge exhibit a degeneracy splitting even at $k_{||} = 0$ [12]. This splitting due to confinement is inversely proportional to the square of the quantum well width and can thus be controlled by design.

The splitting between the HH-like and LH-like bands is enhanced by the Ge quantum well being compressively strained between the two SiGe layers. Namely, the lattice constants of Ge and SiGe are $a_{\text{Ge}} = 5.66\,\text{Å}$ and $a_{\text{SiGe}} = 5.43\,\text{Å}$, and even strains of orders of few percents can cause a splitting between the HH-like and LH-like states of tents of meV. The splitting is controlled by the composition x in the $\text{Si}_{1-\text{x}}\text{Ge}_{\text{x}}$ layers.

The confinement and strain effects add up and finally determine the total splitting between HH-like and LH-like states ΔE_{HH-LH}, as shown in Fig. 2.2(b). Note that the band structure here consists of different subbands corresponding to the in-plane motion in the Ge 2DHG. Interestingly, the HH-like subbands are characterized by rather low effective mass for in-plane motion $m_{HH,||} = 0.055 m_0$, while the LH-like subbands are described by higher effective mass $m_{LH,||} = 0.125 m_0$ [13].

Diamond cubic structure of Ge has a center of inversion, and the Dresselhaus spin-orbit interaction is negligible. The spatial inversion asymmetry for planar Ge only occurs through the structural inversion symmetry breaking via interfaces and gates in real devices. This means that the spin-orbit interaction has the Rashba nature. Moreover, it is cubic, as the Rashba coefficients of k^3 terms dominate. This is because the particular lattice symmetry makes the Rashba coefficients of linear terms small [14].

Holes in planar Ge exhibit highly anisotropic Zeeman effect – with $g_\perp \gg g_{||}$, where $g_\perp$ ($g_{||}$) is the g-factor for perpendicular (in-plane) magnetic fields. Physically, the big anisotropy is mainly caused by the splitting between the HH-like and LH-like subbands. The g-factors are also related to the Rashba coefficients and are, therefore, tunable by external electric fields [15, 16].

2

2.2. SUPERCONDUCTIVITY

Superconductivity is a macroscopic quantum phenomenon that is observed to occur in some metals at sufficiently low temperatures. It is manifested by non-dissipative electron transport in a superconductor below its critical temperature [17]. Some interesting consequences of this are that currents can flow through superconductors without developing voltages and that superconductors exhibit perfectly diamagnetic behaviour [18]. It took nearly five decades in the condensed matter physics community for these and other related striking phenomena to be theoretically understood. Bardeen, Cooper and Schrieffer created the BCS theory [19] that at the time of the development could explain superconducting experimental observations with high precision. However, this theory does not explain high-T_c superconductors that were later discovered, and which full understanding still remains a great challenge [20].

2.2.1. BCS THEORY

The main idea of the BCS theory is that electrons in superconductors pair up in bound states – Cooper pairs. As they consist of two fermions, Cooper pairs are bosons and can form a condensate at the Fermi energy. The formation of Cooper pairs occurs as an attractive electron-electron interaction - mediated by the phonons of the crystal lattice - exceeds the repulsive electron-electron Coulomb interaction. The net interaction energy can thus become negative and the state with paired electrons becomes favourable in energy [21].

With $c^\dagger_{\mathbf{k}\sigma}$ ($c_{\mathbf{k}\sigma}$) being the creation (annihilation) operator of an electron with wave vector $\mathbf{k}$ and spin σ, and under the mean-field approximation, the BCS Hamiltonian reads:

$$H = \sum_{\mathbf{k},\sigma} \epsilon_\mathbf{k} c^\dagger_{\mathbf{k}\sigma} c_{\mathbf{k}\sigma} + \sum_{\mathbf{k}} (\Delta_\mathbf{k} c^\dagger_{\mathbf{k}\uparrow} c^\dagger_{\text{-}\mathbf{k}\downarrow} + \Delta^*_\mathbf{k} c_{\mathbf{k}\uparrow} c_{\text{-}\mathbf{k}\downarrow}) \tag{2.4}$$

where the first sum includes kinetic energy terms $\epsilon_\mathbf{k} = \frac{\hbar^2 k^2}{2m} - E_F$ with respect to the Fermi energy E_F and the second sum includes pairing energy terms with the order parameter $\Delta_\mathbf{k}$. The BCS Hamiltonian can be diagonalized by transforming the electron operators $c_{\mathbf{k}\sigma}$ into the operators of Bogoliubov quasiparticles $\gamma_\mathbf{k}$. This is done by the Bogoliubov transformation [22]:

$$\begin{aligned} c_{\mathbf{k}\uparrow} &= u^*_\mathbf{k} \gamma_{\mathbf{k}+} + v_\mathbf{k} \gamma^\dagger_{\mathbf{k}-} \\ c^\dagger_{\text{-}\mathbf{k}\downarrow} &= -v^*_\mathbf{k} \gamma_{\mathbf{k}+} + u_\mathbf{k} \gamma^\dagger_{\mathbf{k}-} \end{aligned} \tag{2.5}$$

which is due to the normalization condition $|u_{\mathbf{k}}|^2 + |v_{\mathbf{k}}|^2 = 1$ equivalent to:

$$\begin{aligned} \gamma_{\mathbf{k}+} &= u_{\mathbf{k}} c_{\mathbf{k}\uparrow} - v_{\mathbf{k}} c^{\dagger}_{\text{-}\mathbf{k}\downarrow} \\ \gamma^{\dagger}_{\mathbf{k}\text{-}} &= v^{*}_{\mathbf{k}} c_{\mathbf{k}\uparrow} + u^{*}_{\mathbf{k}} c^{\dagger}_{\text{-}\mathbf{k}\downarrow} \end{aligned} \tag{2.6}$$

Each Bogoliubov quasiparticle is a superposition of an electron and a hole that have opposite wave vectors with respect to the Fermi level and have opposite spins. The factors $u_{\mathbf{k}}$ and $v_{\mathbf{k}}$ correspond to the electron and hole components in the superposition. They can be chosen such that the BCS Hamiltonian in the new basis is diagonal:

$$H = E_0 + \sum_{\mathbf{k}} E_{\mathbf{k}} (\gamma^{\dagger}_{\mathbf{k}+} \gamma_{\mathbf{k}+} + \gamma^{\dagger}_{\mathbf{k}\text{-}} \gamma_{\mathbf{k}\text{-}}) \tag{2.7}$$

with a constant condensation energy E_0 and eigenergies $E_{\mathbf{k}} = \sqrt{\epsilon^2_{\mathbf{k}} + \Delta^2_{\mathbf{k}}}$ that correspond to excitations of Bogoliuboc quasiparticles. The factors $u_{\mathbf{k}}$ and $v_{\mathbf{k}}$ satisfy:

$$\begin{aligned} |u_{\mathbf{k}}|^2 &= \frac{1}{2}\left(1 + \frac{\epsilon_{\mathbf{k}}}{E_{\mathbf{k}}}\right) \\ |v_{\mathbf{k}}|^2 &= \frac{1}{2}\left(1 - \frac{\epsilon_{\mathbf{k}}}{E_{\mathbf{k}}}\right) \end{aligned} \tag{2.8}$$

The two operators introduced in Eq. 2.6 mathematically correspond to two particle-hole symmetric solutions of the Bogoliubov-de Gennes equation - with energies $\pm E_{\mathbf{k}}$. However, since one operator creates and the other annihilates a quasiparticle, their excitations have the same energy $E_{\mathbf{k}}$, as visible in Eq. 2.7. The minimal excitation energy is $|\Delta_{\mathbf{k}}|$ and this non-zero value representing an energy gap for excitations is the superconducting gap.

The length scale at which the density of Cooper pairs varies is known as the superconducting coherence length ξ. This parameter roughly represents the size of a Cooper pair. In a clean bulk superconductor, the coherence length ξ_0 is related to the Fermi velocity v_F in the normal state and the superconducting gap Δ as $\xi_0 = \hbar v_F / \pi\Delta$. In a dirty supercnductor with an electron mean free path l, the coherence length ξ is related to the clean bulk coherence length as $\xi = \sqrt{\xi_0 l}$.

2.2.2. DENSITY OF STATES IN SUPERCONDUCTORS

In bulk metals the Fermi surface is spherical and the excitation energies depend on the wave vector magnitude $k = |\mathbf{k}|$. If the superconducting pairing $\Delta_{\mathbf{k}}$ is independent on $\mathbf{k}$ (s-wave superconductors), the superconducting gap Δ uniformly opens at the Fermi surface, where $k_F = \frac{\sqrt{2mE_F}}{\hbar}$.

In Fig. 2.3(a), the excitation spectrum $E = \sqrt{\epsilon^2_k + \Delta^2} = \sqrt{\left(\frac{\hbar^2 k^2}{2m} - E_F\right)^2 + \Delta^2}$ is plotted versus k. The excitations at the Fermi surface ($|k| = k_F$) have energy $E = \Delta$ ($\epsilon_k = 0$) and consequently $u = v = \frac{1}{2}$. These excitations are equal superpositions of electrons and holes. The excitations outside the Fermi surface ($|k| > k_F$) correspond to $\epsilon_k > 0$ and therefore have $u_k > v_k$. The larger electron component in the superposition

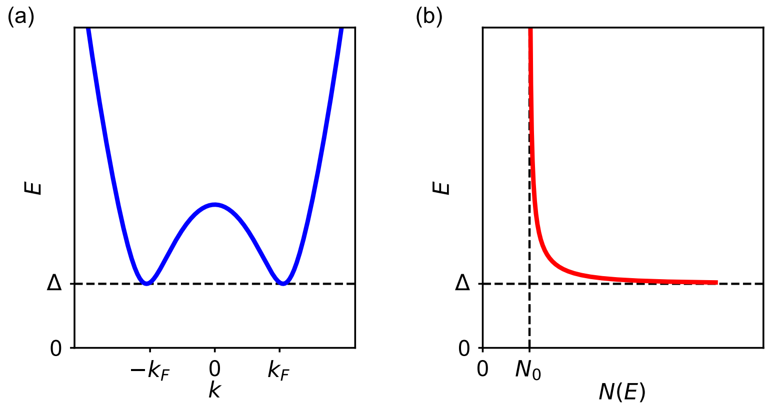

Figure 2.3: **(a)** Quasiparticle energy as a function of the wave vector; **(b)** Density of quasiparticle states as a function of the quasiparticle energy.

makes these excitations electron-like. Similarly, the hole-like excitations originate from the interior of the Fermi surface ($|k| < k_F$), where $\epsilon_k < 0$ and thus $u_k < v_k$. The quasiparticle phase velocity is proportional to the derivative dE/dk. From Fig. 2.3(a), it can be seen that these derivatives have opposite signs for electron-like and hole-like quasiparticles. Electron-like quasiparticles propagate in the direction of the wave vector, while the hole-like quasiparticles propagate in the opposite direction.

As there is one-to-one correspondance between the quasiparticle states and the electron states, a density of quasparticle states $N(E)$ satisfies $N(E)dE = n(\epsilon)d\epsilon$, where $n(\epsilon)$ is the density of electron states in the normal state. If this density is approximated to be constant $n(\epsilon) = N_0$, the quasiparticle density of states is:

$$N(E) = n(\epsilon)\frac{d\epsilon}{dE} = \frac{N_0 E}{\sqrt{E^2 - \Delta^2}} \tag{2.9}$$

and $N(E) = 0$ for $E < \Delta$, inside the gap. The dependence in Eq. 2.9 is shown in Fig. 2.3(b). Density of quasiparticle states diverges and peaks at $E = \Delta$ (coherence peak). For $E \gg \Delta$, $N(E)$ approaches the density of electron states N_0.

When transport in superconductors is considered, the excitation picture described here is conveniently replaced by another - the one-particle picture that is used in normal metals. In this picture, the positive quasiparticle energies are mirror-reflected below the Fermi level such that a branch of holes of quasiparticles is introduced. The ground state is then characterized by all the negative energies being occupied. Excitations in this picture are present either as occupied quasiparticle states at positive energies or as empty (missing quasiparticle) states at negative energies. The convenience of such representation is that all allowed transitions in the transport are "horizontal" in energy diagrams.

2.3. TRANSPORT BETWEEN A NORMAL METAL AND A SUPERCONDUCTOR

Transport between a normal metal (N) and a superconductor (S) is described by Blonder, Tinkham and Klapwijk in the BTK model [23]. Here, we introduce the model and give the main results relevant for the transport through an NS interface.

Dispersive relations on two sides of an NS interface in equilibrium are shown in Fig. 2.4(a). The barrier at the interface has the δ-function profile with strength Z. The dispersive relations close to the Fermi levels are approximated by the linear and parabolic dependences on the N and S side, respectively. The superconductor has a gap Δ.

We consider an electron at an energy $E > \Delta$ that is incident on the NS interface and has a positive group velocity. The electron can undergo different processes which are associated with probability amplitudes a, b, c and d, and corresponding probabilities A, B, C and D, as depicted in Fig. 2.4(a). First, the electron can be elastically reflected (probability B) into a state at the same energy and the opposite velocity – in which case no transport occurs. Next, the electron can be transmitted through the NS interface into quasiparticle states at the same energy, while maintaining the direction of its group velocity. Therefore, the electron can either be transmitted (probability C) into an electron-like quasiparticle with positive wave vector, or (probability D) into a hole-like excitation with negative wave vector. Finally, the electron can undergo the Andreev reflection (probability A), in which an oppositely propagating hole is created at the energy $-E$ on the N side. In this case, a net charge of $2e$ is transferred through the NS interface, as the reflected hole corresponds to the electron that forms a Cooper pair with the incident electron. With taking into account all described processes, the wave function in the normal metal reads:

$$\psi^{(N)} = \begin{pmatrix}1\\0\end{pmatrix} e^{iq_+x} + a\begin{pmatrix}0\\1\end{pmatrix} e^{-iq_-x} + b\begin{pmatrix}1\\0\end{pmatrix} e^{-iq_+x} \tag{2.10}$$

and in the superconductor:

$$\psi^{(S)} = c\begin{pmatrix}u_0\\v_0\end{pmatrix} e^{ik_+x} + d\begin{pmatrix}v_0\\u_0\end{pmatrix} e^{-ik_-x} \tag{2.11}$$

where u_0 and v_0 are the electron and hole coherence factors of the electron-like quasiparticle in the process C. Note that the hole-like quasiparticle in the process D has interchanged electron and hole coherence factors.

By solving the Bogoliubov-de Gennes equation with imposing $A+B+C+D=1$ and continuity of the wavefunction and its first derivative at the NS interface, the BTK model is solved to give the probabilities. The probability for the Andreev reflection is:

$$A(E) = \begin{cases} \dfrac{\Delta^2}{E^2+(\Delta^2-E^2)(1+2Z^2)^2}, & \text{if } E \le \Delta \\ \dfrac{u_0^2 v_0^2}{\gamma^2}, & \text{if } E > \Delta \end{cases} \tag{2.12}$$

2

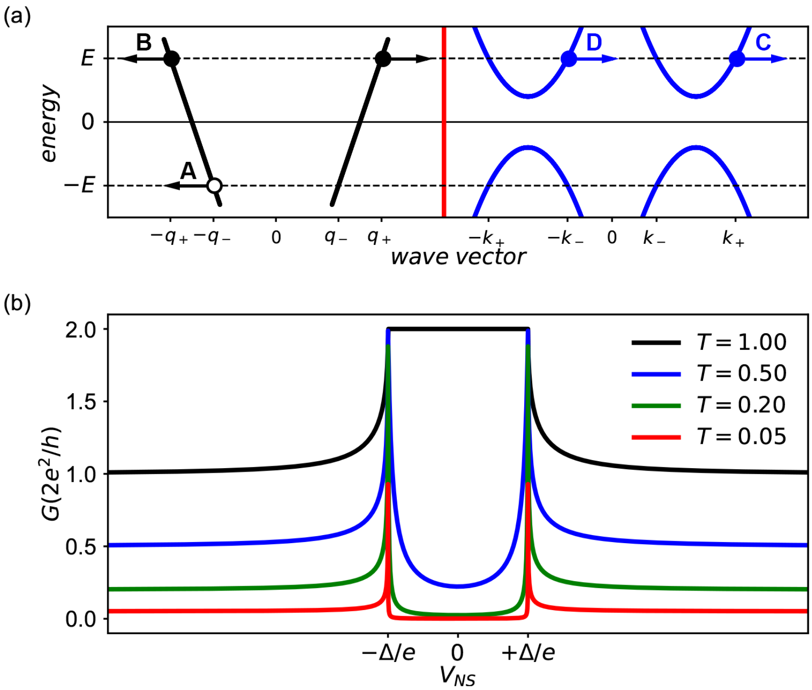

Figure 2.4: **(a)** Dispersive relation for the normal metal (N, black) and the superconductor (S, blue) with the NS interface (red) in equilibrium. q- and k-wave vectors correspond to the excitations at energy E on each side. An incident electron undergoes different processes with probabilities A, B, C and D. **(b)** Differential conductance G through the NS interface as a function of the bias voltage V_{NS} for different interface transparencies T.

and the probability for normal reflection is:

$$B(E) = \begin{cases} 1 - A(E), & \text{if } E \leq \Delta \\ \dfrac{(u_0^2 - v_0^2)^2 Z^2 (1+Z^2)}{\gamma^2}, & \text{if } E > \Delta \end{cases} \tag{2.13}$$

with $\gamma = u_0^2 + Z^2(u_0^2 - v_0^2)$. Note that $A(E)$ vanishes for $E \gg \Delta$ and that the electron is transmitted with probability $1 - B(E) \approx \frac{1}{1+Z^2} = T$, meaning that such defined T is the transmission of the barrier.

The probability coefficients above are needed for calculating the differential conductance G through the NS interface when a bias voltage V_{NS} is applied:

$$G(V_{NS}) = \frac{2e^2}{h}(1 + A(eV_{NS}) - B(eV_{NS})) \tag{2.14}$$

In Fig. 2.4(b), we plot this dependence for different barrier strengths leading to different transparencies T. One can see that for a perfect transmission $T = 1$ (no barrier, $Z = 0$), the conductance inside the gap has a $4e^2/h$ plateau - meaning that each electron is perfectly Andreev reflected into the condensate of the superconductor. This is known as the Andreev enhancement. Far above the gap, the conductance reaches a $2e^2/h$ plateau as each electron is perfectly transmitted into the quasiparticles in the superconductor. As T decreases (finite barrier, $Z > 0$), both in-gap and out-of-gap conductance drop as the normal reflection competes with both Andreev reflection and quasiparticle transmission. Finally, for small T (strong barrier, $Z \gg 1$), the in-gap conductance is suppressed more than the out-of-gap conductance. This in-gap suppression reflects the nature of Andreev reflection -where both an electron and a hole have to tunnel through the interface. Mathematically, this is visible in the Beenakker formula [24]:

$$G(V_{NS} = 0) = \frac{2e^2}{h}\frac{2T^2}{(2-T)^2} \tag{2.15}$$

where the conductance at the zero bias voltage is quadratically suppressed with the transparency of the barrier at the NS interface.

2.4. JOSEPHSON JUNCTIONS

Any weak link between two superconductors (S) that allows for a non-dissipative transport of Cooper pairs represents a Josephson junction (JJ). The weak link can be in the form of a thin insulating (I) barrier, a section of a normal (N) conductor (metal), or a constricted (c) superconductor - therefore, one can define SIS, SNS and ScS junctions [20]. In SIS junctions, the transport of Cooper pairs occurs via tunnelling through the barrier between the superconductors. This gives rise to a non-disspative (super)current I that has a sinusoidal dependence on the phase difference ϕ between the superconductors:

$$I = I_c \sin\phi \tag{2.16}$$

while the voltage drop V over the junction is proportional to the first derivative of ϕ in time:

$$\frac{d\phi}{dt} = \frac{2e}{\hbar}V \tag{2.17}$$

If a bias current I is below I_c, ϕ is constant and $V = 0$ (dc Josephson effect). If a finite bias voltage V is applied, ϕ changes in time and consequently the current I through the junction has varying signs (ac Josephson effect). The critical current in tunnel junction is influenced by the superconducting gap and the junction geometry. If the linear dimensions of the junction are smaller than the superconducting coherence length (short junction limit), the critical current I_c is proportional to the barrier cross-section and anti-proportional to its thickness. Consequently, if R_N is the normal resistance of the junction, the product I_cR_N is constant [25].

In the following sections we are focusing on SNS junctions, since they represent the major building blocks of various devices in this thesis.

2

2.4.1. SNS JOSEPHSON JUNCTIONS

Supercurrent in an SNS Josephson junction is mediated by electron and hole excitations in the N section, that undergo Andreev reflections at two (SN and NS) interfaces. This is illustrated in Fig. 2.5(a). An electron propagating to the right - and being incident on the NS interface at an energy below the superconducting gap Δ - is Andreev-reflected into a hole. The hole is a time-reversed partner of the electron and propagates to the left and is incident on the SN interface. There, it is Andree-reflected into an electron that then propagates to the right and starts a new sequence, as the initial electron started. In the described transport sequence, a Cooper pair is removed from the left superconductor and transferred into the right superconductor, which is manifested as a non-dissipative supercurrent. For each sequence depicted in Fig. 2.5(a), there is a counterpart sequence involving an electron moving to the left and a hole moving to the right. This sequence transfers a Cooper pair from the right lead to the left lead. If the time-reversal symmetry is preserved, these two sequences cancel out at the zero phase difference between the superconducting leads and the supercurrent vanishes. Otherwise, the supercurrent is finite for finite phases.

Andreev reflection is not only crucial for the supercurrent transport in SNS JJs at zero bias voltage. It is also responsible for transport when a finite bias voltage is applied between the superconductors. Namely, multiple Andreev reflections (MARs) give rise to subgap conductance peaks in SNS JJs at certain bias voltage values below $2\Delta/e$ (Δ being the superconducting gap in the leads) [26]. If the bias voltage is above $2\Delta/e$, quasiparticles from one superconductor can simply propagate into empty quasiparticle states of the other superconductor. In Fig. 2.5(b), it is shown how a MARs process gives rise to single electron transport at a finite subgap bias voltage. A quasiparticle in the left superconductor transfers into a right-propagating electron that is incident at the NS interface below the gap. Therefore, it is Andreev reflected into a left-propagating hole that is incident at the SN interface, also below the gap. This hole is finally Andreev reflected into a right-propagating electron that can freely leave the N section and transfer to the continuum of empty quasiparticle states in the right superconducting lead. In the described sequence, the N section is crossed three times and two consecutive Andreev reflections take place. This sequence corresponds to the third-order MARs and it is prominent when the bias voltage equals $2\Delta/3e$. In general, the MARs can be of any order n and then take place at bias voltages $2\Delta/ne$. Under this condition high densities of states of two coherence peaks (filled states on the left and empty states on the right) are matched to yield the enhanced conductance. This is visible in Fig. 2.5(b) for $n = 3$. A more precise treatment shows that the occupation probabilities of electrons and holes acquire saw-tooth profiles which peaks cross the gap edges under the same bias voltage condition [23]. This additionally enhances the MARs conductance at the bias voltages given above.

It should be noted that a non-perfect transmission $T < 1$ of the N section (caused by normal scatterings in the section and at the interfaces) makes that the contributions of n-th order MARs decrease as T^n. Therefore, observing high order MARs implies high transparency of SNS junctions [27–29].

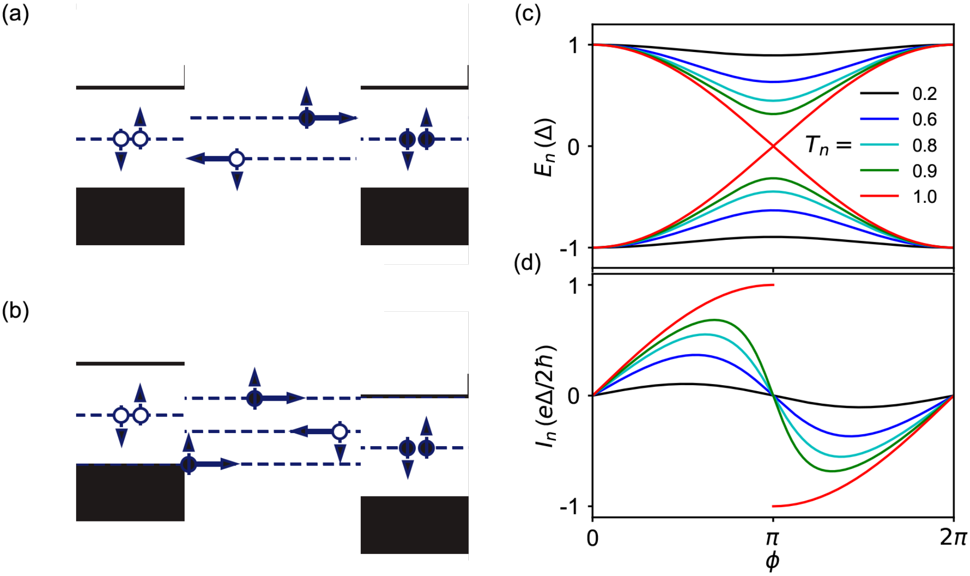

Figure 2.5: **(a)** Supercurrent transport for an SNS JJ. An Andreev bound state (ABS) consisting of an electron (full circle) and a hole (empty circle) is formed inside the junction below the superconducting gap Δ. The electron and the hole have opposite spins and opposite directions of propagation. A Cooper pair is transferred from the left lead to the right lead at the zero bias voltage. **(b)** Multiple Andreev reflection (MAR) transport in the junction. An electron is transferred from the occupied continuum of quasiparticle states of the left lead into the unoccupied continuum of quasiparticle states of the right lead via multiple consecutive Andreev reflections. The panel depicts the third order MAR (with two Andreev reflections) at the bias voltage $2\Delta/3e$. **(c)** Energy E_n of a single Andreev level and **(d)** supercurrent I_n carried by the level as a function of the superconducting phase difference ϕ between the leads. Different traces correspond to different transparencies T_n of the channel n that forms the Andreev level.

The correlated electron-hole pairs that arise in the N segment thanks to the Andreev reflection form Andreev bound states (ABSs). The spectrum of ABSs is derived by considering a scattering matrix problem for electrons and holes inside the N segment [26]. In this problem, the scattering matrix of the N segment is diagonal in the electron-hole space – since a simple propagation over the junction only scatters electrons to electrons and holes to holes, and does not transfer them to each other. Oppositely, at the interfaces, electrons are scattered into holes (and vice versa), and only a phase shift is added if the interface is perfect. If an electron at energy E is scattered at the interface $i = (L, R)$ (the left and right superconductor have phases ϕ_L and ϕ_R) into a hole at energy $-E$, the hole is phase shifted by $-\arccos(E/\Delta) - \phi_i$ with respect to the phase of the electron. Similarly, the scattering of a hole gives an electron shifted by $-\arccos(E/\Delta) + \phi_i$ in phase. If the described three matrices are multiplied to represent a full cycle in propagation, eigenvectors of such matrix product are the ABSs, and are obtained from the condition for non-trivial solutions of the described eigenproblem. The Andreev level formed from the channel n disperses with the junction phase $\phi = \phi_L - \phi_R$ as:

$$E_n = \pm\Delta\sqrt{1 - T_n \sin^2(\phi/2)} \tag{2.18}$$

where T_n is the eigenvalue of the junction transmission matrix for channel n. The energy-phase dispersions are shown for different transmissions in Fig. 2.5(c) (top). Note that the levels are spin-degenerate if no magnetic field is present.

If spin σ is taken into account, the quantity $E_{gs}(\phi) = -\frac{1}{2}\sum_{n,\sigma} E_{n,\sigma}(\phi)$ - where the sum goes over all positive Andreev levels $E_{n,\sigma} < \Delta$ – represents the ground state energy which derivative is proportional to the supercurrent:

$$I(\phi) = \frac{2e}{\hbar}\frac{dE_{gs}}{d\phi} = -\frac{e}{\hbar}\sum_{n,\sigma}\frac{dE_{n,\sigma}}{d\phi} = \frac{e\Delta}{4\hbar}\sum_{n,\sigma}\frac{T_n \sin\phi}{\sqrt{1 - T_n \sin^2(\phi/2)}} \tag{2.19}$$

and $I(\phi)$ represents the current-phase relation (CPR) of the JJ. The contribution to the CPR per a single spin-degenerate Andreev level is shown in Fig. 2.5d as $I_n(\phi)$ for different transmissions T_n as in the panel (c). As the transmission increases, the approximately sinusoidal $I_n(\phi)$ dependence becomes skewed. Therefore, a skewed sinusoidal CPR of a JJ indicates a high junction transparency. In another limit, if there are many channels with low transmission inside the junction, the total supercurrent has approximately sinusoidal dependence on phase $I(\phi) \approx I_c \sin\phi$, with the critical current $I_c = \frac{e\Delta}{2\hbar}\sum_n T_n$. Therefore, a quantization of critical current is a superconducting analogous to the quantization of conductance in normal transport regime [30].

2.4.2. MAGNETIC FIELD EFFECTS

If an external magnetic field is applied to an SNS JJ, an interplay among Zeeman effect, spin-orbit interaction and orbital effects modifies the Andreev levels spectrum and ultimately affects the CPR of the junction. The first two effects are particularly relevant for junctions made of III-V semiconductors with large g factor and spin-orbit interaction. The third effect is prominent in junctions where multiple channels inside the N segment contribute to the supercurrent. Here, we shortly describe these effects by summarizing some results of [31] and [32].

Zeeman and spin-orbit effects studied in [31]. We adjust and display several figures from this work in Fig. 2.6. An SNS JJ is formed in a nanowire along the x-axis and an external magnetic field B is applied along the y-axis (Fig. 2.6(a)). If we focus on a single channel in the N section, the field breaks its spin degeneracy and introduces Zeeman energies of opposite signs to the electron and the hole forming an Andreev level. The Zeeman contributions to the electron and the hole wave vector add up into a spin-dependent phase shift:

$$\theta_B = \pm\frac{g\mu_B BL}{\hbar v_F} \tag{2.20}$$

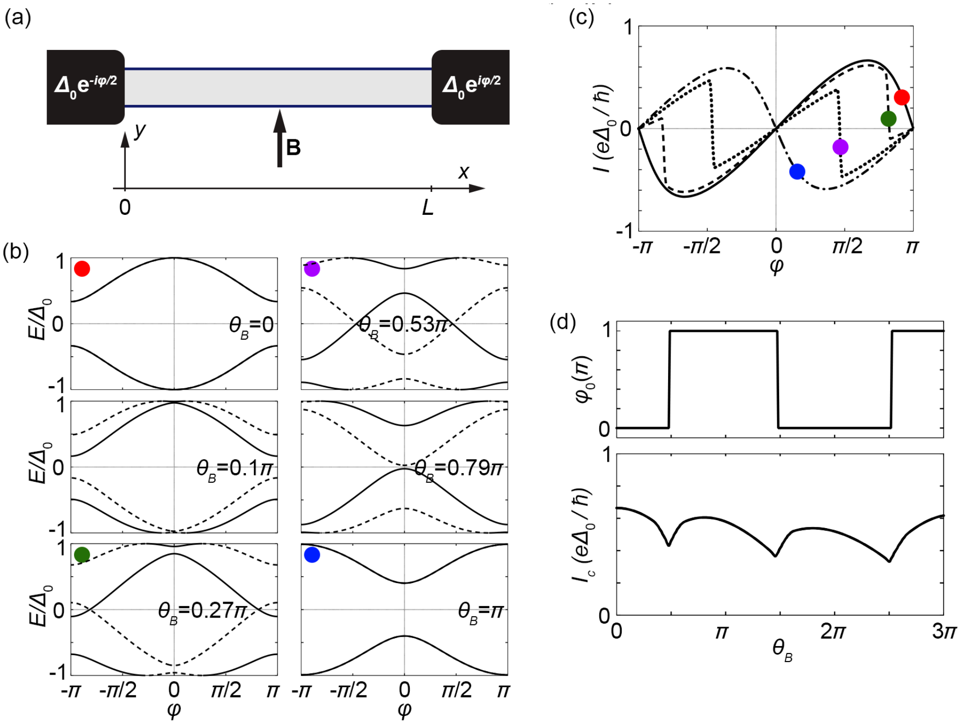

Figure 2.6: **(a)** Schematic of an SNS (nanowire) JJ along the x-axis. The junction length is L, two superconducting leads have phase difference ϕ and a magnetic field B is along the y-axis. **(b)** Andreev levels dispersions with ϕ (single channel) for different values of θ_B. Solid and broken line correspond to two electron-hole pairs with opposite spins. **(c)** Supercurrent dependence on ϕ for several θ_B values taken in (b) (see the markers in different colours). **(d)** Phase of the minimal energy ϕ_0 and critical current I_c as functions of θ_B. The figure has been taken from [31] and modified.

where L is the junction length and v_F is the Fermi velocity of the channel. If multiple transport channels are considered, v_F is replaced with an average Fermi velocity $\overline{v_F}$, where $\frac{1}{\overline{v_F}} = \frac{1}{N}\sum_n \frac{1}{v_{F,n}}$ is the average over the all active channels n. The two signs of θ_B correspond to two oppositely propagating electron-hole pairs.

Fig. 2.6(b) shows how increasing θ_B splits the four subgap Andreev levels of the junction (single channel $N=1$ case) and how the CPR acquires a π shift (Fig. 2.6(c)). For $\theta_B = 0$, the levels are spin-degenerate and the ground state energy has the minimum at $\phi_0 = 0$. As θ_B increases, the Andreev levels split and at sufficiently large fields cross the zero energy. These crossings result in cusps in the CPR, as it can be seen in Fig. 2.6(c). For $\theta_B \approx \pi/2$, the energy minimum moves from $\phi_0 = 0$ to $\phi_0 = \pi$, as visible in Fig. 2.6(d), and the π-junction regime is reached. Finally, at $\theta_B = \pi$, the CPR is smooth and shifted by π relative to the intial CPR at $\theta_B = 0$. Dependences of the ground state phase ϕ_0 and of the maximal supercurrent – critical current I_c – on θ_B are shown in Fig. 2.6(d). Critical current exhibits cusps at θ_B values associated with the $0-\pi$ transitions. Note that by increasing the field some levels move above the gap and do not contribute to the supercurrent [33], while other levels move below the gap – such that the number of Andreev levels remains fixed. The results in Fig. 2.6 are obtained for a single channel, the Zeeman energy is considered only inside the junction and the spin-orbit interaction is neglected. Therefore, although the work considers a perpendicular B field, the results that we show here also hold for a parallel magnetic field. The case with multiple channels are qualitatively similar. A common feature of the spectrum is that the Andreev levels are symmetric with respect to $\phi = 0$ – $E(\phi) = E(-\phi)$. This means that the supercurrent obeys $I(\phi) = -I(-\phi)$ and, thus, $I(\phi = 0) = 0$. In cases with spin-orbit interaction, Andreev levels are not anymore symmetric with respect to the zero phase and a finite supercurrent is present at $\phi = 0$ – a phenomenon known as the anomalous Josephson effect [34–37]. Finally, if multiple channels are considered, the supercurrent magnitude becomes dependent on the supercurrent direction.

Orbital effects are studied in [32]. If an external axial magnetic field B is applied along a nanowire JJ, it couples to the quantized azimuthal motion of electrons and holes. Semi-classically, while an electron in the subband with the orbital number l travels along its spiral path over the junction (Fig. 2.7(a)), it accumulates a phase difference with its partner hole, which is:

$$\delta_{n,l} = \frac{elBL}{mv_{F,l}} \tag{2.21}$$

where m is the electron effective mass and $v_{F,l}$ is the Fermi velocity of the corresponding subband. As a result, the Andreev level is shifted in phase depending on the subband orbital number. If the coupling of B to l is treated fully quantum mechanically, the same result is obtained within the Andreev approximation and the approximations of conduction shell model. The first approximation assumes that the electron and hole wave vectors are approximately the same ($k_e, k_h \gg |k_e - k_h|$) and it breaks close to the bottom of the subband. The second approximation assumes that the electron (hole) states are localized within a certain distance from the interface, propagating through a ring-like cross-section of radius R. The phase shifts depend only weakly on R and the applied normalized flux is $\Phi = \pi R^2 B/(h/e)$. A subband l carries a supercurrent which primary peak occurs for flux:

$$\Phi_1 = \frac{\pi v_{F,l} m R^2}{\hbar l L} \tag{2.22}$$

Since the Fermi velocity exhibits a dependence on flux through the change of the effective chemical potential, the positions of other peaks are aperiodic in flux.

If multiple subbands cross the Fermi level (Fig. 2.7(b)), each pair of subbands has certain flux values for which the sum of their individual contributions to the supercurrent is maximal via the Josephson interference. These conditions are aperiodic in flux and if multiple subbands are involved, the resulting critical

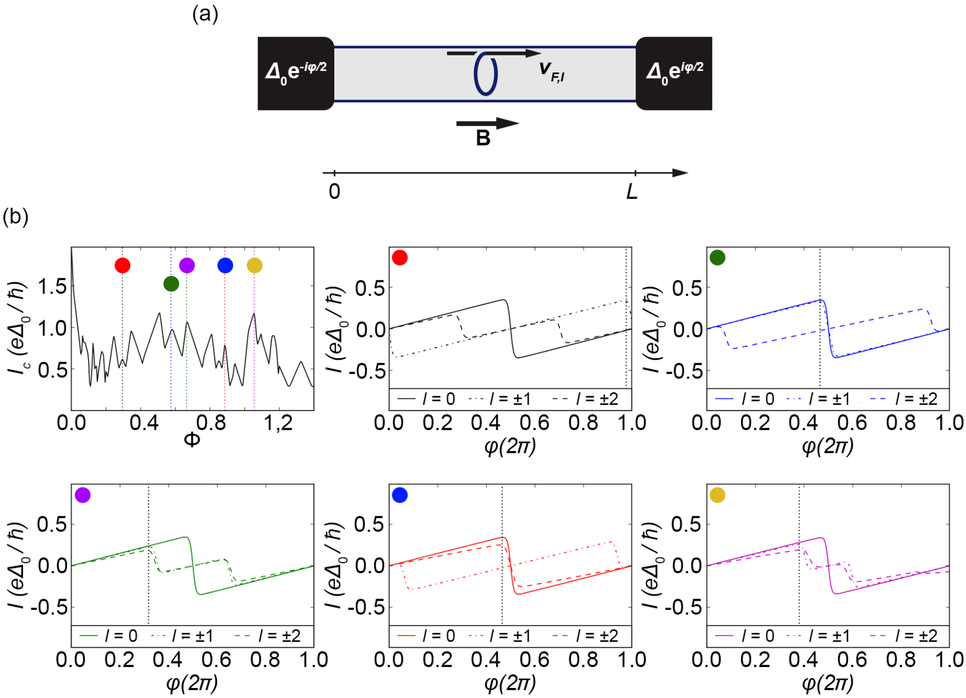

Figure 2.7: **(a)** Schematic of a nanowire JJ of length L and phase difference ϕ between the leads (superconducting gap is Δ_0). A subband l is via the angular motion coupled to the parallel magnetic field B. **(b)** Critical current I_c of the junction as a function of the normalized flux Φ through the nanowire exhibits aperiodic maxima (top left). CPR of the supercurrent carried by individual subbands l for different values of Φ (remaining five panels, colour markers). Dotted vertical lines in the CPR panels mark the phase ϕ for which the Josephson interference gives the maximal supercurrent - the critical current in the top-left panel. The figure has been taken and modified from [32].

current exhibits a complex dependence on the B field, as illustrated in Fig. 2.7(b). Furthermore, scatterings inside the N section and at the interfaces (SN and NS) cause additional phase randomization and can smear out the critical current fluctuations [38].

The phenomena that we have described in this section are analogous in a sense that they all occur due to the pick-up of electron-hole phase difference, which modifies the dispersion of Andreev levels and consequently the supercurrent. Increasing the junction length, magnetic field or the number of active subbands inside the junction all make these effects more prominent.

2

2.4.3. DC-SQUID

When a single JJ is biased with a current below its critical current, the phase difference between its superconducting leads is constant and takes a value such that the junction can support the maximal supercurrent. If the junction CPR is sinusoidal, the phase difference equals $\pi/2$, for which the maximal supercurrent equals the critical current.

If two JJs (JJ1 and JJ2) are connected in parallel by a superconducting loop, they form a dc version of the superconducting quantum interference device (SQUID) shown in Fig. 2.8(a). If both junctions have sinusoidal CPRs with critical currents I_{c1} and I_{c2}, the supercurrent through the SQUID is:

$$I_{SQUID} = I_{c1}\sin(\phi_1) + I_{c2}\sin(\phi_2) \tag{2.23}$$

where ϕ_1 and ϕ_2 are the phase differences over corresponding junctions. Since the junctions are embedded in the superconducting loop, ϕ_1 and ϕ_2 are not independent and, in general, cannot independently take values such that the supercurrents in both junction always reach the critical current values. The phases are connected via the flux Φ through the superconducting loop as:

$$\phi_1 - \phi_2 = 2\pi\frac{\Phi}{\Phi_0} \tag{2.24}$$

where $\Phi_0 = h/2e$ is the superconducting flux quantum. A critical current of the SQUID is thus a function of the flux and each flux value $\Phi = \Phi'$ has a corresponding phase $\phi_1 = \phi'$ such that the expression:

$$I_{SQUID}(\phi_1, \Phi') = I_{c1}\sin(\phi_1) + I_{c2}\sin\left(\phi_1 - 2\pi\frac{\Phi'}{\Phi_0}\right) \tag{2.25}$$

is maximal and $I_{SQUID}(\phi', \Phi') = I_{c,SQUID}$ is the critical current of the SQUID. It can be easily found as the diagonal of a parallelogram spanned on vectors with lengths I_{c1} and I_{c2} that have a phase shift of $2\pi\Phi/\Phi_0$. If we use the cosine theorem:

$$I_{c,SQUID} = \sqrt{I_{c1}^2 + I_{c2}^2 + 2I_{c1}I_{c2}\cos\left(2\pi\frac{\Phi}{\Phi_0}\right)} \tag{2.26}$$

Consequently, the critical current of the SQUID ranges from $|I_{c1} - I_{c2}|$ to $I_{c1} + I_{c2}$. In Fig. 2.8(b), $I_{c,SQUID}(\Phi)$ dependences are shown for $I_{c1} = 1\,\text{nA}$ and I_{c2} taking the values 1 nA, 2 nA and 6 nA. If the SQUID is symmetric ($I_{c1} = I_{c2}$), the critical current of the SQUID can drop to zero and its flux dependence is non-sinusoidal with cusps (red curve). As the SQUID becomes more asymmetric ($I_{c2} > I_{c1}$), $I_{c,SQUID}(\Phi)$ dependence gradually becomes sinusoidal and ultimately for $I_{c2} \gg I_{c1}$ resembles the CPR of the junction with the smaller critical current. This is because, for a highly asymmetric dc-SQUID, the phase difference over the junction with large critical current remains constant in order to maximize the total supercurrent, and an external flux thus effectively modulates only the phase over the junction with small critical current. This is conveniently used in experiments to investigate the CPR of a JJ by embedding it in the SQUID architecture with another (reference) junction that has much larger critical current.

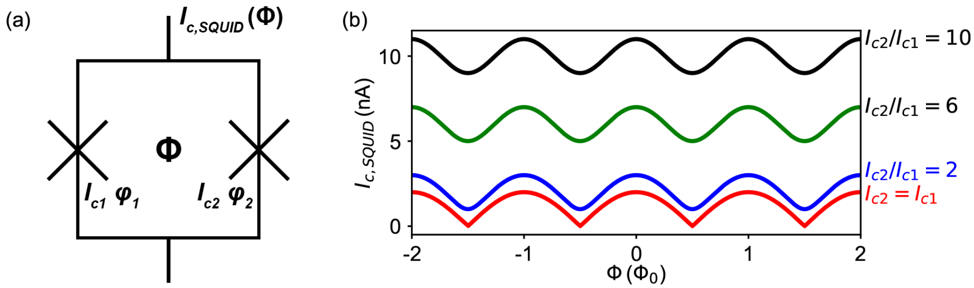

Figure 2.8: **(a)** Schematic of a dc-SQUID with two Josephson junctions JJ1,2 with critical currents $I_{c1,2}$ and phase drops $\phi_{1,2}$ inside the superconducting loop penetrated by the flux Φ. **(b)** Dependence of the SQUID critical current on Φ for different I_{c2}/I_{c1} ratios.

2.5. TOPOLOGICAL SUPERCONDUCTIVITY

Topological superconductors are unconventional superconductors which bulk band structure has an inverted superconducting gap. Consequently, due to the bulk-edge correspondence, a topological superconductor hosts zero-energy excitations at its boundaries and at topological defects. Such mid-gap states are known as Majorana zero modes (MZMs). Topological superconductivity occurs when p-wave superconducting pairing is introduced into a spinless Fermi liquid. Such scenario has so far not been conclusively established in currently known materials [39]. However, there are proposals how such conditions can be reached through engineering by putting together different materials and combining their properties. In this section, we focus on creating topological superconducting phase in hybrid semiconductor-superconductor nanowires.

2.5.1. MAJORANA NANOWIRE MODEL

The proposals for creating MZMs in hybrid nanowires [40, 41] rely on introducing s-wave superconducting pairing into a Rashba nanowire inside a parallel magnetic field (Fig. 2.9(a)). The Rashba nanowire has already been introduced in the first section of this chapter, and the influence of the parallel magnetic field on its band structure $E(k)$ is shown in Fig. 2.1(b). There, we show how the field removes the degeneracy at $k = 0$ and how this results in an effective spinless scenario. Here, we introduce conventional s-wave superconducting pairing into the Rashba Hamiltonian (Eq. 2.3) by adding a term with the induced superconducting gap that couples the states below and above the Fermi energy. The Hamiltonian of a Majorana nanowire then reads:

$$H_{NW} = \left(\frac{\hbar^2 k^2}{2m^*} - \mu\right)(\tau_z \otimes \sigma_0) + \alpha k(\tau_z \otimes \sigma_y) + E_Z(\tau_0 \otimes \sigma_z) + \Delta(\tau_x \otimes \sigma_0) \tag{2.27}$$

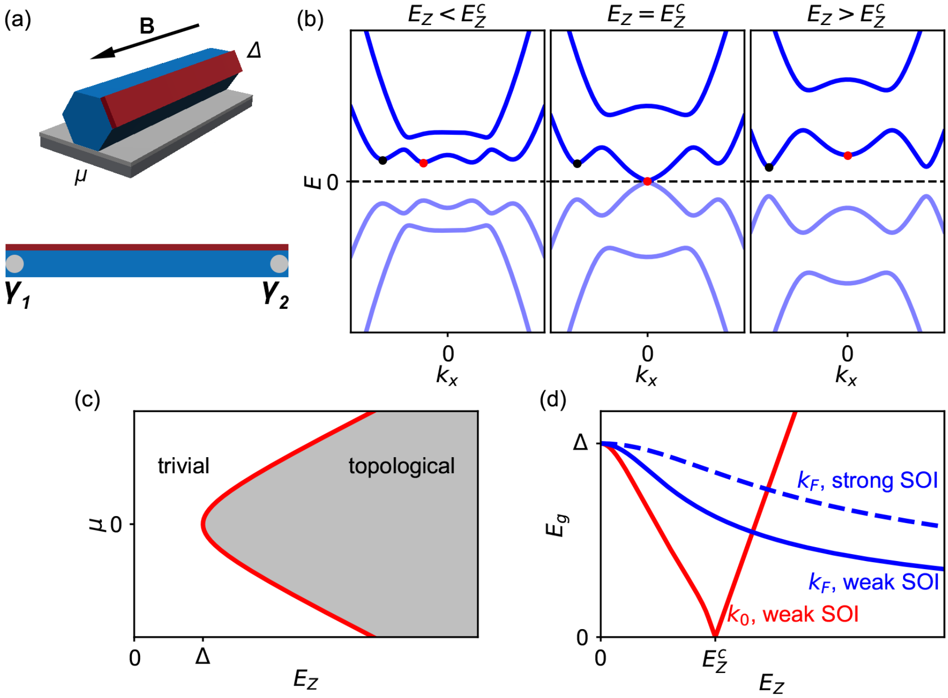

Figure 2.9: **(a)** Schematic of a hybrid semiconductor-superconductor nanowire formed by coupling a Rashba nanowire (blue) to an s-wave superconductor (red), inside a parallel magnetic field B (Zeeman energy E_Z) and on top of a gate (grey) setting the electro-chemical potential μ. Majoranas $\gamma_{1,2}$ are present at the hybrid nanowire ends in the topological phase. **(b)** Energy dispersion of a single band of the hybrid nanowire before (left), at (middle) and after (right) the topological phase transition at the critical Zeeman energy E_Z^c. The black and red dots mark the energy gap E_g at small wave vector k_0 and large wave vector k_F. **(c)** Single band phase diagram in the (μ, E_Z) parameter space with the topological phase in grey and the phase boundary $E_Z^2 = \Delta^2 + \mu^2$ in red. **(d)** The bulk gap at k_0 (full red line) and k_F (full blue line) as a function of E_Z. $E_g(k_F)$ is also shown for a stronger spin-orbit interaction (blue broken line).

where τ and σ are the Pauli matrices in the particle-hole and spin space, respectively. The basis is the Nambu spinor $\Psi = (c_\uparrow, c_\downarrow, c_\downarrow^\dagger, -c_\uparrow^\dagger)^T$ for a single spin-degenerate band. All other terms have already been defined in Eq. 2.3.

The superconducting term opens the gap Δ at the Fermi energy in the particle-hole symmetric spectrum. Since the degeneracy at $k = 0$ is already removed by the combined effect of the Zeeman and spin-orbit interaction, the coupled electrons and holes have finite k and their spins have parallel and anti-parallel components. Therefore, the resulting superconducting pairing has an effective p-wave component.

Energy gaps open at small k (k_0) and large k (k_F) (black and red dots in Fig. 2.9(b). The gap at k_0 closes for a critical Zeeman energy $E_Z^c = \sqrt{\Delta^2 + \mu^2}$. As E_Z further increases, the gap at $k = 0$ reopens and the band inversion takes place. At this point the nanowire enters into a topological superconducting phase and two MZMs γ_1 and γ_2 appear at the ends of the hybrid (Fig. 2.9(a)). The topological phase occurs in the entire parameter range beyond the red phase boundary $E_Z^2 = \Delta^2 + \mu^2$ in Fig. 2.9(c).

In an infinitely long nanowire, the MZMs have exact zero energy and they are protected by the topological gap that corresponds to the minimum between the gaps E_g at $k_0 = 0$ and k_F. We show the E_g dependences on E_Z in Fig. 2.9(d). It can be seen that $E_g(k_0)$ exhibits closely linear dependence on E_Z before the phase transition – as the spin-orbit interaction is small due to small k_0. For $E_Z > E_Z^c$, this dependence is fully linear as $k_0 = 0$ and the spin axis is parallel to the Zeeman field. For $E_g(k_F)$, the evolution with E_Z is non-linear due to the spin-orbit interaction being larger at k_F. Also, the stronger spin-orbit interaction protects the topological gap at k_F for large E_Z (broken line in Fig. 2.9(d).

For the MZMs $\gamma_{1,2}$, the self-conjugate operator relations for Majorana fermions hold - $\gamma_{1,2} = \gamma_{1,2}^\dagger$. Therefore, they are purely real and correspond to the real and imaginary part of a single fermionic mode c_0 at zero energy:

$$\begin{aligned} c_0^\dagger &= \gamma_1 + i\gamma_2 \\ c_0 &= \gamma_1 - i\gamma_2 \end{aligned} \tag{2.28}$$

As the MZMs are present at the nanowire ends, this fermion has the non-local nature and, due to its zero energy, its two occupations correspond to a double-degenerate ground states of the system. The length scale at which the MZMs wavefunction extend from the hybrid ends into the hybrid bulk is the Majorana coherence length ξ^M. The non-locality of the mid-gap fermionic mode is quantified by the overlap between the $\gamma_{1,2}$ wavefunctions, and this overlap quantifies the susceptibility of the system to sources of local noise. In the limit of an infinitely long nanowire ($L \to \infty$) the two MZMs have a zero overlap and the non-local fermionic mode is topologically protected against local noise.

If L is finite, the MZMs exhibit a finite overlap and a finite splitting E_M from the zero energy. These oscillate with E_Z and μ via an effective Fermi wave vector k_F^{eff} that describes the oscillations of the Majorana wavefunctions [42]. In this case, the finite energy E_M reads:

$$E_M = \frac{\hbar^2 k_F^{\text{eff}}}{2m^* \xi^M} \cos(k_F^{\text{eff}} L) e^{-2L/\xi^M} \tag{2.29}$$

The amplitude of the oscillation increases with E_Z and μ, and since neither the overlap nor the energy are fixed at zero anymore, the non-local fermionic mode is not perfectly protected from local noise. However, this sensitivity to noise is exponentially suppressed by increasing the hybrid length L (as visible in Eq. 2.29).

2.5.2. CONSIDERATIONS BEYOND THE MINIMAL MODEL

When the realistic configuration of a hybrid nanowire is considered, the calculations of energy spectrum and topological phase give results that are much more complex

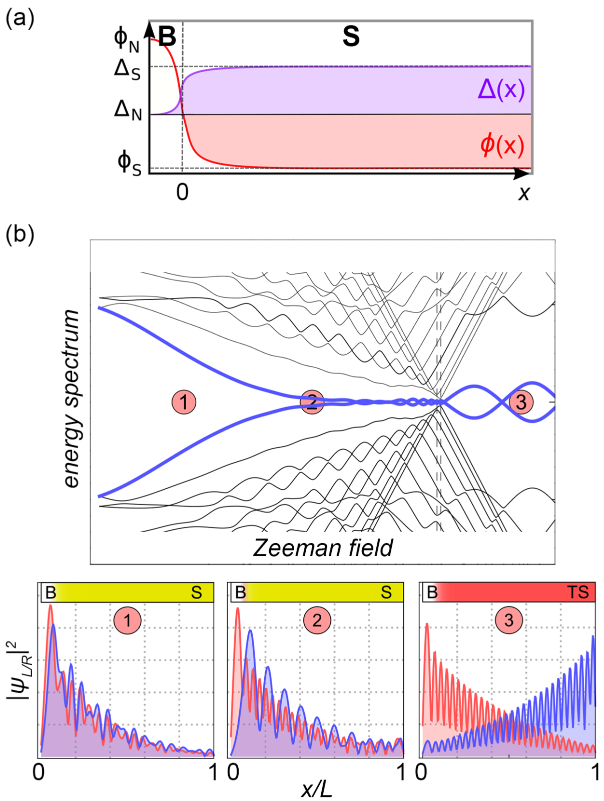

Figure 2.10: Effects of the smooth potential: **(a)** Electro-chemical potential $\phi(x)$ and superconducting (S) gap $\Delta(x)$ along the nanowire (x-axis). Smooth variations are caused by a tunnel barrier (B) at the nanowire end ($x = 0$). **(b)** Evolution of the spectrum with the Zeeman field with three distinct regions: 1 (no states at zero energy, non-topological), 2 (quasi-Majoranas at zero energy, non-topological) and 3 (MZMs with finite splitting, topological). The nanowire length is L. The Majorana wavefunctions are plotted along the nanowire $[0, L]$ for each region 1-3. The figure has been taken from [43]

than those of the minimal model of a Majorana nanowire. In the following paragraphs, we briefly list the main critical aspects beyond the minimal model by following a recent review [44].

While the superconducting pairing enters the minimal model as a fixed value, in realistic hybrid nanowires it is reduced while the parallel magnetic field drives the system into the topological phase. This is a consequence of the parallel field penetrating the superconductor that proximitizes the nanowire and thus reduces the parent superconducting gap in the system. Consequently, subgap states in the nanowire spectrum can be pinned to zero energy and mimic MZMs by causing zero-bias peaks (ZBPs) in tunneling-conductance measurements. This can happen simply because the decaying induced gap pushes subgap states to zero energy as the field is increased.

By considering the three-dimensional nanowire geometry, multiple subbands and orbital effects of the parallel magnetic field reduce the topological gap and make the shape of the topologcal phase much smaller and more irregular than shown by the parabolic phase boundary in Fig. 2.9(c).

The electro-chemical potential inside hybrid nanowires is controlled by electric fields set by gates in experiments. However, unified self-consistent Schrödinger-Poisson studies of realistic nanowires have shown that these electric fields also influence the coupling strength between the semiconductor and the superconductor. Namely, the electric fields influence the cross-sectional distribution of electron wavefunctions. The electric fields can tune the hybridization from a superconducting-like limit - with a hard induced gap, small g factor and weak spin-orbit interaction - to a semiconducting-like limit - with a soft induced gap, large g factor and strong spin-orbit interaction. Importantly, this means that the parameters of the system are neither fixed nor independently tunable. The uniformity and control of the parameters is additional complicated by disorder that can make the parameters vary also longitudinally.

More detailed modellings of hybrid nanowires have found that smooth profiles of the electrostatic potential along the nanowires occur due to the mutual presence of the superconducting shell on the nanowire and local gates. An example of the smooth potential due to a gate-defined tunnel barrier at the nanowire end is depicted in Fig. 2.10 [43]. The smooth variations of the electro-static potential $\phi(x)$ and gap $\Delta(x)$ at the nanowire end give rise to subgap states that are pinned to zero energy in a broad range of the Zeeman energy before the topological phase transition (region 2). When decomposed into the Majorana basis, such states are shown to consist of two Majoranas localized at the nanowire end with the smooth potential. Although the state is at zero energy, its Majorana components are not spatially separated and they have a finite overlap in space. Such states are known as partially-separated ABSs, or non-topological MZMs, or quasi-Majoranas. The latest name comes from the fact that these states can locally give experimental signatures compatible with the true MZMs – in the form of even quantized ZBPs ($2e^2/h$) in tunneling spectrosopy measurements. The quasi-Majoranas ultimately evolve into true MZMs at sufficiently large Zeeman fields (region 3). The Majoranas are then localized at two nanowire ends and the nanowire is in the topological phase..

Based on all the aspects above, the creation of a topological phase in hybrid nanowires turns out to be much more challenging than what has been predicted by the minimal model. Local signatures of MZMs have been shown to occur in various non-topological scenarios and are, therefore, considered insufficient to conclusively establish the evidence of Majoranas in hybrid nanowires. For an unambiguous detection of MZMs, detecting the Majorana non-locality or the bulk-edge correspondance is needed.

2.6. HYBRID NANOWIRE ISLAND

The ground-state degeneracy of an infinitely long topological Majorana nanowire implies that a single electron can be added to the system without costs of energy. However, this means that the electron-parity of a hybrid nanowire is sensitive to the quasiparticle poisoning that can switch the electron parity. To have a control on the parity, systems with Coulomb interaction are studied – as in such systems the degeneracy is lifted by a finite charging energy. An example is a hybrid nanowire which superconducting shell is not connected to a reservoir with electrons and, therefore, represents an island with charges. Hybrid islands based on semiconductor-superconductor nanowires provide a platform in which the interplay between superconductivity and Coulomb interaction can be studied.

A schematic of a hybrid island is shown in Fig. 2.11(a). A gate is coupled to the island and induces a continuous charge $n_g e$, while the charge ne on the island is discrete. The total energy of the system is:

$$E_{tot} = E_C(n - n_g)^2 + E_0 \tag{2.30}$$

The first term corresponds to the Coulomb interaction that is parabolic with n_g and characterized by a charging energy $E_C = e^2/2C$, C being the total capacitance of the island. The second term appears due to the superconductivity. If n is even, all electrons in the ground state form Cooper pairs at zero energy and the total energy has only the Coulomb term. If n is odd, the Coulomb term remains, but there is an electron that does not have a partner to pair up and, therefore, this electron has to occupy the lowest single-electron energy state E_0. If there are no subgap states, this electron has to be added to the gap-edge, giving $E_0 = \Delta$. This means that the states with odd n are lifted by at most Δ with respect to those with even n. This

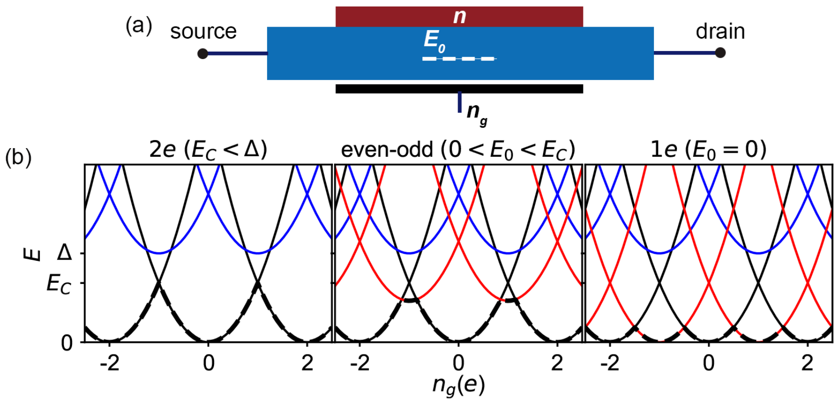

Figure 2.11: **(a)** Schematic of a hybrid semiconductor(blue)-superconductor(red) nanowire island with n electrons and coupled to a gate with charge $n_g e$. The charging energy of the island is E_C and the lowest quasiparticle state has energy E_0. **(b)** Energy dispersion of the island as a function of n_g. Ground state E_{gs} is marked by the thick dashed black lines.

is visible in Fig. 2.11(b), where parabolas for different n are plotted as a function of n_g. The ground-state energy E_{gs} is plotted in thick black. Note that in the left panel neighbouring parabolas cross at $E = E_C$. If $E_0 > E_C$, $E_{gs}(n_g)$ only includes the parabolas with even n and it is $2e$-periodic. If $0 < E_0 < E_C$, in some intervals of n_g the parabolas with odd n have the lowest energy and $E_{gs}(n_g)$ has an even-odd pattern. Finally, if $E_0 = 0$, $E_{gs}(n_g)$ equally includes both parities and it is $1e$-periodic.

Transport through the island takes place at the degeneracy points in the ground state. When two parabolas cross, either a Cooper pair ($2e$-periodic case, $n \to n \pm 2$) or a single electron (even-odd or $1e$-periodic, $n \to n \pm 1$) is added/removed to/from the island. At these points, both the supercurrent and the zero-bias conductance through the island are enhanced (Coulomb peaks). They are both suppressed between the degeneracy points as the charge there is fixed (Coulomb valleys). Besides these generic properties, signatures of topological superconductivity have been proposed in the zero-bias conductance when a topological island is coupled to normal leads [45], and in the supercurrent when coupled to superconducting leads [46].

REFERENCES

[1] T. Ihn. *Semiconductor nanostructures.* Oxford University Press, 2013.

[2] B. J. van Wees, H. van Houten, C. W. J. Beenakker, J. G. Williamson, L. P. Kouwenhoven, D. van der Marel, and C. T. Foxon. “Quantized conductance of point contacts in a two-dimensional electron gas”. In: *Phys. Rev. Lett.* 60 (9 1988), pp. 848–850.

[3] P. Drude. “Zur Elektronentheorie der Metalle”. In: *Annalen der Physik* 306.3 (1900), pp. 566–613.

[4] P. Zeeman. “The Effect of Magnetisation on the Nature of Light Emitted by a Substance”. In: *Nature* 55 (1897), p. 347.

[5] R. Winkler. *Spin-Orbit Coupling Effects in Two-Dimensional Electron and Hole Systems.* Springer, 2003.

[6] H. A. Lorentz. “Electromagnetic phenomena in a system moving with any velocity smaller than that of light”. In: *Proceedings of the Royal Netherlands Academy of Arts and Sciences* 6 (1904), pp. 809–831.

[7] G. Dresselhaus. “Spin-Orbit Coupling Effects in Zinc Blende Structures”. In: *Phys. Rev.* 100 (2 1955), pp. 580–586.

[8] Y. A. Bychkov and E. I. Rashba. “Properties of a 2d electron gas with lifted spectral degeneracy”. In: *JETP Lett.* 39 (78 1984).

[9] R. M. Lutchyn, E. P. A. M. Bakkers, L. P. Kouwenhoven, P. Krogstrup, C. M. Marcus, and Y. Oreg. “Majorana zero modes in superconductor–semiconductor heterostructures”. In: *Nat. Rev. Mater.* 3.52 (2018).

[10] J. M. Luttinger and W. Kohn. “Motion of Electrons and Holes in Perturbed Periodic Fields”. In: *Phys. Rev.* 97 (4 1955), pp. 869–883.

[11] P. Lawaetz. “Valence-Band Parameters in Cubic Semiconductors”. In: *Phys. Rev. B* 4 (10 1971), pp. 3460–3467.

[12] G. L. Bir and G. E. Pikus. *ymmetry and Strain-Induced Effects in Semiconductors.* Willey, 1974.

[13] L. A. Terrazos, E. Marcellina, Z. Wang, S. N. Coppersmith, M. Friesen, A. R. Hamilton, X. Hu, B. Koiller, A. L. Saraiva, D. Culcer, and R. B. Capaz. “Theory of hole-spin qubits in strained germanium quantum dots”. In: *Phys. Rev. B* 103 (12 2021), p. 125201.

[14] R. Winkler. “Rashba spin splitting in two-dimensional electron and hole systems”. In: *Phys. Rev. B* 62 (7 2000), pp. 4245–4248.

2

[15] D. Csontos, P. Brusheim, U. Zülicke, and H. Q. Xu. "Spin-$\frac{3}{2}$ physics of semiconductor hole nanowires: Valence-band mixing and tunable interplay between bulk-material and orbital bound-state spin splittings". In: *Phys. Rev. B* 79 (15 2009), p. 155323.

[16] C. Kloeffel, M. Trif, and D. Loss. "Strong spin-orbit interaction and helical hole states in Ge/Si nanowires". In: *Phys. Rev. B* 84 (19 2011), p. 195314.

[17] H. K. Onnes. "The resistance of pure mercury at helium temperatures". In: *Commun. Phys. Lab. Univ. Leiden* 120.12 (1911), p. 1.

[18] W. Meissner and R. Ochsenfeld. "Ein neuer Effekt bei Eintritt der Supraleitfähigkeit". In: *Naturwissenschaften* 21 (1933), p. 787.

[19] J. Bardeen, L. N. Cooper, and J. R. Schrieffer. "Theory of Superconductivity". In: *Phys. Rev.* 108 (1957), p. 1175.

[20] M. Tinkham. *Introduction to Superconductivity.* Dover, 2004.

[21] L. N. Cooper. "Bound electron pairs in a degenerate Fermi gas". In: *Phys. Rev.* 104 (1956), p. 1189.

[22] N. N. Bogoliubov. "On a new method in the theory of superconductivity". In: *Nuovo Cimento* 7 (1958), pp. 794–805.

[23] M. Octavio, M. Tinkham, G. E. Blonder, and T. M. Klapwijk. "Subharmonic energy-gap structure in superconducting constrictions". In: *Phys. Rev. B* 27.6739 (1983).

[24] C. W. J. Beenakker. "Quantum transport in semiconductor-superconductor microjunctions". In: *Phys. Rev. B* 46 (19 1992), pp. 12841–12844.

[25] V. Ambegaokar and B. I. Halperin. "Voltage Due to Thermal Noise in the dc Josephson Effect". In: *Phys. Rev. Lett.* 22 (25 1969), pp. 1364–1366.

[26] Y. V. Nazarov and Y. M. Blanter. *Quantum Transport - Introduction to Nanoscience.* Cambridge University Press, 2009.

[27] S. Heedt, M. Quintero-Pérez, F. Borsoi, A. Fursina, N. van Loo, G. P. Mazur, M. P. Nowak, M. Ammerlaan, K. Li, S. Korneychuk, J. Shen, M. Y. van de Poll, G. Badawy, S. Gazibegovic, N. de Jong, P. Aseev, K. van Hoogdalem, E. P. A. M. Bakkers, and L. P. Kouwenhoven. "Shadow-wall lithography of ballistic superconductor–semiconductor quantum devices". In: *Nat. Commun.* 12 (2021), p. 4914.

[28] F. Borsoi, G. P. Mazur, N. van Loo, M. P. Nowak, L. Bourdet, K. Li, S. Korneychuk, A. Fursina, J.-Y. Wang, V. Levajac, E. Memisevic, G. Badawy, S. Gazibegovic, K. van Hoogdalem, E. P. A. M. Bakkers, L. P. Kouwenhoven, S. Heedt, and M. Quintero-Pérez. "Single-shot fabrication of semiconducting–superconducting nanowire devices". In: *Adv. Func. Mater.* 31 (2021), p. 2102388.

[29] A. Tosato, V. Levajac, J.-Y. Wang, C. J. Boor, F. Borsoi, M. Botifoll, C. N. Borja, S. Martí-Sánchez, J. Arbiol, A. Sammak, M. Veldhorst, and G. Scappucci. "Hard superconducting gap in germanium". In: *Commun. Mater.* 4.23 (2023).

[30] C. W. J. Beenakker and H. van Houten. “Josephson current through a superconducting quantum point contact shorter than the coherence length”. In: *Phys. Rev. Lett.* 66 (23 1991), pp. 3056–3059.

[31] T. Yokoyama, M. Eto, and Y. V. Nazarov. “Anomalous Josephson effect induced by spin-orbit interaction and Zeeman effect in semiconductor nanowires”. In: *Phys. Rev. B* 89 (2014), p. 195407.

[32] K. Gharavi and J. Baugh. “Orbital Josephson interference in a nanowire proximity-effect junction”. In: *Phys. Rev. B* 91 (2015), p. 245436.

[33] C. W. J. Beenakker. “Universal limit of critical-current fluctuations in mesoscopic Josephson junctions”. In: *Phys. Rev. Lett.* 67 (27 1991), pp. 3836–3839.

[34] T. Yokoyama, M. Eto, and Y. V. Nazarov. “Josephson current through semiconductor nanowire with spin–orbit interaction in magnetic field”. In: *J. Phys. Soc. Jpn.* 82 (2013), p. 054703.

[35] D. B. Szombati, S. Nadj-Perge, D. Car, S. R. Plissard, E. P. A. M. Bakkers, and L. P. Kouwenhoven. “Josephson ϕ_0-junction in nanowire quantum dots”. In: *Nature Phys.* 12 (2016), pp. 568–572.

[36] E. Strambini, A. Iorio, O. Durante, R. Citro, C. Sanz-Fernández, C. Guarcello, I. V. Tokatly, A. Braggio, M. Rocci, N. Ligato, V. Zannier, L. Sorba, F. S. Bergeret, and F. Giazotto. “A Josephson phase battery”. In: *Nat. Nanotechnol.* 15 (2020), pp. 656–660.

[37] J.-Y. Wang, C. Schrade, V. Levajac, D. van Driel, K. Li, S. Gazibegovic, G. Badawy, R. L. M. O. het Veld, J. S. Lee, M. Pendharkar, C. P. Dempsey, C. J. Palmstrøm, E. P. A. M. Bakkers, L. Fu, L. P. Kouwenhoven, and J. Shen. “Supercurrent parity meter in a nanowire Cooper pair transistor”. In: *Sci. Adv.* 8 (2022), eabm9896.

[38] K. Zuo, V. Mourik, D. B. Szombati, B. Nijholt, D. J. van Woerkom, A. Geresdi, J. Chen, V. P. Ostroukh, A. R. Akhmerov, S. R. Plissard, D. Car, E. P. A. M. Bakkers, D. I. Pikulin, L. P. Kouwenhoven, and S. M. Frolov. “Supercurrent interference in few-mode nanowire Josephson junctions”. In: *Phys. Rev. Lett.* 119 (2017), p. 187704.

[39] A. P. Mackenzie and Y. Maeno. “The superconductivity of Sr_2RuO_4 and the physics of spin-triplet pairing”. In: *Rev. Mod. Phys.* 75 (2 2003), pp. 657–712.

[40] R. M. Lutchyn, J. D. Sau, and S. D. Sarma. “Majorana fermions and a topological phase transition in semiconductor-superconductor heterostructures”. In: *Phys. Rev. Lett.* 105 (2010), p. 077001.

[41] Y. Oreg, G. Refael, and F. von Oppen. “Helical liquids and Majorana bound states in quantum wires”. In: *Phys. Rev. Lett.* 105 (2010), p. 177002.

[42] J. Klinovaja and D. Loss. “Composite Majorana fermion wave functions in nanowires”. In: *Phys. Rev. B* 86 (8 2012), p. 085408.

[43] F. Peñaranda, R. Aguado, P. San-Jose, and E. Prada. “Quantifying wave-function overlaps in inhomogeneous Majorana nanowires”. In: *Phys. Rev. B* 98 (23 2018), p. 235406.

[44] E. Prada, P. San-Jose, M. W. A. de Moor, A. Geresdi, E. J. H. Lee, J. Klinovaja, D. Loss, J. Nygård, R. Aguado, and L. P. Kouwenhoven. “From Andreev to Majorana bound states in hybrid superconductor–semiconductor nanowires”. In: *Nat. Rev. Phys.* 2 (2020), pp. 575–594.

[45] E. B. Hansen, J. Danon, and K. Flensberg. “Probing electron-hole components of subgap states in Coulomb blockaded Majorana islands”. In: *Phys. Rev. B* 97 (4 2018), p. 041411.

[46] S. C. and F. L. “Andreev or Majorana, Cooper finds out”. In: *arXiv preprint* (2018), p. 1809.06370.

3

Supercurrent parity meter in a nanowire Cooper pair transistor

We study a Cooper-pair transistor realized by two Josephson weak links that enclose a superconducting island in an InSb-Al hybrid nanowire. When the nanowire is subject to a magnetic field, isolated subgap levels arise in the superconducting island and, due to the Coulomb blockade, mediate a supercurrent by coherent co-tunneling of Cooper pairs. We show that the supercurrent resulting from such co-tunneling events exhibits, for low to moderate magnetic fields, a phase offset that discriminates even and odd charge ground states on the superconducting island. Notably, this phase offset persists when a subgap state approaches zero energy and, based on theoretical considerations, permits parity measurements of subgap states by supercurrent interferometry. Such supercurrent parity measurements could, in a new series of experiments, provide an alternative approach for manipulating and protecting quantum information stored in the isolated subgap levels of superconducting islands.

The work in this chapter has been published as: J.-Y. Wang*, C. Schrade*, V. Levajac, D. van Driel, K. Li, S. Gazibegović, G. Badawy, R. L. M. Op het Veld, J. S. Lee, M. Pendharkar, C. P. Dempsey, C. J. Palmstrøm, E. P. A. M. Bakkers, L. Fu, L. P. Kouwenhoven and J. Shen *"Supercurrent parity meter in a nanowire Cooper pair transistor"*, Science Advances 8 (16), eabm9896 (2022)
*These authors contributed equally to this work.

3.1. INTRODUCTION

When two superconducting (SC) leads couple via a Coulomb-blockaded quantum dot (QD), the isolated energy levels on the dot mediate a supercurrent by coherent co-tunneling of Cooper pairs [1]. For the case of a single-level QD, a control knob for the supercurrent direction is given by the charge parity of dot electrons [1]. Such a parity-controlled supercurrent has been observed in a nanowire (NW) QD Josephson junction (JJ) [2, 3]. It is described by the Josephson relation, $I = (-1)^{n_0} I_c \sin(\varphi)$, where I_c is the critical current, φ is the SC phase difference, and n_0 is the number of dot electrons. In general, the Josephson relation can also acquire a phase offset, $\varphi \rightarrow \varphi + \varphi_0$ with $\varphi_0 \neq 0, \pi$, when time-reversal and mirror symmetry are broken [4]. This breaking occurs, for example, if a spin-orbit coupled QD is subject to a magnetic field [4–7].

A different possibility of coupling two SC leads is via a SC island with finite charging energy: a 'Cooper-pair transistor' (CPT) [8–14]. Unlike in the QD JJ, the SC island carries, within its parity lifetime, an even number of electrons in the ground state, as signified by a charging energy that is a $2e$-periodic function of the island gate charge (e, elementary charge) [9, 11, 13]. In particular, since the odd charge states are energetically unfavorable for a conventional CPT, the Josephson relation is not expected to exhibit a parity-controlled phase offset.

Recently, a CPT has been realized with an Indium Arsenide-Aluminium (Al) hybrid NW [12, 13]. In this case, upon increasing a magnetic field parallel to the NW, a transition from a $2e$-periodic switching current to a switching current with even-odd pattern has been observed [13]. The interpretation is that a low-energy subgap state arises in the SC island, and, depending on its occupancy, the charge ground state carries an even or an odd number of electrons. An open question is if the Josephson relation of a NW CPT exhibits *in the presence of subgap states* a parity-controlled phase offset?

Here, we address this question with a NW CPT integrated in a superconducting quantum interference device (SQUID). We investigate the previously described situation when the NW CPT is subject to a parallel magnetic field so that subgap levels arise in the SC island and mediate a supercurrent by coherent co-tunneling of Cooper pairs. We show that supercurrent resulting from Cooper pair co-tunneling exhibits a phase offset, which distinguishes even and odd charge ground states on the SC island. This phase offset persists when a subgap state approaches zero energy and, based on theoretical considerations, may enable *parity readout* of low-energy subgap states. Such supercurrent parity readout could provide a new approach for manipulating [15–20] and protecting [21, 22] quantum information stored in the isolated subgap levels of SC islands [23–27].

3.2. RESULTS

The device geometry of our experiment is shown in Fig. 3.1. For realizing the CPT, we use a shadow-grown Al SC island on an Indium Antimonide (InSb) NW, which couples to two SC Al leads via gate-tunable tunneling barriers. A plunger gate is used for controlling the electron number on the SC island. As we intend to study the

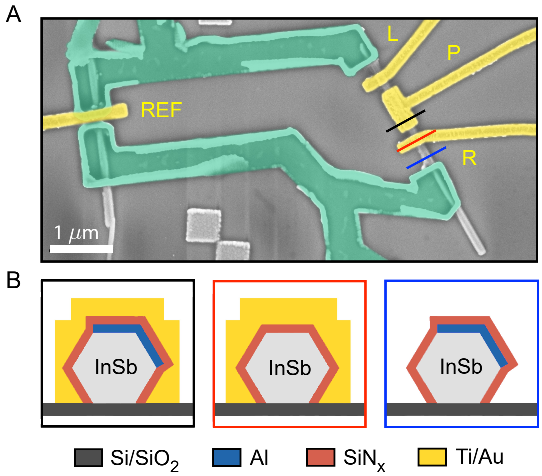

Figure 3.1: **Sketch of the SQUID device.** (**A**) False-color micrograph of the measured NbTiN (green) SQUID device comprising an InSb-Al NW CPT in the right arm and an InSb nanowire reference junction in the left arm. Top gates (L, R, REF) define tunable JJs, and a plunger gate (P) controls the electron number on the hybrid island. The InSb nanowires are ~100 nm in diameter, Al shell is ~10 nm in thickness, three junctions are ~150 nm in length, and the InSb-Al hybrid island is ~1 μm in length. (**B**) Cross-sections along the lines shown in (A).

full Josephson relation of the NW CPT, we integrate our setup in a SQUID loop made of niobium-titanium nitride (NbTiN) and a second InSb NW reference junction. The tunnel coupling of the reference junction is adjustable by a local gate electrode. Concrete fabrication steps are discribed in the Supplementary Material section.

Initially, we pinch off the reference junction and characterize the NW CPT by measuring the differential conductance $\mathrm{d}I/\mathrm{d}V$ versus the source-drain voltage V and the plunger gate voltage V_P. Our results are shown in Fig. 3.2A for zero and finite parallel magnetic fields $B_\parallel$.

At zero magnetic field, we observe a pattern of Coulomb diamonds with sharp edges due to the weak island-lead coupling. Besides the Coulomb diamonds, which signify the importance of charging effects on the SC island, the zero-bias differential conductance exhibits $2e$-periodic oscillations, which implies the transport of Cooper pairs (see the insert curve in Fig. 3.2A). Furthermore, above an onset voltage V_{onset}, a $1e$-periodic modulation of the differential conductance appears, which marks the onset of quasiparticle transport. The charging energy, E_C, is estimated to be ~20 μeV from the 2e−charge diamond at $B_\parallel$=0, and the induced gap, Δ_{ind}, is extracted to be ~50 μeV from onset of quasiparticle transport. The relation $E_C < \Delta_{ind}$ is consistent with the condition for $2e$-periodicity of the Coulomb diamonds at zero field [28–30].

At finite magnetic fields, the aforementioned onset voltage for quasiparticle transport persists. However, below the onset voltage, the Coulomb diamonds split, resulting in an even-odd pattern. We attribute the appearance of this even-odd

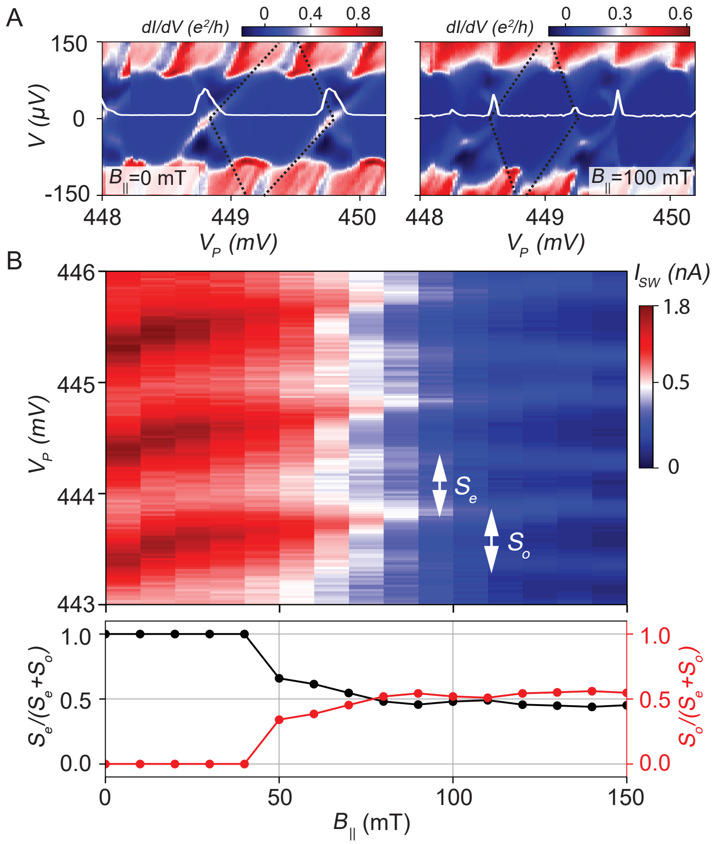

Figure 3.2: **Parity control with magnetic field.** (**A**) Differential conductance, $\mathrm{d}I/\mathrm{d}V$, versus source-drain voltage V and plunger gate voltage V_P. At zero parallel magnetic field, the differential conductance shows a Coulomb diamond pattern with a $2e$-periodicity. At $B_\parallel = 100\,\mathrm{mT}$, the $2e$-periodicity of the Coulomb diamonds is lifted due to the appearance of an odd-parity charge ground state on the SC island. Inset curves show the differential conductance at zero bias. Black dotted lines mark the boundary of a $2e$-charge Coulomb diamond at $B_\parallel = 0$ and the boundary of an even-parity Coulomb diamond at $B_\parallel = 100\,\mathrm{mT}$. (**B**) Top panel: Switching current, I_{sw}, versus parallel magnetic field $B_\parallel$ and plunger gate voltage V_P. Bottom panel: Magnetic field dependence of the normalized even and odd peak spacings, $S_e/(S_e+S_o)$ and $S_o/(S_e+S_o)$, showing a transition from a $2e$-periodicity to an even-odd pattern.

pattern to low-energy subgap states that form on the SC island. More specifically, the magnetic field induces a Zeeman splitting of spinful, odd-parity states and, thereby, reduces the minimum single-particle excitation energy in the NW CPT. As a result, odd-parity states can detach from the quasiparticle continuum and, because of their enhanced effective g-factor in comparison to the Al shell, form isolated levels below the SC gap [13, 31].

Next, we investigate the subgap levels on the SC island in more detail. We lower the island-lead tunneling barriers and, with the reference junction still pinched off, measure the switching current I_{sw} as a function of the parallel magnetic field $B_{\parallel}$ and plunger gate voltage V_P. Our results are given in Fig. 3.2B. At zero magnetic field, the switching current exhibits a $2e$-periodic peak spacing implying that the SC island always carries an even number of electrons in its charge ground state (see also Fig. 3.6A in the Supplementary Material section). The situation changes upon applying a parallel magnetic field. The magnetic field induces a splitting of the $2e$-periodic peaks, and, as a result, the switching current exhibits a peak-spacing with an even-odd pattern (see also Fig. 3.6B in the Supplementary Material section). Similar to the differential conductance, we attribute the appearance of this even-odd pattern to charge ground states with even and odd fermion parity on the SC island. Moreover, as shown in Fig. 3.2B, the extracted peak spacings oscillate as a function of applied magnetic field, as well as the plunger gate voltage, indicating either the anticrossing or the crossing of the lowest-energy subgap state with a second subgap state at higher energy [29, 30].

We now open the reference junction and measure the NW CPT's full Josephson relation in the presence of low-energy subgap states. For the results presented here, we focus on the magnetic field strength $B_{\parallel} = 170\,\mathrm{mT}$, and adopt a highly-asymmetric SQUID configuration so that the phase drop occurs primarily across the NW CPT. Under these conditions, we apply a bias current I_b and measure the voltage drop V across the SQUID as a function of the plunger gate voltage V_P and the flux ϕ piercing through the SC loop. Fig. 3.3 shows our measurement data, which we will now discuss in more detail:

Our main finding is that the Josephson relation of the NW CPT exhibits a substantial relative phase offset φ_0 between Coulomb valleys of opposite charge parity. To determine this phase offset for the Coulomb valleys marked in Fig. 3.3A, we fit the switching current I_{sw} as a function of the flux ϕ. The fitted curves, shown in Fig. 3.3B, allow us to extract $\varphi_0 \sim -1.24\pi$ and $\varphi_0 \sim -1.31\pi$ for the first and second pair of Coulomb valleys, respectively. For the remaining pairs, we find similar values for the phase offset, as summarized in Fig. 3.3C. Notably, the leftmost pair of data points in Fig. 3.3C shows that phase offset persists when the Coulomb peaks are close to a $1e$-spacing (see detailed analysis in Fig. 3.7 in supplementary materials). Therefore, the phase offset facilitates charge parity readout even if a subgap state is close to zero energy.

Next, we discuss a possible mechanism for a parity-dependent phase offset. We introduce a model for the NW CPT, which comprises a mesoscopic SC island coupled to a pair of s-wave SC leads. In our model, we focus on the two lowest isolated subgap levels in the SC island, $\pm\varepsilon_a$ and $\pm\varepsilon_b$, indicated by the peak spacing oscillation as a function of magnetic field and plunger gate in Fig. 3.2B. Here, we consider two types of co-tunneling sequences:

(1) In the first type of sequence, shown in Fig. 3.4A, the Cooper pair splits so that one electron tunnels via $\pm\varepsilon_a$ while the other electron tunnels via $\pm\varepsilon_b$. For such a

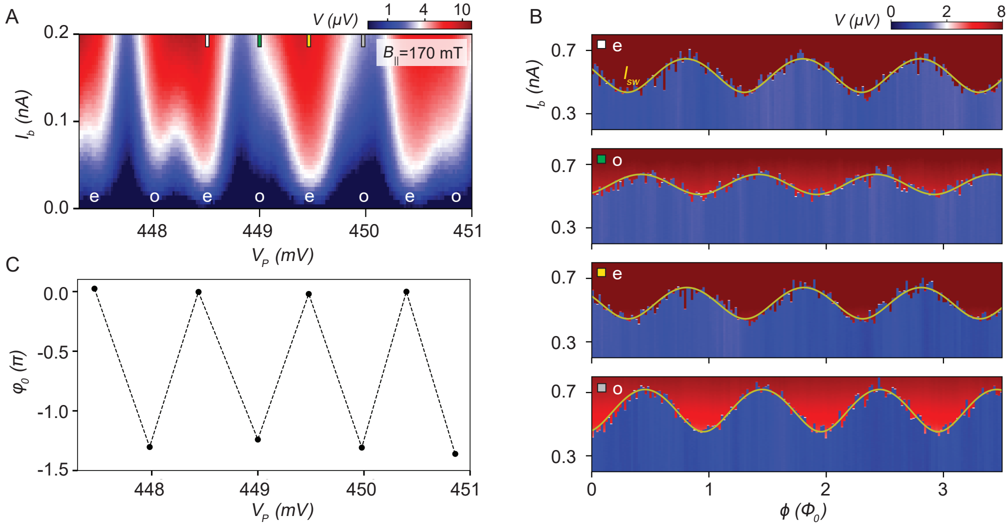

Figure 3.3: **Parity control with magnetic field.** (**A**) Differential conductance, $\mathrm{d}I/\mathrm{d}V$, versus source-drain voltage V and plunger gate voltage V_P. At zero parallel magnetic field, the differential conductance shows a Coulomb diamond pattern with a $2e$-periodicity. At $B_\parallel = 100\,\mathrm{mT}$, the $2e$-periodicity of the Coulomb diamonds is lifted due to the appearance of an odd-parity charge ground state on the SC island. Inset curves show the differential conductance at zero bias. Black dotted lines mark the boundary of a $2e$-charge Coulomb diamond at $B_\parallel = 0$ and the boundary of an even-parity Coulomb diamond at $B_\parallel = 100\,\mathrm{mT}$. (**B**) Top panel: Switching current, I_{sw}, versus parallel magnetic field $B_\parallel$ and plunger gate voltage V_P. Bottom panel: Magnetic field dependence of the normalized even and odd peak spacings, $S_e/(S_e+S_o)$ and $S_o/(S_e+S_o)$, showing a transition from a $2e$-periodicity to an even-odd pattern.

two-level sequence, the corresponding supercurrent contribution acquires a prefactor given by the SC island charge parity, $(-1)^{n_0}$. This parity prefactor is analogous to the parity prefactor appearing in the Josephson relation of a QD JJ, where Cooper pairs tunnel via two dot levels with opposite spin polarization [1].

(2) In the second type of sequence, shown in Fig. 3.4B, both Cooper pair electrons tunnel via either $\pm\varepsilon_a$ or $\pm\varepsilon_b$. For such a single-level sequence, each of the two electrons contributes a prefactor given by the parity of $\pm\varepsilon_a$ or $\pm\varepsilon_b$. In particular, since the same parity prefactor appears twice in the sequence, it squares to one. Consequently, in the single-level supercurrent contribution a parity prefactor is absent.

If we collect all sequences, we obtain the Josephson relation (see details in the Supplementary Material section),

$$I = (-1)^{n_0} I_{ab} \sin(\varphi + \varphi_{ab}) + \sum_{\ell=a,b} I_\ell \sin(\varphi + \varphi_\ell). \tag{3.1}$$

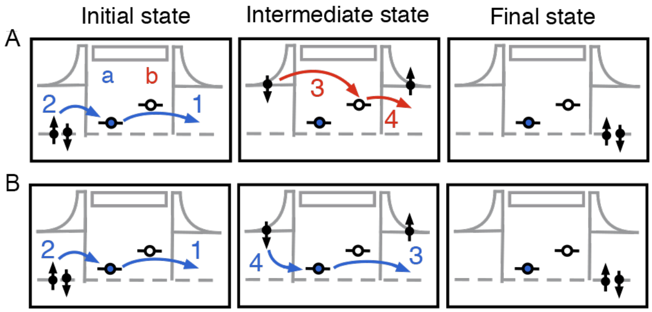

Figure 3.4: **Energy diagrams illustrating Cooper pair transport via subgap levels.** (**A**) A typical sequence of intermediate states in which a Cooper pair tunnels between the SC leads (left, right) via the two lowest isolated subgap levels a, b in the intermediate SC island (center). Such a sequence yields a contribution to the supercurrent proportional to the joint parity of the two subgap levels. In the illustration, numbers indicate the sequence of tunneling events, and solid/empty dots represent filled/empty subgap levels. The occupation numbers of the subgap levels (n_a, n_b) in the sequence are $(1,0) \xrightarrow{1} (0,0) \xrightarrow{2} (1,0) \xrightarrow{3} (1,1) \xrightarrow{4} (1,0)$. The energy of the initial odd parity $(1,0)$ configuration is $(-1)^{n_a+1}\varepsilon_a + (-1)^{n_b+1}\varepsilon_b = \varepsilon_a - \varepsilon_b$, which corresponds to the ground state provided that $\varepsilon_b > \varepsilon_a$. (**B**) A typical sequence of intermediate states that involves Cooper pair transport via a single subgap level yielding no parity-dependent prefactor. The occupation numbers for this sequence are $(1,0) \xrightarrow{1} (0,0) \xrightarrow{2} (1,0) \xrightarrow{3} (0,0) \xrightarrow{4} (1,0)$. In (A) and (B), subgap levels are displayed in an 'excitation picture' representation [32].

Here, I_{ab} and I_ℓ are amplitudes, which are $1e$-periodic in the gate charge if the lowest subgap level is at zero energy. Furthermore, the phase offsets $\varphi_{ab}, \varphi_\ell$ arise if the subgap states couple inequivalently to the SC leads (see the Eq. (3.18) in the Supplementary Material for the detailed condition on the tunneling amplitudes) and if, due to time-reversal symmetry breaking, the tunnel couplings acquire complex phase factors.

We now highlight two differences between the NW CPT and a QD JJ: First, the island which mediates the Josephson current is in a SC state, not a normal state as for a QD JJ. Consequently, not only conventional tunneling events can occur, but also anomalous tunneling events in which an electron is created/destroyed on both the SC island and the leads. Second, for a QD JJ, the wavefuntions on the dot are highly localized which justifies a point-like tunneling contact. In comparison, for a NW CPT, the subgap level wavefunctions can be extended, which induces longer-range island-lead tunnel couplings. In particular, such longer-range couplings can break the mirror symmetry, due to the combined effect of spin-orbit coupling and magnetic field in the tunneling region, and lead to additional contributions to $\varphi_{ab}, \varphi_\ell$.

Returning to Eq. (3.1), the total phase offset is $\varphi_{n_0} \equiv \arg[(-1)^{n_0} I_{ab} e^{i\varphi_{ab}} + \sum_\ell I_\ell e^{i\varphi_\ell}]$ and the relative phase offset between the parity sectors is $\varphi_0 \equiv \varphi_{n_0+1} - \varphi_{n_0}$. In these

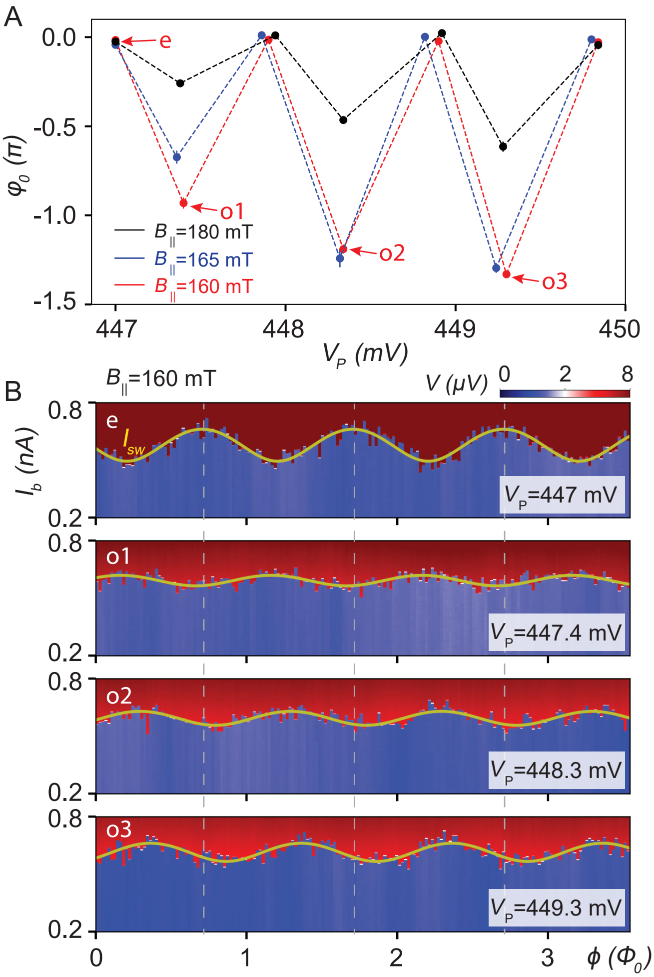

Figure 3.5: **Tunable phase offset.** (**A**) Phase offset φ_0 versus plunger gate voltage V_P for various parallel magnetic fields $B_{\parallel}$. The dashed lines do not represent data, but are merely used for improving data visibility. The phase offset is sensitive to both plunger gate voltage and magnetic field variations. (**B**) Voltage drop V as a function of the applied bias current I_b and the SQUID flux ϕ for a parallel magnetic field $B_{\parallel} = 160\,\text{mT}$. The switching current I_{sw} (yellow) displays a phase offset φ_0 between even (e) and odd (o) Coulomb valleys of the SC island that is tunable by the plunger gate voltage V_P.

expressions, the parity prefactor flips upon tuning the gate charge of the SC island between different charge parity sectors. As a result of these parity-flips, the phase offset does *not* exhibit a $1e$-periodicity in the gate charge even if one of the subgap states is at zero energy. Instead, if $I_{ab} \neq 0$, φ_0 is always $2e$-periodic and permits the measurement of the parity of the lowest subgap level. To practically enable such parity measurements, the two-level contribution should be sizable, $I_{ab} \gg I_\ell$. Also, to avoid thermal excitations, the temperature T should be small compared to the level separation $|\varepsilon_a - \varepsilon_b|$. Interestingly though, if $|\varepsilon_a - \varepsilon_b| \gtrsim T$, the parity prefactor measures the joint parity of $\pm\varepsilon_a$ and $\pm\varepsilon_b$. Such joint parity measurements could be leveraged for entangling qubits stored in the subgap levels of SC islands [15–20].

So far, we have discussed a regime with substantial φ_0 for parity read-out with maximal resolution. However, such an ideal situation is not always realized. In Fig. 3.5A, we display the phase offset versus plunger gate voltage for multiple magnetic field values. For a selection of data points, we also show the fitted switching current I_{sw} in Fig. 3.5B. Detailed analysis is shown in Fig. 3.8-Fig. 3.10 in the Supplementary Material section. In comparison, there is another regime in which NW CPT exhibits phase independence on its parity (see details in Fig. 3.11-Fig. 3.12 in the Supplementary Material). In Fig. 3.5, our findings are two-fold: First, we observe that the phase offset for subsequent Coulomb valley pairs is tunable by the magnetic field and the plunger gate voltage. Such a tunability arises because both control parameters change the support of the subgap level wavefunction and, thereby, alter the lead-island Josephson couplings. Second, we find that the phase offset decreases upon increasing the magnetic field. This decreasing suggests that the level seperation between the lowest-energy and higher-energy subgap states increases so that the supercurrent contribution with the parity-dependent prefactor becomes energetically unfavorable. As a result, in this regime, the NW CPT exhibits a phase dependence that is only weakly dependent on its parity.

3.3. CONCLUSION

We have studied the Josephson relation of an InSb-Al NW CPT. We have demonstrated that upon applying a magnetic field, subgap levels arise in the SC island and mediate a supercurrent with a parity-dependent phase offset. We have shown that the phase offset persists when the subgap state approaches zero energy and enables parity readout of the lowest energy subgap state. Such a supercurrent parity readout could be useful for the manipulation [15–20] and protection [21, 22] of qubits stored in the isolated subgap levels of SC islands [23–27].

3.4. SUPPLEMENTARY MATERIAL

3.4.1. METHODS

DEVICE FABRICATION

The InSb NWs used in the experiment were grown on an Indium phosphide substrate by metalorganic vapor phase epitaxy. In the molecular beam epitaxy chamber, Al flux was deposited along a specific direction to form Al shadows on InSb NWs by neighboring NWs. InSb-Al NWs with shadows were transferred onto a doped Si/SiO_x substrate using a nano-manipulator installed inside an SEM. NbTiN superconductor was sputter deposited right after Ar etching dedicated to removing the oxidized layer. Subsequently, 30 nm SiN_x was sputter deposited to work as a dielectric layer, and 10/120 nm Ti/Au was used as a top gate.

TRANSPORT MEASUREMENT

The sample was measured at a base temperature of ∼20 mK in an Oxford dry dilution refrigerator equipped with a vector magnet. Differential conductance was measured by applying small AC lock-in excitation superimposed on a DC voltage and then measuring AC and DC current through the device. Typically, low frequency of ∼ 27 Hz and AC excitation amplitude of ∼10 μV were used for lock-in measurement. In current bias measurement, current was applied through the device while monitoring voltage drop on device. The direction of the magnetic field was aligned with respect to the InSb-Al island arm by detecting the supercurrent of Cooper-pair transistor while rotating the magnetic field direction.

COULOMB VALLEY EXTRACTION

We note that the measured current-voltage I_b-V curves of Cooper-pair transistor exhibit a finite slope for all voltages, see Fig. 3.7A- 3.10A. The possible reasons are (1) at finite magnetic field, Josephson energy in the Cooper-pair transistor junctions is suppressed and thermal fluctuation results in resistive electron transport [33, 34]; (2) In our device, the leads of Cooper-pair transistor are made from NbTiN/Al and NbTiN is able to push quasiparticles into Al, softening Al gap [35]. Coulomb valleys could still be addressed via resistance peak around zero-bias voltage, albiet smeared IV curve resulting from above mentioned two mechanisms, because electron transport is most resistive at Coulomb valleys in both scenarios. Furthermore, both aforementioned mechanisms would not affect superconducting phase measurement results with the reference arm turned on. When reference arm is turned on, total supercurrent (as well as Josephson energy) becomes much larger. Then, thermal fluctuation plays much less of a role and quasiparticle transport is completely suppressed, which is reflected by very sharp transition from superconducting to resistive regime in superconducting phase measurement.

Discussion on the self-inductance of the SQUID loop

According to the Tinkham's book [36], a superconducting loop subjected to an external magnetic flux can generate screening current to expel the external flux, which could distort the measured current-phase relationship and make precise extraction of superconducting phase difficult. In order to eliminate the doubt, we quantitatively estimate the amplitude of self-generated flux resulting from inductance. In thin superconducting film, the total inductance, L comprises of kinetic inductance, L_k and geometric inductance, L_g. NbTiN film properties have been systematically studied [37]. A typical 100 nm film thick has a T_c of 14 K, a resistivity of 123 $\mu\Omega$·cm, and $L_k/(L_k+L_g)$~0.3. In our device, NbTiN has thickness of 80 nm and we adopt the T_c and resistivity from 100 nm film, and $L_k/(L_k+L_g)$ is ~ 0.5 by interpolating the data of $L_k/(L_k+L_g)$ versus film thickness. Kinetic inductance L_k can be calculated from Eq. (6) in reference [38]. We suppose that the critical current I_c of the loop is 10 nA (actual measured switching current of Cooper-pair transistor is always below 2 nA in our measurement), and the value of $I_c \cdot L \sim 4\times10^{-4}\Phi_0$, where Φ_0 is flux quantum. Thus, self-inductance is negligibly small compared with external flux and was not taken into account in the data analysis.

3.4.2. Supplementary figures

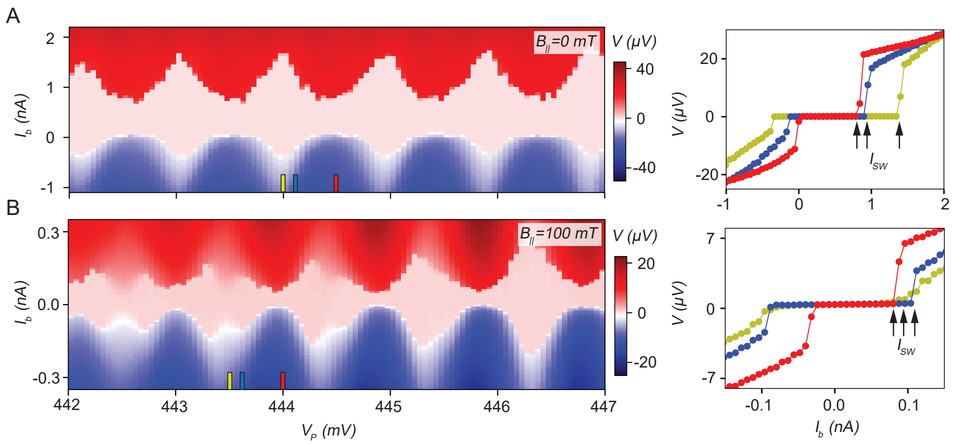

Figure 3.6: **Current-bias measurement results at different magnetic fields.** Current-bias characteristics of the NW CPT at different magnetic fields with the reference arm pinched off. (**A**) Left panel: Voltage drop V across the NW CPT as a function of current bias I_b and plunger gate V_P at $B_{||}$=0 mT. Right panel: Linecuts at three different plunger gate values. (**B**) Left panel: Voltage drop V across the NW CPT as a function of I_b and V_P at $B_{||}$=100 mT. Right panel: Linecuts at three different plunger gate values. Black arrows mark the switching current I_{sw}, where the NW CPT transitions from the SC state to the normal state.

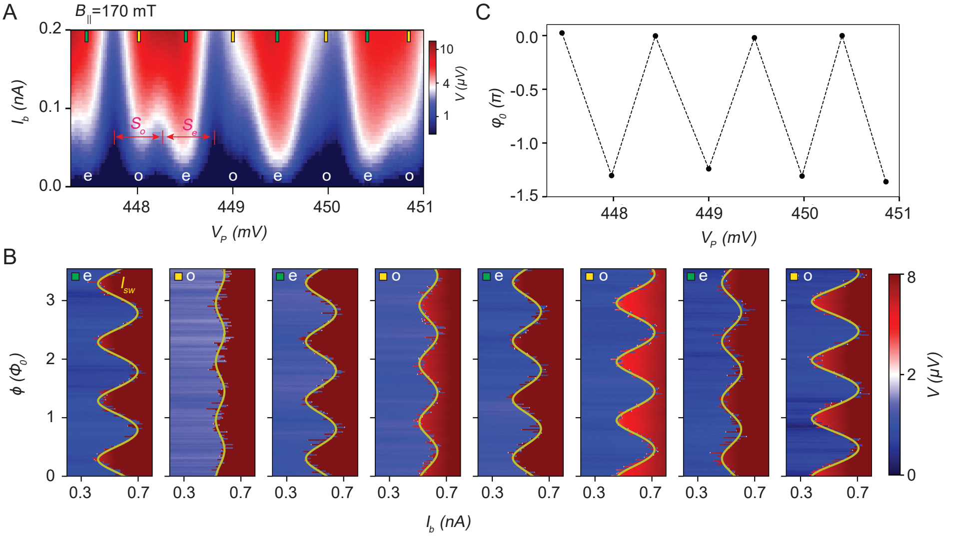

Figure 3.7: **Transport characteristics of the NW CPT for even and odd charge parity sectors at $B_{||}$=170 mT.** (**A**) Voltage drop across the NW CPT as a function of current bias I_b and plunger gate V_P with reference arm pinched off. Labels ‘e’ (‘o’) indicate Coulomb valleys of even (odd) charge parities of the SC island. Black bars mark the positions of three most left supercurrent peaks and distance between two neighboring peaks gives peak space for even (S_e) or odd parity (S_o). S_e and S_o have comparable values, indicating that the lowest sub-gap state is close to zero. (**B**) Voltage drop across the SQUID device as a function of current bias I_b and flux ϕ threading the SQUID loop at different charge parities of the SC island. The fitted switching current (yellow), I_{sw}, display a phase offset between opposite parity sectors. (**C**) Phase offset φ_0 versus plunger gate V_P. Dashed lines are guide lines to the eye. The data shown in this figure was measured after a thermal cycle of the dilution refrigerator, while the data in the subsequent figures was measured before the thermal cycle.

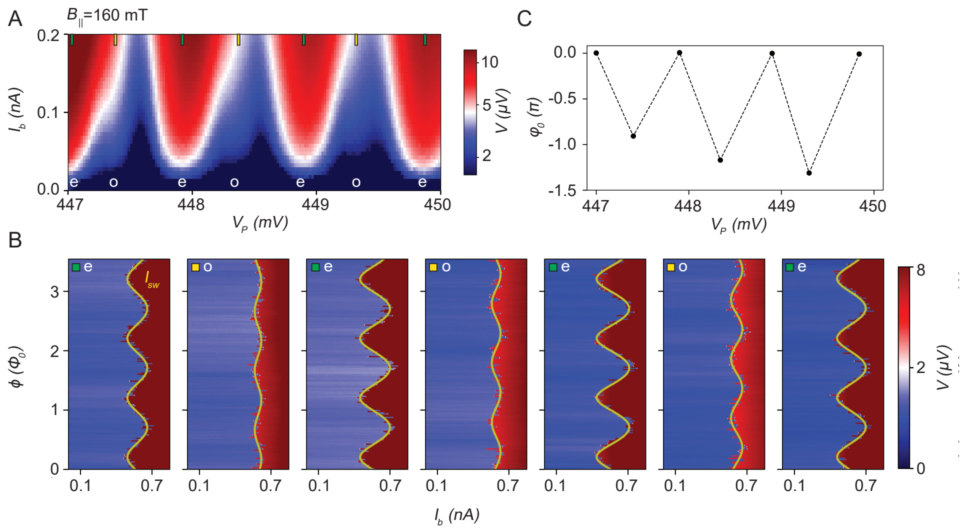

Figure 3.8: **Transport characteristics of the NW CPT for even and odd charge parity sectors at $B_{||}$=160 mT.** (**A-C**) The panels are analogous to those of Fig. 3.7.

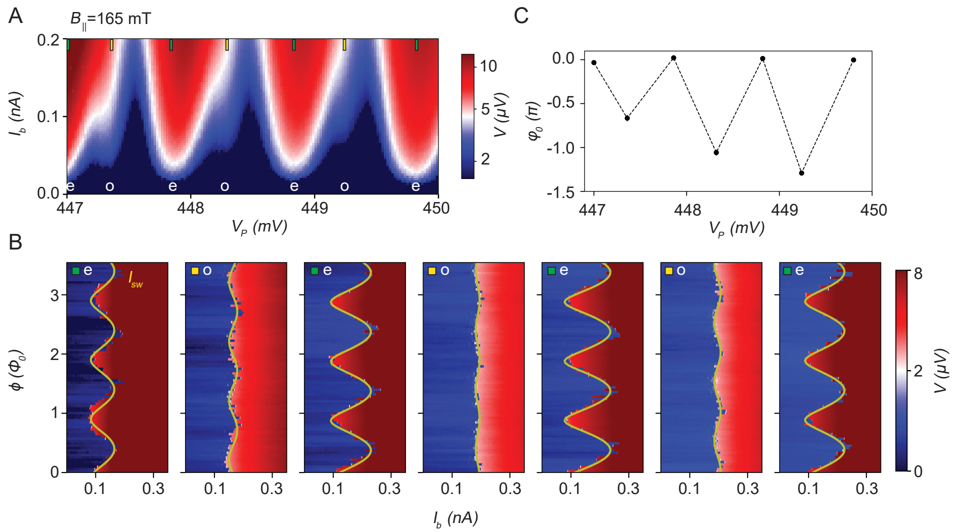

Figure 3.9: **Transport characteristics of the NW CPT for even and odd charge parity sectors at $B_{||}$=165 mT.** (**A-C**) The panels are analogous to those of Fig. 3.7.

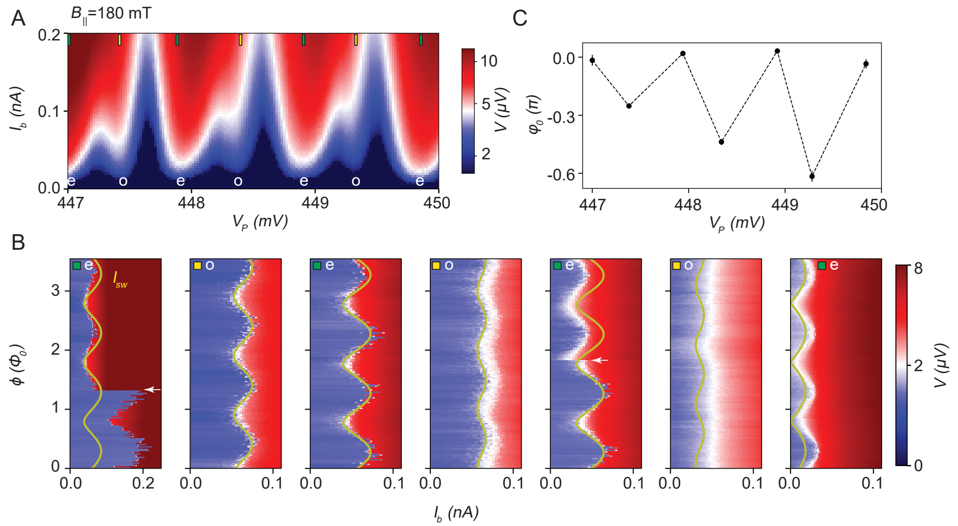

Figure 3.10: **Transport characteristics of the NW CPT for even and odd charge parity sectors at $B_{||}$=180 mT.** (**A-C**) The panels are analogous to those of Fig. 3.7.

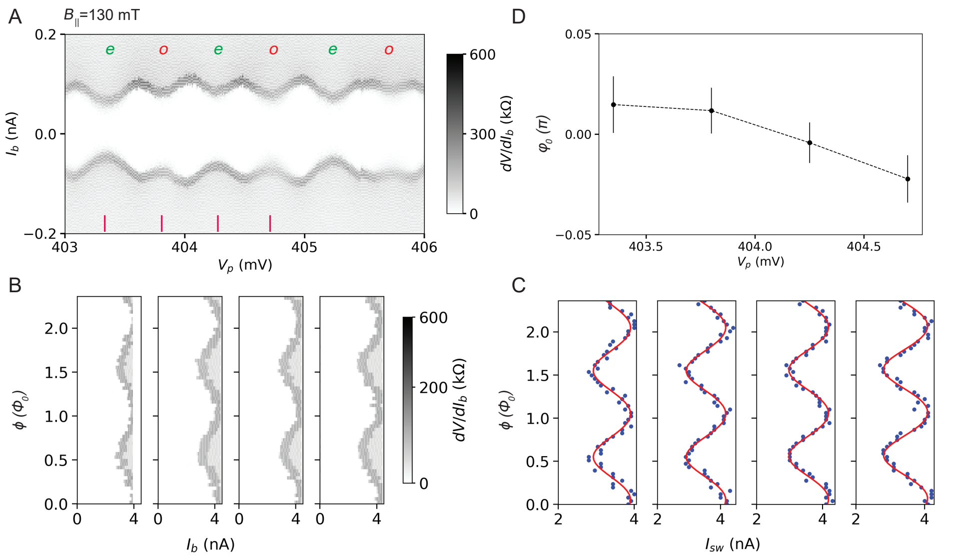

Figure 3.11: **A different plunger gate V_P region having phase independence on parities at $B_{||}$=130 mT.** (**A-D**) The panels are analogous to the ones in Fig. 3.12. Note that the plunger gate region is very close to the one in Fig. 3.12.

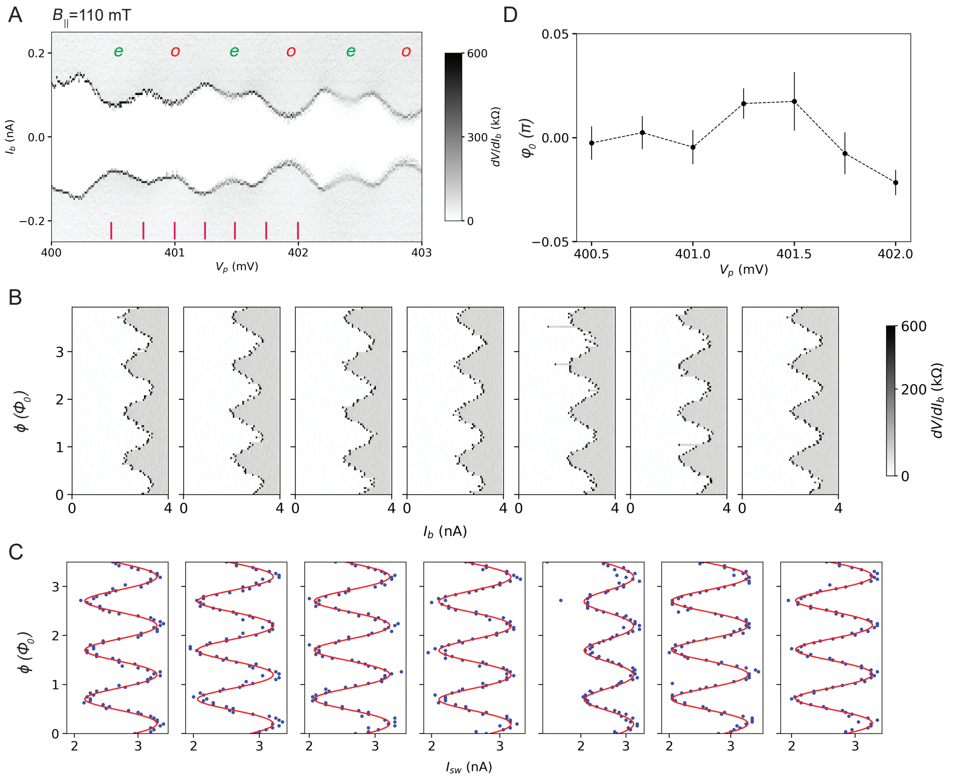

Figure 3.12: **Another example of phase independence on parities at $B_{||}$=110 mT.** (**A**) Differential resistance of the NW CPT as a function of current bias I_b and plunger gate V_P with reference arm pinched off. Green (red) labels 'e' ('o') indicate Coulomb valleys of even (odd) charge parities of the SC island. (**B**) Differential resistance of the SQUID device as a function of current bias I_b and flux ϕ threading the SQUID loop at different plunger gate points marked by red bars in (A). (**C**) Extracted switching current (blue points) versus flux ϕ and corresponding fitting curves (red lines). (**D**) Phase offset φ_0 versus plunger gate V_P. Dashed lines are guide lines to the eye. Note that the values φ_0 are obtained by subtrating mean value of all points. The varying of phase with V_P is within error bar fluctuation.

3.4.3. EFFECTIVE HAMILTONIAN FOR THE NANOWIRE COOPER-PAIR TRANSISTOR

In this section, we present more details on the derivation of the effective Hamiltonian for the NW CPT which yields a Josephson relation with parity-dependent phase offset. We proceed in multiple steps:

STEP 1: MODEL HAMILTONIAN

As a first step, we introduce our model Hamiltonian, which comprises a SC island with subgap states coupled to a pair of s-wave SC leads. The Hamiltonian for the SC leads has the form,

$$H_{\mathrm{SC}} = \sum_{\ell=\mathrm{L,R}} \sum_{\mathbf{k}} \Psi^{\dagger}_{\ell,\mathbf{k}} \left(\xi_{\mathbf{k}} \eta_z + \Delta_\ell \eta_x e^{i\varphi_\ell \eta_z} \right) \Psi_{\ell,\mathbf{k}}, \tag{3.2}$$

where $\Psi_{\ell,\mathbf{k}} = (c_{\ell,\mathbf{k}\uparrow}, c^{\dagger}_{\ell,-\mathbf{k}\downarrow})^T$ denotes the Nambu spinor with the electron annihilation operator $c_{\ell,\mathbf{k}s}$ for momentum $\mathbf{k}$, spin s, and lead ℓ. Furthermore, $\eta_{x,y,z}$ are the Nambu-space Pauli matrices, and $\xi_{\mathbf{k}}$ is the normal state dispersion. The magnitudes and the phases of the SC order parameters are Δ_ℓ and φ_ℓ, respectively. For simplicity, we assume that $\Delta_1 = \Delta_2 \equiv \Delta$.

Next, we introduce the charging Hamiltonian for the mesoscopic SC island,

$$U_{\mathrm{C}}(n) = U\left(n - n_g\right)^2, \tag{3.3}$$

where U denotes the charging energy magnitude. Moreover, n is the number operator that counts the electron charges on the island, and n_g denotes the induced charge, which is continuously tunable through the plunger gate voltage. As outlined in the main text, we focus on the two lowest energy subgap levels in the SC island, which will mediate the Josephson current between the SC leads. In terms of Majorana operators, $\gamma_i = \gamma_i^{\dagger}$, the Hamiltonian for the two subgap states reads,

$$H_{\mathrm{SG}} = i\varepsilon_a \gamma_{1a}\gamma_{2a} + i\varepsilon_b \gamma_{1b}\gamma_{2b}, \tag{3.4}$$

where $\varepsilon_{a,b}$ are the energy splittings. We adjust the induced charge so that the SC island hosts n_0 electron charges in its ground state and, as a result, the joint fermion parity of the subgap levels satisfies,

$$\gamma_{1a}\gamma_{2a}\gamma_{1b}\gamma_{2b} = (-1)^{n_0}. \tag{3.5}$$

Lastly, we introduce the tunneling Hamiltonian to describe the coupling between the SC leads and the SC island,

$$H_{\mathrm{T}} = \sum_{\ell,i} \sum_{\mathbf{k}s} \lambda^{s}_{\ell i}\; c^{\dagger}_{\ell,\mathbf{k}s} \gamma_i e^{-i\phi/2} + \mathrm{H.c.} \tag{3.6}$$

Here, $\lambda^{s}_{\ell i}$ are complex tunneling amplitudes which connect electrons on the SC lead ℓ to the subgap states, which are described by the Majorana operators γ_i. Furthermore, $e^{\pm i\phi/2}$ increases/decreases the number of electrons on the SC island by one unit, $[n, e^{\pm i\phi/2}] = \pm e^{\pm i\phi/2}$, while the Majorana operators γ_i induce flips of the SC island parity. In summary, the total Hamiltonian for our model is given by,

$$H = H_{\mathrm{SC}} + U_{\mathrm{C}} + H_{\mathrm{SG}} + H_{\mathrm{T}}. \tag{3.7}$$

STEP 2: EFFECTIVE HAMILTONIAN (GENERAL FORM)

As a second step, we provide an overview of the effective Hamiltonian for the model that we introduced in the previous subsection. More specifically, up to fourth order in the tunnel couplings $\lambda^s_{\ell i}$, the effective Hamiltonian reads,

$$H_{\text{eff}} = P\,H_{\text{T}}\left\{[u(n_a, n_b) - H_{\text{SC}} - U_{\text{C}} - H_{\text{SG}}]^{-1}(1-P)H_{\text{T}}\right\}^3 P. \tag{3.8}$$

Here, P denotes the projection operator on the subspace of $H_{\text{SC}} + H_{\text{C}} + H_{\text{SG}} + H_{\text{T}}$ with a fixed charge configuration (n_a, n_b) at energy,

$$u(n_a, n_b) = U_{\text{C}}\left(n_a + n_b - n_g\right)^2 + (-1)^{n_a+1}\varepsilon_a + (-1)^{n_b+1}\varepsilon_b. \tag{3.9}$$

To evaluate H_{eff} based on the equation presented above, we need to compute all sequences of intermediate states that mediate a Cooper pair between the SC leads via the SC island. Before going into the details of this calculation, we first present the general result,

$$\begin{aligned} H_{\text{eff}} &= -\gamma_{1a}\gamma_{2a}\gamma_{1b}\gamma_{2b}\left[\beta\sum_{m=1}^{4} J_{ab}^{(m)}\cos(\varphi+\varphi_{ab}^{(m)})\right] - \alpha_a J_a\cos(\varphi+\varphi_a) - \alpha_b J_b\cos(\varphi+\varphi_b) \\ &\equiv -\gamma_{1a}\gamma_{2a}\gamma_{1b}\gamma_{2b}\,\beta J_{ab}\cos(\varphi+\varphi_{ab}) - \alpha_a J_a\cos(\varphi+\varphi_a) - \alpha_b J_b\cos(\varphi+\varphi_b) \end{aligned} \tag{3.10}$$

In the second line, we have defined the Josephson couplings and phase offsets,

$$J_{ab} = \left|\sum_{m=1}^{4} J_{ab}^{(m)} e^{i\varphi_{ab}^{(m)}}\right|, \qquad \varphi_{ab} = \arg\left(\sum_{m=1}^{4} J_{ab}^{(m)} e^{i\varphi_{ab}^{(m)}}\right). \tag{3.11}$$

We present expressions for the Josephson couplings $(J_a, J_b, J_{ab}^{(m)})$, the phase offsets $(\varphi_a, \varphi_b, \varphi_{ab}^{(m)})$, as well as the dimensionless functions $(\alpha_a, \alpha_b, \beta)$ in the subsequent sections. Here, we only note that for a fixed charge configuration (n_a, n_b), the Josephson relation of the NW CPT is given by,

$$I = (-1)^{n_0}\, I_{ab}\cos(\varphi+\varphi_{ab}) + I_a\cos(\varphi+\varphi_a) + I_b\cos(\varphi+\varphi_b), \tag{3.12}$$

where $I_{ab} = 2e\beta J_{ab}/\hbar$, $I_a = 2e\alpha_a J_a/\hbar$, and $I_b = 2e\alpha_b J_b/\hbar$. This is the result presented in Eq. (3.1) of the main text.

STEP 3: EFFECTIVE HAMILTONIAN (JOSEPHSON COUPLINGS)

As a third step, we give the expressions for the Josephson couplings $(J_a, J_b, J_{ab}^{(m)})$ as well as the dimensionless functions $(\alpha_a, \alpha_b, \beta)$, which appear in the previously introduced effective Hamiltonian H_{eff}.

We, initially, define the auxiliary Josephson couplings,

$$J_{k,\ell}^{i,j} = -\frac{8}{\pi^2\Delta}\left(\sqrt{\Gamma^{\downarrow}_{\text{L}i}\Gamma^{\uparrow}_{\text{L}j}} - \sqrt{\Gamma^{\downarrow}_{\text{L}j}\Gamma^{\uparrow}_{\text{L}i}}\right)\left(\sqrt{\Gamma^{\downarrow}_{\text{R}k}\Gamma^{\uparrow}_{\text{R}\ell}} - \sqrt{\Gamma^{\downarrow}_{\text{R}\ell}\Gamma^{\uparrow}_{\text{R}k}}\right), \tag{3.13}$$

together with the linewidths,

$$\begin{aligned} \Gamma^s_{m,1a} &= \pi\nu_F|\lambda^s_{m,1a}|^2 \quad , \quad \Gamma^s_{m,2a} = \pi\nu_F|\lambda^s_{m,2a}|^2 \\ \Gamma^s_{m,1b} &= \pi\nu_F|\lambda^s_{m,1b}|^2 \quad , \quad \Gamma^s_{m,2b} = \pi\nu_F|\lambda^s_{m,2b}|^2. \end{aligned} \tag{3.14}$$

Here, for example, $\Gamma^s_{m,1a}$ denotes the linewidth that the level a acquires due to the tunneling of electrons with spin s from lead m into γ_{1a}. The normal-state density of states at the Fermi level for the leads is given by ν_F. If, we assume an approximate linewidth $\Gamma^{\text{approx}} = 0.01\,\text{meV}$ and a SC gap $\Delta = 0.3\,\text{meV}$ in the SC leads, we find an upper-bound estimate for the critical current $I_c^{\text{approx}} = [16e(\Gamma^{\text{approx}})^2]/(\hbar\pi^2\Delta) \approx 0.1\,\text{nA}$, which is consistent with the values measured in the experiment.

With these definitions, the Josephson couplings, appearing in H_{eff}, are given by,

$$\begin{aligned} &J_a = J^{1a,2a}_{1a,2a} \qquad J_b = J^{1b,2b}_{1b,2b} \\ &J^{(1)}_{ab} = J^{1a,1b}_{2a,2b} \quad , \quad J^{(2)}_{ab} = J^{1b,2a}_{1a,2b} \quad , \quad J^{(3)}_{ab} = J^{1a,2b}_{1b,2a} \quad , \quad J^{(4)}_{ab} = J^{2a,2b}_{1a,1b}. \end{aligned} \tag{3.15}$$

For introducing the dimensionless functions $(\alpha_a, \alpha_b, \beta)$, we first define,

$$g(x) = \sqrt{1+x^2} > 0 \quad , \quad h(n_a+N_a, n_b+N_b) = \frac{u(n_a+N_a, n_b+N_b) - u(n_a, n_b)}{\Delta} > 0, \tag{3.16}$$

and $Z(x, N_a, N_b) = g(x) + h(n_a+N_a, n_b+N_b)$ which allows us to write,

$$\begin{aligned}
\alpha_a &= \int_1^\infty \mathrm{d}x \int_1^\infty \mathrm{d}y \, \frac{1}{g(x)g(y)Z(x,-1,0)[g(x)+g(y)]Z(x,+1,0)}, \\
\alpha_b &= \int_1^\infty \mathrm{d}x \int_1^\infty \mathrm{d}y \, \frac{1}{g(x)g(y)Z(x,0,-1)[g(x)+g(y)]Z(x,0,+1)}, \\
\beta_1 &= \frac{1}{4}\int_1^\infty \mathrm{d}x \int_1^\infty \mathrm{d}y \, \frac{1}{g(x)g(y)Z(y,0,+1)[g(x)+g(y)]Z(x,+1,0)} \\
\beta_2 &= \frac{1}{4}\int_1^\infty \mathrm{d}x \int_1^\infty \mathrm{d}y \, \frac{1}{g(x)g(y)Z(x,0,-1)[g(x)+g(y)]Z(x,+1,0)} \\
\beta_3 &= \frac{1}{4}\int_1^\infty \mathrm{d}x \int_1^\infty \mathrm{d}y \, \frac{1}{g(x)g(y)Z(y,+1,0)[g(x)+Z(y,+1,-1)]Z(x,+1,0)} \\
\beta_4 &= \frac{1}{4}\int_1^\infty \mathrm{d}x \int_1^\infty \mathrm{d}y \, \frac{1}{g(x)g(y)Z(x,0,-1)[g(x)+Z(y,+1,-1)]Z(x,+1,0)} \\
\beta_5 &= \frac{1}{4}\int_1^\infty \mathrm{d}x \int_1^\infty \mathrm{d}y \, \frac{1}{g(x)g(y)Z(x,-1,0)[g(x)+Z(y,-1,+1)]Z(y,-1,0)} \\
\beta_6 &= \frac{1}{4}\int_1^\infty \mathrm{d}x \int_1^\infty \mathrm{d}y \, \frac{1}{g(x)g(y)Z(y,0,+1)[g(x)+Z(y,-1,+1)]Z(y,-1,0)} \\
\beta_7 &= \frac{1}{4}\int_1^\infty \mathrm{d}x \int_1^\infty \mathrm{d}y \, \frac{1}{g(x)g(y)Z(x,0,-1)[g(x)+g(y)]Z(y,-1,0)} \\
\beta_8 &= \frac{1}{4}\int_1^\infty \mathrm{d}x \int_1^\infty \mathrm{d}y \, \frac{1}{g(x)g(y)Z(y,0,+1)[g(x)+g(y)]Z(y,-1,0)} \\
\beta &= \sum_{p=1}^{16} \beta_p.
\end{aligned} \tag{3.17}$$

In the definition of β, we have included parameters $\beta_9,\dots,\beta_{16}$ which are identical to $\beta_1,\dots,\beta_8$ but with the arguments of h interchanged, $h(n,m)\to h(m,n)$. We note that for a substantial charging energy, virtual states with two additional electrons on the SC island are energetically unfavorable and, for simplicity, have not been accounted for in the expressions for $(\alpha_a,\alpha_b,\beta)$.

EFFECTIVE HAMILTONIAN (ANOMALOUS PHASE SHIFTS)

As a fourth step, we give the expressions for the phase offsets $(\varphi_a,\varphi_b,\varphi_{ab}^{(m)})$ appearing in the effective Hamiltonian H_{eff}.

We, therefore, introduce the auxiliary phase offsets,

$$\varphi_{k,\ell}^{i,j}=\arg[(\lambda_{\text{L}i}^{\downarrow}\lambda_{\text{L}j}^{\uparrow}-\lambda_{\text{L}i}^{\uparrow}\lambda_{\text{L}j}^{\downarrow})^*(\lambda_{\text{R}k}^{\downarrow}\lambda_{\text{R}\ell}^{\uparrow}-\lambda_{\text{R}k}^{\uparrow}\lambda_{\text{R}\ell}^{\downarrow})], \tag{3.18}$$

which allow us express the phase offsets appearing in H_{eff} as,

$$\begin{aligned}&\varphi_a=\varphi_{1a,2a}^{1a,2a}\quad,\quad\varphi_b=\varphi_{1b,2b}^{1b,2b}\\&\varphi_{ab}^{(1)}=\varphi_{2a,2b}^{1a,1b}\quad,\quad\varphi_{ab}^{(2)}=\varphi_{1a,2b}^{1b,2a}\quad,\quad\varphi_{ab}^{(3)}=\varphi_{1b,2a}^{1a,2b}\quad,\quad\varphi_{ab}^{(4)}=\varphi_{1a,1b}^{2a,2b}.\end{aligned} \tag{3.19}$$

STEP 5: EFFECTIVE HAMILTONIAN (EXAMPLE CALCULATION)

As a final step, we provide specific examples on sequences of intermediate states that mediate a contribution to the Josephson current with and without a parity-dependent prefactor. We, thereby, focus on the sequences which we have shown in Fig. 3.4 of the main text.

We begin by considering sequences of the type shown in Fig. 3.4A, which comprise a parity-dependent prefactor. An example, for such a sequence is given by,

$$\begin{aligned}&P(c_{\text{R},-\mathbf{q}\downarrow}^{\dagger}\gamma_{2,b}e^{-i\phi/2})(\gamma_{1,b}c_{\text{L},-\mathbf{k}\downarrow}e^{i\phi/2})(\gamma_{1,a}c_{\text{L},\mathbf{k}\uparrow}e^{i\phi/2})(c_{\text{R},\mathbf{q}\uparrow}^{\dagger}\gamma_{2,a}e^{-i\phi/2})P\\&=P(c_{\text{R},-\mathbf{q}\downarrow}^{\dagger}\gamma_{2,b}\gamma_{1,b}c_{\text{L},-\mathbf{k}\downarrow}\gamma_{1,a}c_{\text{L},\mathbf{k}\uparrow}c_{\text{R},\mathbf{q}\uparrow}^{\dagger}\gamma_{2,a})P\\&=-P(\gamma_{1,a}\gamma_{2,a}\gamma_{1,b}\gamma_{2,b})(c_{\text{R},-\mathbf{q}\downarrow}^{\dagger}c_{\text{L},-\mathbf{k}\downarrow}c_{\text{L},\mathbf{k}\uparrow}c_{\text{R},\mathbf{q}\uparrow}^{\dagger})P\\&=e^{i(\varphi_{\text{L}}-\varphi_{\text{R}})}u_{\mathbf{q}}v_{\mathbf{q}}u_{\mathbf{k}}v_{\mathbf{k}}P(\gamma_{1,a}\gamma_{2,a}\gamma_{1,b}\gamma_{2,b})(\gamma_{\text{R},\mathbf{q}\uparrow}\gamma_{\text{L},-\mathbf{k}\downarrow}\gamma_{\text{L},-\mathbf{k}\downarrow}^{\dagger}\gamma_{\text{R},\mathbf{q}\uparrow}^{\dagger})P\\&=e^{i(\varphi_{\text{L}}-\varphi_{\text{R}})}u_{\mathbf{q}}v_{\mathbf{q}}u_{\mathbf{k}}v_{\mathbf{k}}P(\gamma_{1,a}\gamma_{2,a}\gamma_{1,b}\gamma_{2,b})P\end{aligned} \tag{3.20}$$

In the third equality, we have represented the electron operators in the SC leads in terms of Bogoliubov quasiparticles through the relations, $c_{\ell,\mathbf{k}\uparrow}=e^{i\varphi_\ell/2}(u_{\mathbf{k}}\gamma_{\ell,\mathbf{k}\uparrow}+v_{\mathbf{k}}\gamma_{\ell,-\mathbf{k}\downarrow}^{\dagger})$ and $c_{\ell,-\mathbf{k}\downarrow}=e^{i\varphi_\ell/2}(u_{\mathbf{k}}\gamma_{\ell,-\mathbf{k}\downarrow}-v_{\mathbf{k}}\gamma_{\ell,\mathbf{k}\uparrow}^{\dagger})$ with the coherence factors $u_{\mathbf{k}}$, $v_{\mathbf{k}}$. If we sum over all momenta, we find that the amplitude for the example sequence is given by,

$$-\Omega\sum_{\mathbf{k},\mathbf{q}}\frac{v_{\mathbf{q}}u_{\mathbf{k}}u_{\mathbf{q}}v_{\mathbf{k}}}{[E_{\mathbf{q}}+u(n_a,n_b+1)-u(n_a,n_b)][E_{\mathbf{k}}+E_{\mathbf{q}}][E_{\mathbf{q}}+u(n_a-1,n_b)-u(n_a,n_b)]}, \tag{3.21}$$

where $\Omega = (\lambda^{\uparrow}_{\mathrm{L},1a}\lambda^{\downarrow}_{\mathrm{L},1b})^*(\lambda^{\uparrow}_{\mathrm{R},2a}\lambda^{\downarrow}_{\mathrm{R},2b})$ and $E_{\mathbf{k}} = \sqrt{\xi^2_{\mathbf{k}} + \Delta^2}$ denotes the dispersion of the SC leads. If we assume a constant density of states ν_F at the Fermi level, we can rewrite this amplitude as,

$$-\frac{1}{\Delta}\int_1^\infty \mathrm{d}x \int_1^\infty \mathrm{d}y \; \frac{\nu_F^2(\lambda^{\uparrow}_{\mathrm{L},1a}\lambda^{\downarrow}_{\mathrm{L},1b})^*(\lambda^{\uparrow}_{\mathrm{R},2a}\lambda^{\downarrow}_{\mathrm{R},2b})}{g(x)g(y)[g(y)+h(n_a,n_b+1)][g(x)+g(y)][g(y)+h(n_a-1,n_b)]}. \tag{3.22}$$

Hence, we conclude that the sequence contributes to the term $\propto \beta_8$ in the Josephson relation of the NW CPT.

Next, we consider sequences of the type shown in Fig. 3.4B, which do not comprise a parity-dependent prefactor. An example, for such a sequence is given by,

$$\begin{aligned}
&P(\gamma_{1,a}c_{\mathrm{L},-\mathbf{k}\downarrow}e^{i\phi/2})(c^\dagger_{\mathrm{R},-\mathbf{q}\downarrow}\gamma_{2,a}e^{-i\phi/2})(c^\dagger_{\mathrm{R},\mathbf{q}\uparrow}\gamma_{2,a}e^{-i\phi/2})(\gamma_{1,a}c_{\mathrm{L},\mathbf{k}\uparrow}e^{i\phi/2})P \\
&= P(\gamma_{1,a}c_{\mathrm{L},-\mathbf{k}\downarrow}c^\dagger_{\mathrm{R},-\mathbf{q}\downarrow}\gamma_{2,a}c^\dagger_{\mathrm{R},\mathbf{q}\uparrow}\gamma_{2,a}\gamma_{1,a}c_{\mathrm{L},\mathbf{k}\uparrow})P \\
&= P(c_{\mathrm{L},-\mathbf{k}\downarrow}c^\dagger_{\mathrm{R},-\mathbf{q}\downarrow}c^\dagger_{\mathrm{R},\mathbf{q}\uparrow}c_{\mathrm{L},\mathbf{k}\uparrow})P \\
&= -e^{i(\varphi_\mathrm{L}-\varphi_\mathrm{R})}\,u_{\mathbf{q}}v_{\mathbf{q}}u_{\mathbf{k}}v_{\mathbf{k}}P(\gamma_{\mathrm{L},-\mathbf{k}\downarrow}\gamma_{\mathrm{R},\mathbf{q}\uparrow}\gamma^\dagger_{\mathrm{R},\mathbf{q}\uparrow}\gamma^\dagger_{\mathrm{L},-\mathbf{k}\downarrow})P \\
&= -e^{i(\varphi_\mathrm{L}-\varphi_\mathrm{R})}\,u_{\mathbf{q}}v_{\mathbf{q}}u_{\mathbf{k}}v_{\mathbf{k}}
\end{aligned} \tag{3.23}$$

If we again sum over all momenta, we find that the amplitude for the example sequence is given by,

$$\Omega\sum_{\mathbf{k},\mathbf{q}} \frac{v_{\mathbf{q}}u_{\mathbf{k}}u_{\mathbf{q}}v_{\mathbf{k}}}{[E_{\mathbf{k}}+u(n_a-1,n_b)-u(n_a,n_b)][E_{\mathbf{k}}+E_{\mathbf{q}}][E_{\mathbf{k}}+u(n_a+1,n_b)-u(n_a,n_b)]}. \tag{3.24}$$

with $\Omega = (\lambda^{\uparrow}_{\mathrm{L},1a}\lambda^{\downarrow}_{\mathrm{L},1a})^*(\lambda^{\uparrow}_{\mathrm{R},2a}\lambda^{\downarrow}_{\mathrm{R},2a})$. In particular, if we assume constant density of states ν_F at the Fermi level, we can rewrite this amplitude as,

$$\frac{1}{\Delta}\int_1^\infty \mathrm{d}x \int_1^\infty \mathrm{d}y \; \frac{\nu_F^2(\lambda^{\uparrow}_{\mathrm{L},1a}\lambda^{\downarrow}_{\mathrm{L},1a})^*(\lambda^{\uparrow}_{\mathrm{R},2a}\lambda^{\downarrow}_{\mathrm{R},2a})}{g(x)g(y)[g(x)+h(n_a-1,n_b)][g(x)+g(y)][g(x)+h(n_a+1,n_b)]}. \tag{3.25}$$

We, thus, conclude that the sequence contributes to the term $\propto \alpha_a$ in the Josephson relation of the NW CPT.

REFERENCES

[1] B. I. Spivak and S. A. Kivelson. "Negative local superfluid densities: The difference between dirty superconductors and dirty Bose liquids". In: *Phys. Rev. B* 43 (1991), 3740(R).

[2] J. A. van Dam, Y. V. Nazarov, E. P. A. M. Bakkers, S. D. Franceschi, and L. P. Kouwenhoven. "Supercurrent reversal in quantum dots". In: *Nature* 442 (2006), pp. 667–670.

[3] D. Razmadze, E. C. T. O'Farrell, P. Krogstrup, and C. M. Marcus. "Quantum Dot Parity Effects in Trivial and Topological Josephson Junctions". In: *Phys. Rev. Lett.* 125 (11 2020), p. 116803.

[4] A. Zazunov, R. Egger, T. Jonckheere, and T. Martin. "Anomalous Josephson Current through a Spin-Orbit Coupled Quantum Dot". In: *Phys. Rev. Lett.* 103 (14 2009), p. 147004.

[5] A. Brunetti, A. Zazunov, A. Kundu, and R. Egger. "Anomalous Josephson current, incipient time-reversal symmetry breaking, and Majorana bound states in interacting multilevel dots". In: *Phys. Rev. B* 88 (14 2013), p. 144515.

[6] D. B. Szombati, S. Nadj-Perge, D. Car, S. R. Plissard, E. P. A. M. Bakkers, and L. P. Kouwenhoven. "Josephson ϕ_0-junction in nanowire quantum dots". In: *Nature Phys.* 12 (2016), pp. 568–572.

[7] C. Schrade, S. Hoffman, and D. Loss. "Detecting topological superconductivity with ϕ_0-Josephson junctions". In: *Phys. Rev. B* 95 (2017), p. 195421.

[8] L. J. Geerligs, V. F. Anderegg, J. Romijn, and J. E. Mooij. "Single Cooper-pair tunneling in small-capacitance junctions". In: *Phys. Rev. Lett.* 65 (3 1990), pp. 377–380.

[9] M. T. Tuominen, J. M. Hergenrother, T. S. Tighe, and M. Tinkham. "Experimental evidence for parity-based 2e periodicity in a superconducting single-electron tunneling transistor". In: *Phys. Rev. Lett.* 69 (13 1992), pp. 1997–2000.

[10] T. A. Fulton, P. L. Gammel, D. J. Bishop, L. N. Dunkleberger, and G. J. Dolan. "Observation of combined Josephson and charging effects in small tunnel junction circuits". In: *Phys. Rev. Lett.* 63 (12 1989), pp. 1307–1310.

[11] D. J. van Woerkom, A. Geresdi, and L. P. Kouwenhoven. "One minute parity lifetime of a NbTiN Cooper-pair transistor". In: *Nat. Phys.* 11 (2015), pp. 547–550.

[12] A. Proutski, D. Laroche, B. van 't Hooft, P. Krogstrup, J. Nygård, L. P. Kouwenhoven, and A. Geresdi. "Broadband microwave spectroscopy of semiconductor nanowire-based Cooper-pair transistors". In: *Phys. Rev. B* 99 (22 2019), p. 220504.

[13] J. van Veen, A. Proutski, T. Karzig, D. I. Pikulin, R. M. Lutchyn, J. Nygård, P. Krogstrup, A. Geresdi, L. P. Kouwenhoven, and J. D. Watson. "Magnetic-field-dependent quasiparticle dynamics of nanowire single-Cooper-pair transistors". In: *Phys. Rev. B* 98 (17 2018), p. 174502.

[14] S. C. and F. L. "Andreev or Majorana, Cooper finds out". In: *arXiv preprint* (2018), p. 1809.06370.

[15] C. W. J. Beenakker, D. P. DiVincenzo, C. Emary, and M. Kindermann. "Charge Detection Enables Free-Electron Quantum Computation". In: *Phys. Rev. Lett.* 93 (2 2004), p. 020501.

[16] W. Mao, D. V. Averin, R. Ruskov, and A. N. Korotkov. "Mesoscopic Quadratic Quantum Measurements". In: *Phys. Rev. Lett.* 93 (5 2004), p. 056803.

[17] H.-A. Engel and D. Loss. "Fermionic Bell-state analyzer for spin qubits". In: *Science* 309 (2005), pp. 586–588.

[18] K. Lalumière, J. M. Gambetta, and A. Blais. "Tunable joint measurements in the dispersive regime of cavity QED". In: *Phys. Rev. A* 81 (4 2010), p. 040301.

[19] R. Ionicioiu. "Entangling spins by measuring charge: A parity-gate toolbox". In: *Phys. Rev. A* 75 (3 2007), p. 032339.

[20] W. Pfaff, T. H. Taminiau, L. Robledo, H. Bernien, M. L. Markham, D. J. Twitchen, and R. Hanson. "Demonstration of entanglement-by-measurement of solid-state qubits". In: *Nat. Phys.* 9 (2013), pp. 29–33.

[21] C. K. Andersen, A. Remm, S. Balasiu, S. Krinner, J. Heinsoo, J.-C. Besse, M. Gabureac, A. Wallraff, and C. Eichler. "Entanglement stabilization using ancilla-based parity detection and real-time feedback in superconducting circuits". In: *npj Quantum Inf.* 5.69 (2019).

[22] C. C. Bultink, T. E. O'Brien, R. Vollmer, N. Muthusubramanian, M. W. Beekman, M. A. Rol, X. Fu, B. Tarasinski, V. Ostroukh, B. Varbanov, A. Bruno, and L. DiCarlo. "Protecting quantum entanglement from leakage and qubit errors via repetitive parity measurements". In: *Sci. Adv.* 6 (2020).

[23] D. Aasen, M. Hell, R. V. Mishmash, A. Higginbotham, J. Danon, M. Leijnse, T. S. Jespersen, J. A. Folk, C. M. Marcus, K. Flensberg, and J. Alicea. "Milestones Toward Majorana-Based Quantum Computing". In: *Phys. Rev. X* 6 (3 2016), p. 031016.

[24] S. Plugge, A. Rasmussen, R. Egger, and K. Flensberg. "Majorana box qubits". In: *New J. Phys.* 19 (2017), p. 012001.

[25] T. Karzig, C. Knapp, R. M. Lutchyn, P. Bonderson, M. B. Hastings, C. Nayak, J. Alicea, K. Flensberg, S. Plugge, Y. Oreg, C. M. Marcus, and M. H. Freedman. “Scalable designs for quasiparticle-poisoning-protected topological quantum computation with Majorana zero modes”. In: *Phys. Rev. B* 95 (23 2017), p. 235305.

[26] C. Schrade and L. Fu. “Majorana Superconducting Qubit”. In: *Phys. Rev. Lett.* 121 (2018), p. 267002.

[27] C. Schrade and L. Fu. “Parity-controlled 2π Josephson effect mediated by Majorana Kramers pairs”. In: *Phys. Rev. Lett.* 120 (2018), p. 267002.

[28] S. M. Albrecht, A. P. Higginbotham, M. Madsen, F. Kuemmeth, T. S. Jespersen, J. Nygård, P. Krogstrup, and C. M. Marcus. “Exponential protection of zero modes in Majorana islands”. In: *Nature* 531 (2016), pp. 206–209.

[29] J. Shen, S. Heedt, F. Borsoi, B. van Heck, S. Gazibegovic, R. L. M. O. het Veld, D. Car, J. A. Logan, M. Pendharkar, S. J. J. Ramakers, G. Wang, D. Xu, D. Bouman, A. Geresdi, C. J. Palmstrom, E. P. A. M. Bakkers, and L. P. Kouwenhoven. “Parity transitions in the superconducting ground state of hybrid InSb-Al Coulomb islands”. In: *Nat. Commun.* 9 (2018), p. 4801.

[30] J. Shen, G. W. Winkler, F. Borsoi, S. Heedt, V. Levajac, J.-Y. Wang, D. van Driel, D. Bouman, S. Gazibegovic, R. L. M. O. H. Veld, D. Car, J. A. Logan, M. Pendharkar, C. J. Palmstrøm, E. P. A. M. Bakkers, L. P. Kouwenhoven, and B. van Heck. “Full parity phase diagram of a proximitized nanowire island”. In: *Phys. Rev. B* 104 (2021), p. 045422.

[31] S. Vaitiek ėnas, M.-T. Deng, J. Nygård, P. Krogstrup, and C. M. Marcus. “Effective *g* Factor of subgap states in hybrid nanowires”. In: *Phys. Rev. Lett.* 121 (3 2018), p. 037703.

[32] L. Bretheau. *Localized Excitations in Superconducting Atomic Contacts: PROBING THE ANDREEV DOUBLET.* CEA-Saclay, Gif-sur-Yvette Cedex, 2013.

[33] V. Ambegaokar and B. I. Halperin. “Voltage Due to Thermal Noise in the dc Josephson Effect”. In: *Phys. Rev. Lett.* 22 (25 1969), pp. 1364–1366.

[34] H. I. Jørgensen, T. Novotný, K. Grove-Rasmussen, K. Flensberg, and P. E. Lindelof. “Critical Current $0-\pi$ transition in designed Josephson quantum dot junctions”. In: *Nano Lett.* 7 (2007), pp. 2441–2445.

[35] A. C. C. Drachmann, H. J. Suominen, M. Kjaergaard, B. Shojaei, C. J. Palmstrøm, C. M. Marcus, and F. Nichele. “Proximity effect transfer from NbTi into a semiconductor heterostructure via epitaxial aluminum”. In: *Nano Lett.* 17 (2017), pp. 1200–1203.

[36] M. Tinkham. *Introduction to Superconductivity.* Dover Publications, 2004.

[37] J. G. Kroll. *Magnetic field compatible hybrid circuit quantum electrodynamics.* Delft University of Technology, 2019.

[38] A. J. Annunziata, D. F. Santavicca, L. Frunzio, G. Catelani, M. J. Rooks, A. Frydman, and D. E. Prober. “Tunable superconducting nanoinductors”. In: *Nanotechnology* 21 (2010), p. 445202.

4

Impact of junction length on supercurrent resilience against magnetic field in InSb-Al nanowire Josephson junctions

Semiconducting nanowire Josephson junctions represent an attractive platform to investigate the anomalous Josephson effect and detect topological superconductivity. However, an external magnetic field generally suppresses the supercurrent through hybrid nanowire junctions and significantly limits the field range in which the supercurrent phenomena can be studied. In this work, we investigate the impact of the length of InSb-Al nanowire Josephson junctions on the supercurrent resilience against magnetic fields. We find that the critical parallel field of the supercurrent can be considerably enhanced by reducing the junction length. Particularly, in 30 nm*-long junctions supercurrent can persist up to* 1.3 T *parallel field - approaching the critical field of the superconducting film. Furthermore, we embed such short junctions into a superconducting loop and obtain the supercurrent interference at a parallel field of* 1 T. *Our findings are highly relevant for multiple experiments on hybrid nanowires requiring a magnetic field-resilient supercurrent.*

The work in this chapter has been published as: V. Levajac, G. P. Mazur, N. van Loo, F. Borsoi, G. Badawy, s. Gazibegović, E. P. A. M. Bakkers, S. Heedt, L. P. Kouwenhoven and J.-Y. Wang *"Impact of junction length on supercurrent resilience against magnetic field in InSb-Al nanowire Josephson junctions"*, Nano Letters 23, 11, 4716-4722 (2023)

4.1. INTRODUCTION

Semiconducting nanowire Josephson junctions (JJs) are widely used as a versatile platform for studying various physical phenomena that arise in semiconductor-superconductor hybrid systems. Therein, the III-V semiconductors have attracted a particular interest in exploring the anomalous Josephson effect[1–4], topological superconductivity [5–11] and the Josephson diode effect [12–14], due to their strong spin-orbit interaction and large g factor. Recently, the Josephson diode effect has been exceptionally intriguing in both theory[15–18] and experiment[13, 14, 19–22]. In the above research works, an indispensible ingredient is the breaking of time reversal symmetry, which is normally achieved via external magnetic fields. However, an external magnetic field generally suppresses the supercurrent through a hybrid nanowire JJ - therefore significantly limiting the parameter space for addressing the aforementioned effects in hybrid nanowires. Preserving the supercurrent in hybrid nanowire JJs at high magnetic fields becomes thus critically important. Selecting high critical field superconductors, such as NbTiN [23], Pb [24], Sn [25] or Al doped by Pt [26], seems to be an option for improving the magnetic field compatibility of the supercurrent. However, none of these material platforms have yielded a supercurrent at high magnetic fields. Moreover, it has been observed that the supercurrent of nanowire JJs generally vanishes at magnetic fields far below the critical field of the superconducting film [27, 28]. Searching for an alternative way to improve the supercurrent resilience against magnetic field in nanowire JJs is thus needed. In spite of extensive works on nanowire JJs with either evaporated superconducting contacts[28–31] or epitaxially grown superconducting shells[27, 32, 33], a potential impact of the junction length on supercurrent performance in magnetic fields has not been systematically investigated.

In this work, we have studied InSb-Al nanowire JJs with the junction length L varying from 27 nm to 160 nm. The junction length has been found to be an essential parameter that determines the supercurrent evolution in a parallel magnetic field. In the long devices ($L \sim 160$ nm), the supercurrent is suppressed quickly in a magnetic field and fully vanishes at parallel fields of ~ 0.7 T. In contrast, the supercurrent in short devices ($L \sim 30$ nm) persists up to parallel fields of ~ 1.3 T, approaching the critical in-plane magnetic field of the Al film (~ 1.5 T [26, 27, 34]). Despite the influence of the electro-chemical potential in the juntions, the resilient supercurrent is present only in the short devices ($L \sim 30$ nm). We exploit this property to realise a magnetic field-resilient superconducting quantum interference device (SQUID). At a magnetic field of 1 T, the supercurrent through the device displays the characteristic oscillatory pattern as a function of the magnetic flux through the loop. We expect that our demonstration of magnetic field resilient supercurrent in remarkably short nanowire JJs offers a new approach to improving the field-compatibility of not only SQUIDs but many other hybrid nanowire devices utilizing the Josephson effect at high magnetic field.

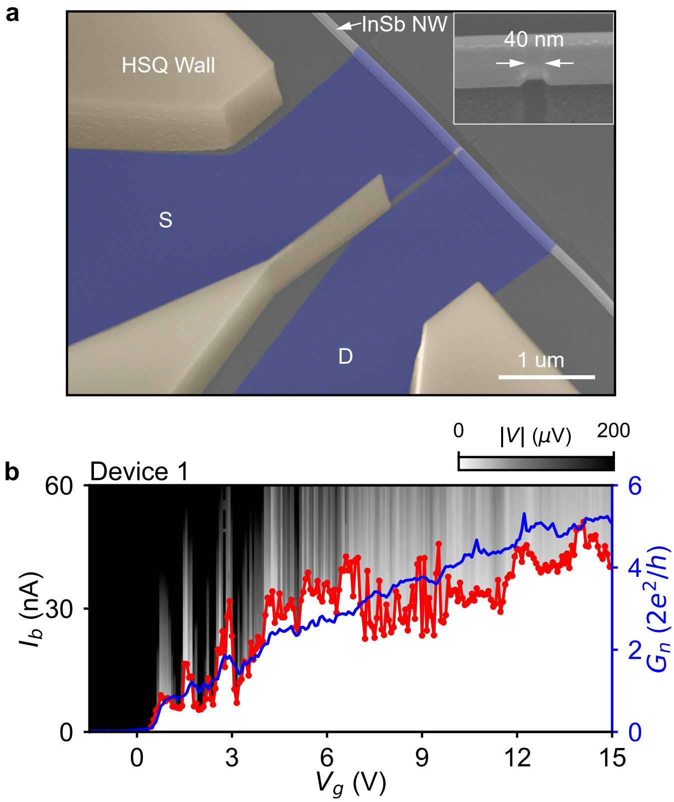

Figure 4.1: **Basic characterization of a nanowire Josephson junction device**: **(a)** False-colored SEM image depicting a representative JJ device with a semiconducting InSb junction defined between the source (S) and drain (D) superconducting Al leads (blue). The junction length is determined by the hydrogen silsesquioxane (HSQ) (yellow) shadow-wall structure. A zoom-in at the junction is shown in the inset. The back side of the substrate is used as a global back gate. **(b)** Zero-field dependence of switching current I_{sw} (red) and normal state conductance G_n (blue) on the back gate voltage V_g, overlapped onto the I_b - V_g two-dimensional (2D) map taken for Device 1 (with junction length $L = 37\,\text{nm}$).

4.2. RESULTS

The hybrid nanowire JJs are fabricated by the recently developed shadow-wall deposition techniques [27, 34]. In Fig. 4.1a, a scanning electron microscope (SEM) image of a representative InSb-Al nanowire JJ device is taken at a tilted angle and shown in false colors. Source (S) and drain (D) superconducting lead (blue) are formed via an in-situ angle deposition of Al film after the preparation of a clean and oxide-free InSb nanowire [35] interface (see the Methods section in the Supporting Information). Pre-patterned dielectric shadow-walls (yellow) selectively define the nanowire sections that are exposed to the Al flux during the deposition. The junction length is determined by the width of the shadow-wall in the vicinity of the nanowire. In comparison with the etched dielectric shadow-walls used in recent works [27, 33, 34] or previous evaporation-defined JJs[28–31], here we use lithographically defined shadow-walls which dimensions therefore can be as small as 20 nm. This allows us to precisely control the length of nanowire JJs and to achieve surpassingly short junctions, as shown in the inset SEM image in Fig. 4.1a. In this work, we present nine nanowire JJ devices (Device 1-9) with the junction length L in the range of 27 nm – 160 nm and one InSb-Al nanowire SQUID with two junctions of ~ 40 nm. The diameter of the nanowires is ~ 100 nm. An overview of nine nanowire JJ devices is shown in Fig. 4.7 in the Supporting Information.

Electrical transport measurements on the nanowire Josephson junction devices have been performed at ~ 20 mK in a dilution refrigerator equipped with a vector magnet. Four-terminal setup is used for dc-current bias I_b measurements. Conductance measurements have employed a two-terminal setup with a dc-voltage bias V_b and a 10 μV ac excitation (see more details in the Supporting Information). The back side of the substrate is used as a back gate and an applied voltage V_g acts globally on the entire nanowire. Figure 4.1b shows how the switching current I_{sw} (red) and the normal state conductance G_n (blue) depend on V_g at zero magnetic field for Device 1. The switching current I_{sw} is extracted from the (V, I_b) traces (see the Data analysis section in the Supporting Information). The normal state conductance G_n is obtained in the voltage-bias range $1\,\mathrm{mV} < |V_b| < 2\,\mathrm{mV}$ - well above the double value of the induced superconducting gap of the leads ($2\Delta \sim 0.5$ meV). The conductance measurements from which G_n and Δ are extracted are shown in Fig. 4.8 and Fig. 4.14. By increasing V_g, both I_{sw} and G_n, in spite of fluctuations, become larger as the carrier states in the junction get populated and more subbands contribute to transport. At $V_g = 15$V, G_n and I_{sw} reach up to $\sim 5\,G_0$ ($G_0 = 2e^2/h$) and ~ 50 nA, respectively. The remaining nanowire JJs (Device 2-9) show comparable zero-field properties, as shown in Fig. 4.8 and Fig. 4.9. The high tunability of G_n as well as of I_{sw} enables the systematic investigation of the junctions in different electro-chemical potential regimes.

Hybrid nanowire JJs have been shown to exhibit a supercurrent evolution in a parallel magnetic field-B that is strongly affected by the electro-chemical potential of the semiconducting junction [28]. Therefore, when exploring the resilience of switching current in a parallel B-field, the electro-chemical potential of a junction has to be taken into account. In the following, the switching current dependence on V_g and the parallel B-field is studied for two JJs of significantly different lengths. In Fig. 4.2a and 4.2b, we show how the switching current I_{sw} evolves with V_g and B for Device 2 ($L = 31$ nm) and Device 7 ($L = 157$ nm), respectively. I_{sw} is extracted from the corresponding (V, I_b) traces taken at each setting of V_g and B. As shown in Fig. 4.2a, the short device shows a remarkable supercurrent resilience with the supercurrent persisting above a parallel field of 1 T. A linecut at 1 T (red bar) is taken and the corresponding data is shown in Fig. 4.2c. I_{sw} (red trace) continuously persists over a ~ 3.5 V interval of V_g. As a comparison, I_{sw} drops more rapidly with magnetic field in the long device, as shown in Fig. 4.2b. Fig. 4.2d shows

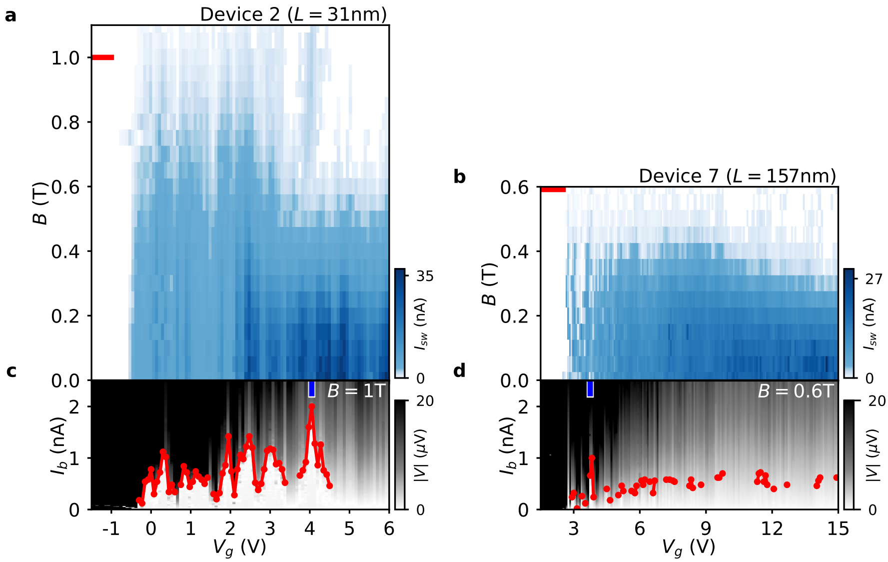

Figure 4.2: **Dependence of switching current on the gate voltage and parallel magnetic field** for **(a)** Device 2 ($L = 31$ nm) and **(b)** Device 7 ($L = 157$ nm). Each data point in the $V_g - B$ 2D map in (a) and (b) is extracted from the corresponding (I_b, V) trace as the gate voltage V_g and the parallel magnetic field B are swept. The red markers in (a) and (b) correspond to the magnetic fields $B = 1$T and $B = 0.6$T at which the $I_b - V_g$ 2D maps in **(c)** and **(d)** are shown, respectively. In these maps the red traces correspond to the extracted switching current I_{sw}. More analogous 2D maps at lower fields are displayed in Fig. 4.10 in the Supporting Information. The blue markers in (c) and (d) denote the gate settings with enhanced supercurrent.

that at 0.6T the supercurrent is barely detectable. Besides this apparent difference, the switching current behaviours in Fig. 4.2a and 4.2b still show some similarities. Namely, I_{sw} of both devices manifests a better resilience against the magnetic field in an intermediate gate interval between the pinch-off and the fully open regime - $(-0.5, 3)$V interval for the short device and $(4, 10)$V interval for the long device (see Fig. 4.10). The switching current ubiquitously fluctuates in the intermediate gate intervals. We suspect that both few-mode interference[28] and finite contact barriers[29] may lead to such fluctuations in supercurrent as well as in normal conductance. For the gate voltage above these intervals I_{sw} in both devices vanishes more rapidly in the magnetic field, especially at $B > 0.3$ T. The suppression of supercurrent in at large positive V_g or high magnetic fields could be explained by a destructive interference between multiple modes[1, 2, 28]. Another explanation could be a gate-tuned semiconductor-superconductor hybridization[36, 37], which is addressed in the discussion part following Fig. 4.4. An ubiquitous feature in Fig.

4.2a and 4.2b is that, as the magnetic field is increased, certain intervals in the intermediate gate regime support more resilient supercurrent. In these V_g intervals we define the "resilient gate settings $V_{g,res}$" (blue markers in Fig. 4.2c and 4.2d). In this work, we quantify the impact of junction length on supercurrent resilience against magnetic field in two ways. The first way is to compare the supercurrent critical fields of different junctions at their $V_{g,res}$, which is addressed in Fig. 4.3. The second way is to compare the supercurrent averaged over a gate range at a finite magnetic field, which is shown in Fig. 4.4.

In Fig. 4.3 we focus on the supercurrent at the resilient gate settings $V_{g,res}$. For Device 1-7 we determine the $V_{g,res}$ values as described in Fig. 4.11, while for Device 8-9 we choose $V_g = 15\,\mathrm{V}$. The normal conductance G_n at $V_{g,res}$ is normally of a few G_0 (G_0=$2e^2/h$), corresponding to a few transport modes, and the value does not show an obvious dependence on the junction length. Figure 4.3a shows the voltage drop V over the junction as a function of I_b and the parallel magnetic field B for Device 1 ($L = 37\,\mathrm{nm}$). The red dotted line marks the extracted switching current I_{sw} at different B-fields. Three linecuts (black, red and blue) are shown in Fig. 4.3c - demonstrating more than 1 nA supercurrent at the parallel field of 1.2 T. Fig. 4.3b and Fig. 4.3d show the results for Device 6 ($L = 160\,\mathrm{nm}$) obtained at its $V_{g,res}$ setting. From the overlaid red trace it can be seen that the supercurrent vanishes at $\sim 0.75\,\mathrm{T}$, as confirmed by the linecuts shown in Fig. 4.3d. Analogous measurements of the switching current evolution with parallel field are carried out for all nine devices (see Fig. 4.12 in the Supporting Information). Finally, these $I_{sw}(B)$ dependences allow for the extraction of the maximal critical parallel magnetic field of switching current B_{Ic} for each Device 1-9. By plotting B_{Ic} versus the junction length L in Fig. 4.3e, it can be seen how the junction length influences the measured critical field of the supercurrent. We reproducibly reach the critical fields of $\sim 1.3\,\mathrm{T}$ in the sub-40 nm junctions while B_{Ic} drops gradually to $\sim 0.7\,\mathrm{T}$ in the longest junctions.

As a next step, we evaluate the supercurrent resilience over a broader gate interval. As our nanowire JJs are highly tunable, in Fig. 4.4 their supercurrent resilience against the parallel magnetic field is studied over the gate ranges in which the junctions are in the few-mode regimes. Fig. 4.4a shows the voltage drop V as a function of I_b and V_g at the parallel field of 0.6 T for Device 2 ($L = 31\,\mathrm{nm}$), together with I_{sw} (red trace) and the normal state conductance G_n (blue trace). To quantify the supercurrent resilience, the switching current in Fig. 4.4a is averaged in the V_g range corresponding to $0.1G_0 < G_n(V_g) < 2G_0$ (denoted by the two white dotted lines) and the obtained average switching current is $I_{sw}^{avg}(0.6\,\mathrm{T}) = 2.73\,\mathrm{nA}$. Such a moderate gate range is selected to keep enough supercurrent flow and meanwhile diminish the multiple mode inteference effects. An analogous averaging is done for the $I_{sw}(V_g)$ dependence measured at zero field and the obtained average switching current at zero field is $I_{sw}^{avg}(0\,\mathrm{T}) = 11.29\,\mathrm{nA}$ (see Fig. 4.9 for the zero-field dependence and the average value). By calculating the ratio $I_{sw}^{avg}(0.6\,\mathrm{T})/I_{sw}^{avg}(0\,\mathrm{T})$, it can be inferred that the junction of Device 2 preserves on average $\sim 25\%$ of its zero field switching current when the parallel field of 0.6 T is applied. The identical procedures of calculating the average switching currents and the $I_{sw}^{avg}(0.6\,\mathrm{T})/I_{sw}^{avg}(0\,\mathrm{T})$ ratios are carried out for Device 1-7 (see Fig. 4.9 and Fig. 4.13 in the Supporting Information).

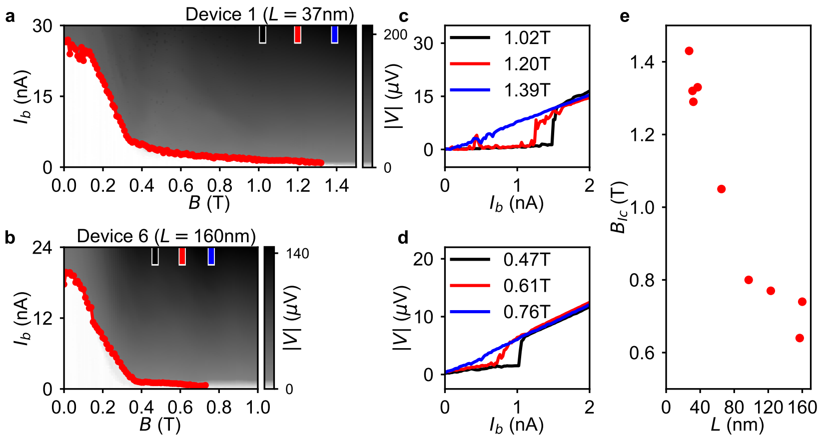

Figure 4.3: **Critical parallel magnetic field of switching current**: Dependence of the switching current (red) on B at the resilient gate settings $V_{g,res}$ for **(a)** Device 1 ($L = 37\,$nm) and **(b)** Device 6 ($L = 160\,$nm). In each 2D map the extracted switching current I_{sw} up to the critical parallel field is plotted in red. The critical parallel fields of the switching current in (a) and (b) are $B_{Ic} = 1.33\,$T and $B_{Ic} = 0.74\,$T, respectively. Black, red and blue markers in (a) and (b) have the corresponding linecuts shown in **(c)** and **(d)**. In **(e)** the dependence of the critical parallel field B_{Ic} is plotted for Device 1-9 versus the junction length L. Note that the uncertainty of B_{Ic} is not added in the plot and the amount is within 20 mT for all data points.

The dependence of the $I_{sw}^{avg}(0.6\,\text{T})/I_{sw}^{avg}(0\,\text{T})$ on the junction length L is shown as red dots in Fig. 4.4b. It can be noticed that at finite parallel field the shorter junctions preserve larger fractions of the corresponding zero field supercurrent in the described conductance ranges. The ratio $I_{sw}^{avg}(0.6\,\text{T})/I_{sw}^{avg}(0\,\text{T})$ drops rapidly around $L \sim 100\,$nm, implying a deteriorated resilience against magnetic field when the junction length is above this value. Moreover, only negligible fractions of switching current (less than 2%) systematically remain in the longer junctions - emphasizing their poor performance in magnetic fields. We emphasize that the particular shape of the dependence of the ratio on junction length could also vary depending on the choice of the normal conductance range and the subsequently determined gate intervals for averaging. However, the main qualitative features of such dependence would still remain. The impact of the junction length will be in particular discussed in the following paragraphs.

4

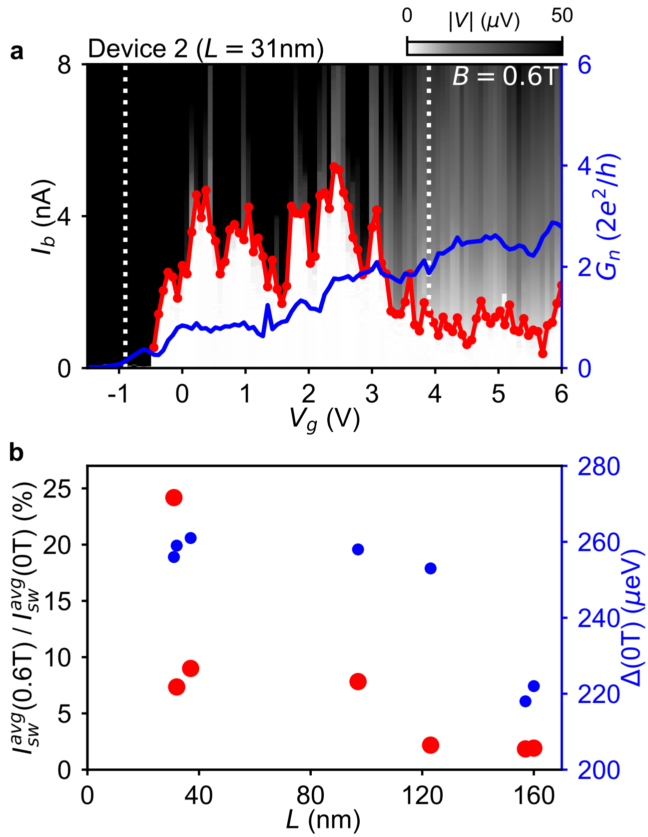

Figure 4.4: **Resilience of switching current in the junctions tunability ranges: (a)** Dependence of the switching current I_{sw} (red) on the gate voltage V_g at the parallel magnetic field $B = 0.6\,\mathrm{T}$ for Device 2 ($L = 31\,\mathrm{nm}$). Two white vertical lines mark the gate interval over which the normal state conductance G_n of the device (blue) is tuned from $0.1G_0$ to $2G_0$. In this gate range the switching current is averaged and $I_{sw}^{avg}(0.6\mathrm{T})$ value is obtained. Analogously, from the switching current dependence on V_g at zero-field the average value $I_{sw}^{avg}(0\mathrm{T})$ is calculated. **(b)** Dependence of the ratio $I_{sw}^{avg}(0.6\mathrm{T})/I_{sw}^{avg}(0\mathrm{T})$ on the junction length L for Device 1-7.

4.3. Discussion

In Fig. 4.3 and Fig. 4.4 two different approaches have been taken when quantifying the supercurrent resilience against magnetic field. Both approaches have led to the same observation - by reducing the junction length supercurrent resilience against magnetic field can be significantly improved. This is a common and reproducible feature of the short JJs in our study. The observations still hold despite variations in the switching current dependences on the gate voltage or the parallel field. In the following two paragraphs, possible mechanisms for the length dependent supercurrent resilience are discussed.

The superconducting Al shell has a mean free path l_e of $\sim 0.9\,\text{nm}$ according to a recent work[26], which uses the same machine for the Al growth. The extraordinarily short l_e in the thin Al shell is most likely due to massive surface scatterings and moderate nonuniformities. Together with a phase coherence length ξ_0 of $\sim 1.6\,\mu\text{m}$ from a bulk Al[38], the superconducting phase coherence length ξ of the Al shell in our work is estimated to be $\sim 38\,\text{nm}$ with the formula $\xi \sim \sqrt{\xi_0 \cdot l_e}$ in the dirty superconductor limit[39]. Then, JJs longer than ξ are in the long junction limit and the superconducting proximity effect in these junctions is weakened in comparison with the short junctions. Then, weakened induced superconductivity in long junctions leads to a poor performance in magnetic fields. Destructive interference between transversal nanowire modes is considered as another dominate reason for reduced supercurrent critical field in longer junctions[28]. The phase differences between modes can be accumulated in magnetic fields either via the Zeeman effect[1, 2] or orbital effect[40]. The Zeeman-induced phase accumulation is proportional to the Zeeman energy and the junction length[1, 2], while the contribution from orbital effect is proportional to the magnetic field and the junction length[40]. Considering the large g factor in InSb (~50[30, 41]) and the relatively large magnetic field (~0.5 T), significant phase accumulations are expected in long junctions. In this case, a prominent destructive interference is likely to appear in small magnetic fields for long junctions, resulting in reduced critical fields of supercurrent.

In this paragraph, we make a further analysis of other relevant effects, including a gate tunable superconductor-semicondutor hybridization under superconducting shells, disorder and spin-orbit interaction. The nine JJs are tuned by a global back gate, which at positive values may reduce the hybridization of the semiconductor under the superconducting leads[37, 42, 43]. In Fig. 4.14, we have observed decreased induced superconducting gaps for long Josephson junctions, implying reduced semiconductor-superconductor couplings in these devices. This is likely due to a different gating effect on semiconductor-superconductor hybrids for different junctions. In order to investigate the relevance of such effect, we have measured an additional short JJ device (Device 10, the right arm of the SQUID device from Fig. 4.5). This device utilizes a bottom gate under the junction and one bottom gate under each superconducting lead. Importantly, we find that applying a positive gate voltage locally under a single superconducting lead does not reduce the superconductor-semiconductor coupling to an extent that systematically limits the resilience of supercurrent (see Fig. 4.15). The mean free path of the InSb nanowires is ~300 nm[41], longer than all junctions. Thus, the influence of disorder is expected to be less important. A different spin-orbit interaction in different devices might happen as gate voltages are not the same for all devices and different electric fields may be present in different junctions. The presence of spin-orbit interaction together with magnetic fields can lead to anomalous superconducting phase[1–3], further complicating the interference effects, especially in long junctions.

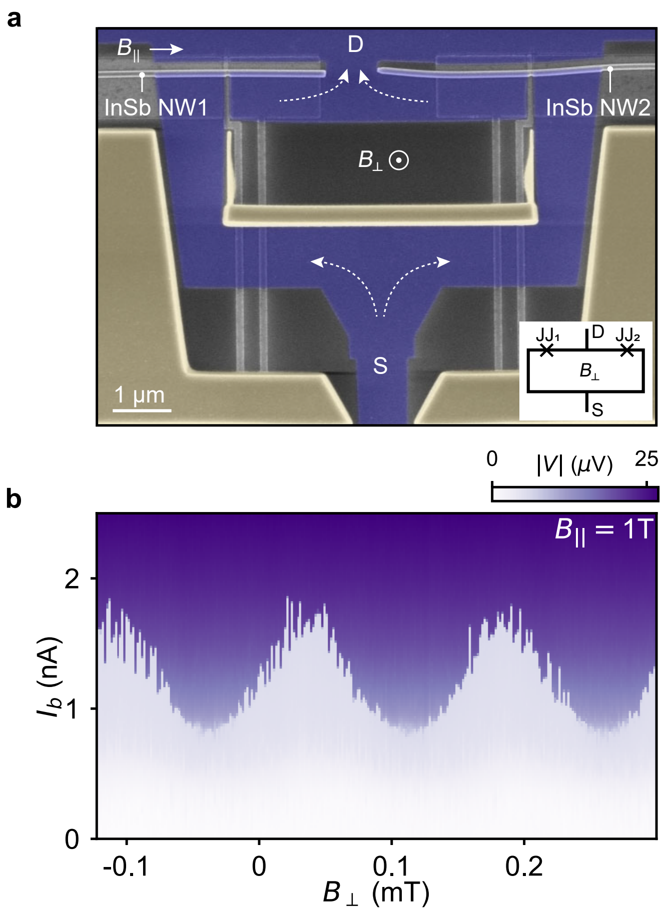

Figure 4.5: **SQUID operating at a parallel magnetic field of** 1 T: **(a)** False-colored SEM image of two hybrid 40 nm long InSb-Al nanowire Josephson junctions defined by the shadow-walls (yellow). The two junctions enclose a superconducting Al (blue) loop in the SQUID architecture. A magnetic field $B_{||}$ is applied along two parallel InSb nanowires hosting the Josephson junctions. A perpendicular out-of-plane magnetic field $B_\perp$ controls the magnetic flux through the superconducting loop between the source (S) and the drain (D). The inset image displays the equivalent device circuit; **(b)** Current bias measurement on the SQUID at the parallel magnetic field $B_{||} = 1$ T shows oscillations of the SQUID switching current as the magnetic flux through the SQUID loop is swept by applying $B_\perp$.

From the above results, we find that significantly reducing the nanowire JJ length is essential for preserving supercurrents in a high magnetic field. Here, we take a step further and incorporate the short nanowire JJs into a SQUID architecture. Figure 4.5a shows a false-colored SEM of a SQUID consisting of two 40 nm JJs formed in two parallel InSb nanowires. The shadow-wall structure (yellow) is lithographically defined such that after the Al (blue) deposition two JJs enclose the superconducting loop denoted by the white arrows. Since the two arms are parallel, a magnetic field $B_{||}$ can be applied parallel to both JJs while the out-of-plane perpendicular magnetic field $B_{\perp}$ is applied to sweep the flux threading the loop. Upon applying $B_{||} = 1\,\mathrm{T}$, both junctions are independently tuned by the underlying local bottom gates to a finite supercurrent. As shown in Fig. 4.5b, the oscillations of the switching current indicate a supercurrent interference persisting despite the high parallel field. In comparison with the previous work on nanowire SQUIDs [3, 44], this observation of supercurrent interference at $B_{||} = 1\,\mathrm{T}$ represents a significant improvement of the SQUID field compatibility. The control and the detection of the phase of supercurrent at high magnetic field is of crucial importance for studying various high field related phenomena in hybrid nanowire devices [10, 18, 45, 46].

4.4. CONCLUSION

We demonstrate that the length of a hybrid nanowire Josephson junction is an essential parameter that determines its supercurrent resilience against magnetic fields. Nanowire JJs with a length of less than 40 nm can be precisely defined by the shadow-wall angle-deposition technique and are shown to reproducibly preserve supercurrent at parallel magnetic fields exceeding 1.3 T. Superconducting quantum interference device (SQUID) utilizing such junctions displays supercurrent interference at the parallel field of 1 T. Our study shows that hybrid nanowire Josephson junctions of significantly reduced junction length can be considered as necessary building blocks in various hybrid nanowire devices which exploit Josephson coupling at high magnetic field.

4.5. SUPPORTING INFORMATION

4.5.1. METHODS

DATA SELECTION AND REPRODUCIBILITY

The study in the main text is based on nine InSb-Al nanowire Josephson junction (JJ) devices (Device 1-9) and one InSb-Al nanowire superconducting quantum interference device (SQUID). The JJ devices are used to investigate the impact of junction length on the supercurrent resilience against magnetic field. The SQUID is used to demonstrate how JJs hosting resilient supercurrent can be embedded into a superconducting loop to yield supercurrent interference at high magnetic field. As an additional measurement, the supercurrent resilience against magnetic field is examined in an additional JJ device (Device 10), that is the single arm of the SQUID.

By systematically sweeping the back gate voltage V_g when measuring Device 1-7, we could identify the resilient gate settings $V_{g,res}$, as described in the main text. However, at the initial phase of the study, when measuring the chips from which Device 8-9 originate, the resilience of supercurrent against magnetic field was only examined at $V_g = 15\,\mathrm{V}$. Therefore, for these devices the identification of the resilient gate setting $V_{g,res}$ (like those shown in Fig. 4.11) was not performed. Still, we include Device 8-9 in our study as they manifest resilient supercurrent even at $V_g = 15$V which is not necessarily their $V_{g,res}$. Other short junction devices from these chips did not manifest such resilient supercurrent (critical parallel field of ~ 0.7T at $V_g = 15$V) and long junction devices from these chips showed very poor supercurrent resilience (critical parallel field of ~ 0.4T at $V_g = 15$V). We do not include these devices in our study as their critical parallel fields at $V_g = 15$V may be significantly smaller in comparison to their critical fields at the back gate tuned to their $V_{g,res}$ settings.

Importantly, we have never measured any long junction device (with or without back gate tuning) that showed better supercurrent resilience than the long junction devices (Device 6-7) presented in the study.

DEVICE FABRICATION

All devices in this work were fabricated on p^+-doped Si wafers covered with ~ 300nm of thermal SiO_2. For Device 1-9, the thermal SiO_2 is used as a global back gate dielectric. For the SQUID, extra steps in the substrate fabrication were taken in order to create local bottom gates. On top of the thermal SiO_2, the local bottom gates were lithographically defined and produced by depositing 3/17nm of Ti/Pd by electron beam evaporation. Then, ~ 20nm of high-quality HfO_2 layer was grown by atomic layer deposition (ALD) at 110°C to act as the bottom gate dielectric.

Dielectric structures corresponding to specific shadow-wall patterns were defined by electron-beam lithography on top of the thermal SiO_2 and ALD HfO_2 for the Device 1-9 and the SQUID, respectively. Namely, FOx-25 (HSQ) was spun at 1.5krpm for one minute, followed by 2 minutes of hot baking at 180°C and patterning lithographically. The HSQ is then developed with MF-321 at 60°C for 5 minutes and the substrates are subsequently dried using critical point dryer. This step was followed by the nanowire deposition by an optical nanomanipulator setup and the stemless InSb nanowires [35] were precisely placed on top of the global back gate (Device 1-9) or the array of local bottom gates (SQUID), close to the HSQ structures.

Deposition of the superconducting Al film was carried out in the nominally identical steps for all devices in this study. After gentle hydrogen cleaning of the nanowire surface, the superconducting film was grown by directional evaporation of Al. The Al flux in the deposition was 17nm and the angle with respect to the substrate was 30° [27, 34]. Due to the specific angle and the regular hexagonal nanowire cross-section, the Al film continuously covers three nanowire facets, as shown in the above cited references. On one facet the Al film is deposited perpendicularly and the film thickness on this facet is ~ 15nm, as ~ 2nm of Al self-terminately oxidizes in the air. The direction of the Al deposition forms an angle of 30° with the other two facets and these two facets therefore receive $\sin 30° = 0.5$ of the Al flux and have the film thickness of ~ 7nm after the oxidation. Lithographically patterned dielectric structures cast shadows during the Al deposition and therefore selectively define the sections along the nanowire where the superconducting film is grown and where the semiconducting junction is formed. Additionally, the arrangement of the shadow-wall structures on the SQUID substrate determines a shadowed substrate area without Al enclosed by the two JJs that represents the superconducting loop of the SQUID. Finally, in all devices the superconducting film on the nanowire facets forms a continuous connection to the substrate and extends to pre-patterned bonding pads such that additional fabrication steps to contact the nanowires are not needed.

In this work, seven nanowire JJ devices (Device 1-7) were fabricated on a single chip, while the other two (Device 8-9) come from other two chips that passed through the nominally identical fabrication steps. The SQUID was fabricated on a separate chip in the fabrication steps as explained above.

MEASUREMENT SETUP

We perform the electrical transport measurements at ~20 mK base temperature in a dilution refrigerator equipped with a vector-rotate magnet. Source and drain leads of the device are bonded each to two printed circuit board (PCB) pads that are via low-pass filters connected to the fridge lines. In this way each device occupies in total four fridge lines - allowing for measurements in a two- and four-terminal configuration.

We perform the conductance measurements in the two-terminal voltage bias setup in the standard lock-in configuration. Source and drain are connected to the measurement setup by two fridge lines, while the remaining two fridge lines are kept floated. The voltage bias V_b is swept by a dc-voltage source while the ac-voltage $dV_b = 10\mu V$ is set by a lock-in amplifier. The total current $I + dI$ through the sample is measured by a current-meter amplifier. The dc- and the ac-voltage drops over the sample are obtained by subtracting the voltage drops over the series resistance $R_s = 8.89 k\Omega$ as $V = V_b - IR_s$ and $dV = dV_b - dIR_s$. This series resistance accounts for other resistive elements in the circuit such as the two fridge lines, the resistance of the voltage source and the current-meter amplifier and the resistance of the low-pass filters on the printed circuit board. For collecting the data from which the switching current is extracted, four-terminal current-bias setup is used. Two fridge lines are used to connect a current source and apply the dc-current bias I_b through a device, while the other two fridge lines are used to connect a voltage-meter and measure the dc-voltage drop V over the device. The current bias is swept in steps of 20 pA - 60 pA, depending on the range of current-bias that is applied. As the voltage-meter measures at the room temperature the sum of the voltage drops over the device and the two fridge lines, a dc-offset of ~0.01 mV are substracted to compensate for the difference in the thermal voltage drops over the fridge lines.

DATA ANALYSIS

All the codes used for the data analysis in this work are available in the data repository. The details of the data analysis procedures performed in these codes are described in the following subsections.

Extracting normal state conductance G_n

Normal state conductance G_n is extracted from the data collected in the voltage-bias measurements of the nanowire JJ devices. After correcting for the series resistance

R_s (as explained in the previous section), the normal state conductance is obtained as $G_n(V_g) = (G_n^+(V_g) + G_n^-(V_g))/2$ where $G_n^+(V_g) = \langle \frac{dI}{dV}(V_g, 1\,\mathrm{mV} < V < 2\,\mathrm{mV}) \rangle$ and $G_n^-(V_g) = \langle \frac{dI}{dV}(V_g, -2\,\mathrm{mV} < V < -1\,\mathrm{mV}) \rangle$ are averaged conductances at the positive and the negative source-drain voltages much larger than the double value of the superconducting gap ($2\Delta \sim 500\,\mu$V).

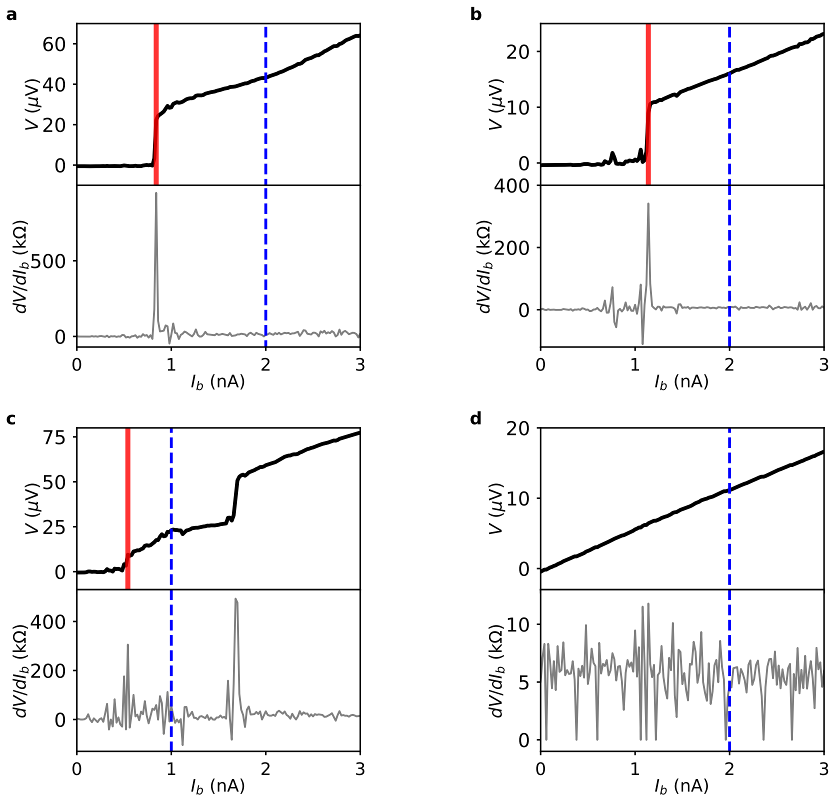

Figure 4.6: **Extraction of switching current:** Examples in **(a)-(d)** show the voltage drop (top) and the numerically calculated differential resistance (bottom) traces as functions of the current bias I_b. The extracted switching current I_{sw} (red) and the ranges over which the presence of a switch is examined (blue) are marked by the lines. These traces were taken in Device 2 ($L = 31\,$nm) at $B = 1\,$T parallel magnetic field.

Extracting switching current I_{sw}

Switching current is extracted for each (V, I_b) trace measured in the current-bias setup. Four-examples of (V, I_b) traces are shown in the top parts of Fig. 4.6a-d. The corresponding differential resistance $(dV/dI_b, I_b)$ traces are calculated as numerical derivatives and are plotted in the bottom parts of Fig. 4.6a-d. The data in Fig. 4.6 corresponds to four traces from the back gate sweep at parallel magnetic field of 1 T in Device 2. These traces are chosen to motivate the particular method used in the switching current extraction.

From a perfectly clean (V, I_b) trace, as the one in Fig. 4.6a, with a single voltage step corresponding to the switching current I_{sw}, I_{sw} can in principle be extracted by setting a threshold voltage V_{th}, such that $V_{th} = V(I_b = I_{sw})$. However, this can give underestimated extracted values as the voltage V can due to noise fluctuate for current bias values lower than the switching current - as shown in the (V, I_b) trace in Fig. 4.6b. Setting higher V_{th} values to prevent this, can, on the other hand, give an overestimation of the extracted value if the switching current is small. Therefore, when extracting I_{sw}, we rather look at the maximum in the differential resistance, as it resembles the sharpness of a switch in a (V, I_b) trace.

For each differential resistance $(dV/dI_b, I_b)$ trace, the maximal value (peak) of dV/dI_b is found and divided by the third value of the same $(dV/dI_b, I_b)$ trace sorted in decreasing order. In this way we quantify how dominant the peak in the differential resistance is. If the obtained value is smaller than the analogous value obtained from the trace in Fig. 4.6d with clearly no switch in it - the peak in differential resistance is not dominant and the switching current is extracted as a "not a number" (NaN) value. These NaN values correspond to the interruptions in the red I_{sw} traces plotted over 2D maps throughout the study.

The trace in Fig. 4.6c depicts that the range over which the dominant peak in $(dV/dI_b, I_b)$ is searched for can affect the extracted value. For example, there is a dominant peak in $(dV/dI_b, I_b)$ in Fig. 4.6c at $I_b \sim 1.7\,\text{nA}$, but it does not correspond to the switching current. Therefore, the range in which the switching current is searched for is an important input parameter that is marked by the blue lines in Fig. 4.6. This parameter is commonly set at sufficiently high values and subsequently adjusted for particular traces where it leads to mistakes as the one described in Fig. 4.6c. The red lines in Fig. 4.6 mark the extracted switching current values and nicely match the dominant peaks of the differential resistance in the relevant ranges of the current bias.

The described algorithm successfully identifies the switching current in most of the traces. After applying it, additional corrections were made after checking how an extracted I_{sw} value matches to its corresponding (V, I_b) trace. Some extracted finite I_{sw} values were set then to NaN if found to have been extracted in a highly smeared (V, I_b) trace. On the other hand, in some non-smeared (V, I_b) traces with NaN extracted I_{sw} values, the switching current is re-extracted by extracting the position of the global maximum in the differential resistance trace. Such post-extraction corrections were performed equally frequently for all devices (5-10% of all (V, I_b) traces).

Extracting critical magnetic field B_{Ic}
By applying the above described algorithm to extract the switching current I_{sw}, we extract $I_{sw}(B)$ from the 2D maps shown in Fig. 4.12 where the voltage drop V is measured as the current bias I_b and the parallel magnetic field B are swept. By analyzing the evolution of the (V, I_b) linecuts in B field, it can be noticed that the algorithm may give an isolated NaN value for I_{sw} at some B value even if the switching current is correctly extracted at higher fields. Therefore, defining the critical field of switching current B_{Ic} as the lowest B field for which the algorithm gives NaN value for I_{sw} can lead to underestimations of B_{Ic}. However, if the algorithm gives NaN values for two consecutive B field values, then even occasionally extracted I_{sw} values different from NaN at higher fields are most often false-positive extracted values. We therefore determine the critical field B_{Ic} as the lowest field such that two consecutive extracted values for I_{sw} are NaN. In Fig. 4.12 I_{sw} is plotted up to the determined B_{Ic} while the entire $I_{sw}(B)$ data is available in the data repository.

4.5.2. EFFECTS OF JUNCTION LENGTH AND GLOBAL BACK GATE ON INDUCED SUPERCONDUCTING GAP

In order to measure the induced superconducting gap for Device 1-9 and study its evolution in parallel magnetic field, tunneling spectroscopy is performed in the voltage bias setup.

In Fig. 4.14 the evolution of induced superconducting gap in parallel magnetic field is shown for Device 1-9. Each subfigure represents a 2D map of the tunneling conductance as a function of the voltage drop over the junction and the parallel field. Two coherence peaks corresponding to the double value of the induced gap Δ appear in the tunneling conductance at $|V| = 2\Delta$. By extracting the peak separation and dividing it by 4 for each Device 1-9 at zero field, the values for induced superconducting gap are calculated. These values are shown as insets in Fig. 4.14, together with the global back gate voltage at which the corresponding conductance maps are obtained.

In Fig. 4.14 it can be seen that the three short junctions (Device 1,2 and 3) have larger values of the induced gap with the critical parallel field of $\sim 1.5\,\mathrm{T}$ - similar to the parent superconducting gap in the Al film [26, 27, 34]. On the other hand, the two longest junctions (Device 6 and 7) are characterized by reduced induced gaps and subgap states evolving towards zero energy and effectively closing the gap well before the parent superconducting gap vanishes. These differences in the induced gap sizes and their evolution in parallel magnetic field for junctions of different lengths are accompanied by differences in the gate settings at which different devices are set into the tunneling regime. Namely, it can be noticed that shorter devices mostly require low or even negative back gate voltages for reaching the tunneling regime, while this value is higher for the longer junctions. A valid question that arises is whether the differences in the tunneling spectroscopy in Fig. 4.14 are due to the differences in the junction lengths or due to the differences in the electrical fields induced by the different gate voltages.

Despite the differences present among the nine devices in the tunneling regime regarding the back gate settings, the junction lengths and the conductance values, some conclusions can be made by looking at specific subsets of the devices for which some of these parameters are comparable. By comparing the data for Device 4, 5 and 7, it can be seen that with almost the same gate settings of $V_g \sim 2.15\,\mathrm{V}$ and the comparable tunneling conductance values $G_n \sim 0.3-0.4\,G_0$, the shortest device out of the three (Device 4) exhibits the largest induced gap that closes at the highest field. The data for the other two devices (Device 5 and 7) suggest that gradual increases of the junction length lead to weaker proximity effect with gradually smaller induced gap and gradually lower critical parallel field of the induced gap. Furthermore, the shortest device in the study (Device 8) requires the largest gate voltage to be tuned into the tunneling regime ($V_g = 5.7\,\mathrm{V}$) and still exhibits larger induced gap than the longest devices (Device 6-7) measured at the lower gate voltages. Despite the high gate voltage, the induced gap of Device 8 closes at $\sim 1.3\,\mathrm{T}$. However, in comparison to the remaining short junctions measured at significantly lower gate voltages (Device 1,2 and 3), Device 8 has poorer induced superconducting properties, probably due to the the high gate voltage and reduced superconductor-semiconductor coupling.

We can conclude that junction length is an important parameter that influences the induced superconducting gap. This does not exclude an effect that the applied back gate voltage has on induced superconductivity. Moreover, the data in Fig. 4.14 demonstrates that both the junction length and the back gate voltage determine the semiconductor-superconductor hybridization. This confirms that the electrostatic profile inside a hybrid nanowire JJ device - influenced by both device geometry and gate voltage - can control the strength of the semiconductor-superconductor hybridization[36, 37].

The band offset at an InSb-Al interface can cause a bending of the InSb conduction band and results in a proximitized electron layer at the interdace with Al. Because of a finite lateral extension of such layers from the two sides of a short JJ, the junction superconducting properties could be enhanced. Note that in some short JJs in our study the normal conductance and supercurrent have been measured to be finite when no back gate voltage is applied (see the data for Device 2 and 3 in Fig. 4.9). This could suggest that the accumulation layers can fully extend over a $\sim 30\,\mathrm{nm}$ junction by extending $\sim 15\,\mathrm{nm}$ laterally at each side.

The evidence of different strengths of hybridization in junctions of different lengths is in agreement with the reported zero-field values of the induced gap in Fig. 4.14 and the average switching current values at zero field in Fig. 4.9. Although the induced gap is characterized in the tunneling regime with no supercurrent, the critical parallel fields of switching current in Fig. 4.3e in the main text roughly match the parallel field values at which the induced gaps close in Fig. 4.14.

4.5.3. EFFECTS OF LOCAL GATES ON SUPERCURRENT RESILIENCE

As an additional measurement, we perform current bias measurements on a single Josephson junction (Device 10) which is one arm of the SQUID (see Fig. 4.15a and the Fabrication section for the details on the device design). The local bottom gates under the nanowire in Device 10 allow for a local tuning of the electro-chemical potential in different sections of the nanowire and can therefore serve to evaluate the effects of the local gating on the supercurrent resilience.

We perform current bias measurements on Device 10 while the other arm of the SQUID is pinched-off. The three bottom gates - TG and SG1/SG2 - approximately align with the junction and the superconducting leads, as shown in Fig. 4.15a. Two bottom gate voltages V_{SG1} and V_{SG2} mainly tune the nanowire sections covered by the superconductor, while the middle gate voltage V_{TG} mainly tunes the semiconducting junction. In this way the electro-chemical potential in the nanowire can be locally controlled, which is not possible in the global back gate configuration of nanowire JJ devices (Device 1-9) in the main text.

The dielectric used for the local bottom gates is ALD HfO_2 of $\sim 20\,nm$ thickness. As a comparison, the global back gate of the Device 1-9 utilizes thermal SiO_2 of $\sim 300\,nm$ thickness. By taking into account the dielectric constant values of HfO_2 and SiO_2 to be ~ 10 and ~ 4, respectively, the gating effect of the local bottom-gates is estimated to be at least 30 times larger than that of the global back gate.

In Fig. 4.15b-e, dependences of the extracted switching current I_{sw} (red) on a single bottom gate voltage are shown, while the other two bottom gates and the parallel magnetic field are fixed. By comparing Fig. 4.15b and Fig. 4.15c, it can be noticed that sweeping just V_{TG} qualitatively resembles the case when the global back gate is swept (Fig. 4.1b, Fig. 4.9 and Fig. 4.13). When V_{SG1} and V_{SG2} are decreased in Fig. 4.15c in comparison to Fig. 4.15b, a slight decrease in I_{sw} can be observed. This can be attributed to V_{SG1} and V_{SG2} cross-coupling to the junction and effectively reducing its transmission. By looking at Fig. 4.15d and Fig. 4.15e, it can be seen that sweeping a single local bottom gate under the superconducting leads over 4.5V does not systematically affect the extracted switching current I_{sw}. In some cases, a slight increase in the background value of I_{sw} can be observed as V_{SG1} or V_{SG2} increase over 4.5V voltage range. This is also in agreement with V_{SG1} and V_{SG2} cross-coupling to the junction.

The fluctuations of the switching current magnitude in the single local bottom gate sweeps in Fig. 4.15b-e are comparable to those observed in the global back gate traces in the main text. Therefore, it cannot be determined whether the fluctuations in the back gate sweeps arise from the modulations of the electro-chemical potential of the junction or the nanowire sections under the superconducting leads. Importantly, we observe that applying positive voltage on the single local bottom gate under the superconducting lead does not diminish the semiconductor-superconductor coupling to an extent that the supercurrent of Device 10 is systematically suppressed.

4.5.4. SUPPORTING FIGURES

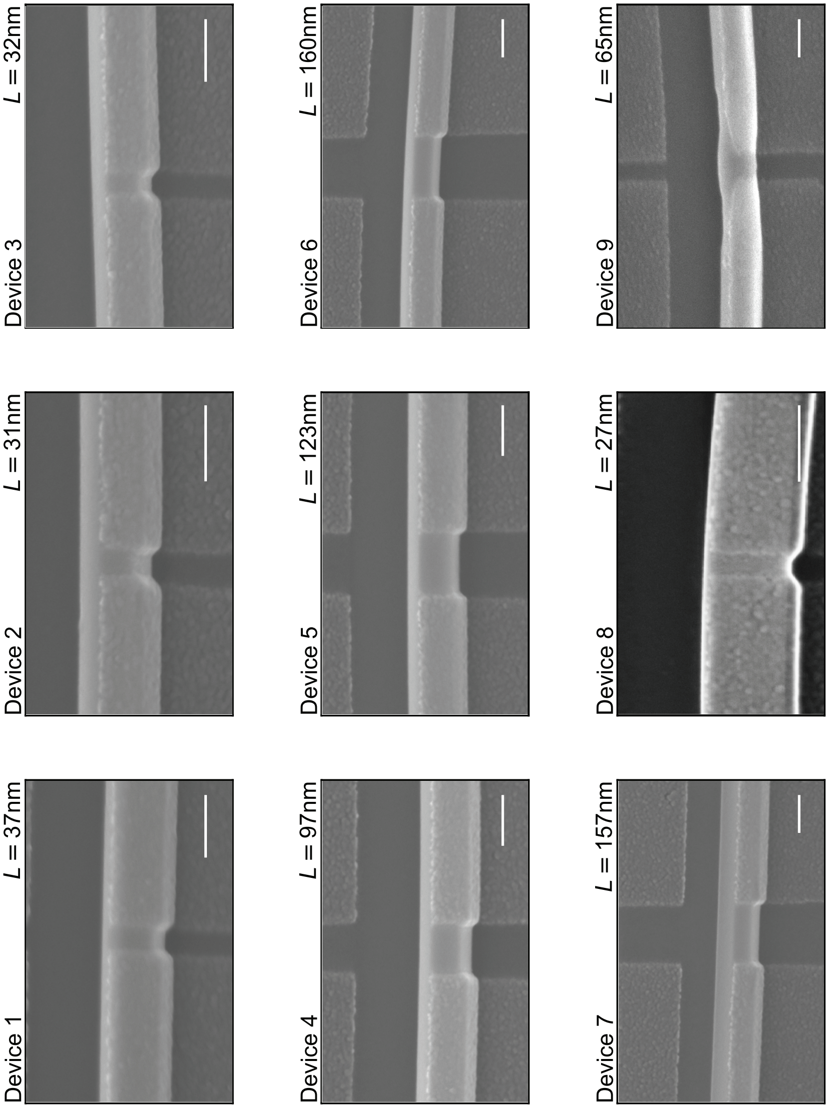

Figure 4.7: **Nine nanowire Josephson junction devices:** SEM images of the junctions with the corresponding device name (Device 1-9) and the junction length L. The diameter of the nanowires is $\sim 100\,\text{nm}$ (between $90\,\text{nm}$ and $110\,\text{nm}$). The scale bars correspond to $100\,\text{nm}$.

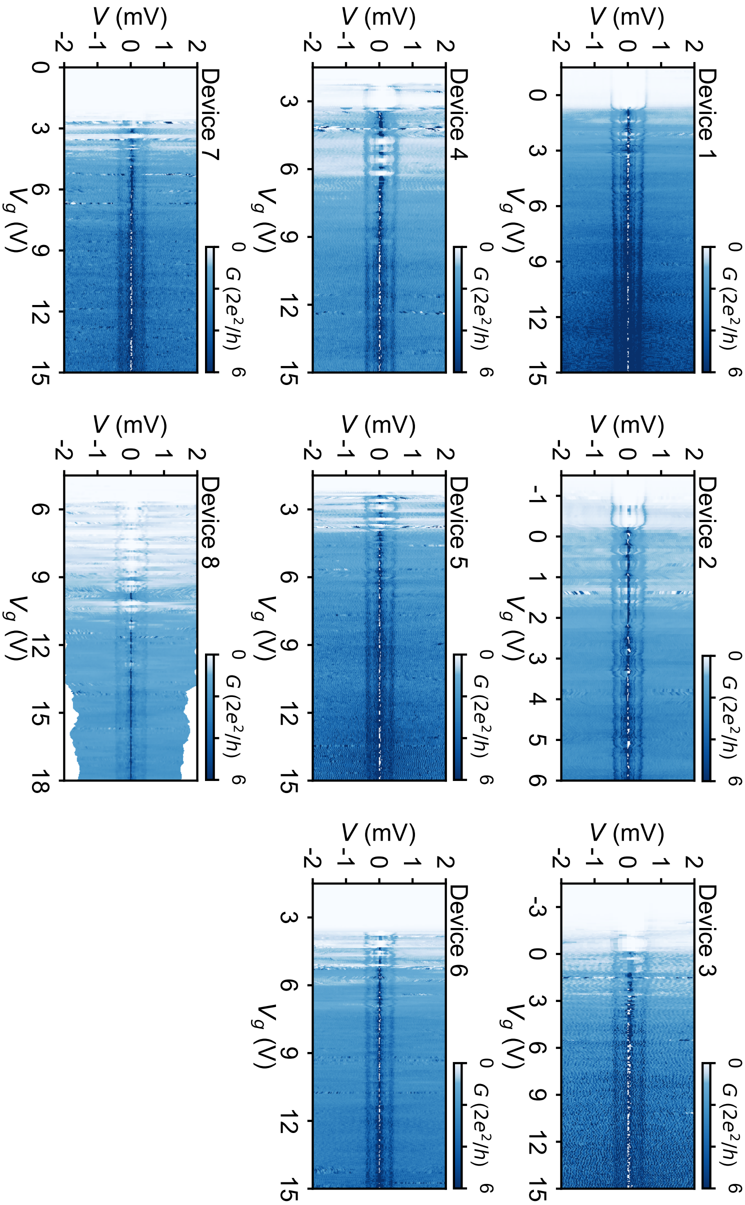

Figure 4.8: **Differential conductance at zero-field:** G for Device 1-8 as a function of the source-drain voltage V and V_g. The normal state conductance dependences $G_n(V_g)$ are obtained from these 2D maps as described in the Data analysis section. An analogous 2D map was not taken for Device 9 and its $G_n(V_g)$ dependence was measured as a single trace at $V > 1\,\text{mV}$.

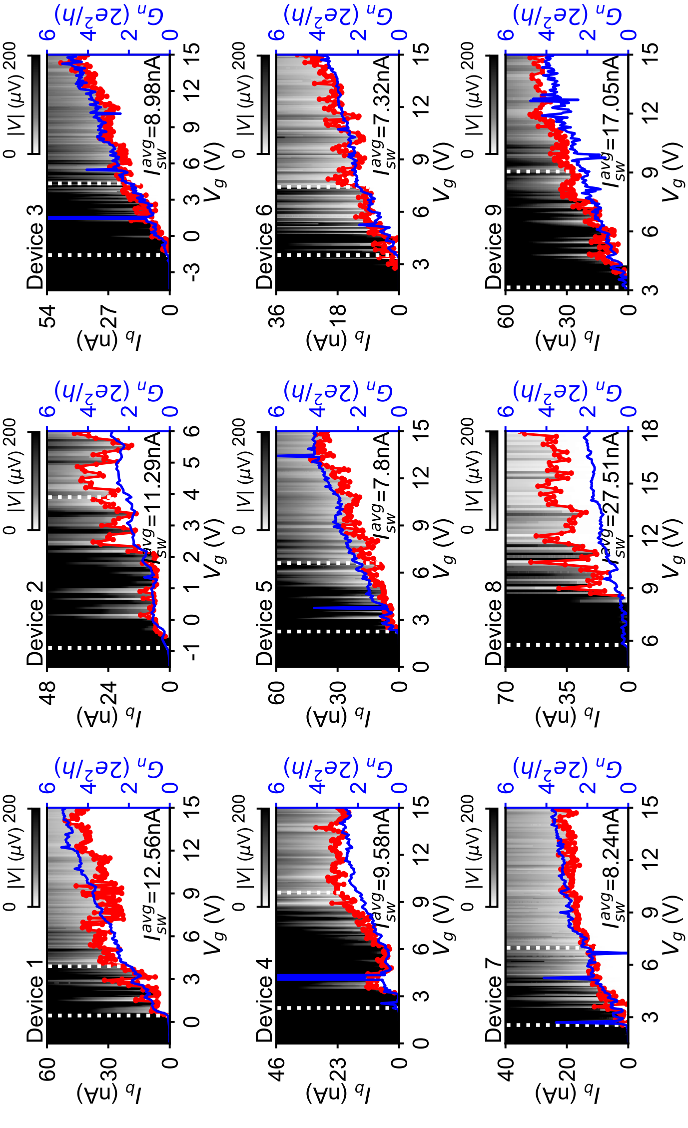

Figure 4.9: **Tunable switching current and normal conductance at zero-field:** Switching current I_{sw} (red) and normal conductance G_n (blue) plotted over $I_b - V_g$ 2D maps obtained in the current-bias measurements at zero-field. All devices show tunability by the back gate from the pinch-off to the open regime. $G_n(V_g)$ dependences are obtained from the data shown in Fig. 4.8. The white dotted lines mark the ranges of V_g over which G_n increases from $0.1G_0$ to $2G_0$. The average switching currents in these intervals are shown as insets.

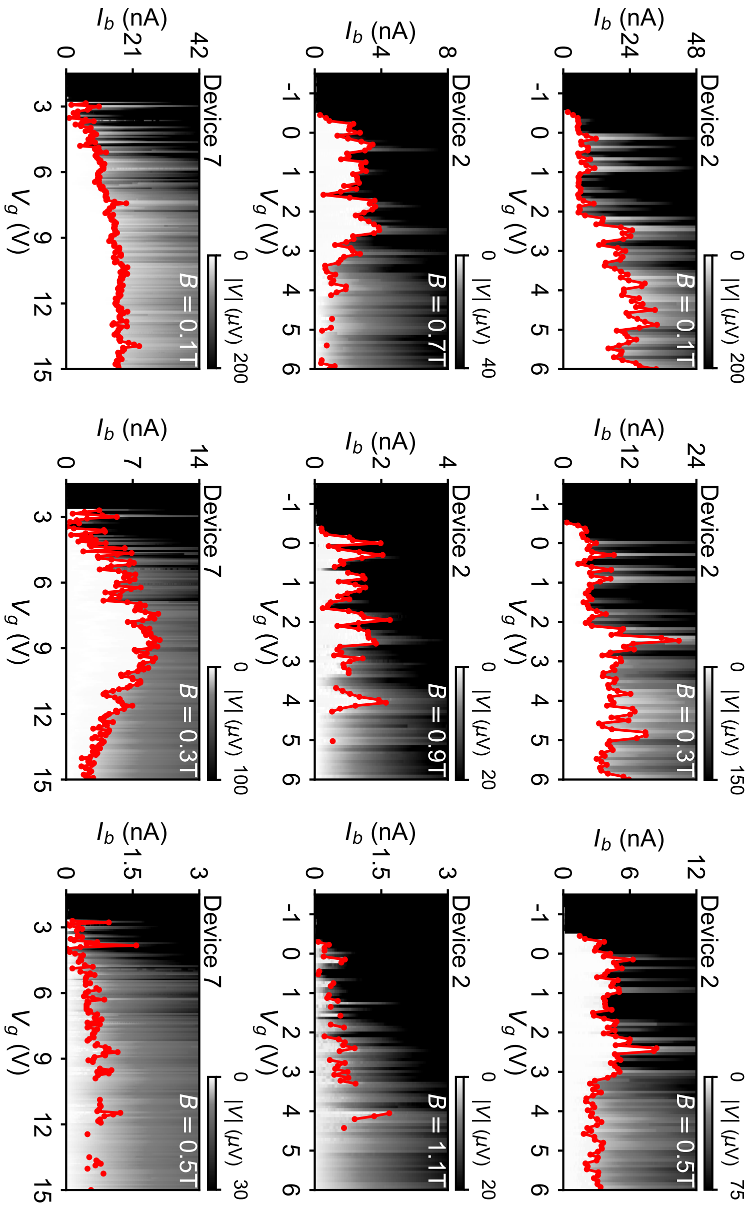

Figure 4.10: I_{sw} (red) as a function of V_g at several parallel field values shown as insets.

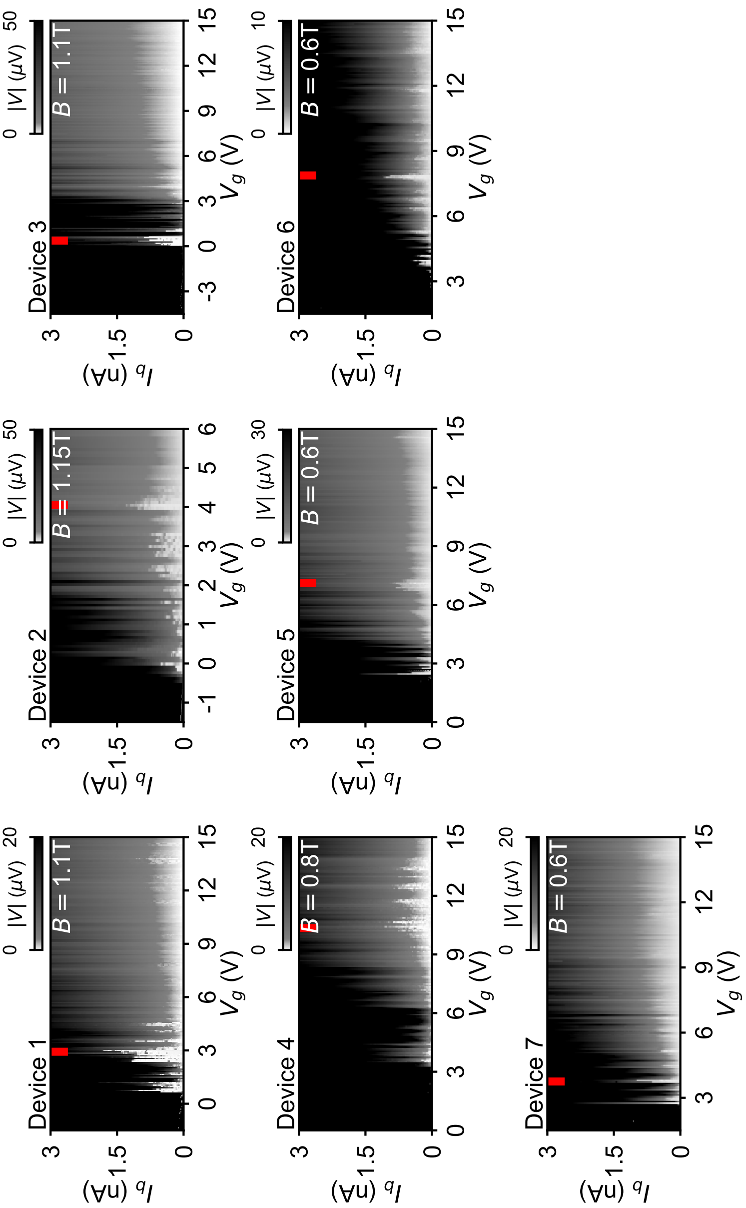

Figure 4.11: **Identifying the resilient gate settings** $V_{g,res}$: V_g is swept at high parallel field for Device 1-7. The red markers denote the resilient gate settings $V_{g,res}$. V_g is set to these values for obtaining the magnetic field dependences shown in Fig. 4.3 and Fig. 4.12. The analogous measurements were not performed for Device 8-9.

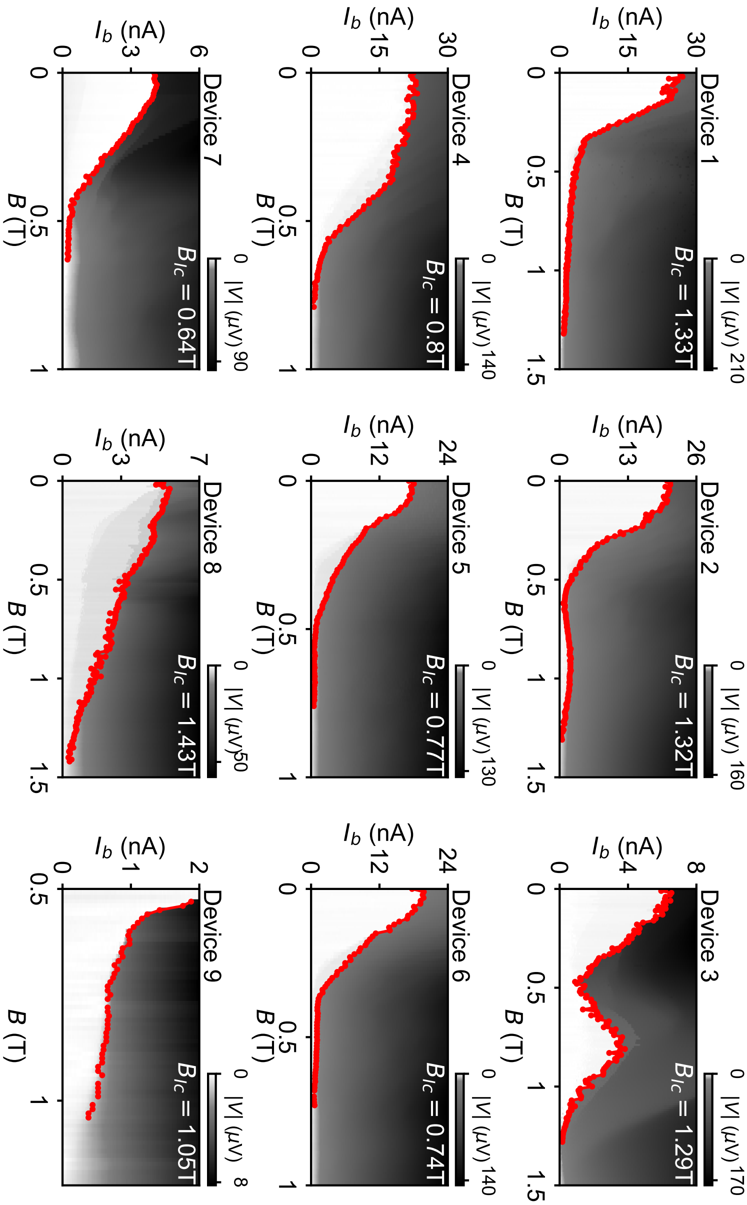

Figure 4.12: **Evolution of switching current in parallel magnetic field:** Dependence of I_{sw} (red) on B for Device 1-9. The back gate is set at the resilient gate setting $V_g = V_{g,res}$ for Device 1-7 and at $V_g = 15\,\mathrm{V}$ for Device 8-9 (see the Data selection and reproducibility section). The corresponding extracted critical field B_c is shown as an inset. The gate settings for Device 1-7 are marked by the red markers in Fig. 4.11.

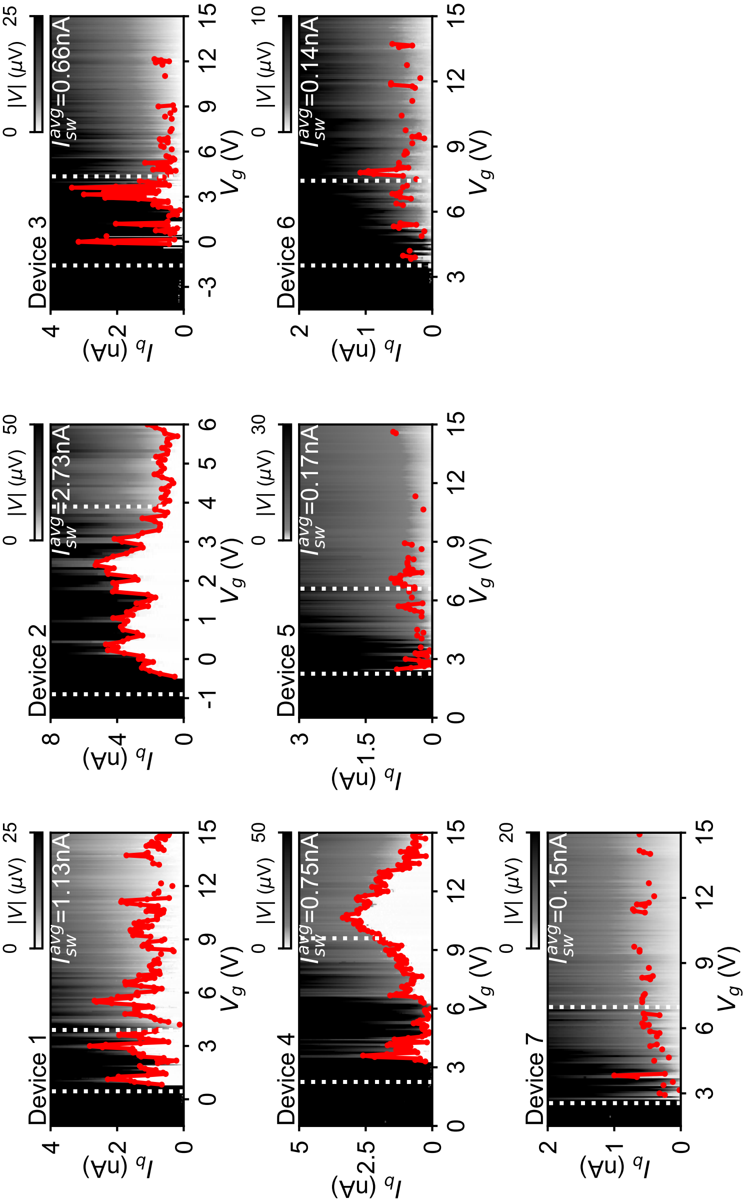

Figure 4.13: **Switching current at** 0.6T **parallel magnetic field:** Dependence of I_{sw} (red) on V_g at $B = 0.6$T for Device 1-7. The white dotted lines indicate the ranges of V_g over which the normal state conductance G_n at the zero-field increases from $0.1G_0$ to $2G_0$. The average switching currents in these intervals are shown as insets. The analogous measurement was not performed for Device 8-9.

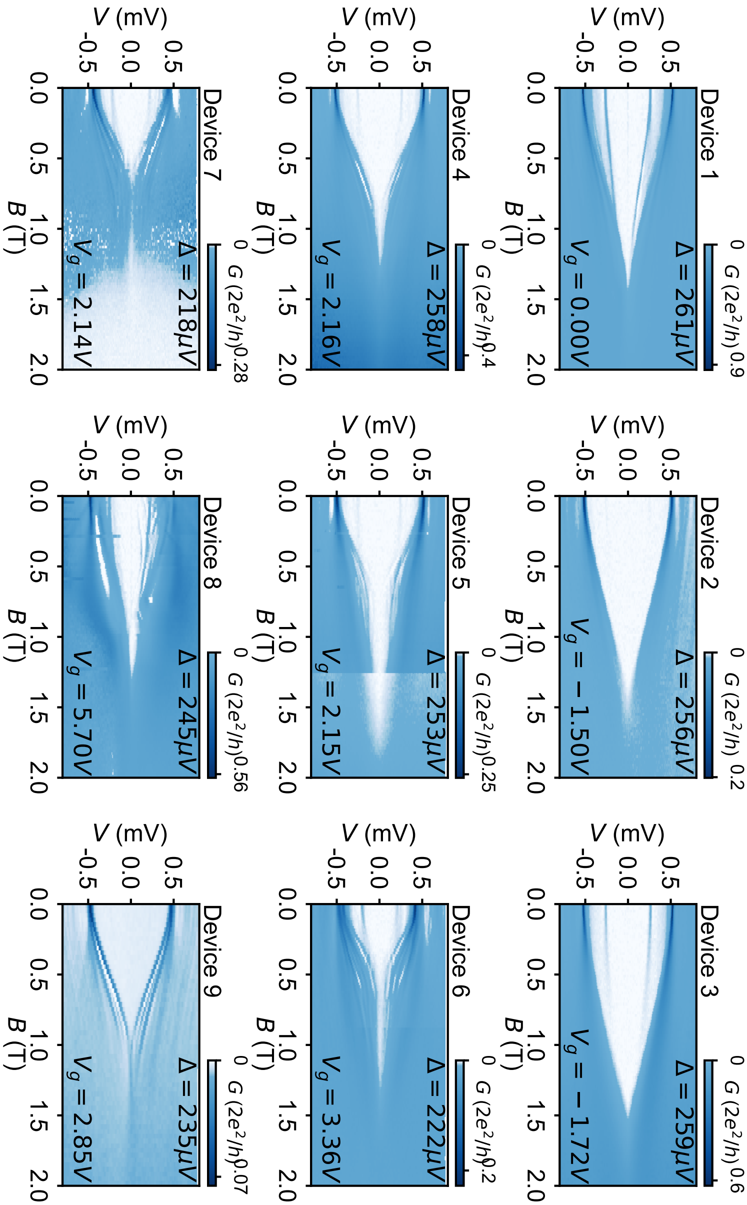

Figure 4.14: **Evolution of the induced superconducting spectra in parallel magnetic field:** Dependence of tunneling conductance G-traces on B for Device 1-9. Extracted induced superconducting gap at zero field Δ and the V_g setting at which the each 2D map is measured are shown as insets.

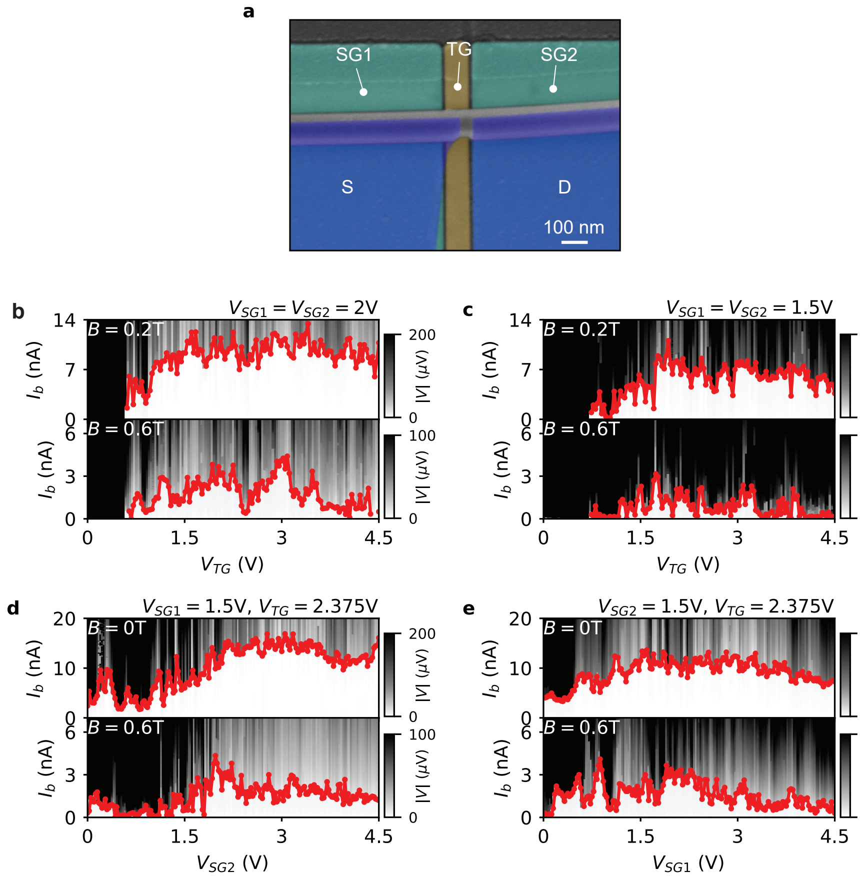

Figure 4.15: **Effects of local gates on supercurrent in the Josephson junction of Device 10**: Measurements were taken on a single arm of the SQUID, while the other arm was pinched-off. **(a)** False-colored SEM image showing a 40 nm junction with the three local bottom gates: SG1, TG and SG2 (a zoom-in at the right junction of Fig. 4.5a. **(b)-(e)** Dependences of the extracted switching current I_{sw} (red) as a single local bottom gate voltage is swept while the other two local bottom gates and the parallel magnetic field are set as written in the corresponding insets.

REFERENCES

[1] T. Yokoyama, M. Eto, and Y. V. Nazarov. "Josephson Current through Semiconductor Nanowire with Spin–Orbit Interaction in Magnetic Field". In: *J. Phys. Soc. Jpn.* 82 (2013), p. 054703.

[2] T. Yokoyama, M. Eto, and Y. V. Nazarov. "Anomalous Josephson effect induced by spin-orbit interaction and Zeeman effect in semiconductor nanowires". In: *Phys. Rev. B* 89 (2014), p. 195407.

[3] D. B. Szombati, S. Nadj-Perge, D. Car, S. R. Plissard, E. P. A. M. Bakkers, and L. P. Kouwenhoven. "Josephson ϕ_0-junction in nanowire quantum dots". In: *Nature Phys.* 12 (2016), pp. 568–572.

[4] E. Strambini, A. Iorio, O. Durante, R. Citro, C. Sanz-Fernández, C. Guarcello, I. V. Tokatly, A. Braggio, M. Rocci, N. Ligato, V. Zannier, L. Sorba, F. S. Bergeret, and F. Giazotto. "A Josephson phase battery". In: *Nat. Nanotechnol.* 15 (2020), pp. 656–660.

[5] P. San-Jose, E. Prada, and R. Aguado. "Mapping the topological phase diagram of multiband semiconductors with supercurrents". In: *Phys. Rev. Lett.* 112 (2014), p. 137001.

[6] R. M. Lutchyn, J. D. Sau, and S. D. Sarma. "Majorana fermions and a topological phase transition in semiconductor-superconductor heterostructures". In: *Phys. Rev. Lett.* 105 (2010), p. 077001.

[7] Y. Oreg, G. Refael, and F. von Oppen. "Helical liquids and Majorana bound states in quantum wires". In: *Phys. Rev. Lett.* 105 (2010), p. 177002.

[8] C. Schrade, S. Hoffman, and D. Loss. "Detecting topological superconductivity with ϕ_0-Josephson junctions". In: *Phys. Rev. B* 95 (2017), p. 195421.

[9] J. Cayao, P. San-Jose, A. M. Black-Schaffer, R. Aguado, and E. Prada. "Majorana splitting from critical currents in Josephson junctions". In: *Phys. Rev. B* 96 (2017), p. 205425.

[10] C. Schrade and L. Fu. "Majorana Superconducting Qubit". In: *Phys. Rev. Lett.* 121 (2018), p. 267002.

[11] J. Cayao, A. M. Black-Schaffer, E. Prada, and R. Aguado. "Andreev spectrum and supercurrents in nanowire-based SNS junctions containing Majorana bound states". In: *Beilstein J. Nanotechnol.* 9 (2018), pp. 1339–1357.

[12] C.-Z. Chen, J. J. He, M. N. Ali, G.-H. Lee, K. C. Fong, and K. T. Law. "Asymmetric Josephson effect in inversion symmetry breaking topological materials". In: *Phys. Rev. B* 075430 (2018), p. 98.

[13] B. Turini, S. Salimian, M. Carrega, A. Iorio, E. Strambini, F. Giazotto, V. Zannier, L. Sorba, and S. Heun. “Josephson Diode Effect in High-Mobility InSb Nanoflags”. In: *Nano Lett.* 22 (2022), pp. 8502–8508.

[14] G. P. Mazur, N. van Loo, D. van Driel, J.-Y. Wang, G. Badawy, S. Gazibegovic, E. P. A. M. Bakkers, and L. P. Kouwenhoven. “The gate-tunable Josephson diode”. In: *arXiv preprint* (2022). https://doi.org/10.48550/arXiv.2211.14283 [Accessed: Nov 25, 2022], p. 2211.14283.

[15] N. F. Q. Yuan and L. Fu. “Supercurrent diode effect and finite-momentum superconductors”. In: *PNAS* 119 (2022), p. 2119548119.

[16] M. Davydova, S. Prembabu, and L. Fu. “Universal Josephson diode effect”. In: *Sci. Adv.* 8 (2022), eabo0309.

[17] H. F. Legg, D. Loss, and J. Klinovaja. “Superconducting diode effect due to magnetochiral anisotropy in topological insulators and Rashba nanowires”. In: *Phys. Rev. B* 106 (2022), p. 104501.

[18] R. S. Souto, M. Leijnse, and C. Schrade. “Josephson Diode Effect in Supercurrent Interferometers”. In: *Phys. Rev. Lett.* 129 (2022), p. 267702.

[19] H. Wu, Y. Wang, Y. Xu, P. K. Sivakumar, C. Pasco, U. Filippozzi, S. S. P. Parkin, Y.-J. Zeng, T. McQueen, and M. N. Ali. “The field-free Josephson diode in a van der Waals heterostructure”. In: *Nature* 604 (2022), pp. 653–656.

[20] B. Pal, A. Chakraborty, P. K. Sivakumar, M. Davydova, A. K. Gopi, A. K. Pandeya, J. A. Krieger, Y. Zhang, M. Date, S. Ju, N. Yuan, L. F. N. B. M. Schröter, and S. S. P. Parkin. “Josephson diode effect from Cooper pair momentum in a topological semimetal”. In: *Nat. Phys.* 18 (2022), pp. 1228–1233.

[21] C. Baumgartner, L. Fuchs, A. Costa, S. Reinhardt, S. Gronin, G. C. Gardner, T. Lindemann, M. J. Manfra, P. E. F. Junior, D. Kochan, J. Fabian, N. Paradiso, and C. Strunk. “Supercurrent rectification and magnetochiral effects in symmetric Josephson junctions”. In: *Nat. Nanotechnol.* 17 (2022), pp. 39–44.

[22] B. Zhang, Z. Li, V. Aguilar, P. Zhang, M. Pendharkar, C. Dempsey, J. Lee, S. Harrington, S. Tan, J. Meyer, M. Houzet, C. Palmstrøm, and S. Frolov. “Evidence of φ0-Josephson junction from skewed diffraction patterns in Sn-InSb nanowires”. In: *arXiv preprint* (2022). https://doi.org/10.48550/arXiv.2212.00199 [Accessed: Dec 1, 2022], p. 2212.00199.

[23] Ö. Gül, H. Zhang, F. K. de Vries, J. van Veen, K. Zuo, V. Mourik, S. Conesa-Boj, M. P. Nowak, D. J. van Woerkom, M. Quintero-Pérez, M. C. Cassidy, A. Geresdi, S. Koelling, D. Car, S. R. Plissard, E. P. A. M. Bakkers, and L. P. Kouwenhoven. “Hard superconducting gap in InSb nanowires”. In: *Nano Lett.* 17 (2017), pp. 2690–2696.

[24] T. Kanne, M. Marnauza, D. Olsteins, D. J. Carrad, J. E. Sestoft, J. de Bruijckere, L. Zeng, E. Johnson, E. Olsson, K. Grove-Rasmussen, and J. Nygård. “Epitaxial Pb on InAs nanowires for quantum devices”. In: *Nat. Nanotechnol.* 16 (2021), pp. 776–781.

[25] M. Pendharkar, B. Zhang, H. Wu, A. Zarassi, P. Zhang, C. P. Dempsey, J. S. Lee, S. D. Harrington, G. Badawy, S. Gazibegovic, J. Jung, A.-H. Chen, M. A. Verheijen, M. Hocevar, E. P. A. M. Bakkers, C. J. Palmstrøm, and S. M. Frolov. "Parity-preserving and magnetic field–resilient superconductivity in InSb nanowires with Sn shells". In: *Science* 372 (2021), pp. 508–511.

[26] G. P. Mazur, N. van Loo, J.-Y. Wang, T. Dvir, G. Wang, A. Khindanov, S. Korneychuk, F. Borsoi, R. C. Dekker, G. Badawy, P. Vinke, S. Gazibegovic, E. P. A. M. Bakkers, M. Q. Pérez, S. Heedt, and L. P. Kouwenhoven. "Spin-mixing enhanced proximity effect in aluminum-based superconductor–semiconductor hybrids". In: *Adv. Mater.* 34 (2022), pp. 1–8.

[27] S. Heedt, M. Quintero-Pérez, F. Borsoi, A. Fursina, N. van Loo, G. P. Mazur, M. P. Nowak, M. Ammerlaan, K. Li, S. Korneychuk, J. Shen, M. Y. van de Poll, G. Badawy, S. Gazibegovic, N. de Jong, P. Aseev, K. van Hoogdalem, E. P. A. M. Bakkers, and L. P. Kouwenhoven. "Shadow-wall lithography of ballistic superconductor–semiconductor quantum devices". In: *Nat. Commun.* 12 (2021), p. 4914.

[28] K. Zuo, V. Mourik, D. B. Szombati, B. Nijholt, D. J. van Woerkom, A. Geresdi, J. Chen, V. P. Ostroukh, A. R. Akhmerov, S. R. Plissard, D. Car, E. P. A. M. Bakkers, D. I. Pikulin, L. P. Kouwenhoven, and S. M. Frolov. "Supercurrent interference in few-mode nanowire Josephson junctions". In: *Phys. Rev. Lett.* 119 (2017), p. 187704.

[29] Y.-J. Doh, J. A. V. Dam, A. L. Roest, E. P. A. M. Bakkers, L. P. Kouwenhoven, and S. D. Franceschi. "Tunable Supercurrent Through Semiconductor Nanowires". In: *Science* 309 (2005), pp. 272–275.

[30] H. A. Nilsson, P. Samuelsson, P. Caroff, and H. Q. Xu. "Supercurrent and Multiple Andreev Reflections in an InSb Nanowire Josephson Junction". In: *Nano Lett.* 12 (2012), pp. 228–233.

[31] S. Abay, D. Persson, H. Nilsson, H. Q. Xu, M. Fogelström, V. Shumeiko, and P. Delsing. "Quantized Conductance and Its Correlation to the Supercurrent in a Nanowire Connected to Superconductors". In: *Nano Lett.* 13 (2013), pp. 3614–3617.

[32] P. Krogstrup, N. L. B. Ziino, W. Chang, S. M. Albrecht, M. H. Madsen, E. Johnson, J. Nygård, C. M. Marcus, and T. S. Jespersen. "Epitaxy of semiconductor–superconductor nanowires". In: *Nat. Mater.* 14 (2015), pp. 400–406.

[33] D. J. Carrad, M. Bjergfelt, T. Kanne, M. Aagesen, F. Krizek, E. M. Fiordaliso, E. Johnson, J. Nygård, and T. S. Jespersen. "Shadow Epitaxy for In Situ Growth of Generic Semiconductor/Superconductor Hybrids". In: *Adv. Mater.* 32 (2020), p. 1908411.

4

[34] F. Borsoi, G. P. Mazur, N. van Loo, M. P. Nowak, L. Bourdet, K. Li, S. Korneychuk, A. Fursina, J.-Y. Wang, V. Levajac, E. Memisevic, G. Badawy, S. Gazibegovic, K. van Hoogdalem, E. P. A. M. Bakkers, L. P. Kouwenhoven, S. Heedt, and M. Quintero-Pérez. "Single-shot fabrication of semiconducting–superconducting nanowire devices". In: *Adv. Func. Mater.* 31 (2021), p. 2102388.

[35] G. Badawy, S. Gazibegovic, F. Borsoi, S. Heedt, C.-A. Wang, S. Koelling, M. A. Verheijen, L. P. Kouwenhoven, and E. P. A. M. Bakkers. "High mobility stemless InSb nanowires". In: *Nano Lett.* 19.6 (2019), pp. 3575–3582.

[36] M. W. A. de Moor, J. D. S. Bommer, D. Xu, G. W. Winkler, A. E. Antipov, A. Bargerbos, G. Wang, N. van Loo, R. L. M. O. het Veld, S. Gazibegovic, D. Car, J. A. Logan, M. Pendharkar, J. S. Lee, E. P. A. M. Bakkers, C. J. Palmstrøm, R. M. Lutchyn, L. P. Kouwenhoven, and H. Zhang. "Electric field tunable superconductor-semiconductor coupling in Majorana nanowires". In: *New J. Phys.* 20 (2018), p. 103049.

[37] J. Shen, G. W. Winkler, F. Borsoi, S. Heedt, V. Levajac, J.-Y. Wang, D. van Driel, D. Bouman, S. Gazibegovic, R. L. M. O. H. Veld, D. Car, J. A. Logan, M. Pendharkar, C. J. Palmstrøm, E. P. A. M. Bakkers, L. P. Kouwenhoven, and B. van Heck. "Full parity phase diagram of a proximitized nanowire island". In: *Phys. Rev. B* 104 (2021), p. 045422.

[38] C. Kittel. *Introduction to Solid State Physics. 8th ed.* New York, NY: John Wiley & Sons, 2004.

[39] M. Tinkham. *Introduction to Superconductivity. 2nd ed.* New York, NY: McGraw-Hill, 1996.

[40] K. Gharavi and J. Baugh. "Orbital Josephson interference in a nanowire proximity-effect junction". In: *Phys. Rev. B* 91 (2015), p. 245436.

[41] I. van Weperen, S. R. Plissard, E. P. A. M. Bakkers, S. M. Frolov, and L. P. Kouwenhoven. "Quantized Conductance in an InSb Nanowire". In: *Nano Lett.* 13 (2013), pp. 387–391.

[42] A. E. G. Mikkelsen, P. Kotetes, P. Krogstrup, and K. Flensberg. "Hybridization at superconductor-semiconductor interfaces". In: *Phys. Rev. X* 8 (2018), p. 031040.

[43] A. E. Antipov, A. Bargerbos, G. W. Winkler, B. Bauer, E. Rossi, and R. M. Lutchyn. "Effects of gate-induced electric fields on semiconductor Majorana nanowires". In: *Phys. Rev. X* 8 (2018), p. 031041.

[44] J.-Y. Wang, C. Schrade, V. Levajac, D. van Driel, K. Li, S. Gazibegovic, G. Badawy, R. L. M. O. het Veld, J. S. Lee, M. Pendharkar, C. P. Dempsey, C. J. Palmstrøm, E. P. A. M. Bakkers, L. Fu, L. P. Kouwenhoven, and J. Shen. "Supercurrent parity meter in a nanowire Cooper pair transistor". In: *Sci. Adv.* 8 (2022), eabm9896.

[45] C.-X. Liu, B. van Heck, and M. Wimmer. "Josephson current via an isolated Majorana zero mode". In: *Phys. Rev. B* 103 (2021), p. 014510.

[46] C. Schrade and L. Fu. "Parity-controlled 2π Josephson effect mediated by Majorana Kramers pairs". In: *Phys. Rev. Lett.* 120 (2018), p. 267002.

5

SUPERCURRENT IN THE PRESENCE OF DIRECT TRANSMISSION AND A RESONANT LOCALIZED STATE

We study the current-phase relation (CPR) of an InSb-Al nanowire Josephson junction in parallel magnetic fields up to 700 *mT. At high magnetic fields and in narrow voltage intervals of a gate under the junction, the CPR exhibits* π*-shifts. The supercurrent declines within these gate intervals and shows asymmetric gate voltage dependence above and below them. We detect these features sometimes also at zero magnetic field. The observed CPR properties are reproduced by a theoretical model of supercurrent transport via interference between direct transmission and a resonant localized state.*

The work in this chapter has been published as: V. Levajac, H. Barakov, G. P. Mazur, N. van Loo, L. P. Kouwenhoven, Y. V. Nazarov and J.-Y. Wang *"Supercurrent in the presence of direct transmission and a resonant localized state"*, arXiv:2310.03296 (2023)

5.1. INTRODUCTION

A Josephson junction (JJ) consists of two superconductors (S) and a weak link between them that supports transport of Cooper pairs in the form of a non-dissipative supercurrent [1]. If the weak link is a normal conductor (N), Andreev reflections at the two SN interfaces give rise to Andreev levels inside the junction that mediate the supercurrent [2]. JJs with semiconducting weak links are widely used to study the influence of their tunable properties on the Andreev spectrum and supercurrent. This is evident in multiple superconducting phenomena, such as topological superconductivity [3–10], the anomalous Josephson effect [11–15] and the Josephson diode effect [16–23]. Semiconducting JJs also have attractive applications in quantum computing, such as gate-tunable superconducting qubits [24–26] and Andreev spin qubits [27–32].

A π-shift in the current-phase relation (CPR) of a JJ can occur due to spin-splitting of the Andreev levels in an external magnetic field. Once the splitting is of the order of the superconducting gap, the minimum of the ground state energy moves from the 0-phase to the π-phase, and the junction undergoes a $0-\pi$ transition [11, 12]. In the presence of Coulomb interaction, sequential coherent single-electron tunneling can result in a supercurrent which direction depends on the junction parity, and $0-\pi$ transitions can occur even at zero magnetic field [33–36]. These phenomena have been studied for quantum dot-based JJs made from semiconducting nanowires (NWs) [37–41], carbon nanotubes (CNTs) [42–44] and two-dimensional electron gases (2DEGs) [45].

In the above works that study JJs in hybrid semiconductor-superconductor nanowires, the CPR has been measured only at low parallel magnetic fields (up to several tens of mT). Studying CPR of nanowire JJs in high parallel fields is motivated by various proposals for detecting signatures of a topological phase transition in supercurrent measurements [5, 7, 46, 47].

In this work, we embed two hybrid InSb-Al nanowire JJs into a superconducting quantum interference device (SQUID) and we study the CPR of one JJ at parallel magnetic fields that are unprecedentedly high for Al-based nanowire JJs - exceeding 700 mT. At zero magnetic field, localized states in the junction are identified by observing resonances in the normal-state conductance. When the localized states become involved in the superconducting transport as they are tuned close to the Fermi energy by a gate under the junction, the supercurrent exhibits asymmetric amplitude modulation by the gate. In these gate intervals at zero magnetic field, either pairs of $0-\pi$ transitions give rise to π-regions in the CPR, or the supercurrent is enhanced with constant phase. We further investigate the CPR of the nanowire JJ by increasing parallel magnetic field and find that high fields can enlarge π-regions or drive $0-\pi$ transitions in the CPR. In order to understand these phenomena, we develop a model involving a transmission channel and a localized resonant state inside a single nanowire JJ. This model can reproduce the main interesting features observed in the experiment by considering the interference between the transmission channel and the localized state. This interference effect of supercurrent represents a novel, superconducting version of the well-known Fano effect [48].

5.2. RESULTS

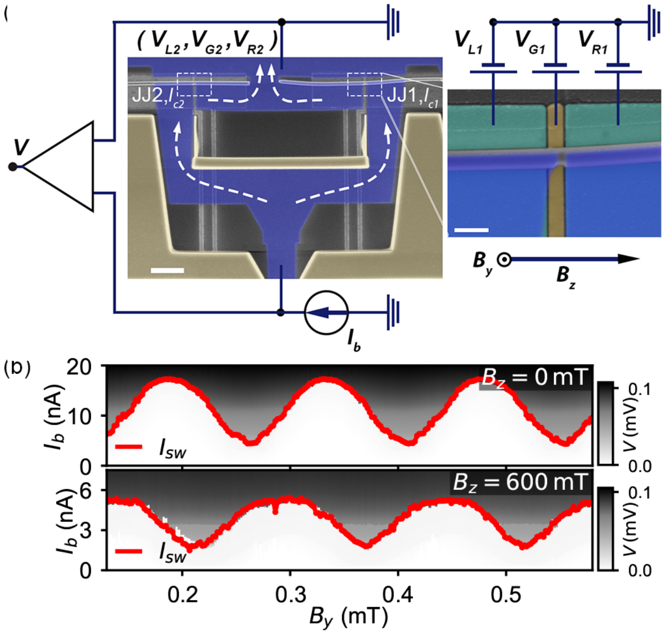

Figure 5.1: **(a)** False-colored SEM image of the nanowire SQUID (left, scale bar 1 μm) and a zoom-in on one arm (right, scale bar 100 nm). Dielectric shadow-walls (yellow) define the two Josephson junctions (JJ1 and JJ2 with critical currents I_{c1} and I_{c2}) in two nearly parallel InSb nanowires, and the superconducting Al (blue) loop on the substrate. Bias current I_b is applied and voltage drop V is measured between the source and drain of the SQUID. White arrows indicate the current directions along the two SQUID arms. JJ1 and JJ2 have ~40 nm-long junctions and are coupled via 20 nm of HfO_2 to corresponding three underlying gates at voltages V_{Li}, V_{Gi} and V_{Ri} (i=1,2). Magnetic fields B_z and B_y are applied parallel to JJ1 and perpendicular to the SQUID loop, respectively. **(b)** V as a function of I_b and B_y at $B_z = 0$ mT (top) and $B_z = 600$ mT (bottom). The red traces I_{sw} are obtained in a setup for fast switching current measurements. The gate settings are $V_{G1} = 2.36$ V, $V_{L1} = V_{R1} = 1.5$ V, $V_{G2} = 2.88$ V and $V_{L2} = V_{R2} = 1.75$ V.

The nanowire SQUID is introduced in Fig. 5.1. In Fig. 5.1(a) on the left, a false-colored scanning electron microscopy (SEM) image displays two InSb-Al nanowire Josephson junctions - JJ1 and JJ2 - enclosed in a superconducting Al (blue) loop. The Al layout is obtained through the shadow-wall (yellow) lithography [49–51]. White arrows indicate the current paths via the two SQUID arms between the source and drain that are shared by JJ1 and JJ2. A zoom-in on JJ1 is displayed in Fig. 5.1(a) on the right. The junction has a length of ~40 nm and its electro-chemical potential is controlled by an underlying gate with a voltage V_{G1}. The other two underlying gates with voltages V_{L1} and V_{R1} predominantly tune the electro-chemical potential in the nanowire sections covered by the left and right lead. JJ2 has nominally the same design as JJ1. An in-plane magnetic field B_z is applied parallel to the nanowire of JJ1 and the flux through the loop is introduced by an out-of-plane magnetic field B_y. For more details of the device fabrication, see our recent work [51] where the identical nanowire SQUID has been introduced.

We characterize the SQUID in the standard four-terminal setup where a bias current I_b is applied and a voltage drop V is measured between the source and drain. $V-I_b$ traces are measured while the flux through the loop is swept by varying B_y. The measurement is performed at $B_z = 0\,\mathrm{mT}$ and $B_z = 600\,\mathrm{mT}$ (see Fig. 5.1(b)). Aside from the measurements shown in the 2D-maps, a setup for switching current measurements in a fast way is employed [22, 52]. In this setup, I_b is ramped and V is monitored without recording the $V-I_b$ trace. For each I_b-ramp, only a single switching current value is recorded as the I_b value for which the SQUID switches from the superconducting to the resistive regime - as V crosses a pre-defined threshold voltage (7 μV in our measurements), see the Methods section. Switching current I_{sw} is obtained as an average of five switching current values measured consecutively upon setting B_y. Such obtained $I_{sw}(B_y)$ dependences (red traces in Fig. 5.1(b)) overlap well with the oscillatory boundaries between the superconducting and resistive regime - demonstrating the accuracy of the fast switching current measurements. The SQUID oscillations at high B_z confirm the resilience of supercurrent interference against large magnetic fields [51]. In the rest of this work, we employ the fast measurement setup to obtain switching current of the SQUID. At zero magnetic field, we use the gates under JJ2 to tune its critical current so that $I_{c2} \gg I_{c1}$. In such a highly asymmetric SQUID configuration, JJ2 serves as the reference arm and the CPR of JJ1 is directly obtained by measuring an $I_{sw}(B_y)$ trace. In our SQUID, parallel magnetic fields simultaneously suppress supercurrent in both JJs, and the condition $I_{c2} \gg I_{c1}$ may not always be satisfied at high B_z. In spite of this, the CPR of JJ1 could still be reflected in the SQUID oscillations. For example, a 0-π transition in JJ1 would cause a half-period shift in the $I_{sw}(B_y)$ trace.

We first pinch-off the reference arm and measure the differential conductance dI/dV_b of JJ1 in a two-terminal setup with the standard lock-in configuration (see the Methods section). In Fig. 5.2(a), dI/dV_b at zero magnetic field is shown as a function of a bias voltage V_b and V_{G1}. By finding the positions of the coherence peaks in the grey linecut, the superconducting gap of the leads $\Delta \sim 0.23\,\mathrm{meV}$ is extracted. Conductance peaks at $0 < |V_b| < 2\Delta/e$ and a zero-bias peak (ZBP) in the 2D-map correspond to the superconducting transport via multiple Andreev reflections (MARs) and supercurrent, respectively. Next to this, in the normal-state transport for $|V_b| > 2\Delta/e$, resonances with positive slope in the (V_b, V_{G1})-plane are observed and one resonance is marked by a red dashed line. The resonances indicate the presence of a state that is localized in the junction and coupled to both leads. Coupling to the leads Γ and charging energy U attributed to the localized state are estimated from the two resonance peaks for $|V_b| > 2\Delta/e$ (grey linecut). From the FWHM of the resonance peaks, the coupling is estimated as $\Gamma \sim 1\,\mathrm{meV} \sim 4\Delta$. Since no resonances with negative slope in the (V_b, V_{G1})-plane are visible, only an

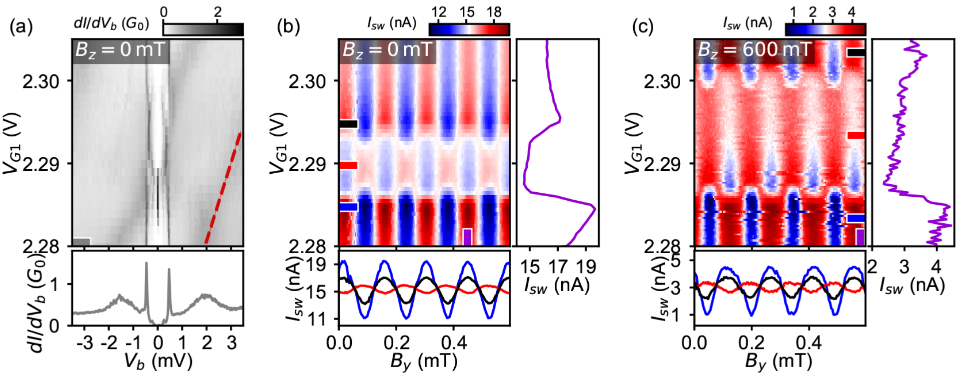

Figure 5.2: **(a)** Differential conductance dI/dV_b of JJ1 as a function of V_b and V_{G1} at zero magnetic field and $V_{L1} = V_{R1} = 1.5\,\text{V}$. JJ2 is pinched-off by setting $V_{G2} = V_{L2} = V_{R2} = 0\,\text{V}$. A linecut (grey marker) with sharp coherence peaks at $\pm 2\Delta/e$ and broad resonance peaks is shown below. One resonance is marked by a red dashed line and the gate lever arm $\alpha \sim 0.5\Delta/\text{mV}$ is estimated from its slope in the (V_b, V_{G1})-plane. **(b)** I_{sw} as a function of B_y and V_{G1} at $B_z = 0\,\text{mT}$ and $V_{L1} = V_{R1} = 1.5\,\text{V}$. JJ2 is turned on by setting $V_{G2} = 2.88\,\text{V}$ and $V_{L2} = V_{R2} = 1.75\,\text{V}$. Horizontal linecuts (red, blue and black marker) are shown below and a vertical linecut (purple marker) is displayed on the right. **(c)** Same as (b), but for $B_z = 600\,\text{mT}$.

5

upper limit for U can be estimated as the separation of two neighbouring resonance peaks along the V_b-axis - giving $U < 4\,\text{meV} \sim 16\Delta$. The features of superconducting transport exhibit strong modulation as the localized state approaches the in-gap energies and contributes to the superconducting transport. In order to investigate the influence of the localized state on the supercurrent, we turn on the reference arm and use the SQUID configuration to investigate the CPR.

Fig. 5.2(b) displays I_{sw} of the SQUID as a function of B_y and V_{G1} in the voltage range studied in Fig. 5.2(a). Three distinct regions can be identified - with the middle region being π-shifted (π-region) relative to the regions below and above (0-regions). Noticeably, the π-region occurs in the same V_{G1} interval in which the localized state is tuned below the superconducting gap (see Fig. 5.2(a)). Two horizontal linecuts in the two 0-regions (blue and black) and one horizontal linecut in the middle of the π-region (red) demonstrates that the supercurrent declines inside the π-region - as the red linecut has the smallest amplitude. The blue and black linecut - taken symmetrically with respect to the red linecut - yet have very different amplitudes. This indicates an asymmetric gate voltage dependence of the supercurrent below and above the π-region. This asymmetry is further confirmed by a vertical linecut (purple). Upon increasing the parallel field to $B_z = 600\,\text{mT}$, I_{sw} is measured in the same B_y and V_{G1} ranges and the result is shown in Fig. 5.2(c). Four linecuts taken analogously as in Fig. 5.2(b) demonstrate that the supercurrent suppression inside the π-region and the asymmetry between the 0-regions remain at $B_z = 600\,\text{mT}$. However, both effects are less prominent in the high parallel field.

In addition, the high magnetic field causes a broadening of the π-region along the gate voltage axis [41]. The observed expansion of $\sim 7.5\,\text{mV}$ in V_{G1} corresponds to an energy of $\sim 0.9\,\text{meV} \sim 4\Delta$ (see Fig. 5.2(a) for the estimation of the gate lever arm) and a same Zeeman energy $g\mu_B B \sim 0.9\,\text{meV}$ would yield a g-factor $g \sim 26$.

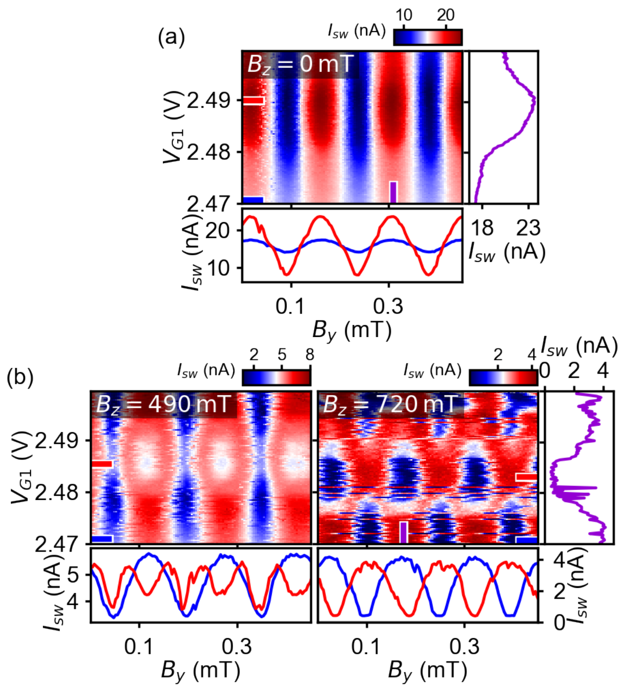

Figure 5.3: I_{sw} as a function of B_y and V_{G1} at: **(a)** $B_z = 0\,\text{mT}$ and **(b)** $B_z = 490\,\text{mT}$ (left) and $B_z = 720\,\text{mT}$ (right). The other gate voltages are $V_{L1} = V_{R1} = 1.75\,\text{V}$, $V_{G2} = 2.88\,\text{V}$ and $V_{L2} = V_{R2} = 1.75\,\text{V}$. Two linecuts (red and blue markers) are shown below and a vertical linecut (purple marker) is shown for $B_z = 0\,\text{mT}$ and $B_z = 720\,\text{mT}$ on the right. Three sharp peaks in the purple linecut at high B_z are caused by instabilities of the flux.

We proceed by studying the CPR in another gate voltage interval, that is above the one presented in Fig. 5.2. In Fig. 5.3(a), I_{sw} dependence on B_y and V_{G1} at $B_z = 0\,\text{mT}$ is presented, with two horizontal linecuts (red and blue) and one vertical linecut (purple). The linecuts show that the supercurrent is enhanced by the gate around $V_{G1} = 2.49\,\text{V}$. Moreover, the purple linecut demonstrates that the supercurrent amplitude is asymmetrically modulated below and above the enhancement. In contrast to Fig. 5.2(b), the asymmetric modulation in this V_{G1} range is not accompanied by $0-\pi$ transitions - as evident from the horizontal linecuts. Next, we increase B_z and measure I_{sw} in the same B_y and V_{G1} ranges - at $B_z = 490\,\text{mT}$ and

$B_z = 720\,\text{mT}$ (see Fig. 5.3(b)). At $B_z = 720\,\text{mT}$, a π-region is observed in the studied V_{G1} interval and the supercurrent amplitudes inside the π-region (red linecut) and 0-region (blue linecut) are comparable, which indicates a very weak suppression of the supercurrent inside the π-region. In addition, the asymmetry between the two 0-regions is also very weak (purple linecut). We see that the $I_{sw}(B_y)$ traces are not sinusoidal any more, with I_{sw} approaching zero at specific B_y values. This indicates that the supercurrent amplitudes in the two SQUID arms are comparable. In spite of this, the π-region could still be well identified in the figure. At $B_z = 490\,\text{mT}$, the frequency of I_{sw} oscillations doubles (red linecut) in a narrow V_{G1} interval. Such a double frequency oscillation has been studied in theory [12, 34, 36] and observed in experiment [41], and is due to an intermediate regime existing in-between a stable 0- and π-region. Therefore, the I_{sw} dependence at $B_z = 490\,\text{mT}$ could be understood as an intermediate regime before a stable π phase is formed at higher magnetic fields.

Common features in Fig. 5.2 and Fig. 5.3 include the peculiarly sharp and asymmetric gate voltage dependence of the supercurrent amplitude in the narrow gate intervals associated with $0-\pi$ transitions. The π-shifted CPR in our experiment occurs over $\sim 10\,\text{mV}$-wide intervals of the gate voltage V_{G1}, which correspond to $\sim 5\Delta$-wide intervals of the junction electro-chemical potential. Sharp dependences generally suggest that a localized state is involved, and the presence of a localized state in our experiment is confirmed by detecting resonances in the normal-state conductance of the junction (Fig. 5.2(a)). The supercurrent and normal-state conductance generally remain finite when the localized state is off-resonant, which implies the existence of a background transport channel.

The simultaneous presence of the localized state and the background transmission motivates us to explain the asymmetric resonant features by considering the interference between the localized state and direct transmission. Our motivation originates from such mechanism giving rise to the peculiar asymmetry of Fano resonances [48].

We develop a model for the transport through a nanowire JJ, in which a localized state and a direct-transmission channel are involved. The top panel in Fig. 5.4(a) shows a schematic of a nanowire JJ with filled states in the leads and the transmission channel given in black. Random potential minima in the junction are either filled (small black regions) or empty (regions with dashed boundaries). The localized state is one such random minimum and is shown in red. For convenience, we treat the direct-transmission channel as a resonance as well, but its energy broadening by far exceeds all other energy scales in the model. Therefore, we develop a two-dot model of a JJ, that is introduced in the bottom panel of Fig. 5.4(a). The first (red) dot represents the localized state and the second (black) dot models the direct-transmission channel. The dot energies and tunnel couplings to the leads should, thus, satisfy the relation $\Gamma_2^{L,R}, E_2 \gg \Gamma_1^{L,R}, E_1$ in order for the second dot to model the transmission channel. Then, we can neglect the influence of the gate voltage and magnetic field on the second dot, and we also neglect its charging energy. Importantly, there is a direct tunnel coupling with the rate κ between the two dots, that allows for the interference between them. Additional non-trivial elements are tunneling rates $\gamma_{L,R}$ that cannot be ascribed to a certain dot, but are required to

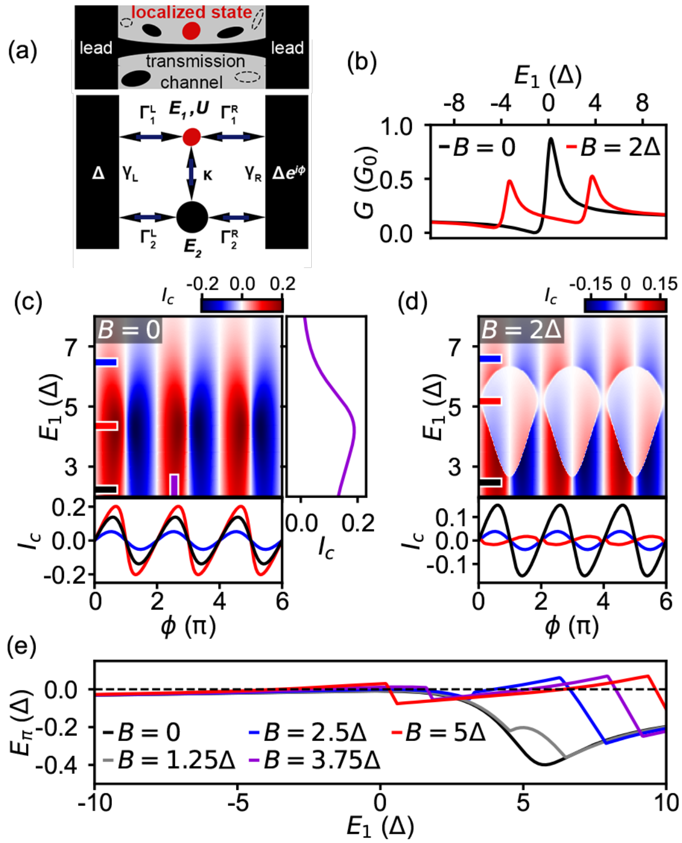

Figure 5.4: **(a)** Schematic of a nanowire JJ and the geometry of electron distribution in the nanowire and the leads - with empty states in grey and filled states in black and red (localized state) (top). Schematic of the two-dot model - with the red dot (energy E_1, charging energy U) modelling the localized state and the black dot (energy E_2, no charging energy) modelling the transmission channel (bottom). The tunnel couplings to the leads (left,right) are $\Gamma_{1,2}^{L,R}$, the tunneling rate between the dots is κ and the dots-superposition tunneling rates to the leads are $\gamma_{L,R}$. **(b)** Normal state conductance G as a function of E_1 for the zero (black) and finite (red) Zeeman energy. The tunneling parameters are taken in ratios $\Gamma_1^L : \Gamma_1^R : \kappa = 0.001 : 0.001 : 1$ and $\Gamma_2^L : \Gamma_2^R : E_2 = 0.33 : 0.67 : 1.2$. **(c)** I_c in the units of $2e\Delta/\hbar$ as a function of ϕ and E_1 for $B = 0$. Horizontal linecuts (blue, red and black marker) are shown below, and a vertical linecut (purple marker) is shown on the right. **(d)** Analogous to (c), but for $B = 2\Delta$. **(e)** Ground-state energy difference $E_\pi = E(\phi = 0) - E(\phi = \pi)$ as a function of E_1 for different Zeeman energies. In (b)-(e), the charging energy is neglected by taking $U = 0$.

describe tunneling of a superposition state of the two dots. These parameters are at an intermediate scale, $\kappa, \gamma_{L,R} \simeq \sqrt{\Gamma_1\Gamma_2}$. The charging energy U of the first dot in general cannot be neglected. A magnetic field is introduced by the Zeeman energy in a simple form $\mathbf{B}\cdot\sigma$, where we use B to represent Zeeman energies in the units of Δ. Spin-orbit coupling is neglected here, but its influence is discussed in the extended data sets in the supplementary section about the theoretical model. The full derivation of the model is shown there as well.

Figure 5.4(b) shows the normal-state conductance G through the two-dot system as a function of E_1 for $B = 0$ (black) and $B = 2\Delta$ (red). The ratio of the coupling rates in the model is chosen such that the total coupling to the leads is $\Gamma = 4\Delta$ (as in the experiment) and the two-dot interference results in competing processes of resonant transmission and resonant reflection that almost compensate - causing the Fano shape of the resonant peculiarity [48]. The coupling parameters remain fixed in the rest of the study. For other possible scenarios, see the normal transport examples in the supplementary section about the theoretical model. Next, we perform calculations on the supercurrent transport via the two coupled dots. In Figs. 5.4(c) and 5.4(d), the junction CPR $I_c(\phi)$ is obtained as a function of E_1 for $B = 0$ and $B = 2\Delta$, respectively. For $B = 0$, the I_c amplitude is enhanced and asymmetrically modulated around the resonance, as confirmed by a vertical linecut. Three horizontal linecuts show that no phase shifts occur and that the CPR is skewed at the resonance, in agreement with the enhanced transmission. For $B = 2\Delta$, the I_c dependence exhibits three distinct regions along the E_1-axis - including a π-region and two 0-regions. The I_c amplitude declines inside the π-region (red linecut) and is asymmetrically modulated in the two 0-regions (blue and black linecut). In order to more easily identify π-regions in our calculations, we define a quantity $E_\pi = E(\phi = 0) - E(\phi = \pi)$ that is the difference between the junction ground state energies at $\phi = 0$ and $\phi = \pi$. Therefore, a π-shifted CPR is obtained whenever $E_\pi > 0$, as the ground state is favored for $\phi = \pi$. In Fig. 5.4(e), we calculate E_π as a function of E_1 for different B. For small B, E_π remains negative in the entire range of E_1 - confirming the absence of $\pi-$shifts at $B = 0$. However, if B is sufficiently large, one obtains intervals in E_1 with $E_\pi > 0$. These intervals correspond to π-regions that appear due to the Zeeman energy - as in the example in Fig. 5.4(d). As B increases, the intervals of E_1 with $E_\pi > 0$ extend, which indicates that the π-regions broaden with the Zeeman energy.

Next, we consider the case with finite charging energy U in the first dot. For $U = 5\Delta$, I_c is calculated as a function of ϕ and E_1 for Zeeman terms $B = 0$ (Fig. 5.5(a)) and $B = 2\Delta$ (Fig. 5.5(b)). A $\pi-$region appears already for $B = 0$ (zero magnetic field), and it expands for $B = 2\Delta$. I_c amplitude is suppressed inside the π-region and asymmetrically modulated in the two neighboring $0-$regions, as emphasized by corresponding horizontal and vertical linecuts. Complementary to Fig. 5.4(e), in Fig. 5.5(c) the ground-state energy difference $E_\pi = E(\phi = 0) - E(\phi = \pi)$ is calculated as a function of E_1 for various charging energies U and fixed Zeeman energy $B = 0$. One obtains that an interval of E_1 in which $E_\pi > 0$ appears for sufficiently large U, despite the absence of the Zeeman energy. This interval corresponds to a π-region in the CPR, as $E_\pi > 0$ means that the ground-state energy minimum is achieved for $\phi = \pi$ rather than $\phi = 0$. Moreover, this interval broadens as U increases. This

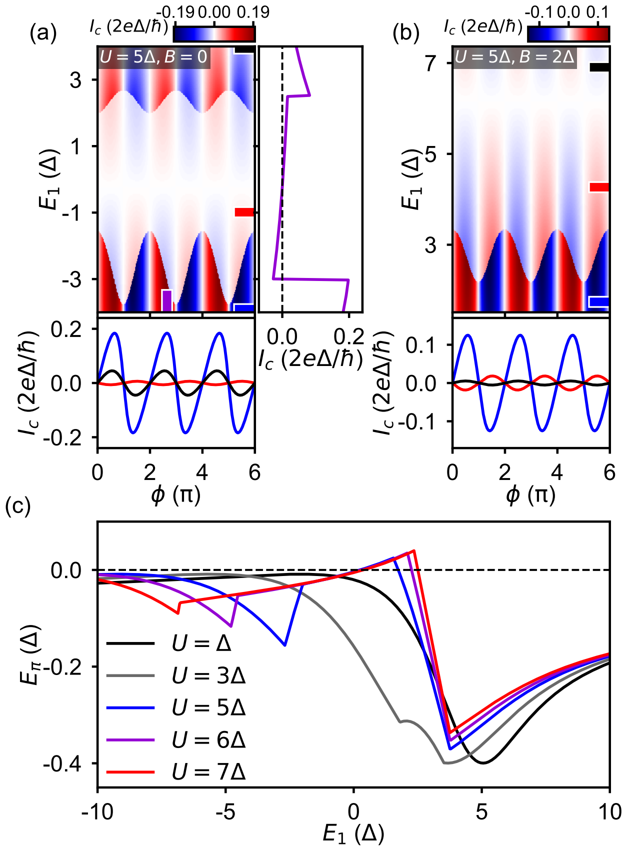

Figure 5.5: The situation with a finite U in the first dot. (a) I_c as a function of ϕ and E_1 for $U = 5\Delta$ and $B = 0$. Three linecuts (blue, red and black marker) are shown in the bottom panel, and a linecut (purple marker) is shown in the right panel. (b) Analogous to (a), but for $B = 2\Delta$. (c) Ground-state energy difference $E_\pi = E(\phi = 0) - E(\phi = \pi)$ as a function of E_1 for $B = 0$ and different charging energies U. $E_\pi > 0$ indicates π-shifted CPR.

demonstrates that a region with $\pi-$shifted CPR can be driven by a finite on-site interaction of the localized state even without magnetic fields, and that increasing the interaction leads to its expansion.

5.3. DISCUSSION

The theoretical model reproduces the magnetic field-driven $0-\pi$ transitions reported in the experiment. The supercurrent suppression inside the π-regions and the asymmetrical modulation outside the π-regions have been captured by the model in which the interference between the direct-transmission channel and the localized state is considered. $0-\pi$ transitions at zero magnetic field are also reproduced by the model with a sufficiently large on-site interaction and the typical features of suppressed supercurrent inside the π-regions and the asymmetrical modulation outside the π-regions still remain. In the calculations, I_c jumps show up due to the Andreev-levels crossing the Fermi energy and changing the ground state parity of the junction. In the experiment, however, the parity of the junction is not controlled and the switching current measured close to parity-transitions represents an average of the two parities. Therefore, the sharp jumps in the calculated I_c data are smeared-out in the measured I_{sw} data. In the model, π-regions are found to occur over $\sim 10\Delta$-wide intervals in the junction electro-chemical potential - matching the scale at which they have been observed in the experiment.

5.4. CONCLUSION

We report on the CPR properties of an InSb-Al nanowire JJ in high magnetic fields. The supercurrent of the device is sharply and asymmetrically modulated in narrow intervals of the junction electro-chemical potential where a localized state is involved in the transport. In these intervals, high parallel magnetic fields can drive $0-\pi$ transitions with π-shifted CPR in-between two 0-regions. The $0-\pi$ transitions are favored by the on-site interaction in the localized state and can also occur at zero magnetic field. These phenomena can be explained by a theoretical model which involves a direct-transmission channel and a resonant localized state inside a single JJ. When one considers the interference between the direct transmission and the localized state, the supercurrent obtained in an effective Fano-resonance regime exhibits CPR features as in the experiment. Our study, thus, introduces a superconducting counterpart of the Fano effect and shows how such effect can lead to $0-\pi$ transitions in high magnetic fields.

5.5. THEORETICAL MODEL

In this Section, we establish a theoretical model to describe the normal and superconducting transport in the situation where a featureless direct transmission in a single channel is combined with that via a resonant state. Technically, it is derived from a two quantum dot model where the channel is represented as a dot with the level width that exceeds much the level width of the dot representing the resonant state. We believe that the model is applicable and useful in many situations not being restricted to concrete experimental conditions at hand. This is why we give here a detailed derivation, include the factors like strong spin-orbit interaction that are not manifested in our experiment, and provide the general examples not necessarily related to the current observations.

5.5.1. HAMILTONIANS

In this subsection, we give the Hamiltonians of the constituents of our model.

THE SINGLE DOT

We start with a dot Hamiltonian. It involves on-site annihilation operators $\hat{d}_\alpha$, α being the spin index, and reads

$$\hat{H}_D = \hat{d}^\dagger_\alpha H_{\alpha\beta}\hat{d}_\beta + U\hat{n}_\uparrow\hat{n}_\downarrow \tag{5.1}$$

$\hat{n}_\alpha = \hat{d}^\dagger_\alpha\hat{d}_\alpha$. The single-particle Hamiltonian reads

$$\check{H} = E + \mathbf{B}\cdot\boldsymbol{\sigma}$$

$\mathbf{B}$ being the magnetic field, $\boldsymbol{\sigma}$ being the vector of Pauli matrices.

Importantly, we treat the interaction in the mean-field approximation. If there is a natural quantization axis (that can be absent in the presence of spin-orbit interaction in the coupling to the leads), the mean field gives the following additions to the single-particle Hamiltonian,

$$H_{\uparrow\uparrow} = U\langle\hat{n}_\downarrow\rangle; H_{\downarrow\downarrow} = U\langle\hat{n}_\uparrow\rangle. \tag{5.2}$$

In general situation,

$$H_{\alpha\beta} = U\left(\delta_{\alpha\beta}\langle\hat{N}\rangle - \langle\hat{d}^\dagger_\alpha\hat{d}_\beta\rangle\right) \tag{5.3}$$

The advantage of this mean-field scheme is that it delivers exact results in the absence of tunnel coupling. In particular, at zero magnetic field the ground state corresponds to single occupation of the dot in the interval $U > E-\mu > 0$. At the ends of the interval, sharp transitions bring the dot to the states of zero and double occupation. The scheme is approximate in the presence of tunnel coupling, yet we use it for the lack of better general approach to interaction.

THE LEADS

We introduce annihilation operators in the leads $\hat{c}_{k,\alpha}$ where k labels the states of quasi-continuous spectrum in the leads. The states k are distributed over the leads and those are labelled with a. We assume the states k are invariant with respect to time inversion.

The leads are described by the usual BSC Hamiltonian

$$\hat{H}_{leads} = \sum_k \xi_k\hat{c}^\dagger_{k,\alpha}\hat{c}_{k,\alpha} + \sum_a\sum_{k\in a}\left(\Delta^*_a\hat{c}_{k,\uparrow}\hat{c}_{k,\downarrow} + \mathrm{h.}c\right) \tag{5.4}$$

ξ_k are the energies of the corresponding states. The superconducting order parameter Δ_a is different in different leads. To describe normal leads, we just put $\Delta_a = 0$.

TUNNEL COUPLING

The tunnel coupling to the states is described by the following Hamiltonian

$$\hat{H}_T = \sum_k \hat{c}^\dagger_{k,\alpha} t^k_{\alpha\beta} \hat{d}_\beta + \text{h.}c \tag{5.5}$$

For time-reversible case, the tunnel amplitudes are given by

$$\check{t} = t_k + i\mathbf{t}_k \cdot \boldsymbol{\sigma} \tag{5.6}$$

with real $t_k, \mathbf{t}_k$. Of course, the multitude of tunneling amplitudes comes to the answers only in a handful of parameters. One of such parameters is the decay rate from the dot to the continuous spectrum of the lead a,

$$\Gamma_a(\epsilon) = 2\pi \sum_{k\in a} \left(|t_k|^2 + |\mathbf{t}_k|^2\right) \delta(\xi_k - \epsilon) \tag{5.7}$$

One can disregard the dependence of the rates on the energy ϵ.

5

5.5.2. NORMAL TRANSPORT FOR MANY DOTS

In this subsection, we will derive the currents in the nanostructure assuming the leads are normal and are kept at different filling factors. We do this derivation for an arbitrary number of the leads and dots, and later specify this for two dots and two terminals. Let us consider the following Hamiltonian where we do not specify spin or dot structure

$$\hat{H} = \sum_k \xi_k \hat{c}^\dagger_k c_k + \hat{d}^\dagger_\alpha H_{\alpha\beta} \hat{d}_\beta + \sum_k (\hat{c}^\dagger_k t^{k\beta} \hat{d}_\beta + h.c) \tag{5.8}$$

The Heisenberg equations read

$$i\dot{\hat{c}}_k = \xi_k \hat{c}_k + t_{k\alpha} \hat{d}_\alpha;\ i\dot{\hat{d}}_\alpha = H_{\alpha\beta} \hat{d}_\beta + t^*_{k\alpha} \hat{c}_k \tag{5.9}$$

The current operators are thus given by

$$\hat{I}_a = \sum_{k\in a} -i t_{k\alpha} \hat{d}^\dagger_k \hat{c}_\alpha + h.c. \tag{5.10}$$

We solve for operators $\hat{c}_k$,

$$\hat{c}_k(t) = \hat{c}^0 e^{-ixi_k t} + \int dt' g_k(t,t') t_{k\alpha} \hat{d}_\alpha(t'),$$

$g_k(t,t') \equiv -ie^{-i\xi_k(t-t')}$, and subsequently for $\hat{d}_\alpha$,

$$\hat{d}_\alpha(t) = \int dt' G_{\alpha\beta}(t,t') t^*_{\beta k} e^{-i\xi_k t'} \hat{d}^0_k$$

where the Green's function obeys

$$\left(i\partial_t - \check{H} - \check{\Sigma}\right) \check{G} = \delta(t - t') \tag{5.11}$$

and

$$\check{\Sigma}(t,t') = \sum_k t^*_{k\alpha} g_k(t,t') t_{k\beta}. \tag{5.12}$$

It is also useful to introduce partial Σ that describe the decay to a certain lead,

$$\check{\Sigma}^a(t,t') = \sum_{k\in a} t^*_{k\alpha} g_k(t,t') t_{k\beta}. \tag{5.13}$$

With this,

$$\hat{c}_k(t) = c^0_k e^{-i\xi_k t} + g_k(t,t') t_{k\alpha} G_{\alpha\beta}(t',t'') t^*_{k'\beta} e^{-i\xi_{k'} t''} \hat{c}^0_{k'} \tag{5.14}$$

in the above expression, we assume summation over t', t'', k'. We substitute this into the current operator, average over the quantum state replacing $\langle \hat{c}^{0\dagger}_k \hat{c}^0_{k'} \rangle = f_k$ and get two contributions corresponding to two terms in Eq. 5.14. The contribution A depends only on the filling factor in the lead a and reads

$$I^a_A = \mathrm{Tr}\left(\check{G}(t,t')\check{F}^a(t',t) - \check{F}^a(t,t')\check{\bar{G}}(t,t')\right) \tag{5.15}$$

where $\bar{G}(t,t') \equiv G^\dagger(t',t)$,

$$\check{F}^a(t,t') = \sum_{k\in a} t^*_{k\alpha} t_{k\beta} f_k e^{-i\xi_k(t-t')} \tag{5.16}$$

The contribution B depends on filling factors in all leads

$$I^a_B = \mathrm{Tr}\left(\check{G}(t,t')\sum_b \check{F}^b(t',t'')\check{\bar{G}}(t'',t''')\Sigma^\dagger_a(t''',t) - \Sigma_a(t,t')\check{G}(t',t'')\sum_b \check{F}^b(t'',t''')\check{\bar{G}}(t''',t)\right) \tag{5.17}$$

We switch to the energy representation. To deal with the tunnel amplitudes, we will use the following relation

$$\check{\Gamma}^a(\epsilon) = 2\pi \sum_k t^*_{k\alpha} t_{k\beta} \delta(\epsilon - \xi_k) \tag{5.18}$$

$\check{\Gamma}^a$ characterizing the decay from all dots to the lead a. Conventionally, we will disregard the energy dependence of Γ (since we are working close to the Fermi level). With this,

$$\check{F}^a = -i\check{\Gamma}^a f_a(\epsilon);\ \check{\Sigma}_a = -\frac{i}{2}\check{\Gamma}^a, \tag{5.19}$$

where we have taken into account that the filling factor depends on energy only, and disregarded real part of Σ (that would lead to a renormalization of the dot Hamiltonian). With this, the Green function is given by

$$\check{G} = \frac{1}{\epsilon - \check{H} + i\check{\Gamma}/2}; \tag{5.20}$$

$\check{\Gamma} \equiv \sum_a \check{\Gamma}_a$. The B contibution for the current for all $b \neq a$ can be written as

$$I_a/e = \sum_{b\neq a} \int \frac{d\epsilon}{2\pi} P_{ab}(\epsilon) f_b(\epsilon) \tag{5.21}$$

P_{ab} being the probability to scatter from all channels of terminal b to the channels of terminal a,

$$P_{ab}(\epsilon) = \mathrm{Tr}\{\check{\Gamma}^a \check{G}(\epsilon) \check{\Gamma}^b \check{\bar{G}}(\epsilon)\} \tag{5.22}$$

This is in accordance with the corresponding part of Landauer formula for multi-terminal case. The contibution A reads:

$$I_A^a/e = -i \int \frac{d\epsilon}{2\pi} f_a(\epsilon) \mathrm{Tr}\{\check{\Gamma}^a (\check{G} - \check{\bar{G}})\} \tag{5.23}$$

We use the relation

$$\check{G} - \check{\bar{G}} = -i \check{G} \check{\Gamma} \check{\bar{G}} \tag{5.24}$$

to represent the contribution A in the form

$$I_A^a/e = -\int \frac{d\epsilon}{2\pi} f_a(\epsilon) \sum_b P_{ab}(\epsilon) \tag{5.25}$$

summing everything together, we reproduce the Landauer formula

$$I_a/e = \int \frac{d\epsilon}{2\pi} \sum_{b\neq a} P_{ab}(\epsilon)(f_a(\epsilon) - f_b(\epsilon)) \tag{5.26}$$

Let us construct a scattering matrix corresponding to the situation. The scattering to a terminal a is described by $\check{\Gamma}^a$. Let us represent this matrix as $\check{\Gamma}^a = \check{W}_a^\dagger \check{W}_a$. So-introduced $\check{W}_a$ is a matrix where the second index goes over the dots and the first one over the channels of the terminal a. The matrix $\check{W}_a$ is apparently an ambiguous representation of $\check{\Gamma}^a$, but the same ambiguity pertains the scattering matrix: both are defined upon a unitary transformation in the space of the channels in each lead. We combine all matrices W_a block by block introducing the matrix W where the first index goes over all channels in all terminals. We note $\check{W}^\dagger \check{W} = \check{\Gamma}$. With this, a scattering matrix describing the situation reads

$$\check{S} = 1 - i \check{W} \check{G} \check{W}^\dagger \tag{5.27}$$

Its unitarity can be proven with using the relation (5.24).

5.5.3. NORMAL TRANSPORT FOR TWO DOTS

We concentrate on the case of two dots and two terminals. It seems a trivial consequence of the above fomulas but requires some elaboration for the limit where Γ in the dots are very different, this is the case under consideration. To warm up, let us first consider a single dot. We note that Γ_a in this case are diagonal in spin owing to time-reversability and can be regarded as numbers. The transmission probability from the left to the right (or vice versa) can be written as

$$T_0(\epsilon) = \frac{\Gamma_L \Gamma_R}{(\epsilon - E)^2 + \Gamma^2/4} \tag{5.28}$$

The ideal transmission is achieved at $\Gamma_L = \Gamma_R = \Gamma/2$ and $\epsilon = E$. Let us go for two dots and list possible parameters of the model. Those are: level energies (split in spin) $E_1 + \boldsymbol{B}_1 \cdot \boldsymbol{\sigma}$, $E_2 + \boldsymbol{B}_2 \cdot \boldsymbol{\sigma}$, decays from the dots $\Gamma_1 = \Gamma_1^L + \Gamma_1^R$, $\Gamma_2 = \Gamma_2^L + \Gamma_2^R$, tunneling between the dots $\kappa + i\boldsymbol{\kappa} \cdot \boldsymbol{\sigma}$, and non-diagonal tunneling to the leads $\Gamma_{12,21} \equiv \gamma \pm i\boldsymbol{\gamma} \cdot \boldsymbol{\sigma}$. Let us write down the Green's function:

$$\check{G}^{-1} = \epsilon - \begin{bmatrix} H_1 & H_{12} \\ H_{12}^\dagger & H_2 \end{bmatrix}; \; H_{1,2} \equiv E_{1,2} + \boldsymbol{B}_{1,2} \cdot \boldsymbol{\sigma} - i\Gamma_{1,2}/2; \; H_{12} \equiv \kappa + i\boldsymbol{\kappa} \cdot \boldsymbol{\sigma} - i(\gamma + i\boldsymbol{\gamma} \cdot \boldsymbol{\sigma})/2 \tag{5.29}$$

5

The idea of further transform is that the second dot provides a featureless background for the first dot. To this end, we consider big $E_2, \Gamma_2 \gg \epsilon, B_{1,2}, E_1, \Gamma_1$. As to γ, κ, they are assumed to be of an intermediate scale, say $\gamma \simeq \sqrt{\Gamma_1 \Gamma_2}$. We note that $\boldsymbol{B}_2$ can be ignored under this condition, and for brevity we define $\boldsymbol{B}_1 = \boldsymbol{B}$.

We will apply a transform that approximately diagonalises the Green function so that

$$\check{G} = \check{U} \check{G}_d \check{U}^{-1} \tag{5.30}$$

where

$$\check{U} = \sqrt{\frac{1+s}{2s}} \begin{bmatrix} 1 & \eta_+ \\ -\eta_- & 1 \end{bmatrix}; \; \check{U}^{-1} = \sqrt{\frac{1+s}{2s}} \begin{bmatrix} 1 & -\eta_+ \\ \eta_- & 1 \end{bmatrix} \tag{5.31}$$

and

$$\eta_\pm = \frac{\mu_\pm}{1+s}; \; s \equiv \sqrt{1 + \mu_+ \mu_-}; \; \mu_\pm = 2\frac{k \pm \boldsymbol{k} \cdot \boldsymbol{\sigma}}{-E_2 + i\Gamma_2/2}; \; k, \boldsymbol{k} \equiv -\kappa + i\gamma/2, -\boldsymbol{\kappa} + i\boldsymbol{\gamma}/2 \tag{5.32}$$

with this, the biggest block of $\check{G}_d^{-1}$ is $-E_2 + i\Gamma_2/2$, while the smallest one reads

$$\epsilon - E_1 + i\Gamma_1/2 - \frac{k^2 + \boldsymbol{k}^2}{-E_2 + i\Gamma_2/2} \tag{5.33}$$

We rewrite it as

$$\epsilon - E_1 + i\Gamma/2 - \Delta E_1 \tag{5.34}$$

where the actual level width Γ is given by

$$\Gamma = \Gamma_1 + \frac{\Gamma_2 C_{11} - 2E_2 C_{10}}{E_2^2 + \Gamma_2^2/4}; \; C_{11} \equiv \kappa^2 - \gamma^2/4 + \boldsymbol{\kappa}^2 - \boldsymbol{\gamma}^2/4; \; C_{10} \equiv \kappa\gamma + \boldsymbol{\kappa}\boldsymbol{\gamma} \tag{5.35}$$

and we neglect insignificant shift of the level position

$$\Delta E_1 = -\frac{C_{10}\Gamma_2/2 + C_{11}E_2}{E_2^2 + \Gamma_2^2/4} \tag{5.36}$$

The Γ_a matrices are transformed as $\check{\Gamma}^L \to \check{U}^\dagger \check{\Gamma}^L \check{U}$, $\check{\Gamma}^L \to \check{U}^{-1\dagger} \check{\Gamma}^L \check{U}^{-1}$.

Keeping terms of the relevant orders only, we obtain

$$\check{\Gamma}^L = \begin{bmatrix} g_L & \Gamma_{12}^{+L} - \eta_-^* \Gamma_2^L \\ \Gamma_{12}^{-L} - \Gamma_2^L \eta_- & \Gamma_2^L \end{bmatrix}; \; g_L \equiv \Gamma_1^L - \Gamma_{12}^{+L}\eta_- - \eta_-^* \Gamma_{12}^{-L} + \eta_-^* \Gamma_2^L \eta_-; \tag{5.37}$$

$$\check{\Gamma}^R = \begin{bmatrix} g_R & \Gamma_{12}^{+R} - \eta_+ \Gamma_2^R \\ \Gamma_{12}^{-R} - \Gamma_2^R \eta_+^* & \Gamma_2^R \end{bmatrix}; \; g_R \equiv \Gamma_1^R - \Gamma_{12}^{+R}\eta_+^* - \eta_+ \Gamma_{12}^{-R} + \eta_+ \Gamma_2^R \eta_+^* - . \tag{5.38}$$

With this, we can summarize the results for the total transmission coefficient T_{tot} (summed over two spin directions). We introduce compact notations that adsorb the energy dependence of the coefficient:

$$G_\pm = \frac{1}{\epsilon - E_1 \pm B + i\Gamma/2}; \; G_{s,a} = \frac{G_+ \pm G_-}{2}; \; \bar{G}_i = G_i^* \tag{5.39}$$

and write it down as

$$T_{tot}(E) = 2T_0 + (\Gamma_L\Gamma_R + \mathbf{\Gamma}^2)(G_+\bar{G}_+ + G_-\bar{G}_-) + 2((\mathbf{\Gamma}\cdot\boldsymbol{B})^2/B^2 - \mathbf{\Gamma}^2)G_a\bar{G}_a \tag{5.40}$$
$$+RX(G_+ + G_- + \bar{G}_+ + \bar{G}_-) - IX\mathrm{I}m(G_+ + G_- - \bar{G}_+ - \bar{G}_-) \tag{5.41}$$

Here, the partial decay rate read ($\Gamma_L + \Gamma_R = \Gamma$)

$$\Gamma_L = \Gamma_1^L + \frac{C_1\Gamma_2^L - C_3^L\Gamma_2 - 2E_2C_2^L}{E_2^2 + \Gamma_2^2/4}; \; C_1 \equiv \kappa^2 + \gamma^2/4 + \boldsymbol{\kappa}^2 + \boldsymbol{\gamma}^2/4; \; C_2^L \equiv \boldsymbol{\kappa}\cdot\boldsymbol{\gamma}_L + \gamma_L\kappa; \; C_3^L \equiv \boldsymbol{\gamma}\cdot\boldsymbol{\gamma}_L + \gamma\gamma_L \tag{5.42}$$

and similar for R. The spin-orbit interaction is represented by the vector $\mathbf{\Gamma}$,

$$\mathbf{\Gamma} = \frac{E_2\boldsymbol{C}_5 + \boldsymbol{\kappa}C_4 + \boldsymbol{C}_6 \times \boldsymbol{\kappa} + \kappa\boldsymbol{C}_6}{E_2^2 + \Gamma_2^2/4}; \; C_4 = \Gamma_2^L\gamma_R - \Gamma_2^R\gamma_L; \tag{5.43}$$

$$\boldsymbol{C}_5 = \boldsymbol{\gamma}_R\gamma_L - \boldsymbol{\gamma}_L\gamma_R + \boldsymbol{\gamma}_R \times \boldsymbol{\gamma}_L; \; \boldsymbol{C}_6 = \Gamma_2^R\boldsymbol{\gamma}_L - \Gamma_2^L\boldsymbol{\gamma}_R \tag{5.44}$$

and the coefficients RX, IY read

$$RX = \frac{1}{E_2^2 + \Gamma_2^2/4}(-E_2C_7 + \kappa C_8 + \boldsymbol{\kappa}\cdot\boldsymbol{C}_9 - T_0(E_2C_{11} + C_{10}\Gamma_2/2)) \tag{5.45}$$

$$IX = \frac{1}{E_2^2 + \Gamma_2^2/4}(-C_7\Gamma_2/2 + \gamma C_8/2 + \boldsymbol{\gamma}\cdot\boldsymbol{C}_9/2 - T_0(E_2C_{10} - C_{11}\Gamma_2/2)) \tag{5.46}$$

$$C_7 = \gamma_R\gamma_L + \boldsymbol{\gamma}_R\cdot\boldsymbol{\gamma}_L; \; C_8 = \Gamma_2^L\gamma_R + \Gamma_2^R\gamma_L; \; \boldsymbol{C}_9 = \boldsymbol{\gamma}_R\Gamma_2^L + \boldsymbol{\gamma}_L\Gamma_2^R \tag{5.47}$$

We will explain the physical significance of each term in Eq. 5.41 in the next subsection.

To treat the interaction self-consistently, we also need the average charge and spin in the dot,

$$\langle \hat{d}_\alpha^\dagger \hat{d}_\beta \rangle \equiv n\delta_{\alpha\beta} + \boldsymbol{n}\cdot\boldsymbol{\sigma} \tag{5.48}$$

This is given by

$$\check{n} = \int \frac{d\epsilon}{2\pi} \check{G}\big((\Gamma_R + \mathbf{\Gamma}\cdot\boldsymbol{\sigma}) f^R(\epsilon) + (\Gamma_L - \mathbf{\Gamma}\cdot\boldsymbol{\sigma}) f^L(\epsilon)\big) \tag{5.49}$$

This can be rewritten in more detail as ($\boldsymbol{b} = \boldsymbol{B}/B$)

$$n = \int \frac{d\epsilon}{2\pi}\big((G_s\bar{G}_s + G_a\bar{G}_a)(\Gamma_R f^R(\epsilon) + \Gamma_L f^L(\epsilon)) + (\boldsymbol{b}\cdot\mathbf{\Gamma})(G_a\bar{G}_s + G_s\bar{G}_a)(f^R(\epsilon) - f^L(\epsilon)\big) \tag{5.50}$$

$$\begin{aligned}\boldsymbol{n} &= \int \frac{d\epsilon}{2\pi}\big(2\boldsymbol{b}(\boldsymbol{b}\cdot\mathbf{\Gamma})G_a\bar{G}_a + \mathbf{\Gamma}(G_s\bar{G}_s - G_a\bar{G}_a) + (\boldsymbol{b}\times\mathbf{\Gamma})i(G_a\bar{G}_s - G_s\bar{G}_a)\big)(f^R(\epsilon) - f^L(\epsilon))\\ &+ \boldsymbol{b}(G_a\bar{G}_s + G_s\bar{G}_a)(\Gamma_R f^R(\epsilon) + \Gamma_R f^R(\epsilon)\big)\end{aligned} \tag{5.51}$$

We substitute filling factors at vanishing temperature $f^{L,R} = \Theta(eV_{L,R} - \epsilon)$ and integrate over ϵ to obtain $n, \boldsymbol{n}$ and full current. It is also advantageous at this stage to switch to dimensionless variables measuring energy in units of Γ and setting $e = 1$. We introduce convenient functions

$$K^{\pm}_{R,L} = \frac{1}{2\pi}atan(2(V_{R,L} - \epsilon_d \pm B));\; L^{\pm}_{R,L} = \frac{1}{2\pi}ln(4(V_{R,L} \pm B)^2 + 1);\; L^{\pm} = L^{\pm}_R - L^{\pm}_L;\; K^{\pm} = K^{\pm}_R - K^{\pm}_L \tag{5.52}$$

With this,

$$n = \sum_{k=L,R} \Gamma_k(1/2 + K^+_k + K^-_k) + (\boldsymbol{b}\cdot\mathbf{\Gamma})(K^+ + K^-), \tag{5.53}$$

$$\begin{aligned}\boldsymbol{n} &= \boldsymbol{b}\big(\Gamma_R(K^-_R - K^+_R) + \Gamma_L(K^-_L - K^+_L)\big) + \frac{\mathbf{\Gamma}}{1+4B^2}\big(K^+ + K^- + B(L^- - L^+)\big)\\ &+ \frac{(\boldsymbol{b}\times\mathbf{\Gamma})}{2(1+4B^2)}\big(B(K^+ + K^-) + L^+ - L^-\big) + \frac{2\boldsymbol{b}(\boldsymbol{b}\cdot\mathbf{\Gamma})B}{1+4B^2}\big(4B(K^+ + K^-) + L^+ - L^-\big)\end{aligned} \tag{5.54}$$

The self-consistency equations then read:

$$\epsilon_d = Un;\; \boldsymbol{B} = \boldsymbol{B}_0 - U\boldsymbol{n} \tag{5.55}$$

$\boldsymbol{B}_0$ being the external magnetic field. This equation has to be solved at each $V_{R,L}$. With this solution, we can evaluate the current

$$\begin{aligned}I &= T_0(V_L - V_R)/\pi + 2(\Gamma_L\Gamma_R + \mathbf{\Gamma}^2)(K^+ + K^-) + 4((\mathbf{\Gamma}\cdot\boldsymbol{b})^2 - \mathbf{\Gamma}^2)\frac{B}{1+4B^2}\big(4B(K^+ + K^-) + L^+ - L^-\big)\\ &+ RX(L^+ + L^-) - IX(K^+ + K^-)/2\end{aligned} \tag{5.56}$$

Let us elaborate on the equilibrium case $V_R = V_L = \mu$. In this case, owing to time-reversibility, the spin-orbit interaction does not cause spin polarization and is irrelevant, so the self-consistency equations read ($\tilde{K} = K^R = K^L$)

$$\epsilon_d = U(1/2 + \tilde{K}^+ + \tilde{K}^-);\boldsymbol{B} = \boldsymbol{B}_0 - \boldsymbol{b}U(\tilde{K}_- - \tilde{K}_+) \tag{5.57}$$

We specify to $\boldsymbol{B}_0 = 0$ and determine the boundary of spontaneously magnetic phase where $B \to 0$. In this limit,

$$\tilde{K}_- - \tilde{K}_+ \to -B\frac{2}{\pi}\frac{1}{1+4(\mu^*)^2};\; \mu^* = \mu - \epsilon_d \tag{5.58}$$

with this, the equations for the boundary read

$$U = (1+4(\mu^*)^2)\frac{\pi}{2};\ \mu = \mu^* + U(1/2 + (1/\pi)arctan(2\mu^*)) \tag{5.59}$$

The splitting occurs above critical value $U_c = \pi/2$, at large U the magnetic phase occurs in the interval $\mu = (0, U)$ as it should be in this limit.

5.5.4. NORMAL TRANSPORT EXAMPLES

In this subsection, we will analyse the peculiarities of normal transport in the model at hand. We restrict ourselves to zero-voltage conductance and non-interacting case where zero-voltage conductance is simply given by T_{tot} at ϵ corresponding to Fermi level,

$$G(V_g) = \frac{G_Q}{2} T_{tot}(\epsilon = E_F). \tag{5.60}$$

Since E_1 is a linear function of the gate voltage, and shift of ϵ in Eq. 5.41 is equivalent to the shift of E_1, the energy dependence of T_{tot} directly gives the gate voltage dependence of the conductance. The conductance with interaction is qualitatively similar to the non-interacting one since the main effect of interaction in our model is the spin-splitting corresponding to $B \simeq U$.

5

Let us explain the physical significance of the terms in Eq. 5.41. All spin-orbit effects are incorporated into a single vector $\mathbf{\Gamma}$ in the spin space. To start with, let us neglect the spin-orbit interaction setting $\mathbf{\Gamma} = 0$, so we can disregard the third term. In this case, T_{tot} is contributed independently by spin orientations $\pm$ with respect to $\boldsymbol{B}$. Their contributions are shifted by $2B$ in energy.

The first term in Eq. 5.41 gives the featureless transmission of the transport channel and asymptotic value of the conductance at $|E_1| \gg \Gamma$. The second term describes the resonant transmission via the localized state and would show up even if there is no interference between the transmissions through the channel and the localized state. It rives rise to a Lorentzian peak - resonant transmission - of the width $\simeq \Gamma$ in conductance that splits into two at sufficiently big spin splitting $\simeq \Gamma$. Let us bring the fifth term into consideration. Since $G - \bar{G} = -i\Gamma G\bar{G}$ its energy dependence is identical to the second one. However, it usually gives a negative contribution to transmission describing destructive interference of the transmissions in the dot and in the channel - resonant reflection.

The fourth term describes the celebrated Fano effect coming about the interference of the resonant and featureless transmission. It is visually manifested as asymmetry of otherwise Lorentzian peaks or dips. The antisymmetric Fano tail $\propto \epsilon^{-1}$ at large distances from the peak/dip centre beats Lorentzian tail $\propto \epsilon^{-2}$. All these terms are hardly affected by spin-orbit interaction, while the second one manifests it fully. It mixes up spin channels and makes conductance to depend on the orientation of $\boldsymbol{B}$ with respect to $\mathbf{\Gamma}$.

We illustrate the possible forms of the energy (or, equivalently, gate-voltage) dependence of the conductance with the plots in Fig. 5.6 for 4 settings of the parameters $\Gamma_2^{L,R}, E_2, \kappa, \boldsymbol{\kappa}, \gamma_{L,R}, \boldsymbol{\gamma}_{L,R}$. Owing to separation of the scales assumed, the relevant parameters $\Gamma_{L,R}, \boldsymbol{\Gamma}, RX, IX$ are invariant with respect to rescale with the factor A,

$$\Gamma_2^{L,R}, E_2 \to A(\Gamma_2^{L,R}, E_2);\ \kappa, \boldsymbol{\kappa}, \gamma_{L,R}, \boldsymbol{\gamma}_{L,R} \to \sqrt{A}(\kappa, \boldsymbol{\kappa}, \gamma_{L,R}, \boldsymbol{\gamma}_{L,R}). \tag{5.61}$$

For all settings, energy is in units of the resulting Γ. For each setting, we give the plots at $B=0$ and $B=2\Gamma$, the latter to achieve a visible separation of resonant peculiarities. Spin-orbit interaction is weak except the last setting where we give separate plots for $\boldsymbol{B} \parallel \boldsymbol{\Gamma}$ and $\boldsymbol{B} \perp \boldsymbol{\Gamma}$.

For Fig. 5.6 (a) we choose $\Gamma_2^L, \Gamma_2^R, E_2 = A(0.2, 0.8, 0.5)$, $\kappa, \gamma_L, \gamma_R = \sqrt{A}(0.5, 0.2, 0.2)$, $\Gamma_1^L, \Gamma_1^R = 1.6, 3.5$. We also specify small but finite spin-orbit terms yet they hardly affect the conductance. In this case, the transmission through the localized state is faster than the interference with the transmission in the channel. This results in a resonant reflection peak at $B=0$ that splits into two upon increasing the magnetic field. A little Fano asymmetry can be noticed upon a close look.

For Fig. 5.6 (b) we choose $\Gamma_2^L, \Gamma_2^R, E_2 = A(0.5, 0.5, 0)$, $\kappa, \gamma_L, \gamma_R = \sqrt{A}(3.5, 0.2, 0.2)$, $\Gamma_1^L, \Gamma_1^R = 0.5, 0.5$. The transmission through the channel is ideal, $T_0 = 1$. The localized state is connected to the channel better than to the leads ($\kappa \gg \gamma_{L,R}$). This results in a pronounced resonant reflection dip at $B=0$ that also splits into two upon increasing the magnetic field.

For Fig. 5.6 (c) we choose $\Gamma_2^L, \Gamma_2^R, E_2 = A(0.2, 1.5, 0)$, $\kappa, \gamma_L, \gamma_R = \sqrt{A}(1.5, 0.3, 0.1)$, $\Gamma_1^L, \Gamma_1^R = 0.8, 0.1$. This choice is such that the competing processes of resonant transmission and reflection almost compensate each other so the resulting resonance peculiarity assumes almost antisymmetric Fano shape. The separation of the peculiarities upon the spin splitting is less pronounced than in the previous examples owing to long-range Fano tails mentioned.

We illustrate the effect of strong spin-orbit interaction in Fig. 5.6 (d). We choose $\Gamma_2^L, \Gamma_2^R, E_2 = A(0.2, 0.8, 0.5)$, $\kappa, \gamma_L, \gamma_R = \sqrt{A}(0.5, 0.2, 0.2)$, $\Gamma_1^L, \Gamma_1^R = 1.6, 3.5$. As to spin-dependent parameters, we choose $\boldsymbol{\kappa} = \sqrt{A}SO[0, 0.2, -0.6]$, $\boldsymbol{\gamma}_L = \sqrt{A}SO[0.3, 0, 0]$, $\boldsymbol{\gamma}_R = \sqrt{A}SO[0.0, 0, 1]$ and set the coefficient SO to 1.6, this is its maximal value that satisfies the positivity conditions imposed on the matrices of the rates. The peculiarity at $B=0$ is a peak with a noticeable Fano addition. It splits at $B=2\Gamma$ changing its shape, that is different for $\boldsymbol{B} \parallel \boldsymbol{\Gamma}$ and $\boldsymbol{B} \perp \boldsymbol{\Gamma}$ as well as for positive and negative energies. Note that owing to Onsager symmetry $G(\boldsymbol{B}) = G(-\boldsymbol{B})$.

We also provide an example with interaction implementing the self-consistent scheme described in the previous subsection (Fig. 5.7). For this example, we choose $\Gamma_2^L, \Gamma_2^R, E_2 = A(0.2, 1.5, -15)$, $\kappa, \gamma_L, \gamma_R = \sqrt{A}(0.8, 0.1, 0.1)$, $\Gamma_1^L, \Gamma_1^R = 1.1, 0.9$. This choice corresponds to very low channel transmission ($T_0 = 10^{-3}$). The average number of electrons in the dot is presented in Fig. 5.7(a) as a function of E_1 for several interaction strengths, at zero voltage difference and magnetic field. All curves change from full occupation at big negative E_1 to zero occupation at big positive E_1. At $U=0$ and $U=\Gamma$ the curves are smooth with no spontaneous spin splitting emerging throught the whole interval of E_1. For higher interaction strengths, there is an interval of E_1 where the spontaneous splitting is present. The ends of this interval are in principle manifested by cusps in the curves. Only cusps at the end of the interval close to zero are visible, the cusps at the other end are too small. It

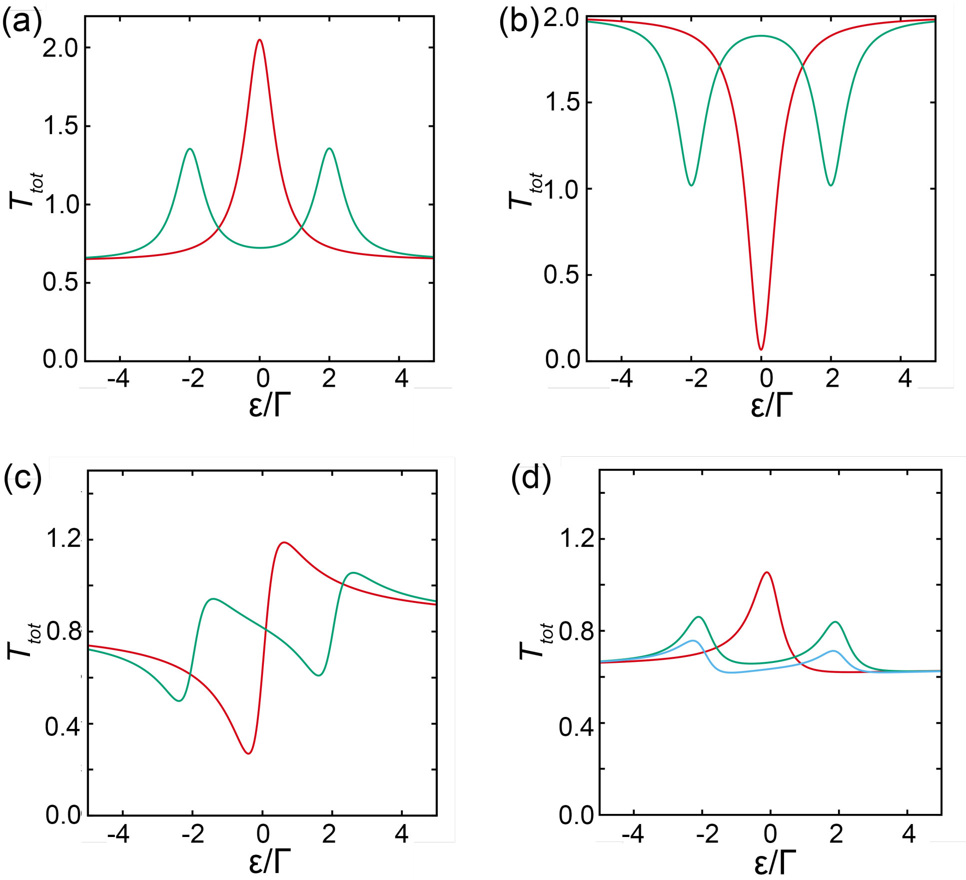

Figure 5.6: Examples of normal transport. The energy dependence of T_{tot} is the same as the conductance dependence on the gate voltage. Red curves correspond to $B=0$, green curves to $B=2\Gamma$. a. Basic example: resonant transmission b. Dip: resonant reflection c. Fano. d. Strong spin-orbit. Here, green (blue) curve is for parallel (perpendicular) orientation of $\boldsymbol{B}$ with respect to $\boldsymbol{\Gamma}$.

might seem that the zero-voltage conductance (Fig. 5.7 (b)) can be computed from T_{tot} at the parameters $\tilde{E}_1, \tilde{B}$ that solve the self-consistency equation at zero voltage difference. However, this is not so, since these parameters also depend on voltage difference. We compute zero-voltage conductance by numerically differentiating the current (Eq. 5.56) at small voltage differences. At zero interaction, we see a resonant transmission peak. Its height does not reach G_Q because of the asymmetry $\Gamma_R \neq \Gamma_L$. At $U=\Gamma$, there is still a single peak. At higher U we see the splitting of the peak. The height of the peaks split is a half of the height of the original peak if they are sufficiently separated. As we have conjectured earlier, this is qualitatively similar to the conductance traces where spin splitting is induced by the magnetic field.

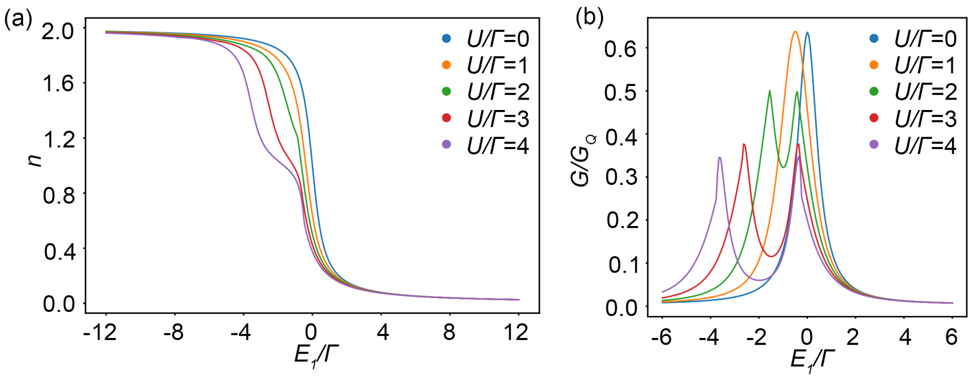

Figure 5.7: Example of normal transport with interaction. Resonant transmission regime, no magnetic field, no SO coupling. The setup parameters are given in the text. a. The average number of electrons in the localized state versus E_1 at various interaction strengths. b. Zero-voltage conductance versus E_1 at various interaction strengths.

5.5.5. SUPERCONDUCTING TRANSPORT

In this subsection, we elaborate on the description of superconducting transport in our model. Since supercurrent is a property of the ground state of the system, it is convenient to work with electron Green functions in imaginary time and introduce Nambu structure. Let us start, as we did previously, with an arbitrary number of dots and superconducting leads. If we neglect tunnel couplings, the inverse Green function $\mathscr{H}(\epsilon)$ is a 8×8 matrix encompassing the spin index, Nambu index and that labelling the dots. It reads:

$$\check{\mathscr{H}} = i\epsilon\tau_z - \check{H}. \tag{5.62}$$

The tunnel couplings to the leads labelled by a add the self-energy part

$$\check{\mathscr{H}} = i\epsilon\tau_z - \check{H} + \frac{i}{2}\sum_a \check{\Gamma}_a \check{Q}_a \tag{5.63}$$

where $\check{\Gamma}_a$ are given by Eq. 5.18 and the matrix $\check{Q}_a$ is a matrix in Nambu space reflecting the properties of the superconducting lead a,

$$Q_a = \frac{1}{\sqrt{\epsilon^2+\Delta_a^2}}\begin{bmatrix} \epsilon & \Delta_a e^{i\phi_a} \\ \Delta_a e^{-i\phi_a} & -\epsilon \end{bmatrix}, \tag{5.64}$$

$Q_a^2 = 1$.

To find supercurrents, we need to evaluate the total energy and take its derivatives with respect to the phase differences. Since the leads with different phases are connected by the dots, the phase-dependent energy is the energy of the dots. The latter can be expressed as

$$\mathscr{E} = -\frac{1}{2}\int \frac{d\epsilon}{2\pi} \ln\det(\check{\mathscr{H}}) \tag{5.65}$$

To see how this works, let us check this formula neglecting tunnel couplings. With this, the energy is the sum over eigenvalues of $\check{H}$, E_n,

$$\mathscr{E} = -\frac{1}{2}\int \frac{d\epsilon}{2\pi} \ln(\epsilon^2 + E_n^2) \tag{5.66}$$

The integral formally diverges at $\epsilon \to \infty$. To regularize it, we subtract its value at $E_n = 0$ to obtain

$$\mathscr{E} = -\sum_n \frac{|E_n|}{2} + const \tag{5.67}$$

To recover a familiar formula, we shift the constant by $\mathrm{T}r(\check{H})/2$,

$$\mathscr{E} = -\sum_n \frac{|E_n|}{2} + \sum_n \frac{E_n}{2} + const = \sum_n E_n \Theta(-E_n) + const, \tag{5.68}$$

so it becomes the energy of the filled states (those with $E_n < 0$). This suggests that we need to handle the integral with care keeping eye on possible problems at big ϵ. Fortunately, no special care has to be taken for the phase-dependent energy since it is accumulated at superconducting gap scale $\epsilon \simeq \Delta$. We have to be careful when expressing the occupation of the dots in terms of derivatives of $\mathscr{E}$ with respect to dot energies (as we do for numerical calculations). For instance, the average occupation of the dot 1 reads

$$\langle \hat{n}_1 \rangle = \frac{\partial \mathscr{E}}{\partial E_1} + 1, \tag{5.69}$$

the last term correcting for high-energy divergences.

For our starting two-dot, two-lead model, the inverse Green function reads (c.f. with Eq. 5.29).

$$\mathscr{H} = \begin{bmatrix} \mathscr{H}_{11} & \mathscr{H}_{12} \\ \mathscr{H}_{21} & \mathscr{H}_{22} \end{bmatrix} \tag{5.70}$$

, where

$$\mathscr{H}_{11} = i\epsilon\tau_z - E_1 - (\boldsymbol{B}_1 \cdot \check{\boldsymbol{\sigma}})\tau_z + \frac{i}{2}(\Gamma_1^R \check{Q}_R + \Gamma_1^L \check{Q}_L);\ \mathscr{H}_{22} = i\epsilon\tau_z - E_2 - (\boldsymbol{B}_1 \cdot \check{\boldsymbol{\sigma}})\tau_z + \frac{i}{2}(\Gamma_2^R \check{Q}_R + \Gamma_2^L \check{Q}_L); \tag{5.71}$$

$$\mathscr{H}_{12} = -\check{\kappa} + \frac{i}{2}\{\check{\gamma}_L \check{Q}_L + \check{\gamma}_R \check{Q}_R\};\ \mathscr{H}_{21} = -\check{\kappa}^\dagger + \frac{i}{2}\{\check{\gamma}_L^\dagger \check{Q}_L + \check{\gamma}_R^\dagger \check{Q}_R\}, \tag{5.72}$$

and we turn back to the compact notations

$$\check{\kappa}, \check{\kappa}^\dagger = \kappa \pm i\boldsymbol{\kappa} \cdot \boldsymbol{\sigma};\ \check{\gamma}_{L,R}, \check{\gamma}_{L,R}^\dagger = \gamma_{L,R} \pm i\boldsymbol{\gamma}_{\boldsymbol{L},\boldsymbol{R}} \cdot \boldsymbol{\sigma} \tag{5.73}$$

and made use of Q matrices corresponding to two leads

$$\check{Q}_{L,R} = \frac{1}{\sqrt{\epsilon^2+\Delta^2}}\begin{bmatrix} \epsilon & \Delta e^{i\phi_{L,R}} \\ \Delta e^{-i\phi_{L,R}} & -\epsilon \end{bmatrix}. \tag{5.74}$$

Next goal is to reduce the number of parameters implementing the separation of scales mentioned and implemented for the normal transport. This is achieved by the following transformation of the determinant

$$\ln\det(\check{\mathscr{H}}) = \ln\det(\check{\mathscr{H}}_{11} - \check{\mathscr{H}}_{12}\check{\mathscr{H}}_{22}^{-1}\check{\mathscr{H}}_{21}) + \ln\det(\check{\mathscr{H}}_{22}) \tag{5.75}$$

and implementing $E_2, \Gamma_2 \gg \gamma, \kappa \gg \epsilon, B_2, E_1, \Gamma_1$.

Let us first evaluate $\det(\check{\mathscr{H}}_{22})$, which is that of a 4×4 matrix with spin structure taken into account. Since we may assume $\epsilon, B_2 \ll \Gamma_2, E_2$ the spin structure is trivial and the answer reads

$$\ln\det(\check{\mathscr{H}}_{22}) = 2\ln(E_2^2 + \frac{1}{4}\Gamma_2^2) + 2\ln(1 - T_0\frac{\Delta^2}{\Delta^2+\epsilon^2}\sin^2\phi/2), \tag{5.76}$$

where, as previously, we define $\Gamma_2 = \Gamma_2^L + \Gamma_2^R$ and $T_0 = \Gamma_2^L\Gamma_2^R/(E_2^2 + \frac{1}{4}\Gamma_2^2)$.

The energies of Andreev levels are determined from zeros of this determinant. We recover the well-known expression for the energy of the spin-degenerate Andreev level in a contact with transparency T_0,

$$E_{Andr} = \Delta\sqrt{1 - T_0\sin^2(\phi/2)} \tag{5.77}$$

The integration of the log of the determinant over the energy gives the expected result for the energy of the ground state,

$$\mathscr{E} = -E_{Andr} \tag{5.78}$$

Let us turn to evaluation of the rest of the expression. We note that

$$\check{\mathscr{H}}_{22}^{-1} = -\frac{E_2 + \frac{i}{2}(\Gamma_{2R}\check{Q}_R + \Gamma_{2L}\check{Q}_L)}{\left(E_2^2 + \frac{\Gamma_2^2}{4}\right)(1 - T_0 s)} \tag{5.79}$$

where we have introduced a convenient compact notation

$$s \equiv \frac{\Delta}{\sqrt{\Delta^2+\epsilon^2}}\sin^2(\phi/2) \tag{5.80}$$

The matrix in the first determinant thus contains a factor $(1 - T_0 s)$ in the denominator. Multiplying with this factor cancels $\det(\check{\mathscr{H}}_{22})$ so the whole expression can be reduced to the following relatively simple form

$$\ln\det(\check{\mathscr{H}}) = \tag{5.81}$$

$$\ln\det\Big((1-T_0 s)(i\epsilon\tau_z - E_1 - (\boldsymbol{B}\cdot\check{\boldsymbol{\sigma}})\tau_z) + \Delta E + s\Delta E_S + \frac{i}{2}(\Gamma^R(s)\check{Q}_R + \Gamma^L(s)\check{Q}_L) + \frac{i}{4}\boldsymbol{\Gamma}\cdot\check{\boldsymbol{\sigma}}(\check{Q}_L\check{Q}_R - \check{Q}_R\check{Q}_L)\Big)$$

where

$$\Gamma^{L,R}(s) = \Gamma^{L,R} + s\Gamma_S^{L,R}. \tag{5.82}$$

The parameters $\Gamma_{L,R}$, ΔE, $\mathbf{\Gamma}$ have been already defined in our consideration of normal transport. The compact description of superconducting transport brings three additional parameters

$$\Delta E_S = \frac{-E_2 C_7 + \kappa C_8 + \boldsymbol{\kappa}\cdot\boldsymbol{C}_9}{E_2^2+\Gamma_2^2/4};\ \Gamma_S^L = -T_0\Gamma_1^L + \frac{\Gamma_R(\gamma_L^2+\boldsymbol{\gamma}_L^2)}{E_2^2+\Gamma_2^2/4};\ \Gamma_S^R = -T_0\Gamma_1^R + \frac{\Gamma_L(\gamma_R^2+\boldsymbol{\gamma}_R^2)}{E_2^2+\Gamma_2^2/4}. \tag{5.83}$$

Here, ΔE_S is a part of the expression (5.45) for RX but is an independent parameter.

Since both normal and superconducting transport originate from the same scattering matrix, there are many examples when the parameters characterizing the superconducting transport can be directly determined from the results of normal transport measurements, a single channel with transparency T_0 being the simplest one. The presence of the additional parameters ΔE_S, $\Gamma_S^{L,R}$is therefore rather disappointing: we cannot predict superconducting transport exclusively from the results of normal transport measurements and have to rely on model assumptions.

Let us outline the physical meaning of the overall structure of the expression (5.81). The first term is a product of the terms whose zeros give the Andreev level in the transport channel and energy level in an isolated localized state, the product indicate that these levels are independent. The rest of the terms thus describe the hybridization of these levels. Note that the terms with ΔE cannot be cancelled by a shift of E_1, so in distinction from the normal case, are active in the presence of superconductivity. The terms with $\Gamma(s)$ are similar to tunnel decay terms in Eq. 5.71, in distinction from normal case the presence of the second dot does not just renormalize Γ. The last term describes spin-orbit effect and is proportional to the same vector $\mathbf{\Gamma}$ as in the normal case. In distinction from all other terms, it is odd in the phase difference since it is proportional to the commutator of two $\check{Q}$. The combination of this term and that with magnetic field results in a shift of the minimum of the phase-dependent energy from 0 or π positions.

5.5.6. NUMERICAL DETAILS

In this subsection, we provide the overall strategy and details of our numerical calculations.

We postpone the discussion of self-consistency assuming that we already know E_1 and $\boldsymbol{B}$. To find the phase-dependent energy, we have to integrate the log of the determinant over ϵ. We compute directly the determinant of 8×8 matrices implementing the difference of scales numerically. For quick computation at each energy, we represent the matrix $\check{\mathcal{H}}$ as a sum over various scalar functions of ϵ,

$$\check{\mathcal{H}} = \check{A} + \epsilon\check{B} + \frac{\epsilon}{\sqrt{\epsilon^2+\Delta^2}}\check{C} + \frac{\Delta}{\sqrt{\epsilon^2+\Delta^2}}\check{D}(\phi_L,\phi_R) \tag{5.84}$$

where the matrices $\check{A}-\check{D}$ do not depend on ϵ and only $\check{D}$ depends on the superconducting phase. We define the function of ϵ as $\log(\det(\check{\mathscr{H}}(\epsilon,\phi=0))-\log(\det(\check{\mathscr{H}}(\epsilon,\phi=0))$ and integrate using scipy.quad. Direct evaluation of the sum over discrete equidistant ϵ the interval of the order of 5Δ provides comparable numerical efficiency and accuracy.

As mentioned, we treat interaction self-consistently, as the interaction-induced shift in E_1 and $\boldsymbol{B}$. The self-consistency equations read as

$$\tilde{E}_1 = E_1 + Un(\tilde{E}_1, \tilde{\boldsymbol{B}});\ \tilde{\boldsymbol{B}} = \boldsymbol{B} - U\boldsymbol{n}(\tilde{E}_1, \tilde{\boldsymbol{B}}) \tag{5.85}$$

,where the average number of particles on the dot are given by derivatives of the total energy $N = (\partial_{E_1}\mathscr{E} + 1)$ and $\boldsymbol{n} = \partial_{\boldsymbol{B}_1}\mathscr{E}$. We compute these derivatives integrating the analytical derivatives of $\det(\check{\mathscr{H}}(\epsilon)$ over ϵ. These integrals may converge at $\epsilon \gg \Delta$ provided $E_1, \boldsymbol{B} \gg \Delta$. An adaptive grid of discrete ϵ could be chosen to speed up the evaluation, yet using scipy.quad suffices for our purposes.

To solve the self-consistency equations, we implement a root-finding minimization algorithm minimizing the function $F = f^2 + |\boldsymbol{f}|^2$, where $f, \boldsymbol{f}$ are defined as

$$f = \tilde{E}_1 - E_1 - Un(\tilde{E}_1, \tilde{\boldsymbol{B}});\ \boldsymbol{f} = \tilde{\boldsymbol{B}} - \boldsymbol{B} + U\boldsymbol{n}(\tilde{E}_1, \tilde{\boldsymbol{B}}), \tag{5.86}$$

and checking if the minimum is achieved at $F = 0$. Alternatively, we can make use of the fact that the solutions of the self-consistency equations correspond to the extrema of the following energy functional

$$E_T(\tilde{E}_1, \tilde{\boldsymbol{B}}) = \mathscr{E}(\tilde{E}_1, \tilde{\boldsymbol{B}}) - \frac{(E_1 - \tilde{E}_1)^2}{2U} + \frac{(\boldsymbol{B} - \tilde{\boldsymbol{B}})^2}{2U} \tag{5.87}$$

Unfortunately, this energy function is not bounded, and the extrema required are rather saddle points than minima. However, they can be found, for instance, by maximization of the function in $\tilde{E}_1$ and subsequent minimization in $\tilde{\boldsymbol{B}}$.

The Andreev bound states are given by the zeros of the determinant at imaginary ϵ (thus real energy $E = i\epsilon$) in the interval $(0, \Delta)$. We find these roots by minimizing $\det(\check{\mathscr{H}}(\epsilon))^2$ and checking if the minimum is achieved at zero. but because of the different scales in the problem and existence of a big scale, we first try to find an equivalent matrix, the determinant of which is more efficiently minimized numerically. Typically, there are multiple Andreev states, so we subdivide the interval $(0, \Delta)$ to find them all.

5.5.7. SUPERCONDUCTING TRANSPORT EXAMPLES

In this subsection, we present the examples of numerical evaluation of supercurrent and Andreev state energies in our model, for 3 sets of parameters. The π state is achieved if $E_T(\phi = \pi) - E_T(\phi = 0) \equiv E_\pi < 0$. Contrary to our initial expectations, it is rather difficult to achieve such inversion for an arbitrary parameter set at high transmission T_0. It is rather easy to find $0-\pi$ transitions at low T_0. The following examples provide interesting illustrations of rich physics captured by the model.

In this subsection and in all plots, we measure the energies, decay rates and the current $I/2e$ in units of Δ.

Example A. (Fig. 5.8) Here, we disregard spin-orbit coupling and interaction. The parameters are $\Gamma_2^L, \Gamma_2^R, E_2 = A(1.9, 1.9, -2)$, $\kappa, \gamma_L, \gamma_R = \sqrt{A}(0.4, 0.1, 0.1)$, $\Gamma_1^L, \Gamma_1^R = 1.2, 0.9$ and correspond to $T_0 = 0.47$, $\Gamma_L = 1.3, \Gamma_R = 0.96, \Gamma = 2.26$. As we can see from the normal conductance traces presented in Fig. 5.8e, for this parameter set we have the resonant transmission accompanied by very weak Fano asymmetry. The resonant transmission peak splits upon increasing the magnetic field.

Actually, this set illustrates an unsuccessful attempt to achieve a pair of $0-\pi$ transitions. This is seen from the plots in Fig. 5.8a that give the (gate-voltage) traces of E_π at various magnetic fields. Zero-field trace peaks near the centre of conductance peak indicating the enhancement of supercurrent upon increasing the transmission, and saturates at finite value at $|E_1| \gg 1$: this saturation is achieved for all magnetic fields. Upon increasing the magnetic field the value of E_T near the resonance gets down. It becomes smaller than the saturated value at $B > 0.8$. It seems it has a chance to pass zero manifesting $0-\pi$ transitions. However, this does not happen: the tendency changes and the minimum of E_T starts to increase at $B > 1.5$. Prominent features in the plots are sharp cusps in energy dependence. They indicate the crossings of Andreev states with zero energy that, for the features in this plot, are located at $\phi = \pi$ and corresponding gate voltages.

Let us set $E_1 = 0$ and look at the phase dependence of energy (Fig. 5.8b) for a set of magnetic fields. Here we also see the cusps corresponding to the crossings at certain values of the phase. Superconducting currents plotted in Fig. 5.8c are obtained by numerical differentiation of the energy, so the cusps become jumps, the discontinuities of the current. The zero-field curve is prominently non-sinusoidal as expected for high transmission at this value of E_1. The current becomes smaller tending to almost sinusoidal curve at high magnetic fields upon increasing magnetic field, but does not get inverted. At intermediate fields, the current jumps between non-sinusoidal and sinusoidal curve.

In Fig. 5.8d we show the phase dependence of ABS energies for $E_1 = 0$ and $|B_1| = 1$. We see four spin-split ABS counting from down up. Eventually, the picture of ABS demonstrates little interference between the transport channel and the localized state. The third and the fourth curves are close to E_{Andr} for $T_0 = 0.47$ and are thus associated with the transport channel, their spin-splitting $\simeq 0.1$ is small coming from the interference. The first and the second state are associated with the dot. The spin splitting is thus big: the first curve looks like the second curve shifted by $\simeq 1$ downwards, with the part shifted to negative energy being flipped to positive ones. This also explains sharp cusps in the first curve.

Although in our model the phase-dependent energy is not a minus half-sum of ABS energies as it would be for energy-independent transmission, we can use this sum for qualitative estimations. With this, the half-sum of the first and second energies would result in an inverted supercurrent, but the half-sum of the third and fourth states, that is, the contribution of the transport channel, adds to the balance a usual supercurrent of slightly bigger amplitude.

Example B. (Fig. 5.9) This inspired us to check if the $0-\pi$ transitions can be achieved at very low transmission of the transport channel. We have taken the following set of parameters $\Gamma_2^L, \Gamma_2^R, E_2 = A(0.2, 1.5, -15)$, $\kappa, \gamma_L, \gamma_R = \sqrt{A}(0.8, 0.1, 0.1)$, $\Gamma_1^L, \Gamma_1^R = 1.1, 0.91$. For this choice, $T_0 \simeq 10^{-3}$ $\Gamma_L = 1.1, \Gamma_R = 0.91, \Gamma = 2.01$. The normal conductance traces (Fig. 5.9d) show a classical scenario of resonant transmission

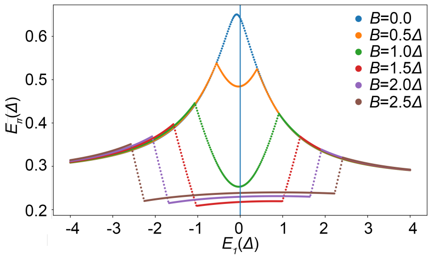

(a) $E_\pi \equiv E_T(\phi = \pi) - E_T(\phi = 0)$ versus E_1 at several values of magnetic field.

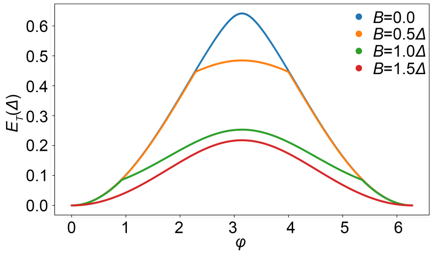

(b) The phase-dependent part of energy $E_T \equiv E_T(\phi) - E_T(\phi = 0)$ at $E_1 = 0$ and several values of magnetic field.

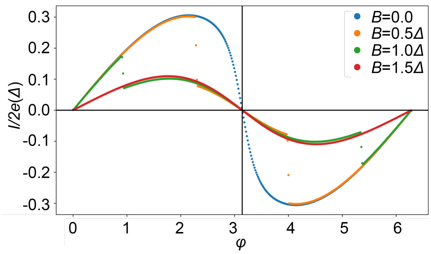

(c) The phase dependence of the superconducting current at $E_1 = 0$ for several values of B.

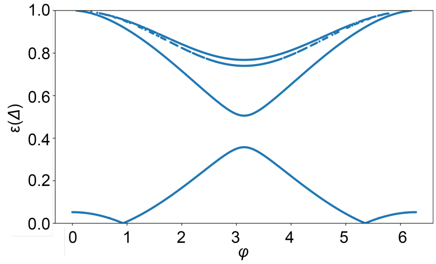

(d) The phase dependence of ABS energies at $E_1 = 0$ and $|B| = 1$.

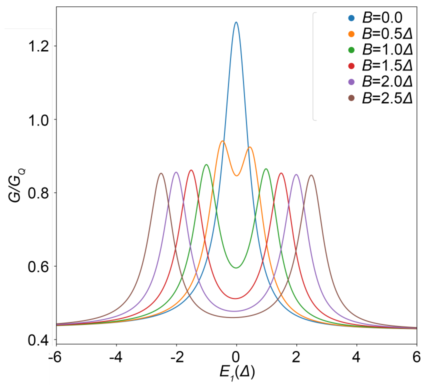

(e) Normal zero-voltage conductance versus E_1 at several values of magnetic field.

Figure 5.8: Example A. Resonant transmission, moderate channel transmission. No SO coupling.

that saturates to almost zero far from the resonance.

The check was successful. We plot the traces of $E_T \equiv E_T(\phi = \pi) - E_T(\phi = 0)$ for various magnetic fields in Fig. 5.9a. The traces look like those in Fig. 5.8a except the shift downwards by $\simeq 0.25$. Owing to this, E_T is negative for $B > 0.8$ in an interval of gate voltages that increases with B, $0-\pi$ transitions are at the ends of the interval.

We plot the phase dependence of the supercurrent for $|B| = 2$ and various E_1 in Fig. 5.9b. The $0-\pi$ transitions at this field take place at $E_1 \approx \pm 1.25$. In accordance with this, the almost sinusoidal curves at $E_1 = -2.5, 2$ are of positive amplitude while those at $E_1 = 0, -1$ are of negative one. Note a rather low value $\simeq 0.02$ of the maximum "negative" current, almost 25 times smaller than the maximum value of the current in a single transport channel. An interesting curve is found close to the transition, at $E_1 = -1.5$. Here, the current jumps between sin-like curves of positive and negative amplitude. The total integral of the current between 0 and π is still positive, so $E_\pi > 0$.

An example of the phase dependence of ABS energies is given in Fig. 5.9c. Since the transmission of the channel is very low, we see only two spin-split ABS. The upper one is close to the gap edge, and eventually merges with continuous spectrum at $\phi \approx 0.6, 2\pi - 0.6$. The lower one is close to zero, and exhibits two zero crossings at $\phi \approx \pi \pm 0.65$ corresponding to the discontinuities in corresponding curve in Fig. 5.9b.

The example presented concerns practically zero background transmission, which is not experimental situation. The Fig. 5.4 in the main text presents the results at small but finite transmission $T_0 \approx 0.3$.

Example C. (Figs. 5.10, 5.11) In this example, we illustrate the effect of SO coupling on the superconducting transport. We choose $\Gamma_2^L, \Gamma_2^R, E_2 = A(1.2, 1.5, -1)$, $\kappa, \gamma_L, \gamma_R = \sqrt{A}(0.2, 0.6, 0.2)$, $\Gamma_1^L, \Gamma_1^R = 1.6, 3.5$. As to spin-dependent parameters, we choose $\boldsymbol{\kappa} = \sqrt{A}SO[0, 0.8, 0]$, $\boldsymbol{\gamma}_L = \sqrt{A}SO[0, 0.2, 0]$, $\boldsymbol{\gamma}_R = \sqrt{A}SO[0, 0.1, 0]$ with $SO = 1$ that gives $T_0 = 0.64, \Gamma_L = 1.1, \Gamma_R = 1.38, \Gamma = 2.48$ and a significant $\boldsymbol{\Gamma} = 0.45\boldsymbol{y}$. As we see from the Figs. 5.10d, 5.11d that give the traces of normal conductance, this set also illustrates a well-developed Fano resonance with antisymmetric features split in sufficiently high magnetic field.

We consider first $\boldsymbol{B} \perp \boldsymbol{\Gamma}$. In this case, the time-reversibility provides the symmetry $\phi \leftrightarrow -\phi$ that was present in all previous plots. Let us concentrate at the $0-\pi$ energy difference (Fig. 5.10a). The curve at zero magnetic field qualitatively follows the normal conductance. Upon increasing the magnetic field we see the multiple cusps that are already familiar from Figs. 5.8, 5.9 and indicate the spin splitting and eventual zero crossing of ABS. The shape of the trace becomes more complex, and the minimum E_T becomes smaller. However, it does not reach zero that is necessary for $0-\pi$ transition.

The phase dependence of superconducting current at $B = 2$ and various E_1 is presented in Fig. 5.10b. Most curves display pronounced discontinuities manifesting the zero crossings at corresponding phases. Except for this, the dependence is rather sinusoidal corresponding to moderate transmission. It looks like the current jumps between two sin-like curves of different amplitudes.

It is interesting to see 3 ABS in the plot presenting the phase dependence of ABS energies for $E_1 = -1.5$ and $B = 2$ (Fig. 5.10c). The fourth state is either shifted over

5

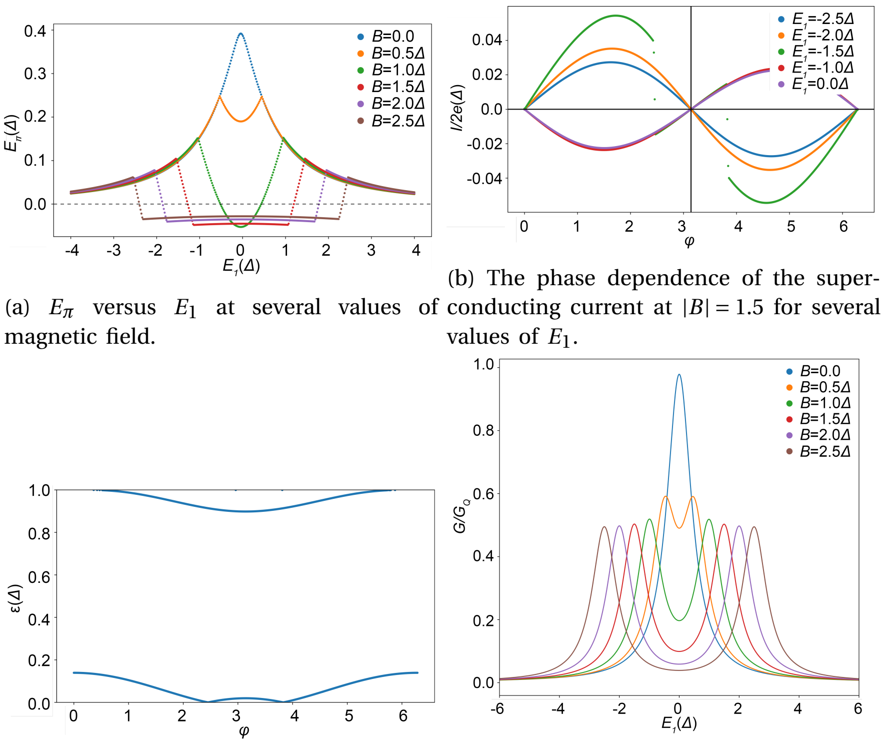

(a) E_π versus E_1 at several values of magnetic field.

(b) The phase dependence of the superconducting current at $|B| = 1.5$ for several values of E_1.

(c) The phase dependence of ABS energies at $E_1 = -1.5$ and $|B| = 1.5$.

(d) Normal zero-voltage conductance versus E_1 at several values of magnetic field.

Figure 5.9: Example B. Resonant transmission, low channel transmission. No SO coupling. A pair of $0-\pi$ transitions occurs at $|B| > 0$.

the gap edge to the continuous spectrum or is present very close to the edge so we cannot resolve it with accuracy of our numerics. The lowest state displays the familiar zero crossings corresponding to the current jumps.

When we change from perpendicular to parallel field (Fig. 5.11) we do not see much change in normal conductance: the difference between the corresponding traces in Figs. 5.11d and 5.10d does not exceed 10 % . This is explained by the fact that the effect is of the second order in $\mathbf{\Gamma}$, $\propto \mathbf{\Gamma}^2/\Gamma^2$, and $|\mathbf{\Gamma}|/\Gamma \simeq 0.2$ is not so big. We also do not see much changes in E_T traces (Fig. 5.10a versus Fig. 5.11a).

The most prominent effect of SO coupling is the breaking of $\phi \leftrightarrow -\phi$ symmetry in magnetic field, the effect $\propto |\mathbf{\Gamma}|/\Gamma$ at $B \simeq \Gamma$. We see this in Fig. 5.11b where the current-phase dependencies for $B = 2$ are now shifted sin-like curves with jumps. The values of the shift vary from trace to trace, also in sign, and are $\simeq 0.2 - 0.3$. In addition to the shifts of the sin-like curves, the positions of jumps are shifted non-symmetrically, these shifts are $\simeq 0 - 0.5$.

Non-symmetry of the phase dependence of ABS energies is clearly seen in Fig.

5.11c that is done at the same parameters as Fig. 5.10c. Also, beside shift, the energy first ABS is significantly affected by the direction of the magnetic field. A fine detail is the crossing of the second and the third ABS near $\phi \approx 1$. It may seem that in the presence of SO coupling all level crossings shall be avoided, since spin is not a good quantum number. However, since $\boldsymbol{\Gamma}$ is the only spin vector in our model, for the particular case $\boldsymbol{B} \parallel \Gamma$ the projection of spin on $\boldsymbol{B}$ is a good quantum number and the levels of different projections may cross.

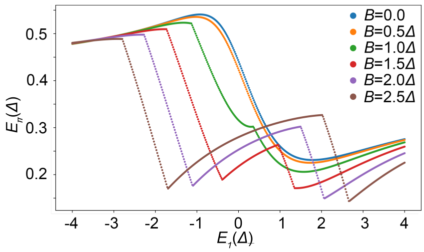

(a) E_π versus E_1 at several values of magnetic field.

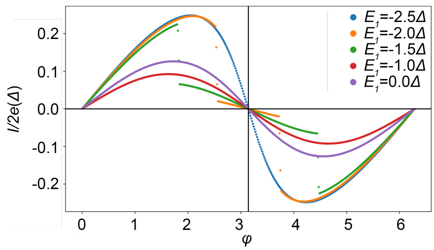

(b) The phase dependence of the superconducting current at $B = 2$ for several values of E_1.

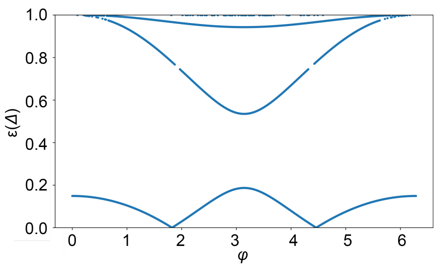

(c) The phase dependence of ABS energies at $E_1 = -1.5$ and $B = 2$.

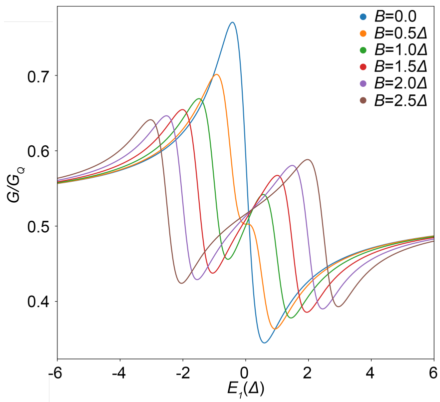

(d) Normal zero-voltage conductance versus E_1 at several values of magnetic field.

Figure 5.10: Example C. Well-developed Fano features, moderate SO coupling. Magnetic field $\boldsymbol{B} \perp \boldsymbol{\Gamma}$

5.5.8. CONCLUSIONS THEORY PART

To conclude, we have developed and presented a model that accurately describes normal and superconducting transport for a situation where a high transmission in a transport channel is accompanied by propagation via a resonant localized state. The motivation came from the experimental observation of a pair of $0-\pi$ transitions separated by a small interval in the gate voltage, and the model explains the main

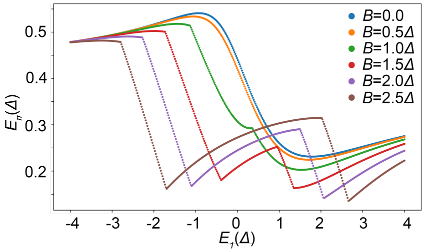

(a) E_π versus E_1 at several values of magnetic field.

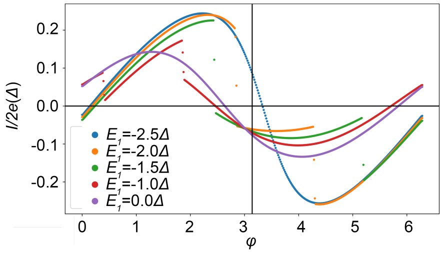

(b) The phase dependence of the superconducting current at $B = 1.5$ for several values of E_1.

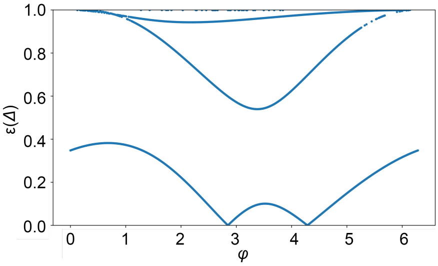

(c) The phase dependence of ABS energies at $E_1 = -2$ and $|B| = 2$.

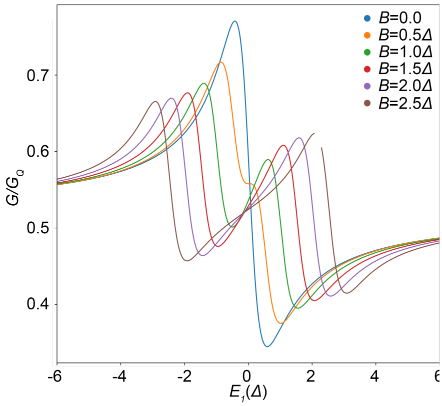

(d) Normal zero-voltage conductance versus E_1 at several values of magnetic field.

Figure 5.11: Example C. Well-developed Fano features, moderate SO coupling. No interaction. Magnetic field $\boldsymbol{B} \parallel \boldsymbol{\Gamma}$. Pronounced asymmetry in ϕ.

features observed at semi-quantitative level. In addition, we gave several examples not immediately related to the experiment to illustrate the rich parameter space of the model. The accurate characterization of normal transport in the experimental setups to choose the model parameters and taking into account more resonant states should bring the agreement between experiment and theory to quantitative level.

5.6. METHODS

5.6.1. DATA SELECTION

Our experimental data provides the evidence of magnetic field-driven $0-\pi$ transitions and π-shifted supercurrent inside narrow intervals of the electro-chemical potential of a hybrid nanowire JJ. The presented intervals of V_{G1} were identified in rough gate sweeps at high parallel fields $B_z = [600, 700]$ mT by detecting π-shifted oscillations of the SQUID switching current. These V_{G1} intervals were subsequently investigated in high resolution - both at high and low B_z-fields. At $B_z = 0\,\text{mT}$, qualitatively different scenarios - with and without π shifts - were observed, as illustrated in Fig. 5.2 and Fig. 5.3. Besides the V_{G1} intervals in these figures, there were also few other V_{G1} intervals with π-shifted supercurrent at high B_z-fields and evolution similar to Fig. 5.2 and Fig. 5.3. Importantly, in the rough gate sweeps at high parallel fields, we also detected many narrow V_{G1} intervals in which supercurrent was sharply modulated without π shifts. Due to the absence of striking π shifts, these intervals were not further examined in high resolution and at low parallel fields. Relatively low occurrence of π shifts at high parallel fields is in agreement with the findings of our theoretical model in which π-shifted supercurrent is not generically obtained for large Zeeman energies.

Oscillations of the SQUID switching current were observed at fields exceeding $B_z = 1\,\text{T}$. However, the reliability of detecting switches in $V - I_b$ traces by the setup for fast switching current measurements was considerably lower for $B_z > 750\,\text{mT}$ - due to less sharp switches in V. Therefore, I_{sw} could be reliably and efficiently measured up to $B_z \sim 720\,\text{mT}$.

5.6.2. MEASUREMENT SETUP

All transport measurements are performed at $\sim 20\,\text{mK}$ base temperature inside a dilution refrigerator equipped with a vector magnet.

The conductance measurement in Fig. 5.2(a) is performed in a two-terminal setup with standard lock-in configuration. A voltage-source sets a dc-bias voltage V_b between the source and drain, and a current-meter measures a dc-current I through the device. A lock-in amplifier sets an ac-bias voltage dV_b which amplitude is $10\,\mu\text{V}$, and measures the ac-current dI. Values of the bias voltages are corrected for a serial resistance $R_s = 8.89\,\text{k}\Omega$ as $V_b \to V_b - IR_s$ and $dV_b \to dV_b - dIR_s$. The R_s includes the resistance of the voltage-source and the current-meter amplifier, the resistance of two fridge lines and the resistance of low-pass filters in the circuits.

The switching current measurements are performed in a four-terminal setup in which two terminals are connected to a current-source setting a bias current I_b, and the other two terminals are connected to a voltmeter measuring a voltage drop V across the device. Depending on the way how I_b is ramped, either a slow or a fast method for switching current measurement is used. When using the slow method, I_b is swept in steps of $20 - 40\,\text{pA}$, and V is recorded for each I_b. Switching current can then be extracted from the recorded $V - I_b$ traces. The slow method was used for the 2D-maps in Fig. 5.1(b).

A scheme of the setup for fast switching current measurements is shown in Fig. 5.12(a) and time traces of relevant signals are shown in Fig. 5.12(b) - for a single measurement period. This setup was used for collecting the data corresponding to the I_{sw} data in the main text - red traces in Fig. 5.1(b), Fig. 5.2(b)-(c) and Fig. 5.3. The current source is controlled by an arbitrary-waveform generator (AWG) applying a sawtooth waveform of voltage V_{ib} (maximal value V_{ib0}) at a frequency of $10\,\text{Hz}$ (period $T = 100\,\text{ms}$). Consequently, I_b is ramped with the same period in the range $[0, I_{b0}]$, where I_{b0} is the maximal bias current. Here, V_{ib0} is pre-selected such that I_{b0} exceeds the switching current to be measured. A time-signal of the measured voltage drop V and a constant voltage $V_{ref} = 7\,\mu$V set by a digital-to-analog converter (DAC) are sent as inputs to a trigger circuit. As V crosses the threshold V_{ref}, the trigger circuit sends a narrow trigger pulse V_{trig} to a sample-and-hold (S&H) circuit. The S&H circuit receives the AWG signal as another input and this signal is sampled by each trigger pulse, and held as the output V_{ic}. Therefore, V_{ic} represents the AWG voltage that sets the current bias for which the switch in the voltage V is detected. Switching current I_c is then extracted for a single AWG period from the conversion between the AWG and the current-source - as $I_c = \frac{I_{b0}}{V_{ib}} V_{ic}$. In our work, I_c was extracted for five AWG periods for each parameter set-point. The final I_{sw} was calculated as an average of the five I_c values. Delays due to the parasitic capacitance in the circuit, in principle, can cause an overestimate of I_c - as the V_{ic} output is updated with a delay with respect to the switch in V. However, from the specifications of the components used in our setup, this delay is estimated to be $\sim 25\,\mu$s at the given frequency and thus has practically negligible effect in our measurements where each ramp takes 100 ms.

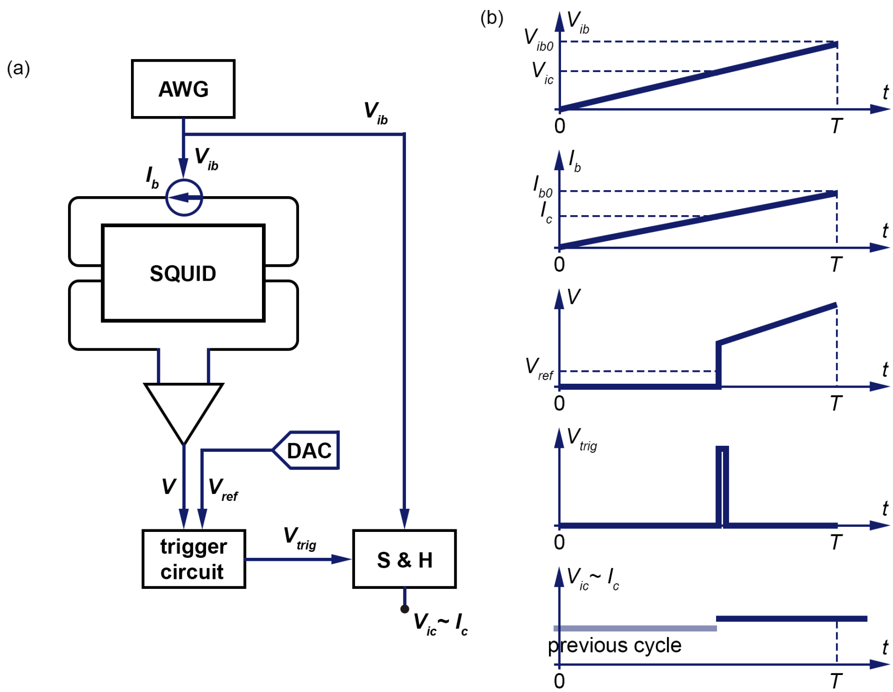

Figure 5.12: Setup for fast switching current measurements: **(a)** schematic and **(b)** time-domain traces of the signals shown in (a). Trigger pulse V_{trig} samples the voltage V_{ic} that sets the bias current $I_b = I_c$ for which the switch in V is detected.

REFERENCES

[1] B. D. Josephson. “Possible new effects in superconductive tunnelling”. In: *Phys. Lett.* 1 (1962), pp. 251–253.

[2] E. Prada, P. San-Jose, M. W. A. de Moor, A. Geresdi, E. J. H. Lee, J. Klinovaja, D. Loss, J. Nygård, R. Aguado, and L. P. Kouwenhoven. “From Andreev to Majorana bound states in hybrid superconductor–semiconductor nanowires”. In: *Nat. Rev. Phys.* 2 (2020), pp. 575–594.

[3] F. Pientka, A. Keselman, E. Berg, A. Yacoby, A. Stern, and B. I. Halperin. “Topological superconductivity in a planar Josephson junction”. In: *Phys. Rev. X* 7 (2017), p. 021032.

[4] M. Hell, M. Leijnse, and K. Flensberg. “Two-dimensional platform for networks of Majorana bound states”. In: *Phys. Rev. Lett.* 118 (10 2017), p. 107701.

[5] C. Schrade, S. Hoffman, and D. Loss. “Detecting topological superconductivity with φ_0 Josephson junctions”. In: *Phys. Rev. B* 95 (2017), p. 195421.

[6] J. Cayao, P. San-Jose, A. M. Black-Schaffer, R. Aguado, and E. Prada. “Majorana splitting from critical currents in Josephson junctions”. In: *Phys. Rev. B* 96 (2017), p. 205425.

[7] C. Schrade and L. Fu. “Majorana Superconducting Qubit”. In: *Phys. Rev. Lett.* 121 (2018), p. 267002.

[8] A. Fornieri, A. M. Whiticar, F. Setiawan, E. Portolés, A. C. C. Drachmann, A. Keselman, S. Gronin, C. Thomas, T. Wang, R. Kallaher, G. C. Gardner, E. Berg, M. J. Manfra, A. Stern, C. M. Marcus, and F. Nichele. “Evidence of topological superconductivity in planar Josephson junctions”. In: *Nature* 569 (2019), pp. 89–92.

[9] H. Ren, F. Pientka, S. Hart, A. T. Pierce, M. Kosowsky, L. Lunczer, R. Schlereth, B. Scharf, E. M. Hankiewicz, L. W. Molenkamp, B. I. Halperin, and A. Yacoby. “Topological superconductivity in a phase-controlled Josephson junction”. In: *Nature* 569 (2019), pp. 93–98.

[10] M. C. Dartiailh, W. Mayer, J. Yuan, K. S. Wickramasinghe, A. Matos-Abiague, I. Žutić, and J. Shabani. “Phase signature of topological transition in Josephson junctions”. In: *Phys. Rev. Lett.* 126 (2021), p. 036802.

[11] T. Yokoyama, M. Eto, and Y. V. Nazarov. “Josephson current through semiconductor nanowire with spin–orbit interaction in magnetic field”. In: *J. Phys. Soc. Jpn.* 82 (2013), p. 054703.

[12] T. Yokoyama, M. Eto, and Y. V. Nazarov. “Anomalous Josephson effect induced by spin-orbit interaction and Zeeman effect in semiconductor nanowires”. In: *Phys. Rev. B* 89 (2014), p. 195407.

[13] D. B. Szombati, S. Nadj-Perge, D. Car, S. R. Plissard, E. P. A. M. Bakkers, and L. P. Kouwenhoven. “Josephson ϕ_0-junction in nanowire quantum dots”. In: *Nature Phys.* 12 (2016), pp. 568–572.

[14] E. Strambini, A. Iorio, O. Durante, R. Citro, C. Sanz-Fernández, C. Guarcello, I. V. Tokatly, A. Braggio, M. Rocci, N. Ligato, V. Zannier, L. Sorba, F. S. Bergeret, and F. Giazotto. “A Josephson phase battery”. In: *Nat. Nanotechnol.* 15 (2020), pp. 656–660.

[15] J.-Y. Wang, C. Schrade, V. Levajac, D. van Driel, K. Li, S. Gazibegovic, G. Badawy, R. L. M. O. het Veld, J. S. Lee, M. Pendharkar, C. P. Dempsey, C. J. Palmstrøm, E. P. A. M. Bakkers, L. Fu, L. P. Kouwenhoven, and J. Shen. “Supercurrent parity meter in a nanowire Cooper pair transistor”. In: *Sci. Adv.* 8 (2022), eabm9896.

[16] C.-Z. Chen, J. J. He, M. N. Ali, G.-H. Lee, K. C. Fong, and K. T. Law. “Asymmetric Josephson effect in inversion symmetry breaking topological materials”. In: *Phys. Rev. B* 98 (2018), p. 075430.

[17] H. F. Legg, D. Loss, and J. Klinovaja. “Superconducting diode effect due to magnetochiral anisotropy in topological insulators and Rashba nanowires”. In: *Phys. Rev. B* 106 (2022), p. 104501.

[18] R. S. Souto, M. Leijnse, and C. Schrade. “Josephson Diode Effect in Supercurrent Interferometers”. In: *Phys. Rev. Lett.* 129 (2022), p. 267702.

[19] H. Wu, Y. Wang, Y. Xu, P. K. Sivakumar, C. Pasco, U. Filippozzi, S. S. P. Parkin, Y.-J. Zeng, T. McQueen, and M. N. Ali. “The field-free Josephson diode in a van der Waals heterostructure”. In: *Nature* 604 (2022), pp. 653–656.

[20] C. Baumgartner, L. Fuchs, A. Costa, S. Reinhardt, S. Gronin, G. C. Gardner, T. Lindemann, M. J. Manfra, P. E. F. Junior, D. Kochan, J. Fabian, N. Paradiso, and C. Strunk. “Supercurrent rectification and magnetochiral effects in symmetric Josephson junctions”. In: *Nat. Nanotech.* 17 (2022), pp. 39–44.

[21] B. Turini, S. Salimian, M. Carrega, A. Iorio, E. Strambini, F. Giazotto, V. Zannier, L. Sorba, and S. Heun*. “Josephson diode effect in high-mobility InSb nanoflags”. In: *Nano Lett.* 22 (2022), pp. 8502–8509.

[22] G. Mazur, N. van Loo, D. van Driel, J.-Y. Wang, G. Badawy, S. Gazibegovic, E. P. A. M. Bakkers, and L. P. Kouwenhoven. “The gate-tunable Josephson diode”. In: *arXiv:2211.14283* (2022).

[23] B. Zhang, Z. Li, V. Aguilar, P. Zhang, M. Pendharkar, C. Dempsey, J. S. Lee, S. D. Harrington, S. Tan, J. S. Meyer, M. Houzet, C. J. Palmstrom, and S. M. Frolov. “Evidence of ϕ_0-Josephson junction from skewed diffraction patterns in Sn-InSb nanowires”. In: *arXiv:2212.00199* (2022).

[24] G. de Lange, B. van Heck, A. Bruno, D. J. van Woerkom, A. Geresdi, S. R. Plissard, E. P. A. M. Bakkers, A. R. Akhmerov, and L. DiCarlo. “Realization of microwave quantum circuits Using hybrid superconducting-semiconducting nanowire Josephson elements”. In: *Phys. Rev. Lett.* 115 (2015), p. 127002.

[25] T. W. Larsen, K. D. Petersson, F. Kuemmeth, T. S. Jespersen, P. Krogstrup, J. Nygård, and C. M. Marcus. “Semiconductor-nanowire-based superconducting qubit”. In: *Phys. Rev. Lett.* 115 (2015), p. 127001.

[26] L. Casparis, M. R. Connolly, M. Kjaergaard, N. J. Pearson, A. Kringhoj, T. W. Larsen, F. Kuemmeth, T. Wang, C. Thomas, S. Gronin, G. C. Gardner, M. J. Manfra, C. M. Marcus, and K. D. Petersson. “Superconducting gatemon qubit based on a proximitized two-dimensional electron gas”. In: *Nat. Nanotech.* 13 (2018), pp. 915–919.

[27] A. Zazunov, V. S. Shumeiko, E. N. Bratus’, J. Lantz, and G. Wendin. “Andreev level qubit”. In: *Phys. Rev. Lett.* 90 (8 2003), p. 087003.

[28] N. M. Chtchelkatchev and Y. V. Nazarov. “Andreev quantum dots for spin manipulation”. In: *Phys. Rev. Lett.* 90 (2003), p. 226806.

[29] C. Janvier, L. Tosi, L. Bretheau, C. Ö. Girit, M. Stern, P. Bertet, P. Joyez, D. Vion, D. Esteve, M. F. Goffman, H. Pothier, and C. Urbina. “Coherent manipulation of Andreev states in superconducting atomic contacts”. In: *Science* 349 (2015), pp. 1199–1202.

[30] M. Hays, V. Fatemi, K. Serniak, D. Bouman, S. Diamond, G. de Lange, P. Krogstrup, J. Nygård, A. Geresdi, and M. H. Devoret. “Continuous monitoring of a trapped superconducting spin”. In: *Nat. Phys.* 16 (2020), pp. 1103–1107.

[31] M. Hays, V. Fatemi, D. Bouman, J. Cerrillo, S. Diamond, K. Serniak, T. Connolly, P. Krogstrup, J. Nygaåd, A. L. Yeyati, A. Geresdi, and M. H. Devoret. “Coherent manipulation of an Andreev spin qubit”. In: *Science* 373 (2021), pp. 430–433.

[32] M. Pita-Vidal, A. Bargerbos, R. Žitko, L. J. Splitthoff, L. Grünhaupt, J. J. Wesdorp, Y. Liu, L. P. Kouwenhoven, R. Aguado, B. van Heck, A. Kou, and C. K. Andersen. “Direct manipulation of a superconducting spin qubit strongly coupled to a transmon qubit”. In: *Nat. Phys.* (2023), pp. 1–6.

[33] B. I. Spivak and S. A. Kivelson. “Negative local superfluid densities: The difference between dirty superconductors and dirty Bose liquids”. In: *Phys. Rev. B* 43 (1991), 3740(R).

[34] E. Vecino, A. Martin-Rodero, and A. L. Yeyati. “Josephson current through a correlated quantum level: Andreev states and π junction behavior”. In: *Phys. Rev. B* 68 (2003), p. 035105.

[35] T. Meng, S. Florens, and P. Simon. “Self-consistent description of Andreev bound states in Josephson quantum dot devices”. In: *Phys. Rev. B* 79 (2009), p. 224521.

[36] M. Lee, R. López, H. Q. Xu, and G. Platero. “Proposal for Detection of the $0'$ and π Phases in Quantum-Dot Josephson Junctions”. In: *Phys. Rev. Lett.* 129 (2022), p. 207701.

[37] J. A. van Dam, Y. V. Nazarov, E. P. A. M. Bakkers, S. D. Franceschi, and L. P. Kouwenhoven. “Supercurrent reversal in quantum dots”. In: *Nature* 442 (2006), pp. 667–670.

[38] H. I. Jørgensen, T. Novotný, K. Grove-Rasmussen, K. Flensberg, and P. E. Lindelof. “Critical Current $0-\pi$ transition in designed Josephson quantum dot junctions”. In: *Nano Lett.* 7 (2007), pp. 2441–2445.

[39] E. J. H. Lee, X. Jiang, M. Houzet, R. Aguado, C. M. Lieber, and S. D. Franceschi. “Spin-resolved Andreev levels and parity crossings in hybrid superconductor–semiconductor nanostructures”. In: *Nat. Nanotech.* 9 (2014), pp. 79–84.

[40] S. Li, N. Kang, P. Caroff, and H. Q. Xu. “$0-\pi$ phase transition in hybrid superconductor–InSb nanowire quantum dot devices”. In: *Phys. Rev. B* 95 (2017), p. 014515.

[41] A. Bargerbos, M. Pita-Vidal, R. Žitko, J. Ávila, L. J. Splitthoff, L. Grünhaupt, J. J. Wesdorp, C. K. Andersen, Y. Liu, L. P. Kouwenhoven, R. Aguado, A. Kou, and B. van Heck. “Singlet-Doublet transitions of a quantum dot Josephson junction detected in a transmon circuit”. In: *PRX Quantum* 3 (2022), p. 030311.

[42] A. Eichler, R. Deblock, M. Weiss, C. Karrasch, V. Meden, C. Schönenberger, and H. Bouchiat. “Tuning the Josephson current in carbon nanotubes with the Kondo effect”. In: *Phys. Rev. B* 79 (2009), p. 161407.

[43] R. Maurand, T. Meng, E. Bonet, S. Florens, L. Marty, and W. Wernsdorfer. “First-Order $0-\pi$ quantum phase transition in the Kondo regime of a superconducting carbon-nanotube quantum dot”. In: *Phys. Rev. X* 2 (2012), p. 011009.

[44] B.-K. Kim, Y.-H. Ahn, J.-J. Kim, M.-S. Choi, M.-H. Bae, K. Kang, J. S. Lim, R. López, and N. Kim. “Transport measurement of Andreev bound states in a Kondo-correlated quantum dot”. In: *Phys. Rev. Lett.* 110 (2013), p. 076803.

[45] A. M. Whiticar, A. Fornieri, A. Banerjee, A. C. C. Drachmann, S. Gronin, G. C. Gardner, T. Lindemann, M. J. Manfra, and C. M. Marcus. “Zeeman-driven parity transitions in an Andreev quantum dot”. In: *Phys. Rev. B* 103 (2021), p. 245308.

[46] P. San-Jose, E. Prada, and R. Aguado. “Mapping the topological phase diagram of multiband semiconductors with supercurrents”. In: *Phys. Rev. Lett.* 112 (2014), p. 137001.

[47] C.-X. Liu, B. van Heck, and M. Wimmer. “Josephson current via an isolated Majorana zero mode”. In: *Phys. Rev. B* 103 (2021), p. 014510.

[48] U. Fano. “Effects of configuration interaction on intensities and phase shifts”. In: *Phys. Rev.* 124 (1961), p. 1866.

5

[49] S. Heedt, M. Quintero-Pérez, F. Borsoi, A. Fursina, N. van Loo, G. P. Mazur, M. P. Nowak, M. Ammerlaan, K. Li, S. Korneychuk, J. Shen, M. Y. van de Poll, G. Badawy, S. Gazibegovic, N. de Jong, P. Aseev, K. van Hoogdalem, E. P. A. M. Bakkers, and L. P. Kouwenhoven. “Shadow-wall lithography of ballistic superconductor–semiconductor quantum devices”. In: *Nat. Commun.* 12 (2021), p. 4914.

[50] F. Borsoi, G. P. Mazur, N. van Loo, M. P. Nowak, L. Bourdet, K. Li, S. Korneychuk, A. Fursina, J.-Y. Wang, V. Levajac, E. Memisevic, G. Badawy, S. Gazibegovic, K. van Hoogdalem, E. P. A. M. Bakkers, L. P. Kouwenhoven, S. Heedt, and M. Quintero-Pérez. “Single-shot fabrication of semiconducting–superconducting nanowire devices”. In: *Adv. Func. Mater.* (2021), p. 2102388.

[51] V. Levajac, G. P. Mazur, N. van Loo, F. Borsoi, G. Badawy, S. Gazibegovic, E. P. A. M. Bakkers, S. Heedt, L. P. Kouwenhoven, and J.-Y. Wang. “Impact of junction length on supercurrent resilience against magnetic field in InSb-Al nanowire Josephson junctions”. In: *Nano Lett.* 23 (11 2023), pp. 4716–4722.

[52] D. J. van Woerkom, A. Geresdi, and L. P. Kouwenhoven. “One minute parity lifetime of a NbTiN Cooper-pair transistor”. In: *Nat. Phys.* 11 (2015), pp. 547–550.

6

SUBGAP SPECTROSCOPY ALONG HYBRID NANOWIRES BY NM-THICK TUNNEL BARRIERS

Tunneling spectroscopy is widely used to examine the subgap spectra in semiconductor-superconductor nanostructures when searching for Majorana zero modes (MZMs). Typically, semiconductor sections controlled by local gates at the ends of hybrids serve as tunnel barriers. Besides detecting states only at the hybrid ends, such gate-defined tunnel probes can cause the formation of non-topological subgap states that mimic MZMs. Here, we develop an alternative type of tunnel probes to overcome these limitations. After the growth of an InSb-Al hybrid nanowire, a precisely controlled in-situ oxidation of the Al shell is performed to yield a nm-thick AlOx layer. In such thin isolating layer, tunnel probes can be arbitrarily defined at any position along the hybrid nanowire by shadow-wall angle-deposition of metallic leads. In this work, we make multiple tunnel probes along single nanowire hybrids and successfully identify Andreev bound states (ABSs) of various spatial extension residing along the hybrids.

The work in this chapter has been published as: V. Levajac*, J.-Y. Wang*, C. Sfiligoj, M. Lemang, J. C. Wolff, A. Bordin, G. Badawy, S. Gazibegović, E. P. A. M. Bakkers and L. P. Kouwenhoven *"Subgap spectroscopy along hybrid nanowires by nm-thick tunnel barriers"*, Nature Communications 14, 6647 (2023)

*These authors contributed equally to this work.

6.1. INTRODUCTION

Topological superconductors have received significant attention in the condensed matter physics community over the last decade due to their potential application in fault-tolerant quantum computation [1–4]. In III-V semiconducting nanowires with thin superconducting shells a topological phase transition is predicted to occur at a sufficiently high magnetic field [5, 6]. An essential precondition for this is a hybridization mechanism in which superconductivity is induced in the semiconducting nanowire with tunable chemical potential, strong spin-orbit interaction and large g factor. The sophisticated interplay of these physical phenomena has motivated in-depth theoretical studies and state-of-the-art material developments [7–9]– with a goal of reaching topological superconducting phase in hybrid nanowires. Hallmarks of the topologically non-trivial phase are Majorana zero modes (MZMs) - zero energy modes localized at two ends of a hybrid nanowire.

Tunneling spectroscopy is commonly used to investigate the energy spectrum in hybrid nanowires and search for MZMs by examining the presence of zero energy states at nanowire ends. In such experiments, a normal lead is tunnel-coupled to the end of a hybrid nanowire and serves as a tunnel probe. The differential conductance is measured as a function of an applied bias voltage between the tunnel probe and a drain lead contacting the hybrid nanowire. Zero bias peaks (ZBPs) measured at hybrid nanowire ends indicate the presence of zero energy end-states and were the first reported signatures of MZMs in hybrid nanowires [10–12]. A semiconducting nanowire section where the superconducting shell ends is generally used to create a tunnel barrier and a local tunnel gate is needed to define and control the barrier profile. Advanced numerical modellings of realistic devices have shown that low energy states can be localized at the end of a hybrid nanowire due to smooth variations in the electrostatic potential induced by the tunnel gate [13–15]. A recent study on three-terminal hybrid nanowire devices has reported such zero energy states of trivial origin coincidentally appearing at both nanowire ends and falsely mimicking an end-to-end correlation of MZMs [16]. Therefore, due to smooth potential effects, ambiguous signatures of MZMs can be measured by tunnel probes with semiconducting tunnel barriers [17]. Another limitation of these tunnel probes is that tunneling spectroscopy is performed only at the ends of a hybrid nanowire. Therefore, a reopening of an induced gap in the hybrid bulk at the topological phase transition can only be detected in non-local conductance measurements on three-terminal hybrid nanowire devices [18]. Measuring the hybrid bulk directly in local tunneling spectroscopy is additionally motivated by recent theoretical studies showing that disorder in a hybrid nanowire can result in MZMs being localized inside the hybrid bulk and undetectable at its ends [19, 20]. An experimental work has shown the possibility to use AlOx as a tunnel barrier for hybrid nanowires with superconducting Al [21]. In that work, the AlOx layer was fabricated ex-situ after the growth of superconducting Al. The lack of in-situ fabrication required physical etching of the nanowire surface oxide prior to the fabrication of the tunnel barriers. This could lead to low-quality tunnel barriers - causing a soft superconducting gap [22].

Here, we develop a new type of tunnel barriers for tunneling spectroscopy in hybrid nanowires in order to overcome the limitations set by the semiconducting tunnel barriers. We fabricate InSb-Al hybrid nanowires in which a nm-thick dielectric layer of AlOx covers the hybrid and can be used to tunnel couple it to a normal metal lead. In contrast to reference [21], our AlOx layer is fabricated in-situ, which improves the quality of the tunnel probes. Such tunnel probes have a sharp potential profile set by the thickness of the AlOx layer. In addition, the AlOx layer extends over the entire length of the hybrid and allows for a formation of tunnel probes at any position along the nanowire. We exploit these advantages and fabricate multiple tunnel probes along single hybrid nanowires in order to investigate the longitudinal evolution of their energy spectra. By comparing tunneling spectroscopy results obtained at different positions along the same nanowire, Andreev bound states (ABSs) of various spatial extension can be identified at the end and inside the bulk of the hybrids.

6.2. RESULTS

Hybrid nanowires that utilize nm-thick tunnel barriers are introduced in Fig. 6.1. A false-colored scanning-electron microscopy (SEM) image of a representative device is shown in Fig. 6.1A and a schematic longitudinal cross-section along the device is displayed in Fig. 6.1B. A superconducting Al (red) film is grown by the shadow-wall lithography technique [23, 24] on a semiconducting InSb (light blue) nanowire [25]. By a subsequent in-situ oxidation, the Al film is partially oxidized to form a dielectric AlOx (pink) layer that covers the hybrid. The shadow-wall lithography technique is used to define three normal Ag (navy) leads along the nanowire on top of the AlOx layer. Two Au (yellow) leads contact the bare semiconducting nanowire part on the left and the hybrid nanowire part on the right. Two Pd (dark grey) gates are coupled to the nanowire via a dielectric HfO_2 (light grey) layer. The gate under the nanowire section with the superconducting shell (super gate) controls the electro-chemical potential in the hybrid. The gate under the bare nanowire section (tunnel gate) tunes a tunnel barrier at the semiconducting junction between the left Au lead and the hybrid. Voltages V_{TG} and V_{SG} are applied to the tunnel and super gate, respectively. A magnetic field B is applied parallel to the nanowire. Four normal leads are tunnel-coupled to the hybrid and denoted as tunnel probes P0, P1, P2 and P3 in Fig. 6.1B. The fifth lead forms a contact to the hybrid and is denoted as a drain contact. The tunnel probe P0 utilizes the semiconducting tunnel barrier controlled by the tunnel gate, while in the tunnel probes P1, P2 and P3 the AlOx layer serves as a nm-thick tunnel barrier. The widths of probes P1, P2 and P3 are designed to be 200 nm and the lateral edge-to-edge distances between neighboring probes are designed to be 200 nm. Schematic transverse cross-sections of the device are displayed in Fig. 6.1C-6.1E. The cross-section through the probes P1, P2 and P3 in Fig. 6.1D indicates that the nanowire has the superconducting Al shell on one of its facets and that the AlOx layer extends over the entire contact area between the hybrid and the Ag leads. Four white arrows indicate transport directions between the Ag lead and the InSb-Al hybrid. The two middle arrows correspond to direct tunneling to the Al shell and possibly through the Al shell into the hybrid. The

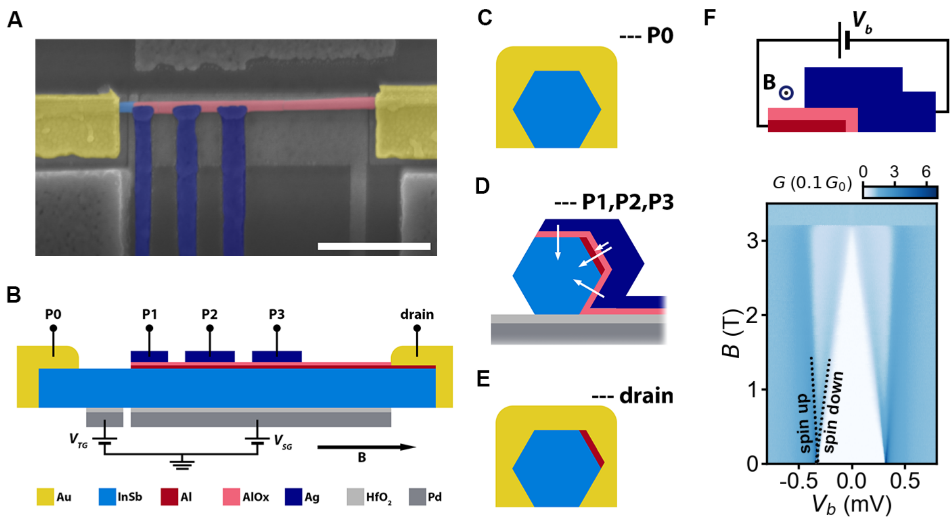

Figure 6.1: **Hybrid nanowire devices with nm-thick tunnel barriers**: (**A**) False-colored SEM image of a representative device. A nm-thick layer of AlOx (pink) fully covers the Al (red) shell that is visible in the schematic cross-sections (B to E). Three Ag (navy) leads are defined on top of the AlOx layer along the hybrid. Two Au (yellow) leads contact the semiconducting InSb (light blue) nanowire on the left and the hybrid on the right. The white scale bar corresponds to 1 μm. (**B**) A schematic longitudinal cross-section along the device with two Pd (dark grey) gates coupled to the nanowire via dielectric HfO_2 (light grey). Voltages V_{TG} and V_{SG} are applied to the tunnel gate and the super gate, respectively. An external magnetic field B is applied parallel to the nanowire as indicated by the black arrow. Four probes P0, P1, P2 and P3 are tunnel-coupled to the hybrid nanowire contacted by the right drain lead. The probe P0 utilizes the semiconducting tunnel barrier and the probes P1, P2 and P3 use nm-thick tunnel barriers in the AlOx layer. (**C** to **E**) Schematic transverse cross-sections through the tunnel probes and the drain. White arrows indicate different tunneling paths between the Ag lead and the InSb-Al hybrid. (**F**) A schematic perpendicular cross-section of a planar tunnel junction with an AlOx layer as the tunnel barrier between an Al and an Ag film as the leads (top). Differential conductance G of the junction as a function of a bias voltage V_b and an in-plane magnetic field B (bottom). A superconducting gap of $325 \pm 5\,\mu$eV and a critical in-plane field of ~ 3.3 T can be extracted for the Al film.

other two arrows indicate transport via hybrid nanowire states. Direct tunneling to the Al shell is dominant at energies above the Al superconducting gap, and is strongly suppressed at energies below the gap - resulting from the hard gap of the Al film. Transport via the hybrid nanowire states takes place only at energies below the gap. The AlOx layer in the drain area is removed by Ar ion milling prior to the deposition of the gold contacts - as shown in the cross-section through the drain lead in Fig. 6.1E. Details can be found in the Device fabrication section and Fig. 6.6 in the Supplementary Materials. A transmission electron microscopy (TEM) analysis of the cross-section corresponding to Fig. 6.1D is made for a hybrid nanowire device and shown in Fig. 6.7 in the Supplementary Materials. We note that the regular hexagonal cross-sections in Fig. 6.1C and Fig. 6.1E are likely distorted in real devices by the Ar ion milling.

A critical step in the fabrication of our hybrid nanowire devices is the formation of the AlOx layer by an in-situ oxidation of the superconducting Al film. In order to test this fabrication step, we fabricate a planar tunnel junction with a perpendicular cross-section shown in the top panel of Fig. 6.1F. The junction leads are a superconducting Al (red) film and a normal Ag (navy) film that partially overlap and that are separated by a thin dielectric AlOx (pink) layer. The AlOx is formed by an in-situ oxidation of the Al film, prior to the deposition of the Ag film. The tunnel junction is characterized in the bottom panel of Fig. 6.1F by measuring the junction conductance as a function of a bias voltage V_b and an in-plane magnetic field B. The result represents typical tunneling spectroscopy of superconducting Al. As shown in the panel, superconducting coherence peaks spin-split with the magnetic field due to the Zeeman effect ($g \approx 2$). This demonstrates that our process for in-situ oxidation of Al can yield an AlOx layer as a nm-thick tunnel barrier for tunneling spectroscopy. Next, we perform such in-situ oxidation on hybrid nanowires and characterize these hybrid nanowire devices in electrical transport measurements.

6

We have studied three hybrid nanowire devices - Device 1, 2 and 3. Devices 1 and 2 are nominally identical and described in Fig. 6.1. For Device 3, Al is deposited instead of Ag, so that three superconducting leads are defined on top of the AlOx layer (see the Device fabrication section in the Supplementary Materials). Therefore, the probes P1, P2 and P3 of Device 3 form three Josephson junctions with the hybrid nanowire. The replacement of Ag by Al in Device 3 is motivated by proposals for studying supercurrent in hybrid devices as an alternative way of detecting MZMs [26, 27] and for realizing MZM-based qubits [28, 29].

As an initial step, Device 1 is characterized in conductance measurements by different probes in a voltage-bias setup. The four probes P0, P1, P2 and P3 are consecutively connected as in Setup V1 to measure the differential conductance (see the Measurement setups section in the Supplementary Materials) and the results are shown in Fig. 6.2. A voltage $V_{TG} = 2.1\,\mathrm{V}$ is applied to the tunnel gate to define a tunnel barrier in the semiconducting junction of probe P0. The super gate is set to $V_{SG} = 0\,\mathrm{V}$. In the top row of Fig. 6.2, the differential conductance $G = dI/dV$ is measured by each probe as a function of a bias voltage V_b and a parallel magnetic field B along the nanowire of Device 1. In the parallel B-field, the superconducting gap detected by the four probes closes at $3-3.5\,\mathrm{T}$. The variations in the critical fields can be explained by small misalignments of the applied fields in different probes - as the nanowire is not perfectly straight. Furthermore, in contrast to the tunneling spectroscopy of the Al film in Fig. 6.1F, there is no splitting of the coherence peaks measured by probes P1, P2 and P3. This is most likely due to spin-mixing by spin-orbit interaction in the semiconducting nanowire [30]. From each 2D-map in Fig. 6.2, a linecut at zero field is taken and shown on logarithmic scale as a red

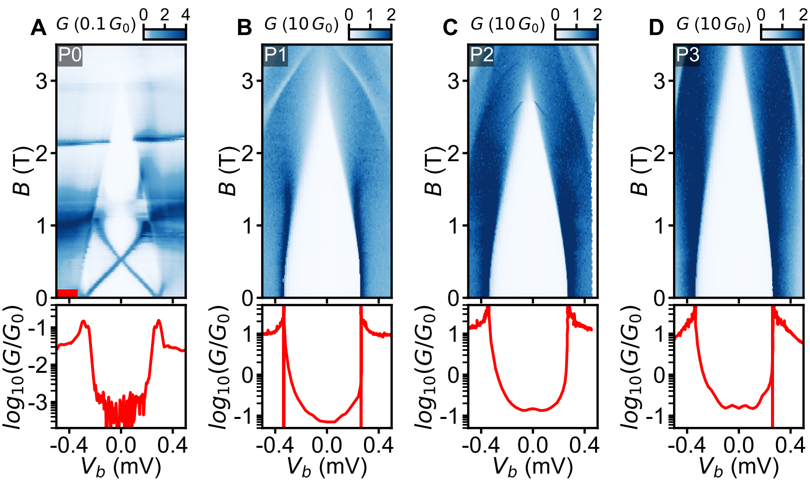

Figure 6.2: **Characterization of the tunnel probes by differential conductance measurements**: G as a function of V_b and B along the nanowire of Device 1 measured by (**A**) probe P0, (**B**) probe P1, (**C**) probe P2 and (**D**) probe P3 consecutively connected as in Setup V1 (top row). The gate settings are $V_{TG} = 2.1\,\mathrm{V}$ and $V_{SG} = 0\,\mathrm{V}$. A red marker indicate the linecuts at zero field and the corresponding traces are shown in logarithmic scale (bottom row). By finding the coherence peak positions, a superconducting gap Δ is extracted to be (A) $290 \pm 6\,\mu\mathrm{eV}$, (B) $298 \pm 3\,\mu\mathrm{eV}$, (C) $305 \pm 11\,\mu\mathrm{eV}$ and (D) $301 \pm 5\,\mu\mathrm{eV}$.

trace in the bottom row of Fig. 6.2. In some traces, large negative values appear at the coherence peaks and their origin is explained in the Measurement setups section in the Supplementary Materials. A superconducting gap $\Delta \sim 300\,\mu\mathrm{eV}$ of the hybrid can be extracted from the positions of the coherence peaks. Noticeably, in all four probes the differential conductance at $V_b < \Delta$ (in-gap conductance) is roughly two orders of magnitude lower than the differential conductance at $V_b > \Delta$ (out-of-gap conductance). However, the out-of-gap conductance in the probes with AlOx tunnel barrier is two orders of magnitude larger than in probe P0 – due to the large number of modes in the metallic leads of P1, P2 and P3. Similarly, the large number of modes in P1, P2 and P3 would also lead to a larger subgap conductance of these probes in comparison with P0. There are likely only a few or even just one mode in the semiconducting junction contributing to the differential conductance of P0. While the out-of-gap conductance in probes P1, P2 and P3 is predominantly determined by direct tunneling to the Al shell, the in-gap conductance in these probes is predominantly determined by the transport via the hybrid nanowire - as a consequence of the hard superconducting gap of the Al (see Fig. 6.1F). In order to measure the high out-of-gap conductance by P1, P2 and P3, the measurement sensitivity is adjusted, and consequently the modulations of the in-gap conductance cannot be precisely detected in Figs. 6.2B-6.2D. The subgap spectra in the probes P1, P2 and P3 are in detail studied in Fig. 6.4 and Fig. 6.5 of this work. A characterization measurement like the one of Device 1 in Fig. 6.2 has been performed for Device 2 and similar results are shown in Fig. 6.10 in the Supplementary Materials.

In order to test the AlOx layer as a weak link for supercurrent measurements, current-bias measurements are performed on Device 3 and the results are shown in Fig. 6.3. Fig. 6.3B is a schematic cross-section through P1 (or P2, or P3). It is shown that probe P1, as well as P2 and P3, uses a superconducting lead made of thick Al. Together with the underlying AlOx layer and the superconducting Al shell on the nanowire, the three superconducting leads of P1, P2 and P3 form three asymmetric Josephson junctions – JJ1, JJ2 and JJ3. In order to characterize JJ1, probes P1 and P2 are connected as in Setup I2 - such that probe P1 is current-biased and a voltage drop V across JJ1 is measured (see the Measurement setups section in the Supplementary Materials). V is measured as a function of a bias current I_b and B, see Fig. 6.3A. The linecuts taken at $B = 0\,\mathrm{T}$ and $B = 0.4\,\mathrm{T}$ are displayed in Fig. 6.3C. The linecut taken at $B = 0\,\mathrm{T}$ (bottom panel of Fig. 6.3C) shows a zero voltage plateau due to the non-dissipative Josephson supercurrent with a switching current of $\sim 200\,\mathrm{nA}$. This demonstrates that at low fields the probe P1 is in the SIS transport regime (S-thin superconducting Al shell, I-thin dielectric AlOx, S-thick superconducting Al lead). As the field increases in Fig. 6.3A, the zero voltage region shrinks and disappears at $B \sim 0.2\,\mathrm{T}$ due to the suppressed superconductivity in the thick Al lead. Consequently, the SIS transport regime changes to SIN transport as the thick Al lead changes from being superconducting (S) to being normal (N). The linecut taken at $B = 0.4\,\mathrm{T}$ (top panel of Fig. 6.3C) confirms this, as it resembles an $I-V$ characteristic of the tunneling transport between a superconductor and a normal metal. This shows that a parallel field of $0.4\,\mathrm{T}$ is sufficient to turn the thick Al lead fully normal and that at high fields the probes P1, P2 and P3 of Device 3 can be used as normal probes for tunneling spectroscopy.

In Fig. 6.2 and Fig. 6.3, we demonstrate that the probes with nm-thick tunnel barriers can serve to characterize superconductivity in hybrid nanowires. In the rest of this work, we focus on measuring in-gap conductance by different probes with the goal to study subgap states in hybrid nanowire devices.

The capability of probes with nm-thick tunnel barriers to detect subgap states is examined for Device 1 in Fig. 6.4. In-gap conductance is measured by two tunnel probes - probe P0 that utilizes the semiconducting tunnel barrier and probe P1 as the nearest probe that utilizes the nm-thick tunnel barrier. Probes P0 and P1 are connected as in Setup V2 (see the Measurement setups section in the Supplementary Materials) and the super gate voltage is set at $V_{SG} = 0\,\mathrm{V}$. In-gap conductance is measured by both probes as a function of V_b and B (Fig. 6.4A) or V_{TG} (Fig. 6.4B). Upon setting B or V_{TG}, V_b is first swept on probe P0 with probe P1 at zero bias voltage and then V_b is swept on probe P1 with probe P0 at zero bias voltage. In this way, two consecutive tunneling spectroscopy traces are obtained for the same (field or gate) parameter – suppressing possible effects from drift in the device or setup. The conductance dependences in the top panels of Fig. 6.4A and 6.4B show that a single subgap state is detected by probe P0 for the given ranges of B and V_{TG}. The strong modulation by V_{TG} (Fig. 6.4B top) suggests that the subgap state is localized

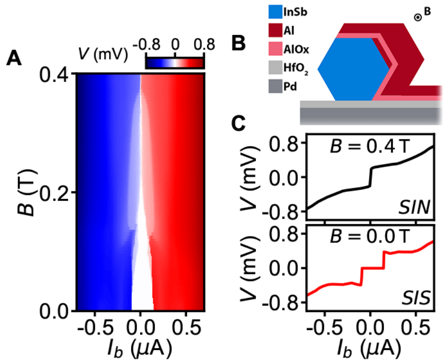

Figure 6.3: **Characterization of the weak links by supercurrent measurements**: Current-bias measurement of Device 3 with probes P1 and P2 connected as in Setup I2 and probe P1 being current-biased. (**A**) V as a function of I_b and B. (**B**) Schematic transverse cross-section through the probes P1, P2 and P3 of Device 3 with superconducting Al (red) leads (the colors are as in Fig. 6.1). A magnetic field parallel to the nanowire is applied as indicated. (**C**) Linecuts from (A) taken at $B = 0\,\mathrm{T}$ (bottom) and $B = 0.4\,\mathrm{T}$ (top). The bottom linecut shows a switching current of $\sim 200\,\mathrm{nA}$ and corresponds to the SIS transport regime. The top linecut indicates the SIN transport regime - as the thick Al of the lead turns normal at sufficiently high B fields.

close to the semiconducting junction. Such subgap states are commonly detected in tunneling spectroscopy with semiconducting tunnel barriers in two-terminal [31] and three-terminal [16, 32–35] hybrid nanowire devices. Interestingly, the conductance dependences in the bottom panels of Fig. 6.4A and 6.4B show that the same subgap state is also detected by probe P1. This is additionally demonstrated by the linecuts taken from Fig. 6.4A (Fig. 6.4B) and displayed in Fig. 6.4C (Fig. 6.4D) in which aligned conductance peaks correspond to the same subgap state detected by the two probes. The larger background subgap conductance of P1 - compared to P0 - is due to the large number of modes in the metallic tunnel probes, as explained when introducing Fig. 6.2. In addition, there are conductance peaks detected by probe P1 that are not detected by probe P0 – indicating that these subgap states most likely reside near P1 and are decoupled from P0. An additional tunnel gate sweep at a finite B-field and positive super gate shows that the subgap states detectable by both P0 and P1 remain detectable by P1 even when the semiconducting junction is pinched-off (see Fig. 6.11 in the Supplementary Materials). This means that the probe P1 can substitute the probe P0 over broader parameter ranges than what is accessible to P0. An analogous measurement to the one in Fig. 6.4 has been carried out on Device 1 with different parameter settings and on Device 2 (see Fig. 6.12 and Fig. 6.13 in the Supplementary Materials) and the capability of AlOx tunnel probes to detect hybrid states is validated there as well. From all our results (e.g. shown in

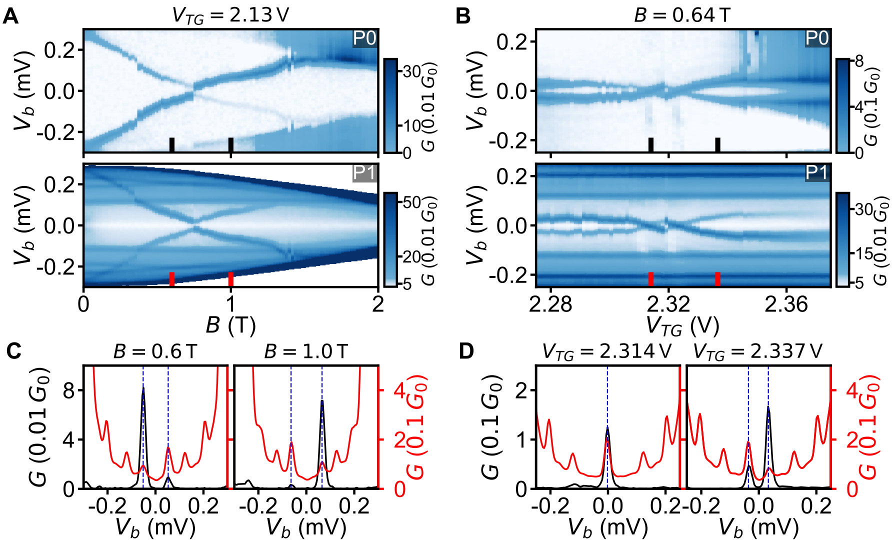

Figure 6.4: **Comparison between the tunneling spectroscopy by probes P0 and P1**: Conductance measurements of Device 1 with the probes P0 and P1 connected as in Setup V2. (**A**) G as a function of V_b and B, $V_{TG} = 2.13$V. (**B**) G as a function of V_b and V_{TG}, $B = 0.64$T. (**C**) Linecuts taken from (A) in black (probe P0) and red (probe P1) at the B settings denoted by the markers. (**D**) Linecuts taken in (B) in black (probe P0) and red (probe P1) at the V_{TG} settings denoted by the markers. In (C) and (D), the black and red linecuts are shown on different scales, see corresponding colors on the left and right axis. Dashed vertical blue lines in (C) and (D) mark the conductance peaks corresponding to the same subgap states detected by both P0 and P1.

Fig. 6.4 as well as Fig. 6.12 and Fig. 6.13), we note that the subgap states detected by P0 have always been also captured by P1. As we demonstrate that tunnel probes utilizing nm-thick tunnel barriers can detect subgap states in hybrid nanowires, in the rest of this work we use only these probes to study the subgap spectra in our hybrids.

An appealing advantage of the tunnel probes with nm-thick AlOx barriers is the opportunity to use multiple probes along a single hybrid nanowire for exploring the spatial distribution of subgap states. In Fig. 6.5, tunneling spectroscopy is performed by the probes P1, P2 and P3 of Device 1 and Device 3 in order to study the subgap spectra at different positions along the hybrid nanowires. The three probes of Device 1 are in pairs consecutively connected as in Setup V2 (first P1 and P2, and then P2 and P3, see the Measurement setups section in the Supplementary Materials) and the tunneling spectroscopy results are shown in Fig. 6.5A. For Device 3, the three probes are consecutively connected as in Setup V1 (see the Measurement setups

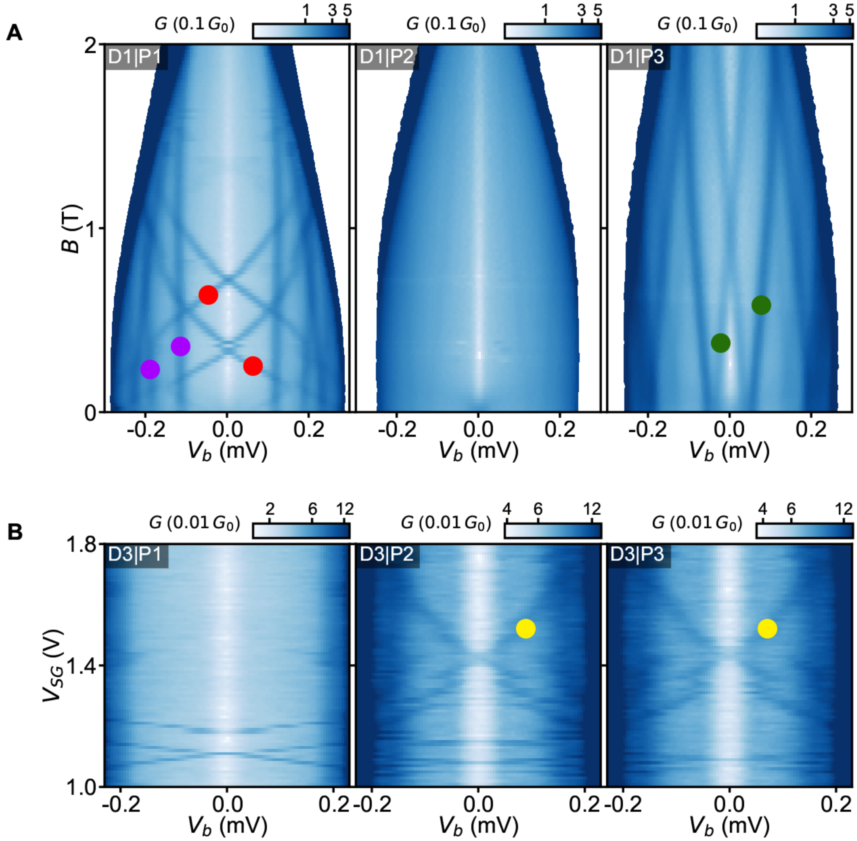

Figure 6.5: **Longitudinal dependence of the subgap spectra measured by probes P1, P2 and P3**: (**A**) G as a function of V_b and B along the nanowire of Device 1. First, probes P1 (left) and P2 (middle) are connected as in Setup V2 and then probes P1 and P3 (right) are connected as in Setup V2. The super gate is at $V_{SG} = 0.6$V and the tunnel gate is floating. All the subgap states are detectable only by single probes. These states are marked by red, purple and green markers. (**B**) G as a function of V_b and V_{SG} of Device 3 measured by probes P1, P2 and P3 consecutively connected as in Setup V1. $B = 1$T is applied along the nanowire and the tunnel gate is floating. There is a subgap state detectable by the probes P2 and P3, and non-detectable by the probe P1. This state is marked by yellow markers.

section in the Supplementary Materials) and the tunneling spectroscopy results are shown in Fig. 6.5B. A high magnetic field is applied for the measurements of Device

3 in order to fully suppress superconductivity in the thick Al leads of the probes P1, P2 and P3.

The measurement in Fig. 6.5A is performed with the super gate of Device 1 at $V_{SG} = 0.6$V and the floating tunnel gate. Differential conductance is measured by probes P1, P2 and P3 as a function of V_b and B. The subgap spectra obtained by the three probes show different evolutions with B field. Probe P1 detects two kinds of subgap states – subgap states insensitive to B (purple markers in Fig. 6.5A left) and subgap states with high g factor ($g \approx 35$) that cross zero energy as B is increased (red markers in Fig. 6.5A left). The measurement in Fig. 6.11 in the Supplementary Materials demonstrates that the subgap states detected by P1 reside at the hybrid end even when the semiconducting junction is pinched-off. This indicates that the states detected by probe P1 are not localized in the section not covered by Al, but at the end of the hybrid. As the junction becomes conductive, the states with high g factor exhibit a finite overlap with the junction and become detectable through the semiconducting tunnel barrier (see Fig. 6.11). The states detected by probe P1 appear to be strongly localized at the hybrid end, as no subgap states are detected by probe P2 (Fig. 6.5A middle). Another subgap state with low g factor ($g \approx 3.5$) (green marker in Fig. 6.5A right) is measured to be localized in the hybrid bulk - as it is detected by probe P3, but is not detected by probe P2. The correlation between the states detected by different probes has been examined while varying the super gate (see Fig. 6.14 and Fig. 6.15 in the Supplementary Materials) or changing the tunnel gate regime (see Fig. 6.16 in the Supplementary Materials). The absence of correlations indicates that the subgap states detected in Device 1 are localized over less than ~ 200 nm. A similar qualitative picture is observed for Device 2 and the corresponding measurements are shown in Fig. 6.17 in the Supplementary Materials. Besides confirming the strong localization of the subgap states in Device 1, the measurements of Fig. 6.14 and Fig. 6.15 show some additional features of the subgap states that can be used to better understand their nature. This is elaborated in the Discussion section.

For the measurements of Device 3, $B = 1$T is applied along the nanowire and the tunnel gate is floating. Superconductivity in the thick Al leads of probes P1, P2 and P3 is fully suppressed due to the high field, and these probes are used as normal tunnel probes. In Fig. 6.5B, each of the three probes is consecutively connected as in Setup V1 (see the Measurement setups section in the Supplementary Materials) and G is measured as a function of V_b and V_{SG}. The order in which the spectroscopy is performed is P2-P1-P3 (middle, left, right in Fig. 6.5B). Striking similarities between the two subgap features detected by probes P2 and P3 indicate the presence of a subgap state coupled to two bulk probes (yellow markers in Fig. 6.5B). However, the absence of any similar feature in the tunneling spectroscopy by probe P1 (taken in between the measurements by P2 and P3) suggests that the same state is not detectable at the end of the hybrid nanowire. This implies that the subgap state extends over more than 200 nm in the hybrid bulk, but does not reach the hybrid end. Importantly, detecting such a state shows the capability of probes with nm-thick tunnel barriers to detect extended subgap states. Another extended subgap state is detected in the same device in another V_{SG} range (see Fig.

6.18 in the Supplementary Materials). Additional tunneling spectroscopy in a broad super gate range ($-10\,\mathrm{V} < V_{SG} < 10\,\mathrm{V}$) in all three probes is performed and the result implies that the induced superconducting gap can be tuned somewhat with V_{SG} (see Fig. 6.19A in the Supplementary Materials). This demonstrates that the AlOx tunnel probes are capable of identifying features of the induced gap - as these are observed at energies below the superconducting gap of the Al shell. At $V_{SG} = 10\,\mathrm{V}$ (and $B = 1\,\mathrm{T}$) the gap remains open along the hybrid of Device 3. Additional supercurrent measurement at zero field shows that sweeping V_{SG} from $-2\,\mathrm{V}$ to $2\,\mathrm{V}$ has no effect on the supercurrent measured by probe P1 (see Fig. 6.19B in the Supplementary Materials). Together with the large switching current value, such insensitivity to the super gate indicates that the hybrid states have a negligible contribution to the supercurrent that is dominantly carried by the condensate in the Al shell.

6.3. DISCUSSION

In order to investigate the origin of various subgap states in our devices, their sensitivity to magnetic and electric fields is examined in several additional measurements shown in Figs. 6.14, 6.15, 6.16 and 6.17 in the Supplementary Materials. We find that subgap states with high g factor are sensitive to local electric fields (Figs. 6.14, 6.16 and 6.17), while the subgap states with low g factor are weakly sensitive or insensitive to local electric fields (Figs. 6.14, 6.15 and 6.16). This is consistent with the nature of hybrid states, where the sensitivity of a hybrid state to both electric and magnetic fields are determined by its wavefunction distribution between the superconductor and semiconductor.

Multiple subgap states with high g factor are formed for sufficiently positive super gate (Fig. 6.14). We mark these states by red markers in Fig. 6.5. Our measurements demonstrate that these states are not bulk states, as they are localized at the hybrid end. They are detected also when the nearby tunnel gate is floating (Fig. 6.16). This suggests that subgap states with high g factor may be inevitably localized at the ends of hybrid nanowires due to variations of the electro-chemical potential caused by the edges of the superconducting film. However, subgap states with high g factor are not localized exclusively at the hybrid ends. Namely, we also detect them - although much more rarely - as single subgap states localized inside the hybrid bulk (Fig. 6.17).

The probes with nm-thick tunnel barriers show subgap states with low g factors (purple and green markers in Fig. 6.5) and these states also show weak sensitivity or insensitivity to the gates. We speculate that these states may be formed at the InSb-Al interface - where the electric field is strongly screened. Besides, strong spin-orbit interaction could be present at the interface due to band bending - leading to the magnetic field-insensitivity of the interface states (purple markers in Fig. 6.5A) [36].

Most of the subgap states in our devices can be detected by only one tunnel probe ($\sim 200\,\mathrm{nm}$ extension) - either at the hybrid end (by probe P1) or inside the hybrid bulk (by probe P2 or P3) - while some subgap states can be detected by two tunnel probes ($> 200\,\mathrm{nm}$ extension). However, we do not report any subgap state being detectable by all three tunnel probes (> 600 nm extension). This is comparable with the results of a previous study [21], where tunnel probes had lateral separations of ~ 500 nm and there was no report on subgap states detected by multiple probes. The presence of the localized subgap states and the absence of extended bulk subgap states can be caused by inhomogeneities in the electro-chemical potential due to disorder in the hybrid nanowires [17]. This could also explain the lack of signatures of a topological phase transition in our subgap spectroscopy - neither at the ends (in the form of ZBPs) nor inside the bulk of the hybrids (in the form of a gap reopening) [19]. Furthermore, we have not observed stable ZBPs of most likely trivial origins. Potentially, additional disorder in our devices can originate from the formation of the tunnel probes as their leads may induce additional stress on the nanowires. However, we emphasize that the tunneling spectroscopy performed by probe P0 in our devices regularly reports subgap states sensitive to electric fields and with high g factor - comparable to subgap states commonly detected in standard two-terminal and three-terminal InSb-Al hybrids that use gate-defined tunnel barriers (same as P0) and have no nm-thick AlOx probes.

A recent work on three-terminal nanowire hybrids has used non-local measurements to study the hybrid bulk [33]. There, finite non-local conductance signals arising at low bias voltages and high positive super gate voltages have been interpreted as closing of an induced superconducting gap in the hybrid bulk due to an electrostatic effect of the super gate. In our work, however, no gap-closing at positive super gate voltages is detected in the hybrid bulk. A possible reason for this is that the bulk states giving rise to the non-local signals are nanowire states that are weakly coupled or even non-coupled to the superconductor. Therefore, such predominantly semiconducting states could contribute weakly to the tunneling spectroscopy signals in our work, since our probes couple most strongly to the nanowire region near the Al facet.

6.4. CONCLUSION

We develop a new type of tunnel probes for tunneling spectroscopy of hybrid InSb-Al nanowires. These probes use a nm-thick layer of AlOx as a tunnel barrier that is created by in-situ oxidation of the superconducting Al shell on the nanowires. Normal or superconducting leads defined by shadow-wall lithography technique on top of the AlOx layer are used to probe the nanowire hybrids in tunneling spectroscopy conductance and supercurrent measurements. We demonstrate that such probes provide an alternative way of measuring subgap spectra at the nanowire ends, and therefore can replace standardly used tunnel probes defined by local gates. This allows for full elimination of gate-defined tunnel barriers in future devices and significant diminishing of smooth potential profiles that inevitably arise due to semiconducting junctions of gate-defined tunnel probes in hybrid nanowires. Furthermore, the tunnel probes with AlOx tunnel barriers can be defined at any position along a hybrid nanowire and therefore can be used to directly probe the hybrid bulk. We exploit this advantage and utilize these tunnel probes to study the longitudinal dependence of the subgap spectra in multiple hybrid nanowires. As a result, we identify Andreev bound states of various extension at the ends and inside the bulks of the hybrids. Our work offers a new way of investigating the bulk-edge correspondence in superconducting-semiconducting nanowires.

6.5. SUPPLEMENTARY MATERIALS

6.5.1. DEVICE FABRICATION

In this work, intrinsic Si wafers covered with 285 nm SiO_2 were used as substrates. On top of the SiO_2 layer, gates were lithographically defined and grown by depositing 3/17 nm Ti/Pd in an electron-beam evaporator. After that, atomic layer deposition (ALD) was used to grow $\sim$20 nm high-quality HfO_2 at 110°C to serve as the gate dielectric. Next, shadow-walls were defined on top of the HfO_2 layer. In this step, FOx-25 (HSQ) was first spun at 1.5 krpm for 1 min and hot-baked at 180°C for 2 min. Then, the HSQ layer was lithographically patterned and developed with MF-321 at 60°C for 5 min. After the formation of the HSQ shadow-walls, stemless InSb nanowires were precisely deposited on top of the gates by an optical nano-manipulator. Fig. 6.6A displays the nanowire (light blue), gates (grey) and shadow-walls (lilac) before further fabrications.

Figure 6.6B shows the deposition of the superconducting Al film. In this step, several sub-steps were carried out. First, the native oxide on the surface of the InSb nanowire was removed by a gentle hydrogen cleaning. Then, Al film was grown at a temperature of 140 K. The Al was deposited at an angle of 30° with respect to the substrate and with a flux of 5.5 nm (this is an aimed value and the actual thickness can be different, see Fig. 6.7). Due to the hexagonal nanowire cross-section and the specific deposition angle, three facets of the nanowire are covered with Al. As the direction of the Al flux is perpendicular to one facet, the thickness of the Al film on this facet corresponds to the flux. The Al flux forms angles of 30° with other two facets and the substrate. Consequently, the Al film thickness there is half of the flux. The Al growth was followed by in-situ oxidation in the load lock chamber of the evaporator. Here, the Al film was oxidized for 10 min at 10 Torr oxygen pressure. This was precisely controlled such that the Al film on one nanowire facet (where it is thicker) is partially oxidized and the Al film on the other two nanowire facets (where it is thinner) and on the substrate is fully oxidized. Therefore, the superconducting Al remains only on one nanowire facet. On this facet, it is covered by the thin dielectric AlOx layer which continuously extends over the other two nanowire facets and the substrate - as the Al there has been completely turned into AlOx (see Fig. 6.7). The full oxidation of the Al on the substrate was additionally confirmed by measuring high resistance ($\sim$ GΩ) of Al films on chips without nanowires after the same Al deposition and in-situ oxidation steps. The thin AlOx layer on top of the InSb-Al nanowire would serve as tunnel barriers for tunnel probes, which are fabricated in the next step.

After the oxidation in the load lock chamber, the sample was warmed up to room temperature and then it was inserted back into the evaporation chamber. As shown in Fig. 6.6C, 80 nm Ag was deposited at an angle of 18° with respect to the substrate. Due to the smaller deposition angle in comparison to the Al deposition

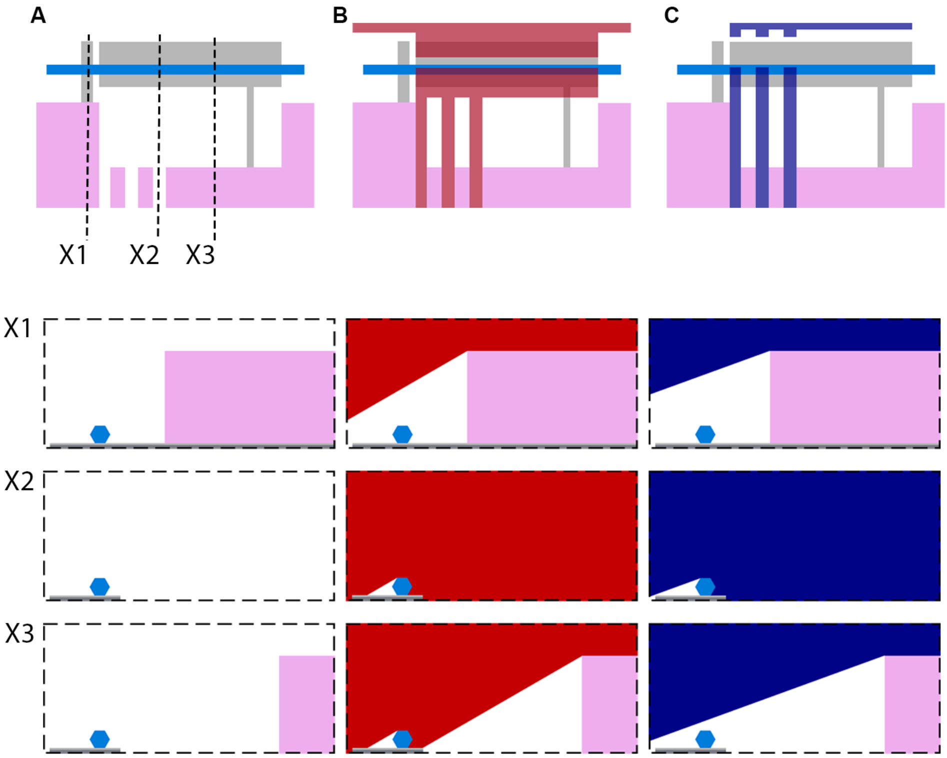

Figure 6.6: **Device fabrication by shadow-wall lithography**: (**A**) A schematic representation of the top view on a substrate with a nanowire (light blue), gates (grey) and shadow-walls (lilac). Dashed black lines denote three transverse cross sections X1, X2 and X3 depicted below. (**B**) A schematic representation of the top view on the substrate and X1, X2 and X3 cuts for the Al (red) deposition at 30° with respect to the substrate. (**C**) Analogous to (B), but for the Ag (navy) deposition at 18° with respect to the substrate. Due to the smaller angle, the shadow-walls create longer shadows during the Ag deposition and three probes are selectively defined along the nanowire.

at 30°, the shadow-walls cast longer shadows and block the growth of Ag on the nanowire sections aligned with the shadow-walls. Consequently, Ag reaches the nanowire only through the interruptions in the shadow-walls, which determine the positions of the three Ag leads along the hybrid. These leads are grown on top of the previously formed AlOx layer and are used as probes P1, P2 and P3. The described Ag deposition was performed for Device 1 and 2. For Device 3, the probes P1, P2 and P3 are made of thick Al rather than Ag, while keeping all the other parameters unchanged.

A transmission electron microscopy (TEM) analysis of a transverse cross-section of a hybrid nanowire device with Ag leads is made and shown in Fig. 6.7. From the figure, we see that the device is composed of materials as designed. On the top and bottom-right facets of the nanowire, O appears where Al exists, indicating a fully oxidized Al layer on these two facets. For top-right facet, O only exists on the surface of the Al layer, leading to an oxidized layer on the surface. From the bottom three panels in Fig. 6.7, we observe that the atomic fraction of Al is always higher than that of O. Though the reason is not known yet, we are confident that the Al layer with O is oxidized enough to be insulating, as the planar SIN junction in Fig. 6.1F is fabricated with similar oxidation condition and the planar junction exhibits appealing tunneling spectroscopy results. Besides, we see that the element Ag appears in the Al region on the top-right facet and the reason is not known yet to us. In addition, we see that the thickness of the AlOx and Al layers in TEM cuts is a bit different from the designed values. However, the device functionality is not influenced.

The normal probe P0 and the drain contact were fabricated ex-situ after the growth of probes P1, P2 and P3. First, the two contacts were lithographically defined at the nanowire ends. Then, Ar ion milling was used to remove the native oxide (for the contact of probe P0) and the AlOx layer (for the drain contact), where also the Al can be affected by the Ar ion milling. Finally, 10/120 nm of Ti/Au was deposited in an electron-beam evaporation step followed by lift-off.

6

For the fabrication of the planar tunnel junction (Fig. 6.1F), a substrate with specifically designed shadow-walls and without gates and nanowires was used. The Al film was deposited and then in-situ oxidized at the pressure of 1 Torr. Next, the Ag film was deposited. See details in Ref. *(32)* cited in the main text.

6.5.2. MEASUREMENT SETUPS

The measurements were performed at a base temperature of $\sim 20\,\mathrm{mK}$ inside a dilution refrigerator equipped with a superconducting vector magnet. As shown in Fig. 6.8, three voltage-bias setups (V1, V2 and V3) are used for conductance measurements and two current-bias setups (I1 and I2) are used for supercurrent measurements. Table 6.1 summarizes the used measurement setups for each figure and corresponding serial resistance in each setup is provided as well. In the following paragraphs, we will discuss each measurement setup in Fig. 6.8 in detail.

In the voltage-bias setups (V1, V2 and V3), dc-voltage sources are used to set dc-components of the bias voltages (V_b) and current-meters are used to measure dc-components of the currents (I). Lock-in amplifiers are used to apply ac-components of the bias voltages (dV_b with amplitudes of $10\,\mu$V) and measure ac-components of the currents (dI) - in order to obtain the differential conductance (G). The values of the dc- and ac-bias voltages are corrected for the voltage drops across a serial resistance R_s as $V_b \rightarrow V_b - IR_s$ and $dV_b \rightarrow dV_b - dIR_s$ (R_s for each setup is given in Table 6.1). The differential conductance at the dc bias voltage of $V_b - IR_s$ is $G = dI/(dV_b - dIR_s)$.

Setup V1 represents a two-terminal voltage-bias setup where a bias voltage $V_b + dV_b$ is applied to a single probe and a current $I + dI$ is measured in the drain

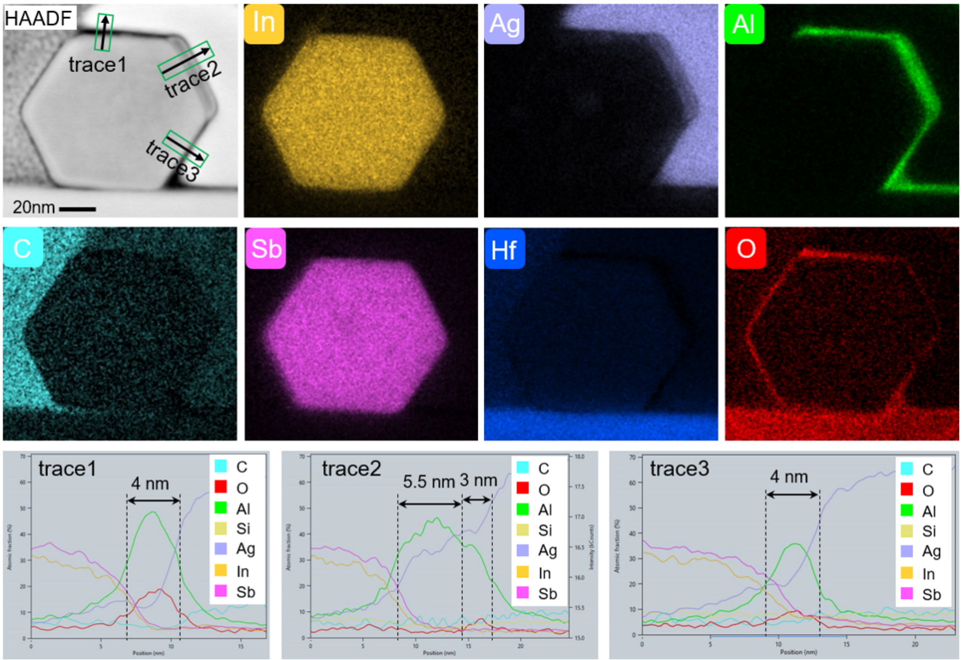

Figure 6.7: **Transmission electron microscopy (TEM) analysis of a transverse cross-section of a hybrid nanowire**. (1) The most left panel in the first row is the high-angle annular dark-field scanning transmission electron microscopy (HAADF STEM) image of the cross-section. Three linecuts of the integrated atomic fractions within the green boxes are shown in the third row. (2) The right three panels in the first row and the four panels in the second row display the energy-dispersive X-ray spectroscopy (EDX) composite maps of different elements, including In, Ag, Al, C, Sb, Hf and O. (3) In the third row, atomic fractions of different elements along the three traces are shown. Traces 1, 2 and 3 come from the top, top-right and bottom-right facet of the hybrid nanowire, respectively. The top and bottom-right facet both have ~4nm of Al, as well as ~4nm of O - indicating fully oxidized facets. For the top-right facet, the AlOx layer is a bit thinner (~3nm). The thickness of the Al layer without oxide is ~5.5nm.

contact. The three remaining probes are floating. Fig. 6.8A shows Setup V1 with the bias voltage applied to the probe P1. The serial resistance $R_s = 8.89\,\mathrm{k\Omega}$ includes the resistances of the two fridge lines and the series resistances of the voltage source, current-meter and low-pass filters on the PCB. When the differential conductance is high, even a slight overestimation of R_s may cause obtaining falsely negative G - due to the negative value of $dV_b - dIR_s$. This is the reason for the large negative values in the traces of Fig. 6.2. The setup can be applied analogously to any other probe.

In Setup V2 bias voltages $V_{b1} + dV_{b1}$ and $V_{b2} + dV_{b2}$ are applied to two probes and a current $I + dI$ is measured in the drain contact. The remaining two probes are

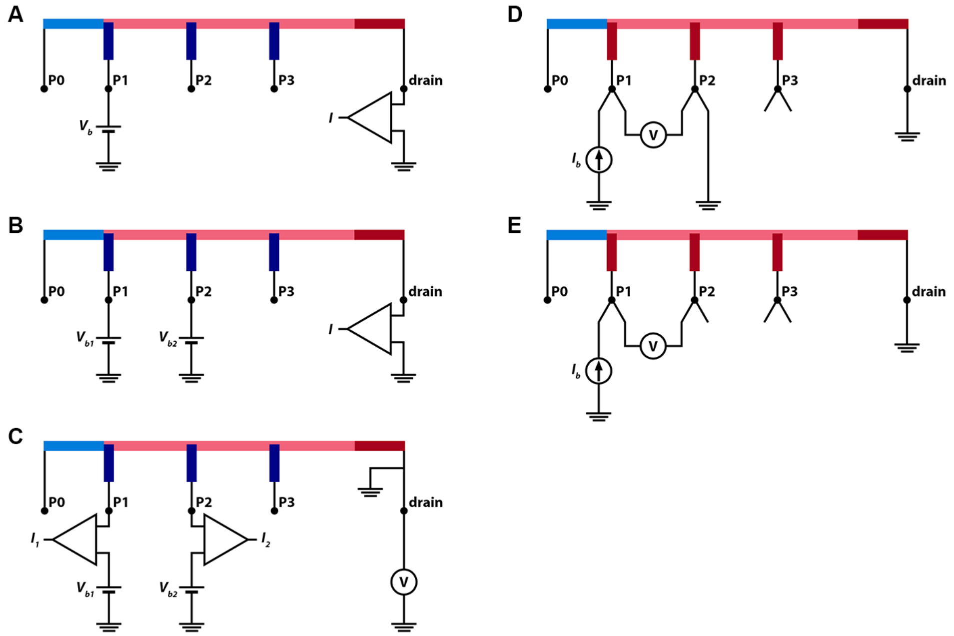

Figure 6.8: **Measurement setups**: Each panel contains a schematic representation of the nanowire device with the four probes P0, P1, P2 and P3 and the drain lead. Five panels represent the five measurement setups: (**A**) Setup V1, (**B**) Setup V2, (**C**) Setup V3, (**D**) Setup I1 and (**E**) Setup I2. For each setup, any probe or pair of probes can be chosen to be analogously connected as in the shown examples.

floating. Fig. 6.8B shows Setup V2 with the bias voltages applied to the probes P1 and P2. Two lock-in amplifiers are used for applying dV_{b1} (lock-in1 at frequency f_1) and dV_{b2} (lock-in2 at frequency f_2). Upon setting a parameter value (magnetic field or gate voltage), the dc-bias voltages are consecutively swept on the two probes and the differential conductance is measured by the corresponding lock-in amplifier. For instance, V_{b1} is swept and the lock-in1 is used to measure the ac-current dI in the drain, while both V_{b2} and dV_{b2} are fixed at zero (P2 is an inactive probe in this case). Then, V_{b2} is swept and the lock-in2 is used to measure the ac-current dI in the drain, while both V_{b1} and dV_{b1} are fixed at zero (P1 is an inactive probe in this case). Consequently, the inactive probe is effectively grounded and the ac-current dI in the drain has the frequency f_i while the dc-bias voltage V_{bi} is being swept ($i = 1, 2$). Grounding the inactive probe opens an additional channel for current that does not flow through the drain contact. Consequently, this could cause underestimations of the dc-current I and the ac-current dI. However, the additional channel has a resistance of the order of hundreds of kΩ (if probe P1, P2 or P3 is grounded), or even of the order of MΩ (if probe P0 is grounded), see the red traces in Fig. 6.2. These resistances are much higher than the resistance in

Setup (R_s) / Fig. 6. ...	V1 (8.89 kΩ)	V2 (8.89 kΩ)	V3 (5.81 kΩ)	I1	I2
1	×				
2	×				
3					×
4		×			
5A		×			
5B	×				
9				×	
10			×		
11	×				
12A		×			
12B			×		
13			×		
14		×			
15		×			
16		×			
17			×		
18	×				
19A	×				
19B					×

Table 6.1: List of figures with corresponding measurement setups marked in grey.

the line of the drain contact (order of few kΩ). Therefore, the current in Setup V2 are predominantly drained by the drain contact and the underestimation due to the additional channel is negligible. This is additionally confirmed in Fig. 6.11, where the conductance measured by probe P1 does not change upon changing probe P0 from a pinch-off to a tunneling regime. Upon disconnecting P1 and P2 in Fig. 6.8B, the setup can be analogously applied to any other pair of probes.

In Setup V3 bias voltages $V_{b1} + dV_{b1}$ and $V_{b2} + dV_{b2}$ are applied to two probes and currents $I_1 + dI_1$ and $I_2 + dI_2$ are measured in these probes while the drain contact is connected to the cold-ground. The remaining two probes are floating. An additional voltmeter is used to detect the cold-ground fluctuation and correct the bias voltages. Fig. 6.8C shows Setup V3 with the bias voltages applied to the probes P1 and P2. Two lock-in amplifiers are used for applying dV_{b1} (lock-in1 at frequency f_1) and dV_{b2} (lock-in2 at frequency f_2). As in Setup V2, upon setting a parameter value (magnetic field or gate voltage), the dc-bias voltages are consecutively swept on the two probes and the differential conductance is measured by the corresponding lock-in amplifier. While the dc-bias voltage is swept at one probe, the other probe is kept effectively grounded, as explained for Setup V2. The serial resistance for each probe is $R_s = 5.81\,\mathrm{k\Omega}$, smaller than that in Setup V2, as the drain contact is connected to the cold-ground. Upon disconnecting P1 and P2 in Fig. 6.8C, the setup can be analogously applied to any other pair of probes.

The use of Setup V2 and Setup V3 is motivated by an advantage to reliably examine the correlation behaviors between two probes. In contrast to Setup V1, the bias voltage is swept consecutively on both probes at each gate or magnetic field set point. This allows for a direct examination of the correlation between the subgap spectra in the two probes. Even if drifts in the device or setup are present, they appear at the same gate or field set point in both probes, and thus do not complicate the evaluation of the correlation in Setup V2 and Setup V3.

In spite of different setups being in use, we do not see that switching between different configurations influences the electrostatic environment. As it can be seen in Fig. 6.18, changing the setups does not affect the measured subgap spectra.

In the current-bias setups (I1 and I2), dc-current sources are used to set dc-bias currents (I_b) and voltmeters are used to measure dc-voltage drops (V). In order to allow for four-terminal configurations, each probe is connected to two fridge lines. Probe P0 is kept floating in the current-bias measurements.

In Setup I1 a bias current I_b is applied between two probes (or between one probe and the drain). A voltage drop V is measured between the two probes (or between the probe and the drain). The remaining probes are floating. Fig. 6.8D shows Setup I1 with the bias current applied between the probes P1 and P2, and the voltage drop measured across the series of two Josephson junctions (JJ1 of P1 and JJ2 of P2). Upon disconnecting P1 and P2 in Fig. 6.8D, bias current can analogously be applied in the same setup between any other pair of probes (or a probe and the drain). Note that if two probes are connected in the setup, a series of two JJs is measured, and if one probe and the drain are connected in the setup, a series of a single JJ and the drain contact is measured. If the drain contact has a finite resistance, $I_b - V$ characteristics exhibit a finite slope instead of a plateau below the switching current of the junction.

In Setup I2 a bias current I_b is applied between one probe and the drain. A voltage drop V is measured between the probe and its first neighboring probe. The remaining probes are floating. Fig. 6.8E shows Setup I2 with the bias current applied to the probe P1, and the voltage drop measured between P1 and P2. Note that the current in P2 is zero and that the measured voltage drop corresponds to the voltage drop only across the Josephson junction of the probe that is current-biased (JJ1). Upon disconnecting P1 and P2 in Fig. 6.8D, bias current can analogously be applied in the same setup to any other probe. In contrast to Setup I1, $I_b - V$ characteristics exhibit a zero-voltage plateau below the switching current of the junction - as the voltmeter measures only the voltage drop across the junction.

Device 3 is first characterized at zero magnetic field and zero gate voltages by measuring $I_b - V$ characteristics in current-bias measurements. First, each superconducting probe (P1, P2 and P3) is connected with the drain contact as in Setup I1 (see the top row in Fig. 6.9). Then, each pair of the superconducting probes is connected as in Setup I1 (see the bottom row in Fig. 6.9). The six measured $I_b - V$ characteristics reveal a residual resistance of $R_{drain} \sim 8.2\,\mathrm{k\Omega}$ in the drain contact, as shown in Fig. 6.9. Therefore, the current-bias measurements of Device 3 are performed in Setup I2, such that voltage drops developed across the drain contact

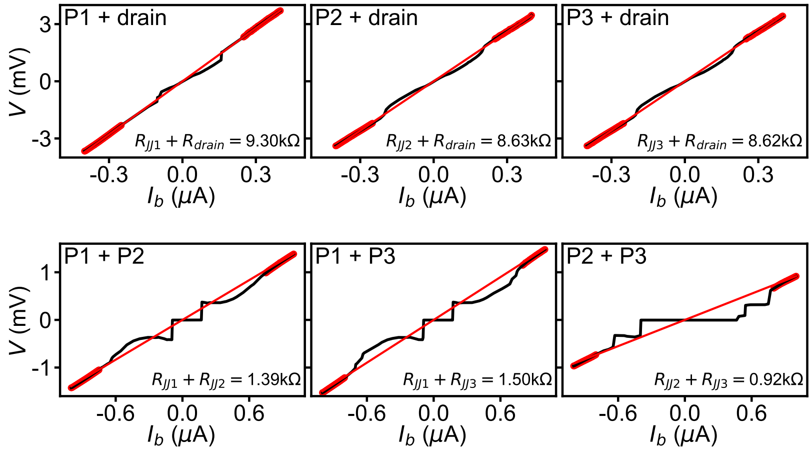

Figure 6.9: **Contact resistance of the drain in Device 3**: $I_b - V$ characteristics (black) obtained in current-bias measurements of Device 3 at zero field. The indicated pairs of leads are connected as in Setup I1. By fitting the characteristics at high bias (red) with linear functions, series resistances of two Josephson junctions or of one Josephson junction and the drain are obtained and denoted in the bottom-right corners. The resistances of the three Josephson junctions and the resistance of the drain contact are estimated to be: $R_{JJ1} \sim 1.1\,\mathrm{k}\Omega$, $R_{JJ2} \sim 0.4\,\mathrm{k}\Omega$, $R_{JJ3} \sim 0.5\,\mathrm{k}\Omega$ and $R_{drain} \sim 8.2\,\mathrm{k}\Omega$,.

are not measured. The residual resistance R_{drain} can be attributed to an incomplete removal of AlOx by the Ar ion milling during the ex-situ fabrication of the drain contact. In order to avoid voltage divider effects due to the residual drain resistance, the conductance measurements of Device 3 are performed only in Setup V1. Since the residual drain resistance is much smaller than the subgap resistance of the tunnel probes (hundreds of kΩ), applied bias voltages predominantly drop across the tunnel probes, and tunneling spectroscopy can reliably be performed in Setup V1.

Tunnel gate of Device 3 was not functional as it had a leakage to the nanowire - likely due to the Ar ion milling damaging the HfO_2 gate dielectric. Therefore, the tunnel gate of Device 3 was floating in all measurements.

6.5.3. EXTENDED DATA

Below we show additional measurement results that reproduce or supplement our findings presented in the main text.

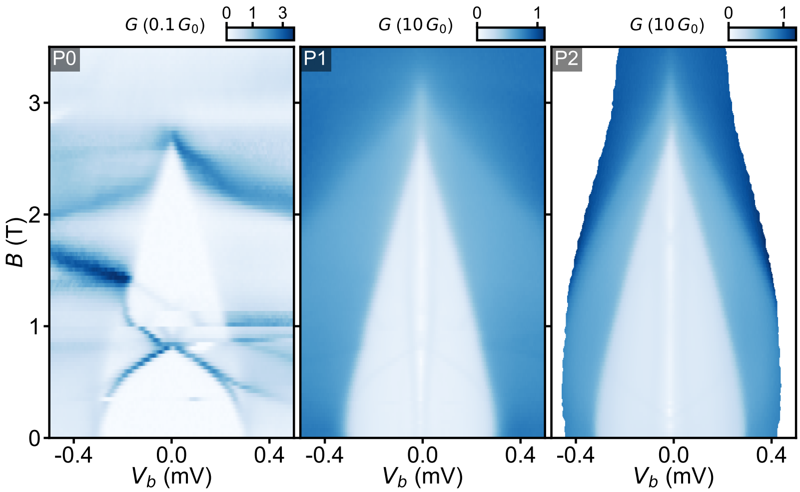

Figure 6.10: **Characterization of the tunnel probes by differential conductance measurements (Device 2)**: G as a function of V_b and B measured by probes P0, P1 and P2. First, probes P0 (left) and P1 (middle) are connected as in Setup V3, and then probes P1 and P2 (right) are connected as in Setup V3. Probe P3 of Device 2 is not functional. The gate voltages are $V_{TG} = 0.75\,\mathrm{V}$ and $V_{SG} = 0\,\mathrm{V}$. Subgap states in P1 and P2 cannot be resolved due to the sensitivity of the lock-in amplifier being adjusted to measure high out-of-gap conductance in these probes, similar as in Fig. 6.2.

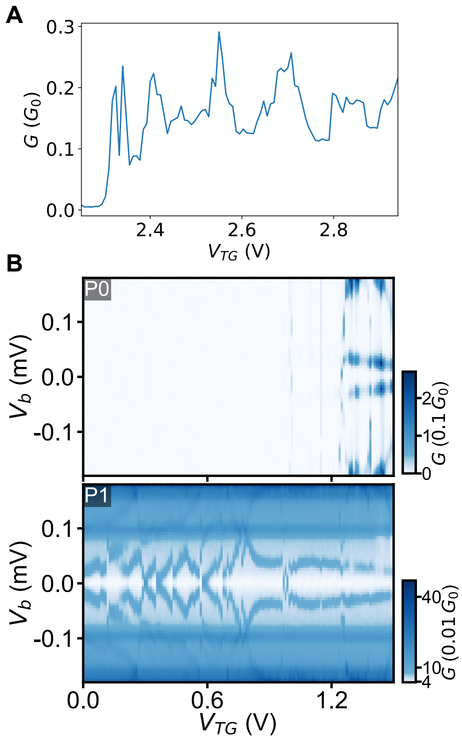

Figure 6.11: **Effect of the tunnel gate on the tunneling spectroscopy by probes P0 and P1 (Device 1)**. (**A**) G as a function of V_{TG} for P0 at a bias voltage of $-0.6\,\text{mV}$ with the super gate and other probes floating. The data is measured as in Setup V1. We would note that the pinch-off trace was taken with different parameter settings from panel (B). In spite of this, the panel shows that the tunnel gate is able to tune the semiconducting junction from a relatively open regime to a tunneling regime. (**B**) G as a function of V_b and V_{TG} measured by probes P0 and P1 connected as in Setup V2. A magnetic field of 0.23 T is applied perpendicular to the substrate - such that a subgap states is detected by P0 and P1- and $V_{SG} = 0.6\,\text{V}$. For V_{TG} above $\sim 1.2\,\text{V}$, the semiconducting junction of probe P0 is conductive and the subgap state is detectable by both probes. The same state can be detected by P1 while the junction of P0 is pinched-off.

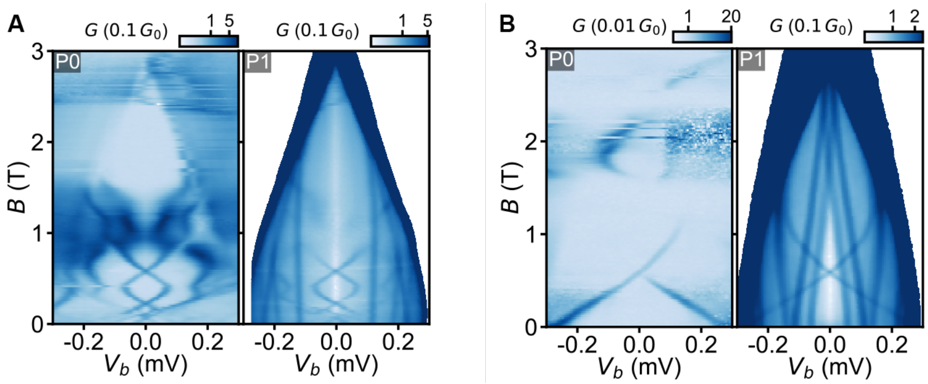

Figure 6.12: **Comparison between the tunneling spectroscopy by probes P0 and P1 with different parameter settings (Device 1)**: G as a function of V_b and B measured by probes P0 and P1 at **(A)** $V_{SG} = 0.6\text{V}$ and $V_{TG} = 1.5\text{V}$ and **(B)** at $V_{SG} = 0.6\text{V}$ and $V_{TG} = 2.12\text{V}$. The panel (A) is measured as in Setup V2 and the panel (B) is measured as in Setup V3.

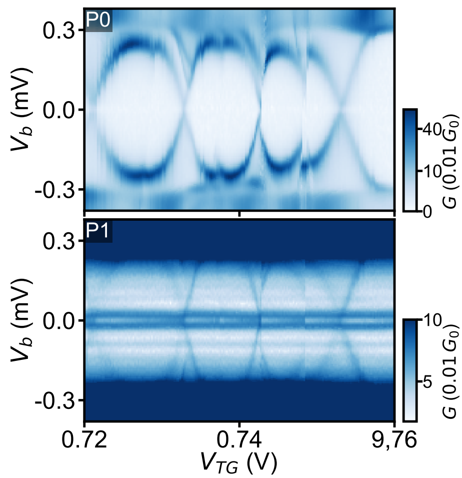

Figure 6.13: **Comparison between the tunneling spectroscopy by probes P0 and P1 (Device 2)**: G as a function of V_b and V_{TG} measured by probes P0 and P1 connected as in Setup V3, at $B = 0\text{T}$ and $V_{SG} = 0\text{V}$. Subgap states sensitive to the tunnel gate are detectable by both probes. Subgap states insensitive to the tunnel gate are only detectable by P1.

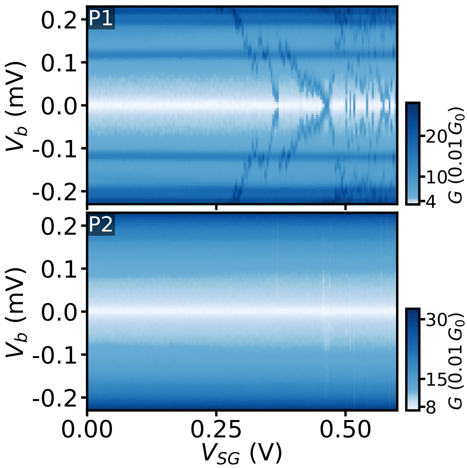

Figure 6.14: **Effect of the super gate on the tunneling spectroscopy by probes P1 and P2 (Device 1)**: G as a function of V_b and V_{SG} measured by probes P1 and P2 connected as in Setup V2. The tunnel gate is floating and $B = 0.34\,\mathrm{T}$. For V_{SG} above $\sim 0.4\,\mathrm{V}$, subgap states sensitive to the super gate are detected by P1. Also, subgap states insensitive to the super gate are detected by P1. None of these states are detectable by P2.

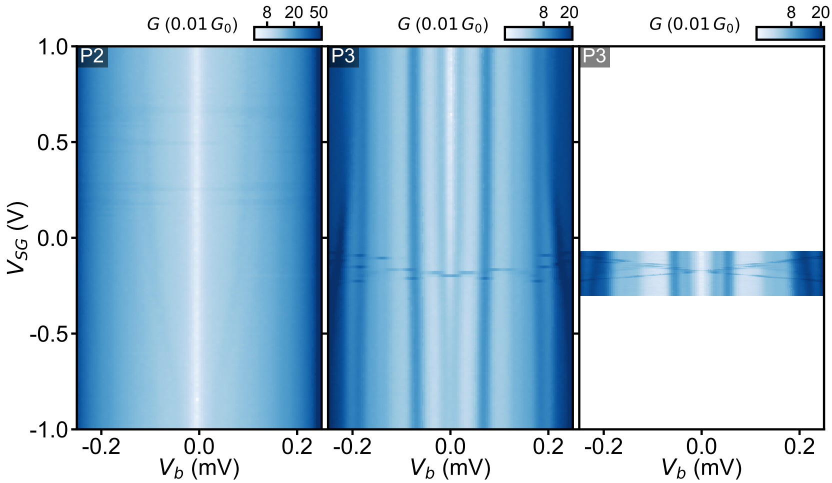

Figure 6.15: **Effect of the super gate on the tunneling spectroscopy by probes P2 and P3 (Device 1)**: G as a function of V_b and V_{SG} measured by probes P2 (left) and P3 (middle) connected as in Setup V2. The tunnel gate is floating and $B = 0.5\,\mathrm{T}$. A narrow V_{SG} range is remeasured by P3 in higher resolution (right). No subgap states are detected by P2. Subgap states weakly sensitive to the super gate and a single subgap state highly sensitive to the super gate are detected only by P3.

6

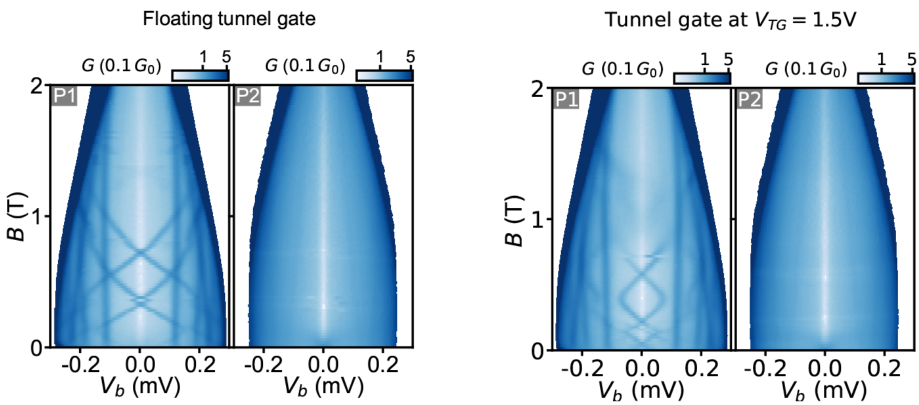

Figure 6.16: **Effect of the tunnel gate on the tunneling spectroscopy by probes P1 and P2 (Device 1)**: G as a function of V_b and B measured by probes P1 and P2 connected as in Setup V2, at $V_{SG} = 0.6\,\mathrm{V}$. The tunnel gate is floating (left) or set to $V_{TG} = 1.5\,\mathrm{V}$ (right). Only the subgap states with high g factor at the end of the hybrid are sensitive to the tunnel gate regime. All other properties of the spectra are not affected by the tunnel gate regime.

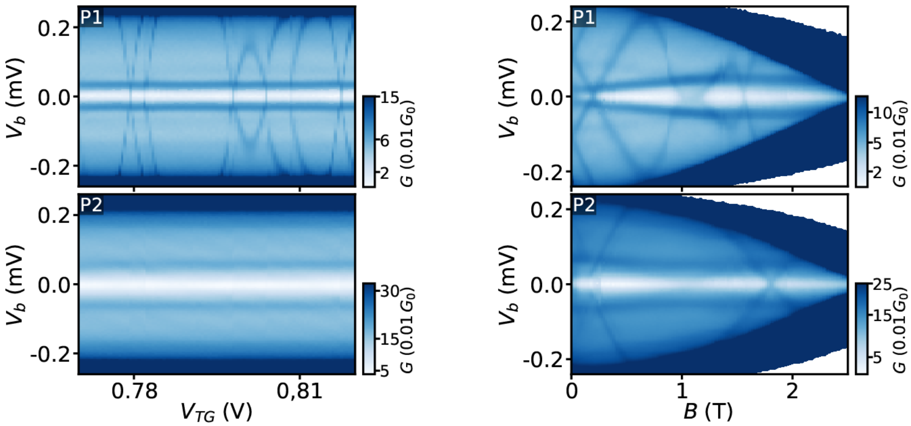

Figure 6.17: **Effect of the tunnel gate and parallel magnetic field on the tunneling spectroscopy by probes P1 and P2 (Device 2)**: G as a function of V_b and V_{TG} (left) or B (right) measured by probes P1 and P2 connected as in Setup V3, at $V_{SG} = 0$V. B is fixed at 0.6T in the gate sweep and V_{TG} is fixed at 0.81V in the field sweep. Multiple subgap states with high g factor are detected by single probes. A subgap state tunable by the tunnel gate is detected only by P1. This implies that all the subgap states are localized within ~ 200nm along the hybrid.

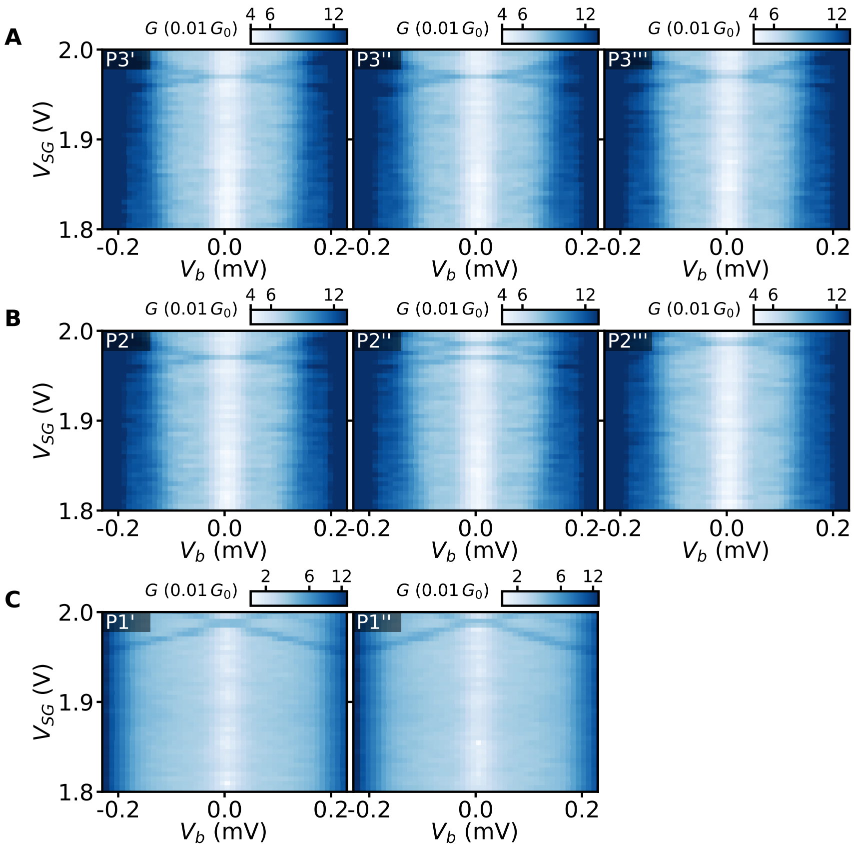

Figure 6.18: **An example of a subgap state detectable by multiple probes (Device 3)**: G as a function of V_b and V_{SG} measured by probes: (**A**) P3, (**B**) P2 and (**C**) P1 consecutively connected as in Setup V1, at $B = 1\,\mathrm{T}$. The measurements are performed in the order P3-P2-P1. The super gate is swept over the same voltage range multiple times for each probe in order to check the charge stability of the electrostatic environment (repeated measurements are shown in the same row of (A-C)). A single subgap state is detected by both P3 and P2. This state is sensitive to a charge jump observed in the second measurement by P2. The same state appears shifted in the third measurement by P2. A subgap state in the same V_{SG} range is detected by P1. However, the lever arm of the super gate in this measurement is different – meaning that the subgap state detected by P1 may be different from the one detected by the other two probes.

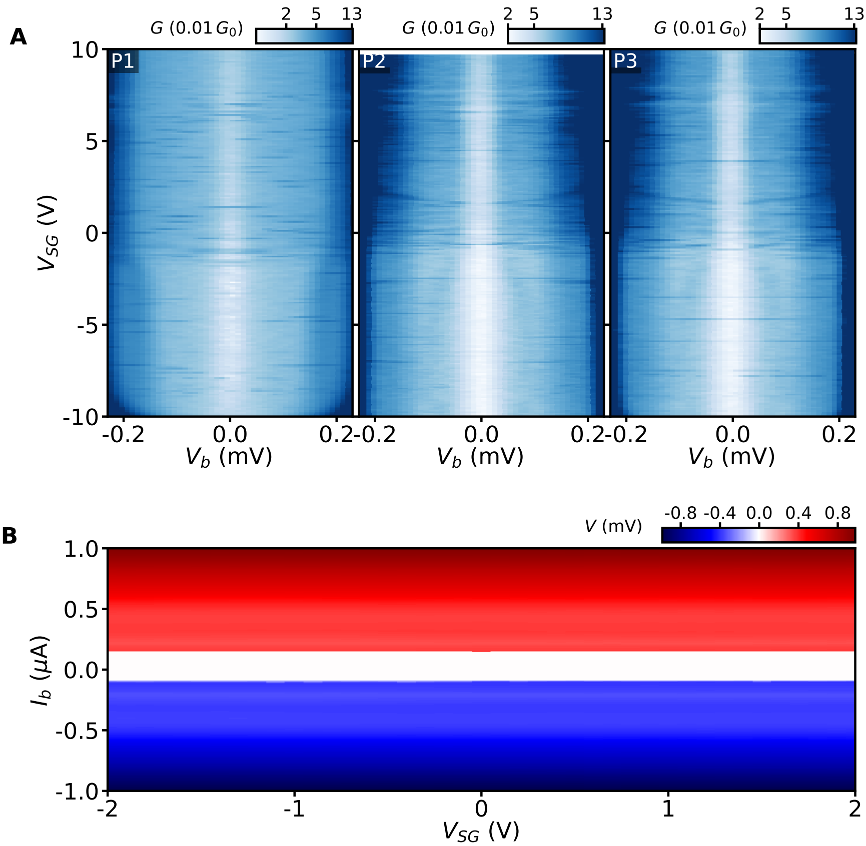

Figure 6.19: **Effects of the super gate over broad voltage ranges (Device 3)**: (**A**) G as a function of V_b and V_{SG} measured by probes P1, P2 and P3 consecutively connected as in Setup V1. The tunnel gate is floating and $B = 1\,\mathrm{T}$. (**B**) V as a function of I_b and V_{SG} at zero magnetic field. Probes P1 and P2 are connected as in Setup I2, with the bias current applied to P1.

REFERENCES

[1] A. Y. Kitaev. “Unpaired Majorana fermions in quantum wires”. In: *Phys. Usp.* 44 (2001), pp. 131–136.

[2] A. Y. Kitaev. “Fault-tolerant quantum computation by anyons”. In: *Annals Phys.* 303 (2003), pp. 2–30.

[3] C. Nayak, S. H. Simon, A. Stern, M. Freedman, and S. D. Sarma. “Non-Abelian anyons and topological quantum computation”. In: *Rev. Mod. Phys.* 80 (2008), p. 1083.

[4] S. D. Sarma, M. Freedman, and C. Nayak. “Majorana zero modes and topological quantum computation”. In: *npj Quantum Inf.* 1 (2015), p. 15001.

[5] Y. Oreg, G. Refael, and F. von Oppen. “Helical liquids and Majorana bound states in quantum wires”. In: *Phys. Rev. Lett.* 105 (2010), p. 177002.

[6] R. M. Lutchyn, J. D. Sau, and S. D. Sarma. “Majorana fermions and a topological phase transition in semiconductor-superconductor heterostructures”. In: *Phys. Rev. Lett.* 105 (2010), p. 077001.

[7] R. Aguado. “Majorana quasiparticles in condensed matter”. In: *La Riv. del Nuovo Cim.* 40 (2017), p. 523.

[8] R. M. Lutchyn, E. P. A. M. Bakkers, L. P. Kouwenhoven, P. Krogstrup, C. M. Marcus, and Y. Oreg. “Majorana zero modes in superconductor–semiconductor heterostructures”. In: *Nat. Rev. Mater.* 3 (2018), pp. 52–68.

[9] E. Prada, P. San-Jose, M. W. A. de Moor, A. Geresdi, E. J. H. Lee, J. Klinovaja, D. Loss, J. Nygard, R. Aguado, and L. P. Kouwenhoven. “From Andreev to Majorana bound states in hybrid superconductor–semiconductor nanowires”. In: *Nat. Rev. Phys.* 2 (2020), pp. 575–594.

[10] V. Mourik, K. Zuo, S. M. Frolov, S. R. Plissard, E. P. A. M. Bakkers, and L. P. Kouwenhoven. “Signatures of Majorana fermions in hybrid superconductor-semiconductor nanowire devices”. In: *Science* 336 (2012), pp. 1003–1007.

[11] A. Das, Y. Ronen, Y. Most, Y. Oreg, M. Heiblum, and H. Shtrikman. “Zero-bias peaks and splitting in an Al–InAs nanowire topological superconductor as a signature of Majorana fermions”. In: *Nat. Phys.* 8 (2012), pp. 887–895.

[12] M. T. Deng, C. L. Yu, G. Y. Huang, M. Larsson, P. Caroff, and H. Q. Xu. “Anomalous zero-bias conductance peak in a Nb–InSb nanowire–Nb Hybrid device”. In: *Nano Lett.* 12 (2012), pp. 6414–6419.

[13] E. Prada, P. San-Jose, and R. Aguado. “Transport spectroscopy of NS nanowire junctions with Majorana fermions”. In: *Phys. Rev. B* 86 (2012), 180503(R).

[14] A. Vuik, B. Nijholt, A. R. Akhmerov, and M. Wimmer. “Reproducing topological properties with quasi-Majorana states”. In: *SciPost Phys.* 7 (2019), p. 061.

[15] J. Avila, F. Pe*ñ*aranda, E. Prada, P. San-Jose, and R. Aguado. “Non-hermitian topology as a unifying framework for the Andreev versus Majorana states controversy”. In: *Commun. Phys.* 2 (2019), p. 133.

[16] J.-Y. Wang, N. van Loo, G. P. Mazur, V. Levajac, F. K. Malinowski, M. Lemang, F. Borsoi, G. Badawy, S. Gazibegovic, E. P. A. M. Bakkers, M. Quintero-Pérez, S. Heedt, and L. P. Kouwenhoven. “Parametric exploration of zero-energy modes in three-terminal InSb-Al nanowire devices”. In: *Phys. Rev. B* 106 (2022), p. 075306.

[17] H. Pan and S. D. Sarma. “Physical mechanisms for zero-bias conductance peaks in Majorana nanowires”. In: *Phys. Rev. Research* 2 (2020), p. 013377.

[18] T. Ö. Rosdahl, A. Vuik, M. Kjaergaard, and A. R. Akhmerov. “Andreev rectifier: A nonlocal conductance signature of topological phase transitions”. In: *Phys. Rev. B* 97 (2018), p. 045421.

[19] S. Ahn, H. Pan, B. Woods, T. D. Stanescu, and S. D. Sarma. “Estimating disorder and its adverse effects in semiconductor Majorana nanowires”. In: *Phys. Rev. Mater.* 5 (2021), p. 124602.

[20] B. D. Woods, S. D. Sarma, and T. D. Stanescu. “Charge-impurity effects in hybrid Majorana nanowires”. In: *Phys. Rev. Applied* 16 (2021), p. 054053.

[21] A. Grivnin, E. Bor, M. Heiblum, Y. Oreg, and H. Shtrikman. “Concomitant opening of a bulk-gap with an emerging possible Majorana zero mode”. In: *Nat. Comm.* 10 (2019), p. 1940.

[22] S. Takei, B. M. Fregoso, H.-Y. Hui, A. M. Lobos, and S. Das Sarma. “Soft Superconducting Gap in Semiconductor Majorana Nanowires”. In: *Phys. Rev. Lett.* 110 (18 2013), p. 186803.

[23] S. Heedt, M. Quintero-Pérez, F. Borsoi, A. Fursina, N. van Loo, G. P. Mazur, M. P. Nowak, M. Ammerlaan, K. Li, S. Korneychuk, J. Shen, M. Y. van de Poll, G. Badawy, S. Gazibegovic, N. de Jong, P. Aseev, K. van Hoogdalem, E. P. A. M. Bakkers, and L. P. Kouwenhoven. “Shadow-wall lithography of ballistic superconductor–semiconductor quantum devices”. In: *Nat. Commun.* 12 (2021), p. 4914.

[24] F. Borsoi, G. P. Mazur, N. van Loo, M. P. Nowak, L. Bourdet, K. Li, S. Korneychuk, A. Fursina, J.-Y. Wang, V. Levajac, E. Memisevic, G. Badawy, S. Gazibegovic, K. van Hoogdalem, E. P. A. M. Bakkers, L. P. Kouwenhoven, S. Heedt, and M. Quintero-Pérez. “Single-shot fabrication of semiconducting–superconducting nanowire devices”. In: *Adv. Func. Mater.* 31 (2021), p. 2102388.

[25] G. Badawy, S. Gazibegovic, F. Borsoi, S. Heedt, C.-A. Wang, S. Koelling, M. A. Verheijen, L. P. Kouwenhoven, and E. P. A. M. Bakkers. “High mobility stemless InSb nanowires”. In: *Nano Lett.* 19.6 (2019), pp. 3575–3582.

[26] C.-X. Liu, B. van Heck, and M. Wimmer. “Josephson current via an isolated Majorana zero mode”. In: *Phys. Rev. B* 103 (2021), p. 014510.

[27] C. Schrade and L. Fu. “Andreev or Majorana, Cooper finds out”. In: *arXiv:1809:06370* (2018).

[28] C. Schrade and L. Fu. “Majorana Superconducting Qubit”. In: *Phys. Rev. Lett.* 121 (2018), p. 267002.

[29] C. Schrade, S. Hoffman, and D. Loss. “Detecting topological superconductivity with ϕ_0-Josephson junctions”. In: *Phys. Rev. B* 95 (2017), p. 195421.

[30] J. D. S. Bommer, H. Zhang, Ö. Gül, B. Nijholt, M. Wimmer, F. N. Rybakov, J. Garaud, D. Rodic, E. Babaev, M. Troyer, D. Car, S. R. Plissard, E. P. A. M. Bakkers, K. Watanabe, T. Taniguchi, and L. P. Kouwenhoven. “Spin-orbit protection of induced superconductivity in Majorana nanowires”. In: *Phys. Rev. Lett.* 122 (2019), p. 187702.

[31] M. W. A. de Moor, J. D. S. Bommer, D. Xu, G. W. Winkler, A. E. Antipov, A. Bargerbos, G. Wang, N. van Loo, R. L. M. O. het Veld, S. Gazibegovic, D. Car, J. A. Logan, M. Pendharkar, J. S. Lee, E. P. A. M. Bakkers, C. J. Palmstrøm, R. M. Lutchyn, L. P. Kouwenhoven, and H. Zhang. “Electric field tunable superconductor-semiconductor coupling in Majorana nanowires”. In: *New J. Phys.* 20 (2018), p. 103049.

[32] G. P. Mazur, N. van Loo, J.-Y. Wang, T. Dvir, G. Wang, A. Khindanov, S. Korneychuk, F. Borsoi, R. C. Dekker, G. Badawy, P. Vinke, S. Gazibegovic, E. P. A. M. Bakkers, M. Q. Pérez, S. Heedt, and L. P. Kouwenhoven. “Spin-mixing enhanced proximity effect in aluminum-based superconductor–semiconductor hybrids”. In: *Adv. Mater.* 34 (2022), p. 2202034.

[33] N. van Loo, G. P. Mazur, T. Dvir, G. Wang, R. C. Dekker, J.-Y. Wang, M. Lemang, C. Sfiligoj, A. Bordin, D. van Driel, G. Badawy, S. Gazibegovic, E. P. A. M. Bakkers, and L. P. Kouwenhoven. “Electrostatic control of the proximity effect in the bulk of semiconductor-superconductor hybrids”. In: *Nat. Commun.* 14 (2023), p. 3325.

[34] G. L. R. Anselmetti, E. A. Martinez, G. C. Ménard, D. Puglia, F. K. Malinowski, J. S. Lee, S. Choi, M. Pendharkar, C. J. Palmstrøm, C. M. Marcus, L. Casparis, and A. P. Higginbotham. “End-to-end correlated subgap states in hybrid nanowires”. In: *Phys. Rev. B* 100 (2019), p. 205412.

[35] G. C. Ménard, G. L. R. Anselmetti, E. A. Martinez, D. Puglia, F. K. Malinowski, J. S. Lee, S. Choi, M. Pendharkar, C. J. Palmstrøm, K. Flensberg, C. M. Marcus, L. Casparis, and A. P. Higginbotham. “Conductance-matrix symmetries of a three-terminal hybrid device”. In: *Phys. Rev. Lett.* 124 (2020), p. 036802.

[36] C. Jünger, R. Delagrange, D. Chevallier, S. Lehmann, K. A. Dick, C. Thelander, J. Klinovaja, D. Loss, A. Baumgartner, and C. Schönenberge. “Magnetic-field-independent subgap states in hybrid Rashba nanowires”. In: *Phys. Rev. Lett.* 125 (2020), p. 017701.

7

HARD SUPERCONDUCTING GAP IN GERMANIUM

The co-integration of spin, superconducting, and topological systems is emerging as an exciting pathway for scalable and high-fidelity quantum information technology. High-mobility planar germanium is a front-runner semiconductor for building quantum processors with spin-qubits, but progress with hybrid superconductor-semiconductor devices is hindered by the difficulty in obtaining a superconducting hard gap, that is, a gap free of subgap states. Here, we address this challenge by developing a low-disorder, oxide-free interface between high-mobility planar germanium and a germanosilicide parent superconductor. This superconducting contact is formed by the thermally-activated solid phase reaction between a metal, platinum, and the Ge/SiGe semiconductor heterostructure. Electrical characterization reveals near-unity transparency in Josephson junctions and, importantly, a hard induced superconducting gap in quantum point contacts. Furthermore, we demonstrate phase control of a Josephson junction and study transport in a gated two-dimensional superconductor-semiconductor array towards scalable architectures. These results expand the quantum technology toolbox in germanium and provide new avenues for exploring monolithic superconductor-semiconductor quantum circuits towards scalable quantum information processing.

The work in this chapter has been published as: A. Tosato, V. Levajac, J.-Y. Wang, C. J. Boor, F. Borsoi, M. Botifoll, C. N. Borja, S. Marti-Sánchez, J. Arbiol, A. Sammak, M. Veldhorst and G. Scappucci *"Hard superconducting gap in germanium"*, Communications Materials 4, 23 (2023)

7.1. INTRODUCTION

The intimate coupling between superconductors and semiconductors in hybrid devices is at the heart of exciting pursuits, including topological qubits with Majorana zero modes [1, 2], superconducting (Andreev) spin qubits [3], and gate-tunable superconducting qubits [4]. Combining hybrid devices with high-fidelity semiconductor spin qubits in a single material platform may resolve key challenges for scalable quantum information processing. In particular, quantum information transfer between spin and topological qubits [5–8] may enable a universal gate set for topological quantum computation and, conversely, superconductors may be used to coherently couple spin qubits at a distance via crossed Andreev reflection [5, 9] or topologically protected links [10].

The use of epitaxial superconducting Al to induce a hard superconducting gap in III-V semiconductors [11, 12] stimulated great progress with hybrid devices, leading to experimental reports of topological superconductivity in planar Josephson junctions [13] and in electrostatically defined quasi-1D wires [14], the demonstration of Andreev spin qubits [3], and the realization of a minimal Kitaev chain in coupled quantum dots [15]. However, spin qubits in III-V semiconductors suffer from the hyperfine interactions with the nuclear spin bath [16] that severely deteriorate their quantum coherence [17] and challenges their integration with hybrid devices.

On the other hand, spin qubits with quantum dots in Ge [18–21] can achieve long quantum coherence due to the suppressed hyperfine interaction [22] and the possibility of isotopic purification into a nuclear spin-free material [23]. Thanks to the light effective mass [24] and high mobility exceeding one million cm^2/Vs [25], holes in planar Ge/SiGe heterostructures have advanced semiconductors spin qubits to the universal operation on a 2×2 qubit array [26], and the shared control of a 16 semiconductor quantum dot crossbar array [27]. Moreover, the ability of holes to make contacts with low Schottky barrier heights to metals [28], including superconductors, makes Ge a promising candidate for hybrid devices. Initial work used superconducting Al to contact Ge either via thermal diffusion [29–31] or by deposition on the sidewalls of etched mesas [32, 33]. However, the key demonstration of a superconducting gap in Ge free of subgap quasiparticle states is lacking, challenged by the difficulty of contacting uniformly a buried quantum well (QW) with a superconductor, whilst maintaining the low disorder at the superconductor-semiconductor interface and in the semiconductor channel.

Here we address these challenges and demonstrate a hard superconducting gap in Ge. We contact the quantum well with a superconducting germanosilicide (PtSiGe), similar to the silicidation process used by the microelectronics industry for low resistance contacts [34]. The superconductor is formed uniformly within the heterostructure and reaches the buried quantum well via a controlled thermally-activated solid phase reaction between the metal (Pt) and the semiconductor stack (Ge/SiGe). This process is simple, robust, and does not require specialised vacuum conditions or etching because the superconductor-semiconductor interface is buried into the pure semiconducting heterostructure and consequently remains pristine. This represents a conceptually different approach compared to the subtractive nanofabrication processes commonly used for hybrid devices, since our additive process does not deteriorate the active area of the semiconductor. As a result, we demonstrate a suite of reproducible Ge hybrid devices with low disorder and excellent superconducting properties.

7.2. RESULTS

7.2.1. MATERIAL PROPERTIES

Our approach to superconductor-semiconductor hybrid devices in Ge is illustrated in Fig. 7.1a. We use an undoped and compressively-strained Ge quantum well, grown by chemical vapor deposition on a Si(001) wafer [35] and separated from the surface by a SiGe barrier (Methods). This heterostructure supports a two-dimensional hole gas (2DHG) with high mobility ($\sim 6\times10^5$ cm^2/Vs), long transport scattering time τ (~ 30 ps), and long mean free path ($\sim 7\,\mu$m) (Supplementary Fig. 7.6) and hosts high-performance spin-qubits [20]. Crucial for the reliable search of topological superconductivity [36] and for scaling to large spin-qubit architectures [37], the disorder in our buried Ge quantum wells is characterised by an energy level broadening $\hbar/2\tau$ of ~ 0.01 meV, which is more than one order of magnitude smaller than in the other material systems exhibiting a hard superconducting gap (Supplementary Table 7.1).

As shown by the schematics in Fig. 7.1a, we obtain PtSiGe contacts to the quantum well by room-temperature evaporation of a Pt supply layer, metal lift-off, and rapid thermal process at 400 °C (Methods). This low-temperature process preserves the structural integrity of the quantum well grown at 500 °C, whilst activating the solid phase reaction driving Pt into the heterostructure and Ge and Si into the Pt (Supplementary Fig. 7.8). As a result, low-resistivity germanosilicide phases are formed [38, 39] and under these process conditions the obtained PtSiGe films are superconducting with a $T_c \approx 0.5$ K and an in-plane critical field of $B_{c\parallel} \approx 400$ mT (Supplementary Fig. 7.7). Finally, we use patterned electrostatic gates, insulated by dielectric films in between, to accumulate charge carriers in the quantum well and to shape the electrostatic confinement potential of the hybrid superconductor-semiconductor devices (Methods). This approach to hybrid devices is different compared to the conventional process with 1D nanowires, where an epitaxial superconductor proximitizes the semiconductor region underneath. Because we do not perform any etch during the nanofabrication of hybrid devices, the low-disorder landscape that determines the 2DHG high mobility is likely to be preserved when further dimensional confinement is achieved by means of electrostatic gates. By contrast, for processes where etching of the superconductor is required, the fabrication of hybrid devices yields to mobility degradation [40].

The morphological, structural, and chemical properties of the hybrid devices are inferred by aberration corrected high-angle annular dark-field scanning transmission electron microscopy (HAADF-STEM) and electron energy-loss spectroscopy (EELS). Fig. 7.1b shows a HAADF-STEM image of a cross-section of a superconductor-normal-superconductor quantum point contact (SNS-QPC) taken off-center to visualise the two gate layers (Fig. 7.2a shows a top view of the device). We observe a uniform quantum well of high-crystalline quality, with sharp interfaces to

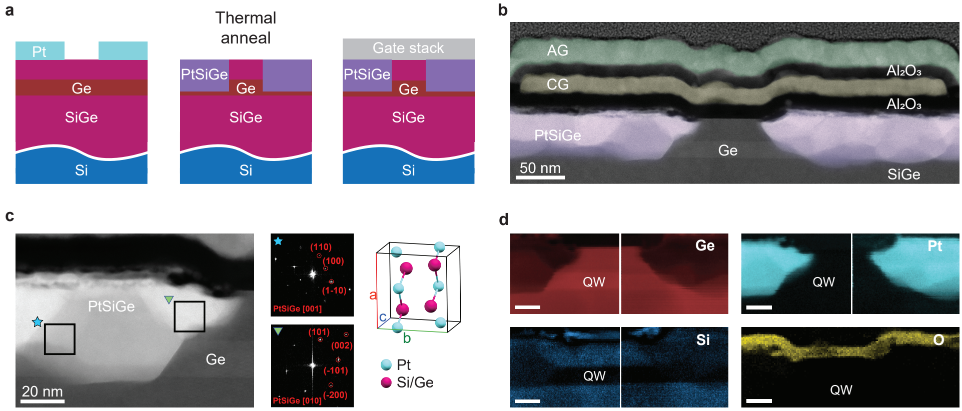

Figure 7.1: **Material properties of superconductor-semiconductor Ge devices. a**) Schematics of the fabrication process for a superconductor-normal-superconductor quantum point contact (SNS-QPC). First, platinum is deposited on the heterostructure, then thermal annealing at 400 °C drives Pt in the heterostructure to form PtSiGe, finally two gate layers are deposited, insulated by Al_2O_3. **b**) False-color high angle annular dark field scanning transmission electron microscopy (HAADF STEM) image of a cross-section of a SNS-QPC. The PtSiGe contacts are violet, the Ti/Pd constriction gate (CG) operated in depletion mode is yellow, the Ti/Pd accumulation gate (AG), used to populate the quantum well, is green. A scanning electron microscopy top view image of this device is shown in Fig. 7.2, **c**) Atomic resolution HAADF STEM image of the Ge/PtSiGe interface along with the indexed fast Fourier transforms (FFTs) of the two regions (black squares) within the PtSiGe contacts and a schematics of the PtSiGe orthorhombic unit cell. The corresponding ternary lattice parameters $T = a_T, b_T, c_T$ that define the dimensions of the unit cell can be calculated, in a first approximation, by Vegard's law: $T_{\mathrm{PtSi_{1-x}Ge_x}} = x\ B_{\mathrm{PtGe}} + (1-x)\ B_{\mathrm{PtSi}}$ where $B = a_B, b_B, c_B$ are the lattice parameters of the binary compounds PtSi and PtGe, and x is the relative content of Ge with respect to Si. **d**) Electron energy-loss spectroscopy (EELS) composition maps showing the Pt, Ge, Si and O signals for the central area of the TEM lamella of panel b, the scale-bar indicates 50 nm. The PtGeSi stoichiometry is extracted by quantitative EELS analysis and reported in Supplementary Fig. 7.9

the adjacent SiGe and absence of extended defects. As a result of the annealing, Pt diffuses predominantly vertically through the SiGe spacer reaching the quantum well. The sharp lateral interfaces between the two PtSiGe contacts and the QW in between set the length of the channel populated by holes via the top-gates. The PtSiGe film presents poly-crystalline domains with a crystal size up to 50×50 nm and orthorhombic phase (PBNM, space group number 62) [41]. This is inferred from the power spectra or fast Fourier transforms (FFTs) taken from the two PtSiGe domains interfacing with the QW from the left contact, shown in Fig. 7.1c along with a schematic view of the unit cell of such phase. More detailed studies by high-resolution plane TEM are required to assess the junction uniformity in the direction parallel to the junction and whether this would impact Majorana experiments. The analysis of EELS elemental concentration profiles across the Ge QW→PtSiGe heterointerface (Supplementary Fig. 7.9) reveals that the threefold PtSiGe stoichiometry is Ge-rich, with relative composition in the range between $Pt_{0.1}Si_{0.2}Ge_{0.7}$ and $Pt_{0.1}Si_{0.05}Ge_{0.85}$ depending locally on the analysed grain. The EELS compositional maps in Fig. 7.1d show the elemental distribution of Ge, Si, Pt, Al, and O, at the key regions of the device. We observe Pt well confined to the two contacts areas, which also appear Ge-rich. Crucially, O is detected only in the Al_2O_3 dielectric layer below the gates, pointing to a high-purity quantum well and a pristine superconductor-semiconductor interface.

7.2.2. HIGHLY TRANSPARENT JOSEPHSON JUNCTION

We perform low-frequency four-terminal current and voltage bias measurements (Methods) on the SNS-QPC device shown in Fig. 7.2a to infer the properties of the superconductor-semiconductor interface. Accumulation (AG, in green) and constriction (CG, in yellow) gates control transport within the 70 nm long channel between the two PtSiGe leads. We apply a large negative voltage to the accumulation gate to populate the quantum well with holes, and we then control the effective width of the channel by applying a more positive voltage to the constriction gates, thus depleting the underlying quantum well.

The current bias measurements (Fig. 7.2b) reveal a tunable supercurrent with a plateau when the constriction gate voltage V_{CG} is in the range $\approx [-1.75, -1.50]$ V. This is the same range where we observe the first conductance plateau in the normal-state conductance G_{N} (Fig. 7.2b, right inset), indicating that the switching current (I_{sw}) plateau observed in the color plot stems form the supercurrent discretization due to the discrete number of modes in the QPC [30, 42]. Supercurrent discretization up to the third conductance plateau is shown in Supplementary Fig. 7.10 (data are for a different SNS-QPC device with identical design to the one presented here). The discretization of the supercurrent at zero magnetic field, indicates that the quality of the 2DHG is preserved also upon the formation of the superconducting contacts. We use the switching current as a lower bound for the critical current and we estimate an $I_{\mathrm{sw}}R_{\mathrm{N}}$ product of $51\,\mu$V, showing an improvement as compared to previous results obtained with pure Al contacts in Ge QWs [30, 32, 33], despite the Al T_{c} is higher than the PtSiGe T_{c}. The measured $I_{\mathrm{sw}}R_{\mathrm{N}}$ product is ~ 0.5 the theoretical $I_{\mathrm{c}}R_{\mathrm{N}}$ product calculated for a ballistic short junction using the Ambegaokar–Baratoff formula $\pi\Delta^*/2e = 110\,\mu$V with I_{c} being the critical current, Δ^* the induced superconducting gap and e the electron charge [43]. This discrepancy has been observed in previous works [30, 44] and is consistent with a premature switching due to thermal activation [45].

By operating the device in voltage-bias configuration and stepping the constriction gates, we observe in the conductance color plot the typical signature of multiple Andreev reflections (MARs) (Fig. 7.2c). When the applied voltage bias corresponds to an integer fraction of $2\Delta^*$, with Δ^* being the induced superconducting gap, we observe differential conductance dI/dV peaks (dips) in the tunneling (open)

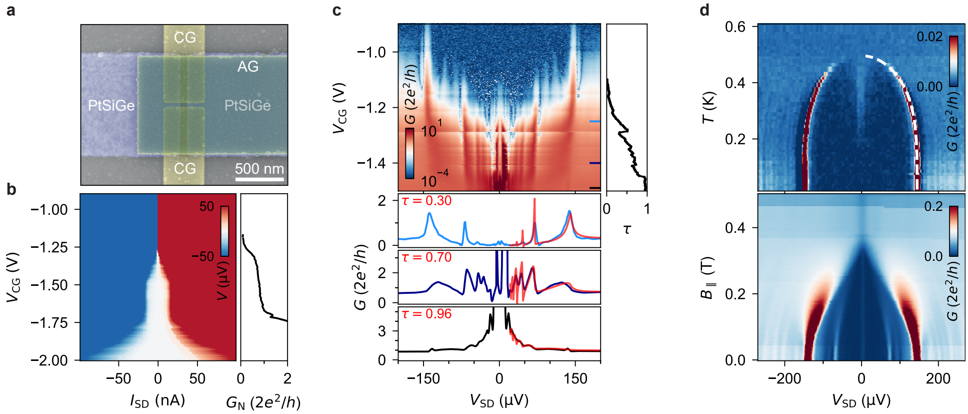

Figure 7.2: **Highly-transparent Josephson junctions.** **a**) False-color scanning electron microscope image of the SNS device. The PtSiGe contacts are violet, the constriction gates (CG) are yellow and the accumulation gate (AG) is green. The channel length between the two super-conducting leads is 70 nm and the channel width between the constriction gates is 40 nm. The two constriction gates are separate by design but always shorted together during measurements. **b**) Color map of the voltage drop across the junction V *vs* source-drain current I_{SD} and constriction-gate voltage V_{CG} at zero magnetic field along with normal-state conductance (G_N) trace *vs* V_{CG}. G_N is calculated as the conductance average where the voltage drop across the device is in the range [500, 650] mV or -[650,500] mV, that is much higher than the estimated superconducting gap. **c**) Color map of G in units of $2e^2/h$ *vs* the source-drain voltage V_{SD} and V_{CG}. Bottom panel shows line-cuts of conductance at $V_{CG} = [-1.25, -1.4, -1.49]$ V, red lines are the fit with the coherent scattering model from which transparency τ is extracted. Right inset shows the evolution of the transparency, as extracted from the fitting of conductance curves to the coherent scattering model (Methods), with the constriction gate V_{CG}. **d**) Color map of G *vs* T and V_{SD} (top panel), and *vs* $B_\parallel$ and V_{SD} (bottom panel), where $B_\parallel$ is the in-plane magnetic field in the direction of transport and T the temperature. The color scale in panel d has been saturated to better infer the low conductance limit. The source-drain bias is applied between the PtSiGe contacts, and the voltage drop across the junction is measured with a standard four-terminal setup. The accumulation voltage for measurements in b,c and d was set to -4.5 V, where the 2DHG is expected to reach saturation density (see Supplementary Fig. 7.6) of $\simeq 6 \times 10^{11}$ cm^{-2} [35]. Measurement presented in b, c and in panel d (bottom), are performed at 15 mK, corresponding to an electron temperature of ~ 25 mK.

regime [46, 47]. We measure MARs up to the 5th order, suggesting that the coherence length ξ_N in the Ge QW is a few times larger than the junction length L, and setting a lower bound to the phase coherence length in the QW $l_\psi > 5L = 350$ nm. These observations are consistent with the findings of ref. [33] where a similar Ge/SiGe heterostructure is used. Fitting the differential conductance with the coherent scattering model described in ref. [48] (and used in refs. [44, 47, 49]) reveals single channel transport with gate tunable transparency up to 96%. Such a high transparency confirms the high quality interface between the PtSiGe and the Ge QW. From the MARs fit we estimate an induced superconducting gap $\Delta^* = 70.6 \pm 0.9\,\mu$eV, which is about half compared to the $\Delta^* = 129\,\mu$eV [14] and 150 μeV [50] for recent InAs-Al devices reporting topological superconductivity.

Further, we characterise the evolution of the induced superconducting gap with temperature and magnetic field. After setting the device in tunneling regime, where sharp coherence peaks are expected at $e|V_{SD}| = 2\Delta^*$ (Fig. 7.2d), we observe the induced superconducting gap closing with increasing temperature and magnetic field. By fitting the temperature dependence of the coherence peaks with the empirical formula from ref. [51] we obtain a critical temperature of 0.5 K. The peak close to zero bias emerging at $T > 0.2$ K can be explained in terms of thermally-activated quasiparticle current [49]. The in-plane magnetic field in the transport direction quenches the superconductivity at $B_{c\parallel} = 0.37$ T. The same critical field is found for the in-plane direction perpendicular to the transport direction while for the out of plane direction $B_{c\perp} = 0.1$ T (Supplementary Fig. 7.11). This in-plane *vs* out-of-plane anisotropy is expected given the thin-film nature of the PtSiGe superconductor [45].

7.2.3. HARD INDUCED SUPERCONDUCTING GAP

To gain insights into the quality of the Ge/PtSiGe junction we characterise transport through the normal-superconductor quantum point contact (NS-QPC) device shown in Fig. 7.3a. Importantly, the methodology based on spectroscopy of NS devices alleviates the ambiguity of measuring the amount of quasiparticle states inside the gap with SNS junctions [31]. On the left side of the QPC there is a PtSiGe superconducting lead and on the right side a normal lead consisting of a 2DHG accumulated in the Ge QW. With the accumulation gate (AG) set at large negative voltages to populate the QW we apply a more positive voltage to the constriction gates (CG), creating a tunable barrier between the superconducting and the normal region. In Fig. 7.3b we progressively decrease the barrier height (decreasing V_{CG}) going from the tunneling regime, where conductance is strongly suppressed, to a more open regime where conductance approaches the single conductance quantum G_0. Line-cuts of the conductance color map are presented in the bottom panel of Fig. 7.3c. In the tunneling regime, we observe a hard induced superconducting gap, characterised by a two orders of magnitude suppression of the in-gap conductance to the normal-state conductance, and the arising of coherence peaks at $e|V_{SD}| \approx \Delta^* = 70\,\mu$eV. Fig. 7.3b also shows that the induced superconducting gap varies with the constriction gate voltage. This observation brings confidence that we are measuring the induced superconducting gap rather than the parent gap [52]. A possible explanation is that, upon increasing the density in the semiconductor nearby the junction, the coupling to the parent superconductor might vary, as also observed in other hybrid nanostructures [53].

The evolution of the gap as a function of in-plane magnetic field ($B_\parallel$) shown in Fig. 7.3c confirms that the gap remains hard for finite magnetic fields up to 0.25 T, ultimately vanishing at $B_\parallel \approx 0.37$ T. The magnetic field evolution of the gap in all

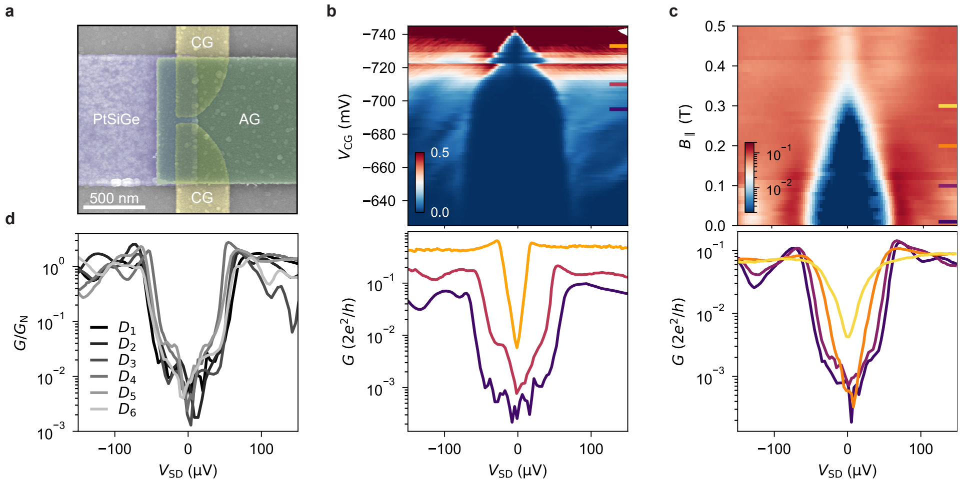

Figure 7.3: **Hard induced superconducting gap.** **a**) False-color SEM image of the normal-superconductor quantum point contact device (NS-QPC). The PtSiGe contact is violet, the constriction gate (CG) are yellow and the accumulation gate (AG) is green. The two constriction gates are separate by design but always shorted together during measurements. **b**) Color map of conductance G *vs* the source-drain voltage V_{SD} and constriction gate V_{CG}, along with line cuts in log-scale of G at the constriction gate voltages $V_{CG} = [-733, -710, -695]$ mV marked by the colored segment in the color-plot. **c**) Color map of G in units of $2e^2/h$ *vs* the in-plane magnetic field $B_{\parallel}$ perpendicular to the transport direction and constriction gate V_{CG}, along with line cuts in log-scale of G at the field strength $B_{\parallel} = [0.01, 0.1, 0.2, 0.3]$ T marked by the colored segment in the color-plot. **d**) Conductance traces normalised to the above-gap conductance (G/G_N) *vs* V_{SD} in tunneling regime for 6 different NS-QPC devices D_1-D_6 processed in the same fabrication run, device D_1 is the one reported in Fig 7.3 a-c, in the remaining devices the constriction gates separation varies (specifications of these devices are provided in Supplementary Fig. 7.13).

three directions matches the behaviour observed in the SNS-QPC (Supplementary Fig. 7.12).

Finally, Fig. 7.3d reports the conductance traces in tunneling regime for all the six measured devices (an overview of the geometries of these devices and the respective measurements are available in the Supplementary Fig. 7.13, the conductance maps for all these devices are shown in Supplementary Fig. 7.14). For all devices we observe suppression of conductance equal or larger than two orders of magnitude. At a quantitative level, the conductance traces of Fig. 7.3d are well fitted by the BTK theory [54] (Supplementary Fig. 7.14) consistent with a hard induced superconducting gap free of subgap states [11, 44]. This finding is the signature of a robust process that yields a reproducible high-quality superconductor-semiconductor interface, overcoming a long-standing challenge for hybrid superconductor-semiconductor quantum devices in Ge.

7.2.4. SUPERCONDUCTING QUANTUM INTERFERENCE DEVICES

We use the superconducting quantum interference device (SQUID) in Fig. 7.4a to demonstrate phase control across a Josephson junction, an important ingredient for achieving topological states at low magnetic field [50, 55–57]. The device is composed of two Josephson field-effect transistors (JoFETs) with a width of 2 µm and 1 µm for JoFET_1 and JoFET_2 respectively, and equal length of 70 nm. The critical current of the junctions I_{c1} and I_{c2} can be tuned independently by applying the accumulation gate voltages V_{AG1} and V_{AG2} to the corresponding gates. We investigate the oscillations of the SQUID switching current as a function of the out-of-plane-magnetic field penetrating the SQUID loop. Namely, we set V_{AG1} and V_{AG2}, such that both arms support supercurrent and $I_{c1} \gg I_{c2}$. This condition provides that the first junction is used as a reference junction and that the phase drop on it is flux-independent, while the phase drop over the second junction is therefore modulated by the external flux through the loop. This allows the measurement of the current-phase-relation (CPR) of the second junction. This is demonstrated in Fig. 7.4b where the shown SQUID oscillations are well fitted by the relation: $I_{c,SQUID} = I_{c1}(B_\perp A_1) + I_{c2}(B_\perp A_2)\sin(2\pi(B_\perp A_{SQUID} - LI_{c1}(B_\perp A_1))/\Phi_0)$ where $I_{c1,2}(BA_{1,2})$ are the Fraunhofer dependencies of the critical current obtained from fitting the Fraunhofer pattern of each junction (Supplementary Fig. 7.15), $A_{1,2}$ are the junction areas, $B_\perp$ is the out-of-plane magnetic field and Φ_0 the flux quantum. From the fit of the data in Fig. 7.4b (red dashed-line) we extract the effective SQUID loop area $A_{SQUID} = 8.9\,\mu\mathrm{m}^2$ (comparable to the $10\,\mu\mathrm{m}^2$ SQUID geometric area) and the self-inductance $L = 1.65\,\mathrm{pH}$. In order to confirm for the self-inductance effects, we also fit SQUID oscillations for the opposite direction of the current bias (blue dashed-line) and we get similar values for the effective loop area and self-inductance.

7.2.5. SCALABLE JUNCTIONS

As a first step towards monolithic superconductor-semiconductor quantum circuits in two dimensions, we fabricate and study transport in a macroscopic hybrid device comprising a large array of 510 PtSiGe islands (Fig. 7.5a) and a global top gate. Each pair of neighbouring islands forms a Josephson junction whose transparency can be tuned by the global accumulation gate. The top panel of Fig. 7.5b shows a current bias measurement of the junctions array resistance. As the accumulation gate becomes more negative, all the junctions are proximitized and a supercurrent flows through the device. Remarkably, as the source-drain current approaches the junctions critical current the whole array simultaneously switches from superconducting to resistive regime, as shown from the sharp resistance step (Fig. 7.5b top).

With this device we also study the evolution of the switching current in a small perpendicular magnetic field. In the bottom panel of Fig. 7.5b we observe Fraunhofer-like interference, along with the fingerprint of flux commensurability effects associated with the periodicity of the array. At integer numbers of flux quantum per unit area of the periodic array $f = B_\perp/B_0$, where $B_0 = \Phi_0/A$ with A the junction area and Φ_0 the flux quanta, we observe switching current peaks at $\pm 1f$, $2f$, $3f$, $4f$ and $5f$, denoted by a black arrow in the plot. We also notice this effect

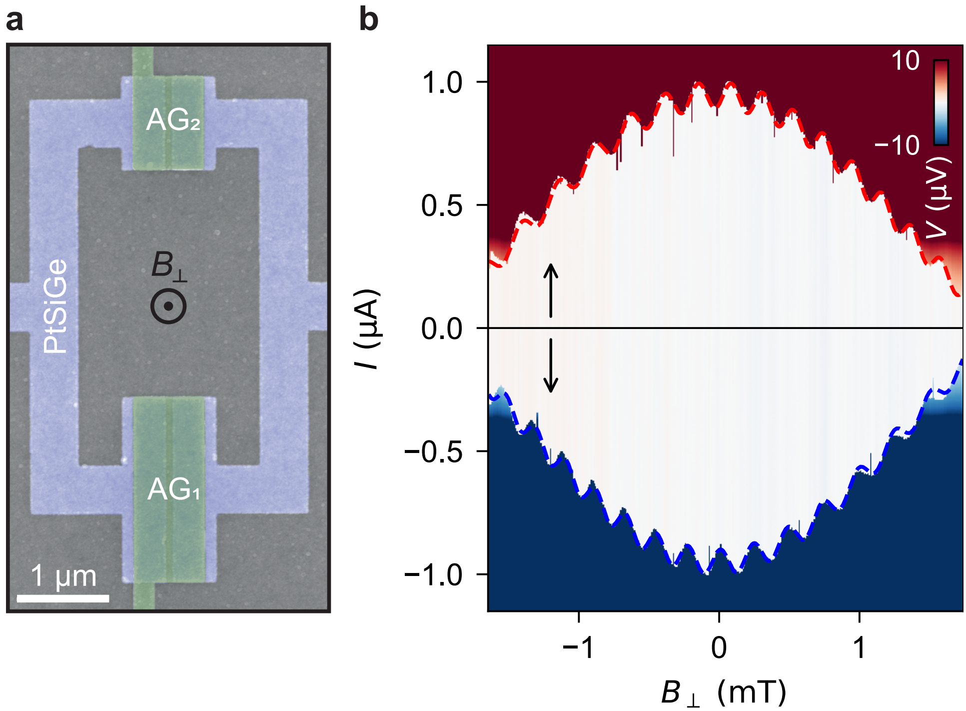

Figure 7.4: **Phase control of a Josephson junction in a SQUID. a**) False-color SEM image of the two JoFET SQUID device. The JoFETs have a channel length of 70 nm and a channel width of 1 µm and 2 µm respectively and can be independently controlled by gates AG_1 and AG_2. The geometric loop area of the SQUID is of $10\,\mu m^2$, calculated assuming a rectangle with sides positioned in the center of the PtSiGe loop cross-section. **b**) Color-plot of voltage drop (V) across the SQUID *vs* current (I) and out-of-plane magnetic field ($B_\perp$). Arrows represent the direction of the current (I) sweep. With the gate voltages set at $V_{AG1} = -3.5$V and $V_{AG2} = -1.65$V the superconducting phase drops mainly over the second junction. Upon sweeping the out-of-plane magnetic field $B_\perp$ we observe oscillations of the switching current. Red and blue dashed lines are the fit of the evolution of the critical current with magnetic field. The magnetic field is applied in the out of plane direction as depicted in panel a.

at fractional values of f, most notably at $f/2$ (red arrow). Flux commensurability effects, due to the pinning and interference of vortices in Josephson junctions arrays, have been previously reported [58, 59].

The observation of simultaneous switching of super-current and of the Fraunhofer pattern with flux commensurability effects, suggests that all islands effective areas are similar and that the supercurrent through the various junctions is comparable, meaning that all junctions respond synchronously to the applied gate voltage.

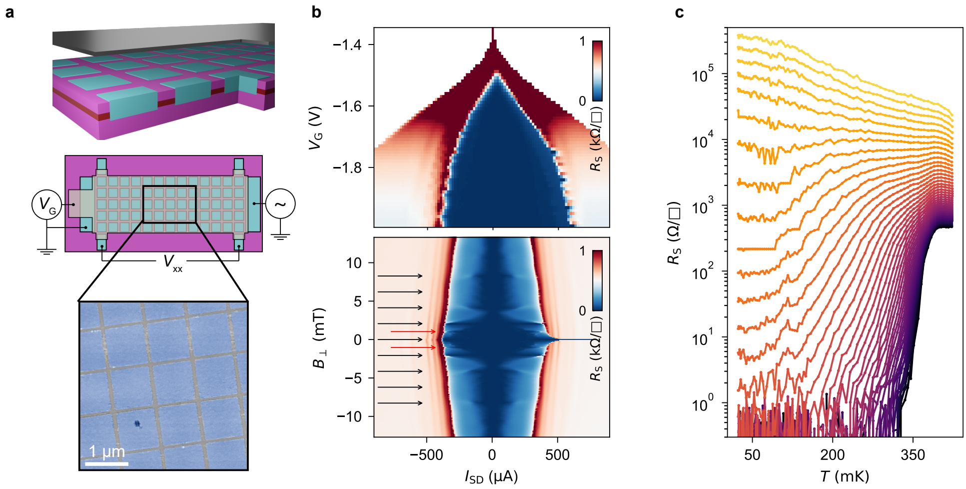

Figure 7.5: **A gated 2D superconductor-semiconductor array.** **a**) 3D and top view schematics of an array of 51×10 PtSiGe islands. The inset shows an atomic force microscopy image of the PtSiGe islands of the array. The PtSiGe islands are 930×930 nm wide and the separation between neighbouring islands is of 70 nm. **b**) Top panel shows a color map of sheet resistance (R_S) *vs* accumulation gate voltage V_G and source-drain current I_{SD}. Bottom panels shows a color map of sheet resistance *vs* out of plane magnetic field B and source-drain current I_{SD}. The measurement is taken at gate voltage $V_G = -1.99$V, where we expect carriers in the quantum well to approach a saturation density value of about 6×10^{11} cm^{-2} and have a mean free path ($\sim 7\,\mu$m) much longer than the separation between neighbouring islands. Black arrows denote the magnetic field corresponding to one flux quantum Φ_0 per unit cell of the array. Red arrows correspond to one-half flux per unit cell. **c**) Sheet resistance as a function of temperature for gate voltages ranging from -2 V to -1.55 V. Yellow curves correspond to small negative gates, and purple curves to large negative gates.

This is further supported by the observation of sharp switching of super-current and the Fraunhofer pattern of a 1D array of superconducting islands presented in Supplementary Fig. 7.16.

Finally we present in Fig. 7.5b the sheet resistance as a function of temperature for different gate voltages. As the gate voltage becomes more negative, the coupling between neighbouring superconducting islands increases and the system transitions from an insulating to a superconducting regime. At low gate voltage the resistance increases with decreasing temperature (yellow curves) indicating the insulating state, while at high gates the resistance drops to zero (purple curves) owing to the global superconducting state. At intermediate gate voltages ($-1.95\text{V} \leq V_G \leq -1.93\text{V}$, orange curves) there is a transition where the resistance shows a weak temperature dependence. It will be interesting to study this regime in detail, in light of the recent claims of an anomalous metallic state between the superconducting and the insulating phases [59].

7

7.3. CONCLUSION AND FUTURE PROSPECTIVES

We have developed superconducting germanosilicides for contacting Ge quantum wells, which has resulted in excellent superconducting properties imparted to the high-mobility 2DHG. We induced a hard superconducting gap in Ge, a large advancement compared to previous work on Ge hybrid superconductor-semiconductor devices [30–33]. We were able to observe a hard gap with 100% yield across all the six measured devices, pointing to a robust and reproducible fabrication process. Next to this central result, we further demonstrate phase control across a Josephson junction and take advantage of the planar geometry to scale these devices in 2D arrays.

While we focused on the poly-crystalline superconducting PtSiGe compound, we anticipate two strategies to further increase the size of the induced superconducting gap, which sets a relevant energy scale for hybrid devices. Firstly, following the approach in ref. [33] a superconducting layer with a larger gap, such as Al or Nb, may be deposited on top of the superconducting PtSiGe. Secondly, other ternary superconducting germanosilicides with a higher critical temperature may be explored, starting from the deposition and thermal anneal of other platinoid metals such as Rh and Ir [60].

Based on our findings, we foresee the following use cases for superconductor-semiconductor hybrids in high mobility planar Ge. Although a hard gap is necessary but not sufficient on its own for achieving a topologically protected system, this work positions planar Ge as a promising platform to explore Majorana bound states in phased-biased Josephson junctions [13, 61, 62]. Calculations with experimentally realistic material parameters [57] show that accessing the topological phase is feasible by careful design of Ge planar Josephson junctions geometries that relaxes magnetic field and spin-orbit constrains. More advanced future experiments should build on our current results to fully assess the readiness of Ge for Majorana bound states experiments, such as increasing the induced superconducting gap and measuring it by non local spectroscopy in multi-terminal devices and demonstrate the two-electron charging effect in hybrid Ge/PtSiGe islands, a pre-requisite for their use in topological quantum computation.

Crucially, the realization of a hard superconducting gap positions planar Ge as a unique material platform to pursue the coherent coupling of high fidelity spin qubits using crossed Andreev reflection to enable two-qubit gates over micrometer distances [5, 9]. Remote coupling of spin qubits in Ge may also be achieved by coupling spin qubits via superconducting quantum dots [5, 6], potentially offering a topological protection[10]. Coupling on an even longer distance may be obtained via superconducting resonators [63]. In such a scenario, a capacitive interaction may suffice, but connecting the resonator to a superconducting ohmic, such as PtSiGe, could result in a larger lever arm and therefore boost the coupling, while a direct tunnel coupling would give further directions to explore. The ability to couple qubits over different length scales is highly relevant and a critical component in network-based quantum computing [37].

Furthermore, the demonstration of a hard gap in Ge motivates the investigation of alternative spin qubits systems, such as Andreev spin qubits (ASQ) [64, 65], that may be coupled with gatemons [66] or superconductors [67]. Similar to semiconductor spin qubits, the use of isotopically purified Ge [23] may overcome the strong decoherence from the nuclear environment currently limiting progress with ASQs in III-V materials [3, 66].

All together, these findings represent a major step in the Ge quantum information route, aiming to co-integrate spin, superconducting, and topological systems for scalable and high-fidelity quantum information processing on a silicon wafer.

7.4. SUPPLEMENTARY INFORMATION

7.4.1. METHODS

Ge/SiGe heterostructure growth. The Ge/SiGe heterostructure of this study is grown on a 100-mm n-type Si(001) substrate using an Epsilon 2000 (ASMI) reduced pressure chemical vapor deposition reactor. The layer sequence comprises a $Si_{0.2}Ge_{0.8}$ virtual substrate obtained by reverse grading, a 16 nm thick Ge quantum well, a 22 nm-thick $Si_{0.2}Ge_{0.8}$ barrier, and a thin sacrificial Si cap [35]. Detailed electrical characterisation of heterostructure field effect transistors from these heterostructures are presented in ref. [35].

Device fabrication. The fabrication of the devices presented in this paper entails the following steps. Wet etching of the sacrificial Si-cap in buffer oxide etch for 10 s. Deposition of the Pt contacts via e-gun evaporation of 15 nm of Pt at pressure of 3×10^{-6} mbar at the rate of 0.5 Å/s. Rapid thermal anneal of Pt contacts at 400 °C for 15 minutes in a halogen lamps heated chamber in argon atmosphere. Atomic layer deposition of 10 nm of Al_2O_3 at 300 °C. Deposition of the first gate layer via e-gun evaporation of 3 nm of Ti and 17 nm of Pd. For the devices with a second gate layer the last two steps are repeated, 27 nm of Pd are deposited for the second gate layer to guarantee film continuity where overlapping with first gate layer.

Transport measurements. Electrical transport measurements of the SNS-QPC, NS-QPC, SQUID devices are carried out in a dry dilution refrigerators at a base temperature of 15 mK, corresponding to an electron temperature of ≈25 mK measured with a metallic N–S tunnel junction thermometer. This refrigerator is equipped with a 3-axis vector magnet. Measurements of the junctions array are carried out in a wet dilution refrigerator with base temperature of 50 mK and z-axis magnet.

Measurements are performed using a standard 4-terminals low-frequency lock-in technique at the frequency of 17 Hz. Voltage bias measurements are performed with an excitation voltage $V_{AC} < 4\,\mu V$. By measuring in a four-terminal setup, additional data processing to subtract series resistances of various circuit components is avoided. For the measurements in Fig. 7.2b, c, d and Fig. 7.5b the (maximum) gate voltage is tuned to be just below the threshold for hysteresis, caused by trapped charges in the surface states at the semiconductor/dielectric. In these electrostatic conditions the valence band edge at the semiconductor/dielectric interface and the Fermi level align and the density in the buried channel is expected to approach a saturation density of about 6×10^{11} cm^{-2} [35].

Fraunhofer meeasurements for SQUID arms We measured the Fraunhofer pattern for each junction of the SQUID device independently (Supplementary Fig. 7.15) by measuring the dependence of its critical current on the out-of-plane magnetic field while the gate voltage of the measured junction is set to −3.5V and the other junction is pinched-off. By fitting the obtained dependencies $I_{c1,2}(\Phi_{1,2})$ as $I_{c1,2}(BA_{1,2}) = I_{c01,2}\sin(\pi BA_{1,2}/\Phi_0)/(\pi BA_{1,2}/\Phi_0)$, where B is the out-of-plane magnetic field and Φ_0 is superconducting flux quantum, we obtain from the fits the areas of the two junctions to be $A_1 = 1\,\mu\text{m}^2$ and $A_2 = 0.48\,\mu\text{m}^2$. Note that the ratio $A_1/A_2 \sim 2$, as designed and shown in Fig. 7.4a, while the values for both areas are smaller than the geometrical areas in the design due to the flux focusing effects.

Simulations and fitting of MARs. The experimentally measured conductance $G_{exp}(V)$ of an SNS junction is assumed to be superposition of N single-mode contributions [47]:

$$G_{theory}(V)\sum_{i=1}^{M} N_i G^{(\tau_i,\Delta)}(V) \tag{7.1}$$

where $G^{(\tau_i,\Delta)}$ is the simulated conductance for the N_i modes with transparency τ_i. We allow for M different transparencies, but all N_i modes have the same superconducting gap Δ. The simulations of conductance were implemented in Python using a modified version of the code presented in ref. [68].

The theoretically computed conductance $G_{theory}(V)$ is fitted to $G_{exp}(V)$ using a nonlinear least-squares procedure: $\chi = \int [G_{exp}(V) - G_{theory}(V)]^2 dV$ is minimised for the fitting parameters Δ, N_i, τ_i with $i \in 1,...,M$. The fitting is performed for increasing M, provided that all N_i and τ_i are nonzero. We note that we assume a coherent 1D system. When the MAR contribution is significant, this assumption leads to an overestimation of the sharpness and amplitude of the peaks. Nonetheless, overall we find a good agreement between the data and the model.

7

7.4.2. KEY METRICS

In Table 7.1 we present a comparison of key metrics for material systems for hybrid superconductor-semiconductor applications. Given that in this paper the main focus is on applications that require the presence of a hard gap, we limit the table only to semiconductor-superconductor material systems with a hard gap assessed via NS spectroscopy, which is a reliable measurement for verifying the absence of subgap states.

On the first half of Table 7.1 we present the typical values for different platforms for (peak) mobility (μ), disorder quantified by the transport level broadening ($\hbar/2\tau$, where τ is the elastic scattering time), size of induced superconducting gap (Δ^*), spin orbit length (l_{SO}) and g-factor (g^*), important metrics for accessing the topological phase. On the second half of Supplementary Table 7.1 we illustrate the metrics that are significant for control and operation of spin qubits: relaxation time (T_1), dephasing time (T_2^*) and 1 qubit gate fidelity (1Q gate fidelity). For a comprehensive review of performance metrics of spin qubits in gated semiconducting nanostructures see ref. [17]. While III-V materials benefit from a larger induced superconducting gap and g-factor, planar Ge proximitized by PtSiGe stands out for the exceptionally low disorder (quantified by the high μ and low $\hbar/2\tau$), which is necessary for the emergence of topological Majorana zero modes [36]. In line with the remarks made

Semiconductor	Superconductor	μ ($\times 10^3$ cm^2/Vs)	$\hbar/2\tau$ (µeV)	Δ^* (µeV)	l_{SO} (nm)	g^*	T_1 (ms)	T_2^* (ns)
Ge/SiGe, 2D	PtSiGe	615	10	70	76	0.76-15	32	833
InSb, nw	Al	44	940	250	100	26-51	na	8
InAs, nw	Al	25	890	270	60	8	0.001	8
	Pb			1250				
InAs, 2D	Al	60	370	190	45	10	na	na
InSbAs, 2D	Al	28	1200	220	60	55	na	na

Table 7.1: Comparison of key metrics for building quantum information processing devices based on topological or spin-qubit systems. We consider only systems where a hard hap is assessed via NS spectroscopy, the most reliable measurement for verifying the absence of subgap states. From left to right, columns indicate: the semiconductor system and whether it is a planar heterostructures (2D) or a nanowire (nw); the superconductor material used to proximitize the semiconductor; maximum carrier mobility (μ), typically Hall mobility in 2D systems and estimated field effect mobility in nanowires; the disorder quantified by the transport level broadening ($\hbar/2\tau$, where τ is the elastic scattering time)[36]; maximum induced superconducting gap (Δ^*); spin-orbit length (l_{SO}); g-factor (g^*), the range can be large when the g-factor is strongly anisotropic; longest relaxation time (T_1) measured in a spin qubit, longest dephasing time (T_2^*) measured in a spin-qubit; largest measured 1 qubit gate fidelity (1Q gate fidelity). The metrics reported in this table are reported from the references below as following. Ge/SiGe, 2D: μ from this work; $\hbar/2\tau$ calculated using $m^* = 0.09$ [24]; Ge/SiGe-PtSiGe Δ^* from this work; $l_{SO} = 76$ nm (corresponding to a spin-orbit energy of 2.2 meV) follows from the cubic Rashba coefficient α_3 reported in ref. [69] at a density of 6.1×10^{11} cm^{-2}, for which we assume an effective mass of 0.09 [35]; g^* [70]; T_1 [71]; T_2^* [20]; 1Q gate fidelity [72]. InSb, nw: μ [73]; $\hbar/2\tau$ calculated using $m^* = 0.014$ [74]; InSb-Al Δ^* [75]; l_{SO} [76]; g^* [77]; T_2^* [78].; 1Q gate fidelity. InAs nw: μ [79]; $\hbar/2\tau$ calculated using $m^* = 0.0026$ [74]; InAs-Pb Δ^* [80]; InAs-Al Δ^* [81]; l_{SO} [82]; g^* [79]; T_1 [83]; T_2^* [84]. InAs 2D: μ [14], $\hbar/2\tau$ calculated using $m^* = 0.026$ [74], InAs-Al Δ^* [12], l_{SO} [12, 40], g^* [12]. InSbAs 2D: μ [85], $\hbar/2\tau$ calculated using $m^* = 0.018$ [85], Δ^* [85], l_{SO} [85], g^* [85].

in the introductory section, planar Ge also shows excellent spin qubit metrics. This comparison positions Ge/SiGe-PtGeSi as a compelling platform for topological devices, where small disorder is necessary to preserve the topological gap ($\delta_\tau > \frac{\hbar}{2\tau}$, where δ_τ is the topological gap and and for hybrid devices, were we envision the coupling of spins via cross Andreev reflection mechanisms, Andreev spin qubits, and the co-integration of spins, topological, and superconducting qubits.

7.4.3. SUPPLEMENTARY FIGURES

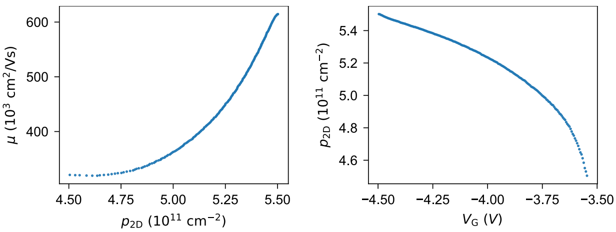

Figure 7.6: **2DHG transport properties.** Mobility μ vs 2D-carrier density p_{2D} (left panel) and 2D-carrier density vs accumulation gate V_G for a Hall-bar shaped heterostructure field-effect transistor fabricated on the same 22 nm deep Ge/SiGe heterostructure used for all devices in this work. The maximum mobility of 615×10^3 cm^2/Vs is reached at the density of 5.5×10^{11} cm^{-2}, corresponding to an elastic transport scattering time $\tau = 31$ ps, calculated using $m^* = 0.09$ [24] and a mean free path of 7.4 μm. The density vs gate curve deviates from the expected linear behaviour due to tunneling of charges from the quantum well to the the trap states at the oxide interface, partly screening the electric field in the quantum well. The density and mobility reach saturation when the states at the triangular well in the SiGe barrier at the oxide interface start to populate and thus screen the electric field in the QW.

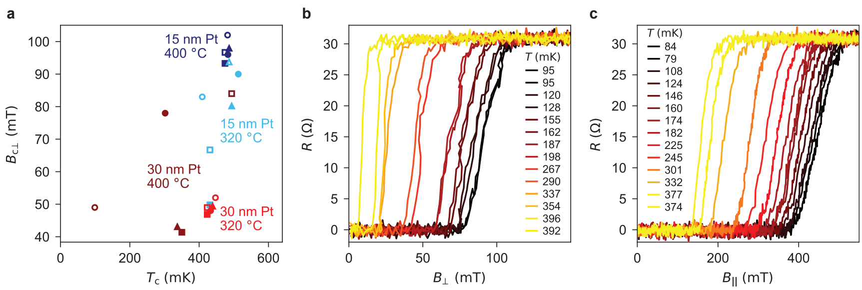

Figure 7.7: **PtSiGe film characterization.** **a**) Critical perpendicular magnetic field $B_{c\perp}$ and critical temperature T_c of a PtSiGe film deposited and anneled in a 22 nm deep Ge/SiGe QW for different process conditions. The colours of the markers indicate the thickness of the deposited platinum layer (that covers the whole surface of a 3 × 3 mm Ge/SiGe heterostructure) and the anneal temperature. The filled (open) markers correspond to an anneal time of 15 (30) minutes. The marker's shape signifies the used atomic layer deposition (ALD) of Al_2O_3 process: no ALD (circles), ALD with 60 min pre-heating at 300 °C (squares), or ALD with 15 min pre-heating (triangles). In both ALD processes, 10 nm of Al_2O_3 was deposited. **b, c**) Analysis of the critical temperature and fields of a 3 μm wide PtSiGe strip (15 nm Pt has been annealed for 15 minutes at 400 °C). Resistance R versus perpendicular magnetic field ($B_\perp$) and parallel magnetic field ($B_\parallel$) for various temperatures T. These measurements were performed in a 4-probe configuration with standard low frequency lock-in technique in a wet dilution refrigerator with electron temperature of 100 mK.

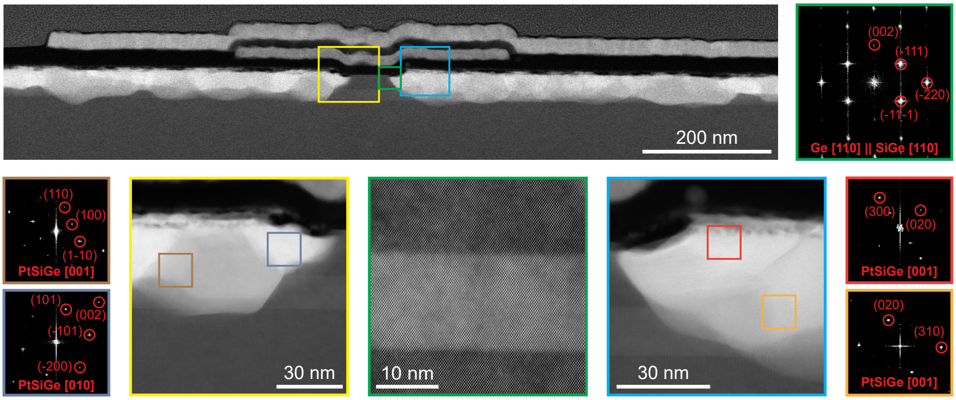

Figure 7.8: **Structural details of the PtSiGe poly-cristalline phase.** High-angle annular dark field scanning transmission electron microscopy (HAADF STEM) and crystallographic information of the SNS-QPC device. The yellow and blue insets show atomic-resolution images of both the left and right contacts highlighting the sharp interfaces between the QW and the PtSiGe film. The atomic-resolution micrograph in the center (green) displays the high quality of the Ge QW interfaces with diamond-structure (FD3-MS, space group number 227). The local contrast variations observed here are attributed to uneven thickness distribution of the lamella due to the focused ion beam (FIB) sample preparation. The fast Fourier transform (FFT) on the top right (green) indicates that the (002) planes in the QW grow epitaxially following the [001] axis. In addition, no dislocations were identified. The insets on the bottom left and right show the power spectra that identify the orthorhombic phase (PBNM, space group number 62) of the PtSiGe film.

7

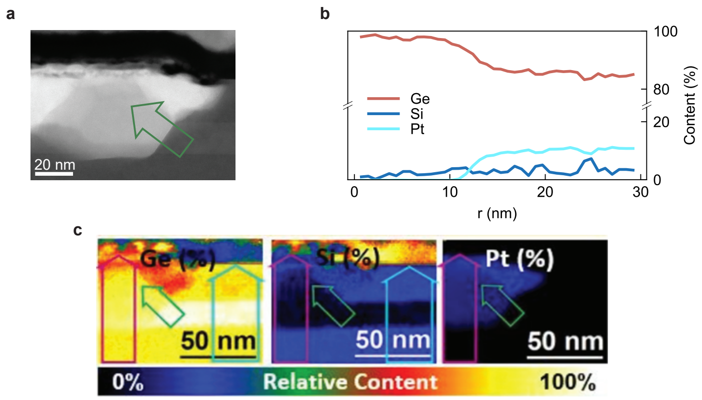

Figure 7.9: **PtSiGe stoichiometry.** Electron energy-loss spectroscopy (EELS) quantitative compositional map of the region indicated from the white arrow in the HAADF STEM image (a) of the Ge/PtSiGe interface of the SNS-QPC. The threefold PtSiGe stoichiometry presented in panel (b) is Ge-rich, with relative composition in the range between $Pt_{0.1}Ge_{0.7}Si_{0.2}$ and $Pt_{0.1}Ge_{0.85}Si_{0.05}$ depending locally on the analysed grain. Panel (c) shows the quantitative EELS compositional maps for Ge, Si and Pt. The averaged signal in the region along the green arrows is shown in panel (b).

7

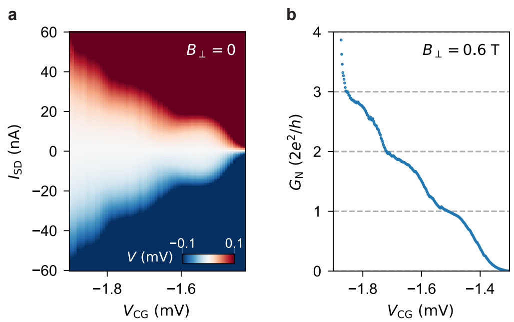

Figure 7.10: **Supercurrent discretization.** **a**) Voltage drop V across an SNS-QPC device as a function of the source drain current I_{SD} and constriction gate voltage V_{CG}. Discrete plateaus in the switching current can be observed, indicating a discrete number of modes in the QPC. **b**) Normal-state differential conductance G versus V_{CG} taken at out-of-plane magnetic field $B_\perp = 0.6\,\mathrm{T}$, showing plateaus at quantized value of conductance. The plateaus in the two plots are slightly shifted with respect to each other due to the hysteretic behaviour of the device.

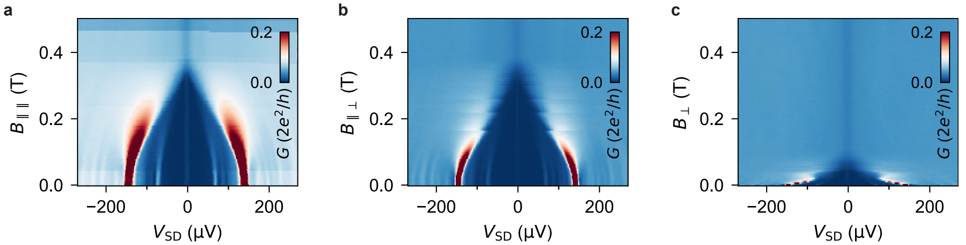

Figure 7.11: **SNS-QPC, evolution of the superconducting gap with magnetic field.** Color map of conductance G in units of $2e^2/h$ vs source-drain bias V_{SD} and magnetic field B for the SNS-QPC. From left to right the magnetic field direction is: in-plane parallel to transport ($B_{\parallel\parallel}$), in-plane perpendicular to transport ($B_{\parallel\perp}$), out of plane ($B_{\perp}$). The device is tuned in the tunneling regime to show the evolution of the induced superconducting gap with the strength of the magnetic field.

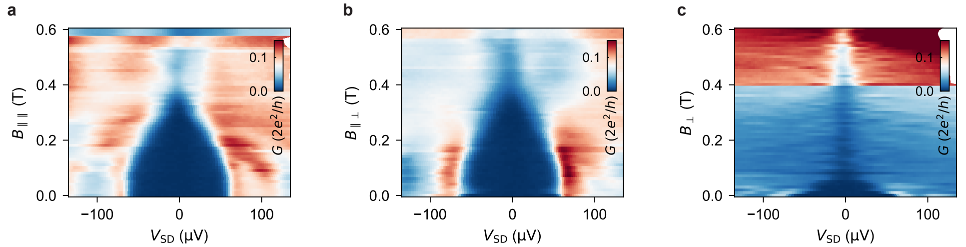

Figure 7.12: **NS-QPC, evolution of the induced superconducting gap with magnetic field.** Color map of conductance G in units of $2e^2/h$ vs source-drain bias V_{SD} and magnetic field B for the NS-QPC. From left to right the magnetic field direction is: in-plane parallel to transport ($B_{\parallel\parallel}$), in-plane perpendicular to transport ($B_{\parallel\perp}$), out of plane ($B_{\perp}$). The device is tuned in the tunneling regime to show the evolution of the induced superconducting gap with the strength of the magnetic field.

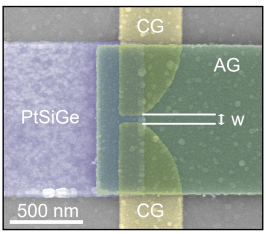

Device	*Constriction width (nm)*
1	25
2	25
3	50
4	50
5	50
6	75

Figure 7.13: **NS-QPCs devices specifications.** False-color SEM image of a normal-superconductor quantum point contact device (NS-QPC). The PtSiGe contact is violet, the constriction gates (CG) are yellow and the accumulation gate (AG) is green. The constriction width (w) between the two CGs is varied across the 6 measured devices and is reported in the table. The 6 devices were fabricated in the same fabrication run.

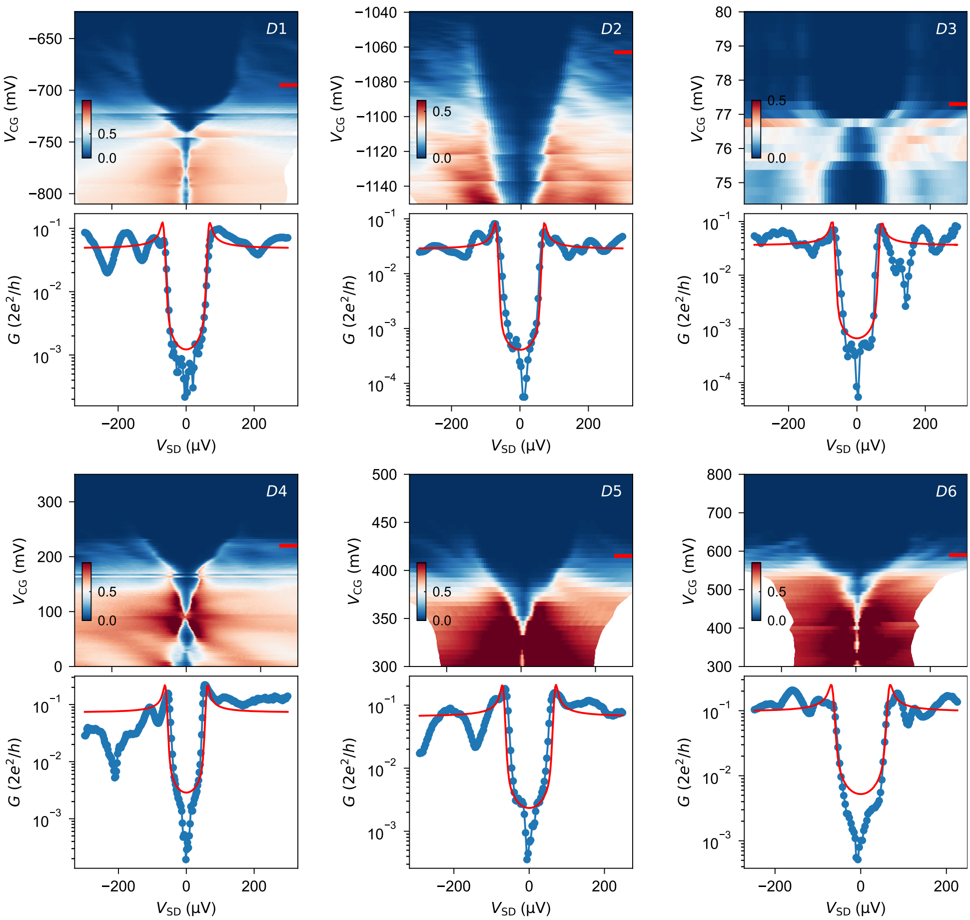

Figure 7.14: **Conductance maps of 6 NS-QPC devices.** Color map of G in units of $2e^2/h$ vs. the source-drain voltage V_{SD} and constriction gate V_{CG}, for the 6 NS-QPC devices presented in the main text, along with the conductance line-cuts presented in Fig. 7.3d main text. The red segment in the color maps indicates the V_{CG} of each linecut. Fits of the conductance linecuts to the BTK model [54] (red lines) are consistent with a hard induced superconducting gap. Variation on the V_{CG} operational window can be ascribed both to the different constriction gate size and to the accumulation gate voltage used for the specific measurement. The different evolution of G as a function of V_{CG} can also be related to the different accumulation gate voltages.

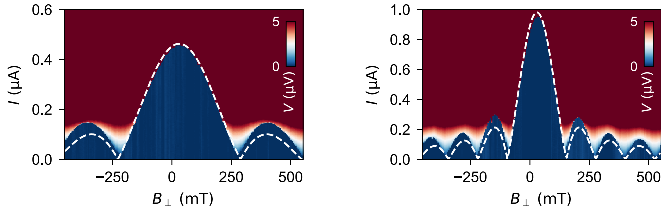

Figure 7.15: **JoFETs Fraunhofer pattern for the SQUID device.** Fraunhofer pattern of the small junction (JoFET$_2$, left panel) and large junction (JoFET$_1$, right panel) of the SQUID device. White dashed line represents the fitting of the switching current to the theoretical Fraunhofer formula.

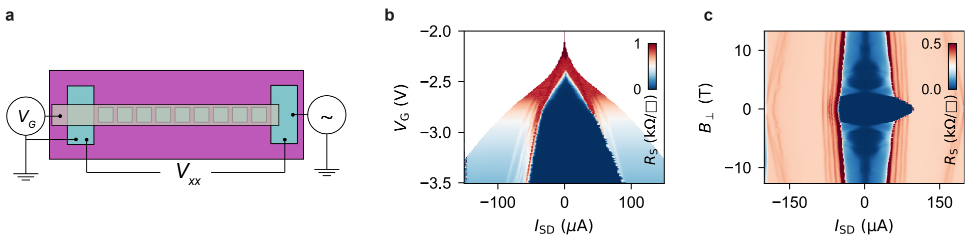

Figure 7.16: **1D PtSiGe superconducting array.** **a**) Top view schematics of an array of 51 × 1 PtSiGe islands on a Ge/SiGe heterostructure. The PtSiGe islands are 930 × 930 nm wide and the separation between the PtSiGe islands is of 70 nm. **b**) Color map of the sheet resistance (R_S) vs accumulation gate voltage V_G and source-drain current I_{SD}. Increasing the negative voltage of the accumulation gate the array becomes superconducting (R_S goes to zero) when the source-drain current is below the switching current. **c**) Color map of the sheet resistance vs out-of-plane magnetic field $B_\perp$ and source-drain current I_{SD}. The switching current shows the typical Fraunhofer pattern expected for a single Josephson junction. Compared to the 2D PtSiGe array this device does not present any signature of commensurability effects in the switching current, as expected for a linear array.

REFERENCES

[1] R. M. Lutchyn, E. P. Bakkers, L. P. Kouwenhoven, P. Krogstrup, C. M. Marcus, and Y. Oreg. "Majorana zero modes in superconductor-semiconductor heterostructures". In: *Nat. Rev. Mater.* 3.5 (2018), pp. 52–68.

[2] K. Flensberg, F. von Oppen, and A. Stern. "Engineered platforms for topological superconductivity and Majorana zero modes". In: *Nat. Rev. Mater.* 6.10 (2021), pp. 944–958.

[3] M. Hays, V. Fatemi, D. Bouman, J. Cerrillo, S. Diamond, K. Serniak, T. Connolly, P. Krogstrup, J. Nygård, A. Levy Yeyati, A. Geresdi, and M. H. Devoret. "Coherent manipulation of an Andreev spin qubit". In: *Science* 373.6553 (2021), pp. 430–433.

[4] L. Casparis, M. R. Connolly, M. Kjaergaard, N. J. Pearson, A. Kringhøj, T. W. Larsen, F. Kuemmeth, T. Wang, C. Thomas, S. Gronin, G. C. Gardner, M. J. Manfra, C. M. Marcus, and K. D. Petersson. "Superconducting gatemon qubit based on a proximitized two-dimensional electron gas". In: *Nat. Nanotechnol.* 13.10 (2018), pp. 915–919.

[5] M.-S. Choi, C. Bruder, and D. Loss. "Spin-dependent Josephson current through double quantum dots and measurement of entangled electron states". In: *Phys. Rev. B* 62.20 (2000), pp. 13569–13572.

[6] M. Leijnse and K. Flensberg. "Quantum information transfer between topological and spin qubit systems". In: *Phys. Rev. Lett.* 107.21 (2011), p. 210502.

[7] M. Leijnse and K. Flensberg. "Hybrid topological-spin qubit systems for two-qubit-spin gates". In: *Phys. Rev. B* 86.10 (2012), p. 104511.

[8] S. Hoffman, C. Schrade, J. Klinovaja, and D. Loss. "Universal quantum computation with hybrid spin-Majorana qubits". In: *Phys. Rev. B* 94.4 (2016), p. 045316.

[9] M. Leijnse and K. Flensberg. "Coupling spin qubits via superconductors". In: *Phys. Rev. Lett.* 111.6 (2013), p. 060501.

[10] A. Y. Kitaev. "Unpaired Majorana fermions in quantum wires". In: *Physics-Uspekhi* 44.10S (2001), pp. 131–136.

[11] W. Chang, S. M. Albrecht, T. S. Jespersen, F. Kuemmeth, P. Krogstrup, J. Nygård, and C. M. Marcus. "Hard gap in epitaxial semiconductor-superconductor nanowires". In: *Nat. Nanotechnol.* 10.3 (2015), pp. 232–236.

[12] M. Kjaergaard, F. Nichele, H. J. Suominen, M. P. Nowak, M. Wimmer, A. R. Akhmerov, J. A. Folk, K. Flensberg, J. Shabani, C. J. Palmstrøm, and C. M. Marcus. "Quantized conductance doubling and hard gap in a two-dimensional semiconductor-superconductor heterostructure". In: *Nat. Comm.* 7 (2016), pp. 1–6.

[13] A. Fornieri, A. M. Whiticar, F. Setiawan, E. Portolés, A. C. C. Drachmann, A. Keselman, S. Gronin, C. Thomas, T. Wang, R. Kallaher, G. C. Gardner, E. Berg, M. J. Manfra, A. Stern, C. M. Marcus, and F. Nichele. "Evidence of topological superconductivity in planar Josephson junctions". In: *Nature* 569.7754 (2019), pp. 89–92.

[14] M. Aghaee *et al.* "InAs-Al hybrid devices passing the topological gap protocol". In: *Phys. Rev. B* 107 (24 2023), p. 245423.

[15] T. Dvir, G. Wang, N. van Loo, C.-X. Liu, G. P. Mazur, A. Bordin, S. L. D. t. Haaf, J.-Y. Wang, D. van Driel, F. Zatelli, X. Li, F. K. Malinowski, S. Gazibegovic, G. Badawy, E. P. A. M. Bakkers, M. Wimmer, and L. P. Kouwenhoven. "Realization of a minimal Kitaev chain in coupled quantum dots". In: *Nature* 614.7948 (2023), pp. 445–450.

[16] Ł. Cywiński, W. M. Witzel, and S. Das Sarma. "Electron spin dephasing due to hyperfine interactions with a nuclear spin bath". In: *Phys. Rev. Lett.* 102.5 (2009), pp. 1–4.

[17] P. Stano and D. Loss. "Review of performance metrics of spin qubits in gated semiconducting nanostructures". In: *Nat. Rev. Phys.* 4.10 (2022), pp. 672–688.

[18] G. Scappucci, C. Kloeffel, F. A. Zwanenburg, D. Loss, M. Myronov, J. J. Zhang, S. De Franceschi, G. Katsaros, and M. Veldhorst. "The germanium quantum information route". In: *Nat. Rev. Mater.* 6.10 (2020), pp. 926–943.

[19] H. Watzinger, J. Kukučka, L. Vukušić, F. Gao, T. Wang, F. Schäffler, J. J. Zhang, and G. Katsaros. "A germanium hole spin qubit". In: *Nat. Comm.* 9.1 (2018), pp. 1–6.

[20] N. W. Hendrickx, D. P. Franke, A. Sammak, G. Scappucci, and M. Veldhorst. "Fast two-qubit logic with holes in germanium". In: *Nature* 577.7791 (2020), pp. 487–491.

[21] D. Jirovec, A. Hofmann, A. Ballabio, P. M. Mutter, G. Tavani, M. Botifoll, A. Crippa, J. Kukucka, O. Sagi, F. Martins, J. Saez-Mollejo, I. Prieto, M. Borovkov, J. Arbiol, D. Chrastina, G. Isella, and G. Katsaros. "A singlet-triplet hole spin qubit in planar Ge". In: *Nat. Mater.* 20.8 (2021), pp. 1106–1112.

[22] J. H. Prechtel, A. V. Kuhlmann, J. Houel, A. Ludwig, S. R. Valentin, A. D. Wieck, and R. J. Warburton. "Decoupling a hole spin qubit from the nuclear spins". In: *Nat. Mater.* 15.9 (2016), pp. 981–986.

[23] K. M. Itoh and H. Watanabe. "Isotope engineering of silicon and diamond for quantum computing and sensing applications". In: *MRS Communications* 4.4 (2014), pp. 143–157.

[24] M. Lodari, A. Tosato, D. Sabbagh, M. A. Schubert, G. Capellini, A. Sammak, M. Veldhorst, and G. Scappucci. "Light effective hole mass in undoped Ge/SiGe quantum wells". In: *Phys. Rev. B* 100.4 (2019).

[25] M. Lodari, O. Kong, M. Rendell, A. Tosato, A. Sammak, M. Veldhorst, A. R. Hamilton, and G. Scappucci. "Lightly strained germanium quantum wells with hole mobility exceeding one million". In: *Appl. Phys. Lett.* 120.12 (2022), p. 122104.

[26] N. W. Hendrickx, W. I. Lawrie, M. Russ, F. van Riggelen, S. L. de Snoo, R. N. Schouten, A. Sammak, G. Scappucci, and M. Veldhorst. "A four-qubit germanium quantum processor". In: *Nature* 591.7851 (2021), pp. 580–585.

[27] F. Borsoi, N. W. Hendrickx, V. John, S. Motz, F. van Riggelen, A. Sammak, S. L. de Snoo, G. Scappucci, and M. Veldhorst. *Shared control of a 16 semiconductor quantum dot crossbar array*. 2022.

[28] A. Dimoulas, P. Tsipas, A. Sotiropoulos, and E. K. Evangelou. "Fermi-level pinning and charge neutrality level in germanium". In: *Appl. Phys. Lett.* 89.25 (2006), p. 252110.

[29] N. W. Hendrickx, D. P. Franke, A. Sammak, M. Kouwenhoven, D. Sabbagh, L. Yeoh, R. Li, M. L. Tagliaferri, M. Virgilio, G. Capellini, G. Scappucci, and M. Veldhorst. "Gate-controlled quantum dots and superconductivity in planar germanium". In: *Nat. Comm.* 9.1 (2018), p. 2835.

[30] N. W. Hendrickx, M. L. Tagliaferri, M. Kouwenhoven, R. Li, D. P. Franke, A. Sammak, A. Brinkman, G. Scappucci, and M. Veldhorst. "Ballistic supercurrent discretization and micrometer-long Josephson coupling in germanium". In: *Phys. Rev. B* 99.7 (2019), pp. 7–9.

[31] J. Ridderbos, M. Brauns, F. K. De Vries, J. Shen, A. Li, S. Kölling, M. A. Verheijen, A. Brinkman, W. G. Van Der Wiel, E. P. A. M. Bakkers, and F. A. Zwanenburg. "Hard Superconducting Gap and Diffusion-Induced Superconductors in Ge–Si Nanowires". In: *Nano Lett.* 20.1 (2020), pp. 122–130. (Visited on 02/20/2023).

[32] F. Vigneau, R. Mizokuchi, D. C. Zanuz, X. Huang, S. Tan, R. Maurand, S. Frolov, A. Sammak, G. Scappucci, F. Lefloch, and S. De Franceschi. "Germanium Quantum-Well Josephson Field-Effect Transistors and Interferometers". In: *Nano Lett.* 19.2 (2019), pp. 1023–1027.

[33] K. Aggarwal, A. Hofmann, D. Jirovec, I. Prieto, A. Sammak, M. Botifoll, S. Martí-Sánchez, M. Veldhorst, J. Arbiol, G. Scappucci, J. Danon, and G. Katsaros. "Enhancement of proximity-induced superconductivity in a planar Ge hole gas". In: *Phys. Rev. Res.* 3.2 (2021), p. L022005.

[34] J. A. Kittl, K. Opsomer, C. Torregiani, C. Demeurisse, S. Mertens, D. P. Brunco, M. J. Van Dal, and A. Lauwers. "Silicides and germanides for nano-CMOS applications". In: *Materials Science and Engineering B* 154.1-3 (2008), pp. 144–154.

[35] A. Sammak, D. Sabbagh, N. W. Hendrickx, M. Lodari, B. Paquelet Wuetz, A. Tosato, L. Yeoh, M. Bollani, M. Virgilio, M. A. Schubert, P. Zaumseil, G. Capellini, M. Veldhorst, and G. Scappucci. "Shallow and Undoped Germanium Quantum Wells: A Playground for Spin and Hybrid Quantum Technology". In: *Adv. Func. Mater.* 29.14 (2019), p. 1807613.

[36] S. Ahn, H. Pan, B. Woods, T. D. Stanescu, and S. D. Sarma. "Estimating disorder and its adverse effects in semiconductor Majorana nanowires". In: *Phys. Rev. Mater.* 5 (2021), p. 124602.

[37] L. M. K. Vandersypen, H. Bluhm, J. S. Clarke, A. S. Dzurak, R. Ishihara, A. Morello, D. J. Reilly, L. R. Schreiber, and M. Veldhorst. "Interfacing spin qubits in quantum dots and donors — hot , dense , and coherent". In: *npj Quantum Information* (2017), pp. 1–10.

[38] S. Gaudet, C. Detavernier, A. J. Kellock, P. Desjardins, and C. Lavoie. "Thin film reaction of transition metals with germanium". In: *Journal of Vacuum Science & Technology A: Vacuum, Surfaces, and Films* 24.3 (2006), pp. 474–485.

[39] C. J. Raub, W. H. Zachariasen, T. H. Geballe, and B. T. Matthias. "Superconductivity of some new Pt-metal compounds". In: *Journal of Physics and Chemistry of Solids* 24.9 (1963), pp. 1093–1100.

[40] J. Shabani, M. Kjaergaard, H. J. Suominen, Y. Kim, F. Nichele, K. Pakrouski, T. Stankevic, R. M. Lutchyn, P. Krogstrup, R. Feidenhans'L, S. Kraemer, C. Nayak, M. Troyer, C. M. Marcus, and C. J. Palmstrøm. "Two-dimensional epitaxial superconductor-semiconductor heterostructures: A platform for topological superconducting networks". In: *Phys. Rev. B* 93.15 (2016), pp. 1–6.

[41] E. Alptekin, C. J. Kirkpatrick, V. Misra, and M. C. Ozturk. "Platinum germanosilicide contacts formed on strained and relaxed Si1-xGex layers". In: *IEEE Transactions on Electron Devices* 56.6 (2009), pp. 1220–1227.

[42] H. Irie, Y. Harada, H. Sugiyama, and T. Akazaki. "Josephson coupling through one-dimensional ballistic channel in semiconductor-superconductor hybrid quantum point contacts". In: *Phys. Rev. B* 89.16 (2014), pp. 1–6.

[43] V. Ambegaokar and A. Baratoff. "Tunneling between superconductors". In: *Physical Review Letters* 10.11 (1963), p. 486.

[44] S. Heedt, M. Quintero-Pérez, F. Borsoi, A. Fursina, N. van Loo, G. P. Mazur, M. P. Nowak, M. Ammerlaan, K. Li, S. Korneychuk, J. Shen, M. A. Y. van de Poll, G. Badawy, S. Gazibegovic, N. de Jong, P. Aseev, K. van Hoogdalem, E. P. Bakkers, and L. P. Kouwenhoven. "Shadow-wall lithography of ballistic superconductor–semiconductor quantum devices". In: *Nat. Comm.* 12.1 (2021), pp. 1–9.

[45] M. Tinkham. *Introduction to superconductivity*. 2nd ed. Mineola, N.Y., 2004. ISBN: 9781621985983.

[46] M. Octavio, M. Tinkham, G. E. Blonder, and T. M. Klapwijk. "Subharmonic energy-gap structure in superconducting constrictions". In: *Phys. Rev. B* 27.11 (1983), pp. 6739–6746.

[47] M. Kjaergaard, H. J. Suominen, M. P. Nowak, A. R. Akhmerov, J. Shabani, C. J. Palmstrøm, F. Nichele, and C. M. Marcus. “Transparent Semiconductor-Superconductor Interface and Induced Gap in an Epitaxial Heterostructure Josephson Junction”. In: *Phys. Rev. Appl.* 7.3 (2017), p. 034029.

[48] D. Averin and A. Bardas. “ac Josephson Effect in a Single Quantum Channel”. In: *Phys. Rev. Lett.* 75.9 (1995), pp. 1831–1834.

[49] F. Borsoi, G. P. Mazur, N. van Loo, M. P. Nowak, L. Bourdet, K. Li, S. Korneychuk, A. Fursina, J.-Y. Wang, V. Levajac, E. Memisevic, G. Badawy, S. Gazibegovic, K. van Hoogdalem, E. P. A. M. Bakkers, L. P. Kouwenhoven, S. Heedt, and M. Quintero-Pérez. “Single-Shot Fabrication of Semiconducting–Superconducting Nanowire Devices”. In: *Adv. Func. Mater.* 31.34 (2021), p. 2102388.

[50] A. Fornieri, A. M. Whiticar, F. Setiawan, E. Portolés, A. C. Drachmann, A. Keselman, S. Gronin, C. Thomas, T. Wang, R. Kallaher, G. C. Gardner, E. Berg, M. J. Manfra, A. Stern, C. M. Marcus, and F. Nichele. “Evidence of topological superconductivity in planar Josephson junctions”. In: *Nature* 569.7754 (2019), pp. 89–92. ISSN: 14764687. DOI: 10.1038/s41586-019-1068-8. URL: https://doi.org/10.1038/s41586-019-1068-8.

[51] H. A. Nilsson, P. Samuelsson, P. Caroff, and H. Q. Xu. “Supercurrent and Multiple Andreev Reflections in an InSb Nanowire Josephson Junction”. In: *Nano Lett.* 12 (2012), p. 233.

[52] N. van Loo, G. P. Mazur, T. Dvir, G. Wang, R. C. Dekker, J.-Y. Wang, M. Lemang, C. Sfiligoj, A. Bordin, D. van Driel, G. Badawy, S. Gazibegovic, E. P. A. M. Bakkers, and L. P. Kouwenhoven. “Electrostatic control of the proximity effect in the bulk of semiconductor-superconductor hybrids”. In: *Nat. Commun.* 14.3325 (2023).

[53] M. W. De Moor, J. D. Bommer, D. Xu, G. W. Winkler, A. E. Antipov, A. Bargerbos, G. Wang, N. V. Loo, R. L. Op Het Veld, S. Gazibegovic, D. Car, J. A. Logan, M. Pendharkar, J. S. Lee, E. P. M Bakkers, C. J. Palmstrom, R. M. Lutchyn, L. P. Kouwenhoven, and H. Zhang. “Electric field tunable superconductor-semiconductor coupling in Majorana nanowires”. In: *New Journal of Physics* 20.10 (2018), p. 103049.

[54] G. E. Blonder, M. Tinkham, and T. M. Klapwijk. “Transition from metallic to tunneling regimes in superconducting microconstrictions: Excess current, charge imbalance, and supercurrent conversion”. In: *Phys. Rev. B* 25.7 (1982), pp. 4515–4532.

[55] F. Pientka, A. Keselman, E. Berg, A. Yacoby, A. Stern, and B. I. Halperin. “Topological superconductivity in a planar Josephson junction”. In: *Phys. Rev. X* 7.2 (2017), pp. 1–17.

[56] H. Ren, F. Pientka, S. Hart, A. T. Pierce, M. Kosowsky, L. Lunczer, R. Schlereth, B. Scharf, E. M. Hankiewicz, L. W. Molenkamp, B. I. Halperin, and A. Yacoby. “Topological superconductivity in a phase-controlled Josephson junction”. In: *Nature* 569.7754 (2019), pp. 93–98.

7

[57] M. Luethi, K. Laubscher, S. Bosco, D. Loss, and J. Klinovaja. *Planar Josephson junctions in germanium: Effect of cubic spin-orbit interaction.* 2022.

[58] N. Poccia, T. I. Baturina, F. Coneri, C. G. Molenaar, X. R. Wang, G. Bianconi, A. Brinkman, H. Hilgenkamp, A. A. Golubov, and V. M. Vinokur. "Critical behavior at a dynamic vortex insulator-to-metal transition". In: *Science* 349.6253 (2015), pp. 1202–1205.

[59] C. G. Bøttcher, F. Nichele, M. Kjaergaard, H. J. Suominen, J. Shabani, C. J. Palmstrøm, and C. M. Marcus. "Superconducting, insulating and anomalous metallic regimes in a gated two-dimensional semiconductor–superconductor array". In: *Nature Physics* 14.11 (2018), pp. 1138–1144. ISSN: 17452481. DOI: 10.1038/s41567-018-0259-9. URL: https://doi.org/10.1038/s41567-018-0259-9.

[60] B. T. Matthias, T. H. Geballe, and V. B. Compton. "Superconductivity". In: *Reviews of Modern Physics* 35.1 (1963), pp. 1–22.

[61] M. Hell, M. Leijnse, and K. Flensberg. "Two-Dimensional Platform for Networks of Majorana Bound States". In: *Phys. Rev. Lett.* 118.10 (2017), p. 107701.

[62] F. Pientka, A. Keselman, E. Berg, A. Yacoby, A. Stern, and B. I. Halperin. "Topological Superconductivity in a Planar Josephson Junction". In: *Phys. Rev. X* 7.2 (2017), p. 021032.

[63] G. Burkard, M. J. Gullans, X. Mi, and J. R. Petta. "Superconductor–semiconductor hybrid-circuit quantum electrodynamics". In: *Nat. Rev. Phys.* 2.3 (2020), pp. 129–140.

[64] N. M. Chtchelkatchev and Y. V. Nazarov. "Andreev Quantum Dots for Spin Manipulation". In: *Physical Review Letters* 90 (June 2003), p. 226806.

[65] C. Padurariu and Y. V. Nazarov. "Theoretical proposal for superconducting spin qubits". In: *Phys. Rev. B* 81.14 (2010), p. 144519.

[66] M. Pita-Vidal, A. Bargerbos, R. Žitko, L. J. Splitthoff, L. Grünhaupt, J. J. Wesdorp, Y. Liu, L. P. Kouwenhoven, R. Aguado, B. van Heck, A. Kou, and C. K. Andersen. "Direct manipulation of a superconducting spin qubit strongly coupled to a transmon qubit". In: *Nat. Phys.* (2023), pp. 1–6.

[67] M. Spethmann, X.-P. Zhang, J. Klinovaja, and D. Loss. "Coupled superconducting spin qubits with spin-orbit interaction". In: *Phys. Rev. B* 106.11 (2022), p. 115411.

[68] M. P. Nowak, M. Wimmer, and A. R. Akhmerov. "Supercurrent carried by nonequilibrium quasiparticles in a multiterminal Josephson junction". In: *Phys. Rev. B* 99.7 (2019), p. 075416.

[69] P. Del Vecchio, M. Lodari, A. Sammak, G. Scappucci, and O. Moutanabbir. "Vanishing Zeeman energy in a two-dimensional hole gas". In: *Phys. Rev. B* 102.11 (2020), p. 115304.

[70] R. Mizokuchi, R. Maurand, F. Vigneau, M. Myronov, and S. De Franceschi. "Ballistic One-Dimensional Holes with Strong g-Factor Anisotropy in Germanium". In: *Nano Lett.* 18.8 (2018), pp. 4861–4865.

[71] W. I. Lawrie, H. G. Eenink, N. W. Hendrickx, J. M. Boter, L. Petit, S. V. Amitonov, M. Lodari, B. Paquelet Wuetz, C. Volk, S. G. Philips, G. Droulers, N. Kalhor, F. Van Riggelen, D. Brousse, A. Sammak, L. M. Vandersypen, G. Scappucci, and M. Veldhorst. "Quantum dot arrays in silicon and germanium". In: *Appl. Phys. Lett.* 116.8 (2020), p. 80501.

[72] W. I. L. Lawrie, M. Russ, F. van Riggelen, N. W. Hendrickx, S. L. de Snoo, A. Sammak, G. Scappucci, and M. Veldhorst. "Simultaneous single-qubit driving of semiconductor spin qubits at the fault-tolerant threshold". In: *Nat. Comm.* 14.3617 (2023).

[73] G. Badawy, S. Gazibegovic, F. Borsoi, S. Heedt, C. A. Wang, S. Koelling, M. A. Verheijen, L. P. Kouwenhoven, and E. P. Bakkers. "High Mobility Stemless InSb Nanowires". In: *Nano Lett.* 19.6 (2019), pp. 3575–3582.

[74] Y.-S. Kim, K. Hummer, and G. Kresse. "Accurate band structures and effective masses for InP, InAs, and InSb using hybrid func-tionals". In: *Phys. Rev. B* 80.3 (2009), p. 035203.

[75] R. L. Op het Veld, D. Xu, V. Schaller, M. A. Verheijen, S. M. Peters, J. Jung, C. Tong, Q. Wang, M. W. de Moor, B. Hesselmann, K. Vermeulen, J. D. Bommer, J. Sue Lee, A. Sarikov, M. Pendharkar, A. Marzegalli, S. Koelling, L. P. Kouwenhoven, L. Miglio, C. J. Palmstrøm, H. Zhang, and E. P. Bakkers. "In-plane selective area InSb–Al nanowire quantum networks". In: *Comm. Phys.* 3.1 (2020), pp. 1–7.

[76] I. Van Weperen, B. Tarasinski, D. Eeltink, V. S. Pribiag, S. R. Plissard, E. P. Bakkers, L. P. Kouwenhoven, and M. Wimmer. "Spin-orbit interaction in InSb nanowires". In: *Phys. Rev. B* 91.20 (2015), pp. 1–5.

[77] F. Qu, J. Van Veen, F. K. De Vries, A. J. Beukman, M. Wimmer, W. Yi, A. A. Kiselev, B. M. Nguyen, M. Sokolich, M. J. Manfra, F. Nichele, C. M. Marcus, and L. P. Kouwenhoven. "Quantized Conductance and Large g-Factor Anisotropy in InSb Quantum Point Contacts". In: *Nano Lett.* 16.12 (2016), pp. 7509–7513.

[78] J. W. Van Den Berg, S. Nadj-Perge, V. S. Pribiag, S. R. Plissard, E. P. Bak-kers, S. M. Frolov, and L. P. Kouwenhoven. "Fast spin-orbit qubit in an indium antimonide nanowire". In: *Phys. Rev. Lett.* 110.6 (2013).

[79] S. Heedt, W. Prost, J. Schubert, D. Grützmacher, and T. Schäpers. "Ballistic Transport and Exchange Interaction in InAs Nanowire Quantum Point Contacts". In: *Nano Lett.* 16.5 (2016), pp. 3116–3123.

[80] T. Kanne, M. Marnauza, D. Olsteins, D. J. Carrad, J. E. Sestoft, J. de Bruijckere, L. Zeng, E. Johnson, E. Olsson, K. Grove-Rasmussen, and J. Nygård. "Epitaxial Pb on InAs nanowires for quantum devices". In: *Nat. Nanotechnol.* 16.7 (2021), pp. 776–781.

[81] M. T. Deng, S. Vaitiekenas, E. B. Hansen, J. Danon, M. Leijnse, K. Flensberg, J. Nygård, P. Krogstrup, and C. M. Marcus. "Majorana bound state in a coupled quantum-dot hybrid-nanowire system". In: *Science* 354.6319 (2016), pp. 1557–1562.

[82] D. Liang and X. P. Gao. “Strong tuning of rashba spin-orbit interaction in single InAs nanowires”. In: *Nano Lett.* 12.6 (2012), pp. 3263–3267.

[83] K. D. Petersson, L. W. McFaul, M. D. Schroer, M. Jung, J. M. Taylor, A. A. Houck, and J. R. Petta. “Circuit quantum electrodynamics with a spin qubit”. In: *Nature* 490.7420 (2012), pp. 380–383.

[84] S. Nadj-Perge, S. M. Frolov, E. P. Bakkers, and L. P. Kouwenhoven. “Spin-orbit qubit in a semiconductor nanowire”. In: *Nature* 468.7327 (2010), pp. 1084–1087.

[85] C. M. Moehle, C. T. Ke, Q. Wang, C. Thomas, D. Xiao, S. Karwal, M. Lodari, V. Van De Kerkhof, R. Termaat, G. C. Gardner, G. Scappucci, M. J. Manfra, and S. Goswami. “InSbAs Two-Dimensional Electron Gases as a Platform for Topological Superconductivi-ty”. In: *Nano Lett.* 21.23 (2021), pp. 9990–9996.

8

CONCLUSIONS & OUTLOOK

8.1. CONCLUSIONS

We have studied quantum transport in multiple hybrid semiconductor-superconductor device architectures realized by different fabrication techniques and on various material platforms. Our conclusions refer either to advantages that we have achieved in the fabrication and design of these hybrid devices, or to the rich physics that we have encountered in them. Below we intend to give the conclusion of each chapter in a compact form. The conclusions are also given more elaborately at the end of each chapter.

Chapter 3: An InSb-Al nanowire Cooper pair transistor can exhibit a current-phase relation which phase offset depends on the electron parity on its superconducting island. Therefore, current-phase relation measurements can be used to directly detect the electron parity on the island. This can be done even in the $1e$-regime - where measuring only supercurrent amplitude or tunneling conductance cannot distinguish the two parities.

Chapter 4: Reducing the length of a nanowire Josephson junction enhances the resilience of its supercurrent against magnetic fields. The supercurrent through an InSb-Al nanowire Josephson junction can persist up to parallel magnetic fields of $\sim 1.4\,\mathrm{T}$ - that approach the critical field of the superconducting Al film. This occurs in $\sim 40\,\mathrm{nm}$-long junctions that can be defined through the shadow-wall lithography.

Chapter 5: The supercurrent through a Josephson junction can exhibit an asymmetric modulation by a resonant localized state inside the junction in the presence of interference with a broad direct-transmission channel. At high magnetic fields this mechanism can give rise to π-shifts of the supercurrent. We show this effect in an InSb-Al nanowire Josephson junction at parallel magnetic fields of up to $\sim 700\,\mathrm{mT}$.

Chapter 6: Tunnel probes with nm-thick AlOx tunnel barriers can be realized in hybrid InSb-Al nanowires by the controlled oxidation of the superconducting Al film. The shadow-wall lithography allows for defining such multiple probes arbitrarily along a single hybrid. Tunneling spectroscopy results obtained by neighboring probes reveal localized Andreev bound states along the hybrids.

Chapter 7: A hard superconducting gap can be induced in a Ge two-dimensional hole gas. This can be realized by depositing Pt on top of a Ge/SiGe quantum well and thermally diffusing it into the SiGe. As a result, the superconducting PtSiGe is formed, and superconductivity is induced in the Ge.

Although some devices in our studies were - according to their design - suitable for observing signatures of a topological phase with Majorana zero modes, this did not happen.

8.2. OUTLOOK

In the past decade, creating Majorana zero modes (MZMs) in hybrid semiconducting-superconducting nanostructures has turned out to be much more complex than what initial theoretical proposals predicted [1, 2]. Most recently, hybrid InAs-Al nanowires defined in two-dimensional electron gases (2DEGs) have been reported to pass a topological gap protocol [3]. This protocol includes exhibiting zero-bias peaks (ZBPs) in the local tunneling spectroscopy at the hybrid ends, and a reopening of the bulk gap ($\sim 30\,\mu$eV) in the non-local spectroscopy. Observing ZBPs simultaneously at the hybrid ends has already been shown insufficient to claim a continuous topological phase in hybrid nanowires. However, their coincidence with the gap reopening represents a stricter condition, which has been satisfied in some devices. Still, an unambiguous demonstration of a topological superconducting phase cannot be made [4, 5].

Disorder in hybrid nanowires can break the topological phase by causing local variations in the parameters that are uniform in the model of a Majorana nanowire. In order to have more control over the effects of disorder, hybrid nanowire devices consisting of semiconducting quantum dots (QDs) coupled to superconductors have recently caught significant attention. In such devices, QDs are coupled via elastic cotunneling (ECT) and crossed Andreev reflection (CAR) into a chain known as the Kitaev chain. A Majorana nanowire is the limit of a Kitaev chain with an infinitely large number of QDs [6]. In finite Kitaev chains, MZMs are localized on the two end-QDs and the topological protection is improved by increasing the number of QDs in-between them. An advantage of the Kitaev chain devices is that each QD in the chain can be independently tuned such that the amplitudes of ECT and CAR become equal and satisfy the condition for an effective topological superconductor. Consequently, by fine-tuning each QD, one could compensate for local non-uniformity due to disorder. Realization of a minimal Kitaev chain has recently been reported for two QDs in an InSb nanowire with Al [7]. Coupling mechanisms required for a three-site Kitaev chain have been reported in a chain with three QDs [8]. A demonstration of a three-site Kitaev chain has not been reported yet. Doing so and subsequently realizing longer Kitaev chains is needed in order to establish coupled QDs as a competitive platform for topological qubits.

Before the Kitaev chains prove experimentally superior for unambiguously detecting MZMs, further experiments on hybrid nanowires are also worth considering. Below we introduce several experiments on hybrid nanowires that are directly inspired by some of the main results presented in this thesis. The devices that we introduce here are readily obtainable through the shadow-wall lithography [9, 10].

8.2.1. MAGNETIC FIELD RESILIENT COOPER-PAIR TRANSISTOR

The Cooper-pair transistor (CPT) studied in Chapter 3 consisted of hybrid InSb-Al nanowire Josephson junctions (JJs) that were defined by nanowires casting shadows onto each other during the directional Al deposition. Therefore, the lengths of JJs were limited by the nanowire diameter and could not be reduced below ~ 100 nm. The current-phase relation (CPR) measurements have been performed up to parallel magnetic fields of ~ 200 mT where the supercurrent vanished. We show in Chapter 4

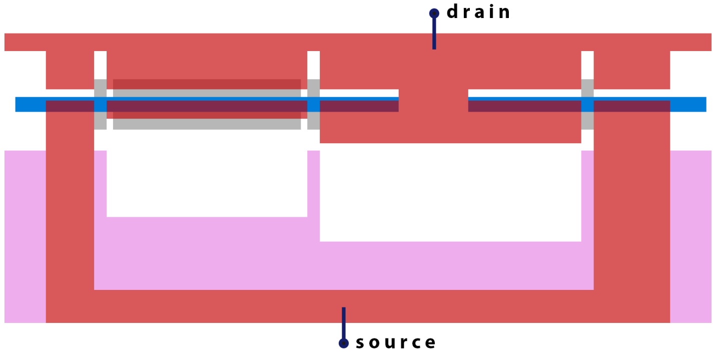

Figure 8.1: Schematic of a SQUID with two parallel hybrid InSb-Al (blue-red) nanowires defined through the shadow-wall (lilac) lithography. Two electrically isolated sections of the Al loop correspond to the source and drain of the SQUID. A Cooper-pair transistor and a single JJ (reference arm) are defined in the left and right nanowire, respectively. Underlying gates (grey) control the transparency of the JJs and the electro-chemical potential of the superconducting island. All JJs are $\sim 40\,\mathrm{nm}$ long in order to support a magnetic-field resilient supercurrent.

that the resilience of supercurrent against magnetic fields is dramatically improved in JJs obtained through the shadow-wall lithography technique where the junctions are $\sim 40\,\mathrm{nm}$ long. Obtaining a CPT with such magnetic-field resilient JJs and embedding it into the superconducting quantum interference device (SQUID) could allow for CPR measurements at high magnetic fields.

Here, we propose a shadow-wall design for a magnetic-field resilient CPT in the SQUID architecture. In Fig. 8.1, two InSb nanowires (blue) are placed on top of an array of gates (grey) next to shadow-walls (lilac). During the angle-deposition of Al (red), the shadow-walls determine the positions of three JJs on two nanowires and a superconducting loop on the substrate - analogously as in Chapter 5. Consequently, the JJs have lengths of $\sim 40\,\mathrm{nm}$ and are aligned with the underlying gates. The left nanowire hosts a CPT and the right nanowire serves as the reference arm for CPR measurements.

8.2.2. NANOMETER-THICK TUNNEL BARRIERS ON THREE-FACET HYBRID NANOWIRES

In Chapter 6, we have used tunnel probes with nm-thick tunnel barriers to examine the subgap spectra along single-facet hybrid InSb-Al nanowires. We have observed mostly highly localized states at the ends and inside the bulks of the hybrids. Such localized states can arise due to disorder causing non-uniformities of the electro-chemical potential along the nanowires. However, such non-uniformities could also be caused by multiple tunnel probes locally modifying the electro-chemical potential when biased with different bias voltages. This could be the case particularly in single-facet hybrids, where two out of three nanowire facets contacting the tunnel

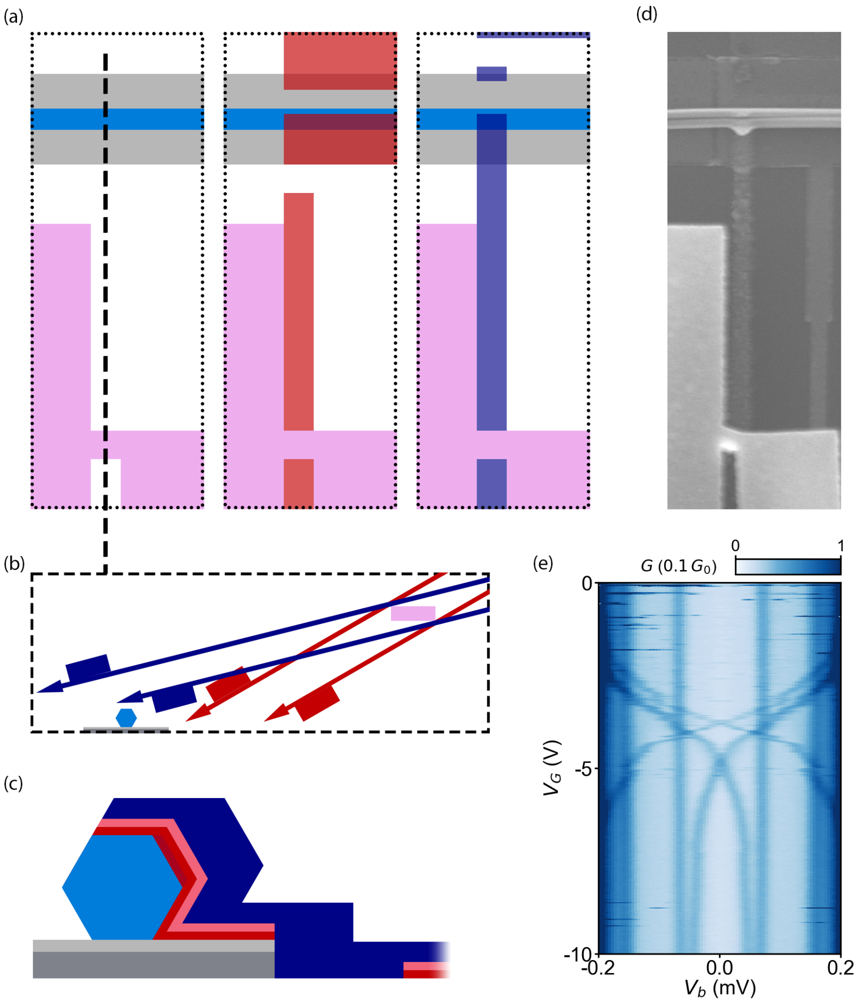

Figure 8.2: **(a)** Schematic of a top view on an InSb (blue) nanowire on top of a gate (grey). Superconducting Al (red) shell and a normal Ag (navy) probe are defined by the shadow-wall (lilac). The wall contains a bridge-like section. **(b)** Schematic of the transverse cut (broken black line) in (a). The deposition directions are shown by red (Al) and navy (Ag) arrows. **(c)** Schematic of a transverse cross-section through the probe. nm-thick tunnel barrier is made of AlOx (pink) and Al remains on all three nanowire facets that are tunnel-coupled to the Ag lead. The Al film on the substrate is interrupted. **(d)** Scanning electron microscopy (SEM) image of a three-facet hybrid InSb-Al nanowire device with a single AlOx tunnel probe. The nanowire is grounded by a normal drain contact on the right (not visible). **(e)** Differential conductance G as a function of V_b and V_G at $B = 0.25\,\mathrm{T}$.

probes do not have Al and, therefore, do not screen the bias voltages.

In Fig. 8.2, we propose a design and show an initial realization of a three-facet InSb-Al (blue-red) nanowire hybrid with a single normal Ag (navy) lead that is tunnel coupled via nm-thick AlOx (pink). Here, the Al film is present on all three facets contacting the tunnel probe (see Fig. 8.2(c)), which makes that the tunnel probe is screened by the Al and it does not affect the electro-chemical potential in the hybrid. Obtaining three-facet hybrids with nm-thick AlOx can be done similarly as in Chapter 6. An important difference is that the Al thickness is bigger – such that the Al remains on all three-facets after the AlOx is formed. This means, however, that the Al film remains also on the substrate and is covered by the AlOx. Crucially, the Al film thus has to be interrupted on the substrate in order to ensure that electrons tunnel through the AlOx on the nanowire (see Fig. 8.2(c)). This interruption is realized by using a bridge-like shadow-wall (lilac), as shown in Fig. 8.2(a)-(b). The Al is deposited at an angle of 30° such that the Al film is interrupted on the substrate (see Fig. 8.2(a) middle), and. the Ag is deposited at an angle of 18° such that the shadow falls above the nanowire (see Fig. 8.2(a) right) and the Ag lead is continuous. The Al film can be contacted by a drain normal lead as in Chapter 6.

We show an initial realization of the described device with a single tunnel probe. A scanning electron microscopy (SEM) image is displayed in Fig. 8.2(d) and a tunneling spectroscopy measurement at a parallel magnetic field $B = 0.25\,\mathrm{T}$ is given in Fig. 8.2(e). Differential conductance G is measured as a function of a bias voltage V_b applied between the Ag lead and the grounded drain and a voltage V_G applied to the gate under the nanowire. The obtained spectrum is qualitatively similar to the spectra reported in Chapter 6 – consisting of both subgap states that are sensitive and insensitive to the gate. A follow-up realization with multiple tunnel probes, as in Chapter 6, is needed to examine the spatial extension of these subgap states. This can lead to a conclusion whether and how much does the screening of the tunnel probes by the Al film improve the uniformity along the hybrids.

8

8.2.3. NON-LOCAL SPECTROSCOPY OF A HYBRID NANOWIRE WITH A SUPERCONDUCTOR-FREE BULK

In the tunneling spectroscopy in Chapter 6, subgap states have been found to be mostly localized over $\sim 200\,\mathrm{nm}$ along the hybrids. Inside the bulks, no extended subgap states with a systematic collective response to the super gate have been found. On the other hand, a recent work on three-terminal InSb-Al nanowire hybrids has used the non-local spectroscopy to study the properties of hybrid bulk states [11]. It has been argued there that the super gate controls the proximity effect inside the bulk such that positive super gate voltages reduce the coupling between the semiconductor and the superconductor and systematically reduce the energy of the hybrid bulk-states. These states then give rise to non-local signals below the gap. For sufficiently positive super gates, a weak-coupling regime with a closed induced gap has been identified as non-local signals have been measured for all in-gap energies.

The systematic detection of non-local signals in the weak-coupling regime demonstrates that there are bulk-states that are systematically and collectively tuned by the super gate and give rise to transport below the gap even over $\sim 8\,\mu$m-long

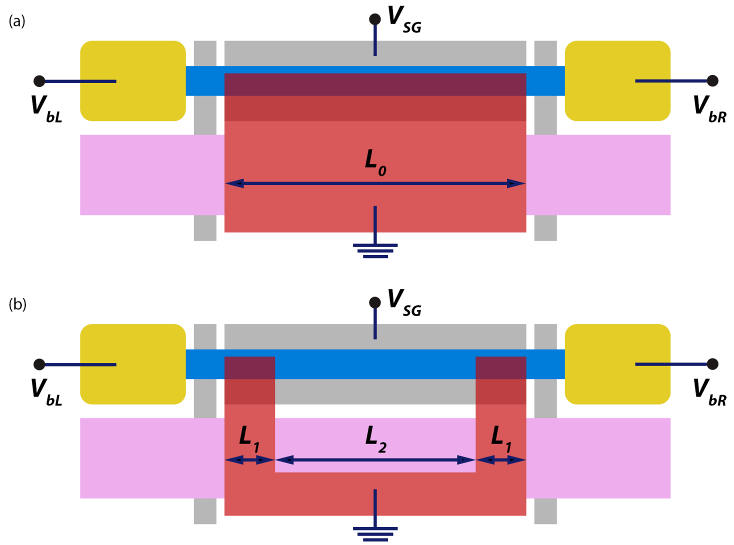

Figure 8.3: **(a)** A typical three-terminal hybrid device including an InSb (blue) nanowire with grounded superconducting Al (red) shell. Bias voltages $V_{bL,bR}$ are applied to two normal (yellow) leads defined by the shadow-walls (lilac). **(b)** A three terminal hybrid device analogous to (a), but with Al only at the hybrid ends (L_1 sections) and without Al in the bulk (L_2 section). The Al layout is obtained by the middle shadow-wall. In both devices, two underlying tunnel gates and one super gate (grey) tune the tunnel barrier transparencies and the nanowire bulk, respectively.

hybrids. Subgap states with such properties have not been observed in Chapter 6. On the other hand, it is known that at positive super gates fully semiconducting states can be induced inside hybrid nanowires. Such states are localized close to the nanowire facets that do not have the superconductor, and, in principle, could also give rise to non-local signals both in short and long hybrids. Interestingly, if such states form a transport channel at an energy E_0 below the induced superconducting gap Δ, non-local signals will arise even below Δ.

Non-local signals in standard three-terminal hybrids have antisymmetric dependences on bias voltages at which charge carriers (electrons and holes) are injected. The global phase factor has been shown to depend on the local superconducting properties (electron-like versus hole-like) of the hybrid end where the carriers leave the hybrid and are collected by the non-local lead [12]. Therefore, the local superconducting nature at the hybrid ends essentially determines the non-local signals measured in three-terminal hybrid nanowires. This is important for our proposal below, where one could test whether superconductivity inside the bulk is also essential, or even necessary, to obtain non-local signals with the reported properties.

We propose fabricating two InSb-Al (blue-red) nanowire hybrids shown in Fig. 8.3.

The nanowires have identical lengths, meaning that $L_0 = 2L_1 + L_2$. The hybrid in Fig. 8.3(a) is a typical three-terminal hybrid of a length L_0, while the hybrid in Fig. 8.3(b) has a large segment of its bulk (length L_2) that is superconductor-free. Importantly, there are shorter Al segments (length L_1) at the hybrid ends. The layouts of both devices are easily achievable through the shadow-wall (lilac) lithography. A possible realization of the parameters could be: $L_0 = 8\,\mu$m, $L_1 = 0.5\,\mu$m and $L_2 = 7\,\mu$m. In this case, L_2 is long enough to ensure that no hybrid states can couple the two superconducting end-segments and that, if detected, non-local signals are carried by purely semiconducting states. L_1 is chosen such that the elastic cotunneling and crossed Andreev reflection can be mediated by single Andreev bound states (ABSs) forming at the hybrid ends [7].

After performing non-local spectroscopy measurements on the two three-terminal devices in Fig. 8.3 while varying the underlying super gate, a comparison between the two non-local spectra could be made. Due to different electrostatic screening inside the bulks of the two devices, quantitatively same responses to the super gate are not likely to be observed. However, observing qualitatively similar features in the two non-local spectra would demonstrate that semiconducting states in the L_2-section of the device in Fig. 8.3(b) can carry non-local signals with the same features as in standard three-terminal hybrids. This would further mean that the non-local signals in standard three-terminal hybrids could also be carried by fully semiconducting states and only “dressed-up” with particular superconducting features by entering and exiting the hybrid via the ABSs at the hybrid ends. In this case, the onset bias voltage ($V_{bL,bR}$) at which non-local signals arise in typical three-terminal devices would be the minimum between the induced gap and the lowest purely semiconducting transport channel. Therefore, if semiconducting states have energies below the induced gap, non-local signals would not provide conclusive information about the induced gap and the proximity effect in the bulk.

REFERENCES

[1] Y. Oreg, G. Refael, and F. von Oppen. "Helical liquids and Majorana bound states in quantum wires". In: *Phys. Rev. Lett.* 105 (2010), p. 177002.

[2] R. M. Lutchyn, J. D. Sau, and S. D. Sarma. "Majorana fermions and a topological phase transition in semiconductor-superconductor heterostructures". In: *Phys. Rev. Lett.* 105 (2010), p. 077001.

[3] M. Aghaee *et al.* "InAs-Al hybrid devices passing the topological gap protocol". In: *Phys. Rev. B* 107 (24 2023), p. 245423.

[4] R. Hess, H. F. Legg, D. Loss, and J. Klinovaja. "Trivial Andreev Band Mimicking Topological Bulk Gap Reopening in the Nonlocal Conductance of Long Rashba Nanowires". In: *Phys. Rev. Lett.* 130 (20 2023), p. 207001.

[5] S. Das Sarma and H. Pan. "Density of states, transport, and topology in disordered Majorana nanowires". In: *Phys. Rev. B* 108 (8 2023), p. 085415.

[6] J. D. Sau and S. D. Sarma. "Realizing a robust practical Majorana chain in a quantum-dot-superconductor linear array". In: *Nat. Commun.* 3 (2012), p. 964.

[7] T. Dvir, G. Wang, N. van Loo, C.-X. Liu, G. P. Mazur, A. Bordin, S. L. D. ten Haaf, J.-Y. Wang, D. van Driel, F. Zatelli, X. Li, F. K. Malinowski, S. Gazibegovic, G. Badawy, E. P. A. M. Bakkers, M. Wimmer, and L. P. Kouwenhoven. "Realization of a minimal Kitaev chain in coupled quantum dots". In: *Nature* 614 (2023), pp. 445–450.

[8] A. Bordin, X. Li, D. van Driel, J. C. Wolff, Q. Wang, S. L. D. ten Haaf, G. Wang, N. van Loo, L. P. Kouwenhoven, and T. Dvir. "Crossed Andreev reflection and elastic co-tunneling in a three-site Kitaev chain nanowire device". In: *arXiv:2306.07696* (2023).

[9] S. Heedt, M. Quintero-Pérez, F. Borsoi, A. Fursina, N. van Loo, G. P. Mazur, M. P. Nowak, M. Ammerlaan, K. Li, S. Korneychuk, J. Shen, M. Y. van de Poll, G. Badawy, S. Gazibegovic, N. de Jong, P. Aseev, K. van Hoogdalem, E. P. A. M. Bakkers, and L. P. Kouwenhoven. "Shadow-wall lithography of ballistic superconductor–semiconductor quantum devices". In: *Nat. Commun.* 12 (2021), p. 4914.

[10] F. Borsoi, G. P. Mazur, N. van Loo, M. P. Nowak, L. Bourdet, K. Li, S. Korneychuk, A. Fursina, J.-Y. Wang, V. Levajac, E. Memisevic, G. Badawy, S. Gazibegovic, K. van Hoogdalem, E. P. A. M. Bakkers, L. P. Kouwenhoven, S. Heedt, and M. Quintero-Pérez. "Single-shot fabrication of semiconducting–superconducting nanowire devices". In: *Adv. Func. Mater.* 31 (2021), p. 2102388.

[11] N. van Loo, G. P. Mazur, T. Dvir, G. Wang, R. C. Dekker, J.-Y. Wang, M. Lemang, C. Sfiligoj, A. Bordin, D. van Driel, G. Badawy, S. Gazibegovic, E. P. A. M. Bakkers, and L. P. Kouwenhoven. “Electrostatic control of the proximity effect in the bulk of semiconductor-superconductor hybrids”. In: *Nat. Commun.* 14 (2023), p. 3325.

[12] G. Wang, T. Dvir, N. van Loo, G. P. Mazur, S. Gazibegovic, G. Badawy, E. P. A. M. Bakkers, L. P. Kouwenhoven, and G. de Lange. “Nonlocal measurement of quasiparticle charge and energy relaxation in proximitized semiconductor nanowires using quantum dots”. In: *Phys. Rev. B* 106 (6 2022), p. 064503.

ACKNOWLEDGEMENTS

This thesis offers an insight into what I have done and what I have learned during my PhD work. However, I am afraid that it cannot represent many moments of great excitement that I have experienced along this research path. I associate these moments mainly with the research process itself, rather than with external evaluations or recognitions that would often come even years after the experiments had been performed. A single click to refresh my measurement screen would be often enough to truly surprise me, disappoint me, make my day or completely change the course of measurements and postpone going to bed. The excitement of discovering new scientific truths has been my main driving force and source of pleasure on this research path. I want to thank to all the people thanks to whom I could feel such pleasure, who have shared it with me and thanks to whom I managed to materialize it in the form of this thesis.

First of all, **Leo**, thank you for giving me the opportunity to do my PhD in your group. You managed to bring many smart and ambitious people together and give them all imaginable tools to work together towards common goals. In such environment I could learn how to efficiently work with others while benefiting from the diversity of their ideas and personalities. Your presence has always remained essential when setting broader perspectives and discussing deep physics. I joined your group when the collaboration with Microsoft was at its highest point, and I could notice both advantages and disadvantages of a collaboration between academia and industry. This is a valuable experience for anyone growing up as a scientist nowadays and I am thankful for it. Finally, my most personal gratitude is for letting me continue even though shortly after I started, we both realized that I could not do the fabrication myself reliably. You helped me to develop my strengths instead of letting my physical weaknesses stop me.

I sincerely thank to **Yuli**, **Silvano**, **Elsa**, **Menno** and **Lieven** for accepting to evaluate my thesis and take part in my PhD defence as committee members. **Yuli**, I especially thank you for the great collaboration we have had on the π-junction project. It was my honour just to see you interested in our project and measured data. Later, it has been my pleasure to provide useful inputs for your theory work, discuss your results and together organize our paper. I am proud to have worked with you so closely. **Michael**, thank you for regularly following up my progress as my copromotor and particularly for the fruitful discussions about the field-resilient junctions.

Without one person this thesis would have been dramatically different, if not even impossible. **Ji-Yin**, it is at the same time easy and difficult to express my gratitude to you in this way. We have gone through everything together and I have learned a lot from you - about physics, measurements, paper writing, peer-review process... You have always had a helping hand for me, and your knowledge, enthusiasm and hard work are truly admirable. I appreciate how you managed to find a balance between letting me try out and develop my ideas while at the same time never, never making me feel that I am left

alone. Your pure personality, your sincerity and honesty have made me unconditionally trust you. Above all, thank you for this trust.

Lin, thank you for being my paranymph and always there to share your experience, talk and laugh together. I wish you all the best in finalizing your thesis and I am looking forward to your defence. **Guan**, thank you for being my Dutch paranymph and so positive to take part in hilarious jokes at any moment. Your knowledge of physics is very exceptional, and I am happy you will be continuing your academic path at Stanford. You deserve it, zus!

Jie, thanks for taking me into your team in the first year of my PhD. I am grateful for your help with initial measurements and my first-year proposal. **Greg** and **Nick**, you managed to fix the UTS at the peak of the pandemics, and this has been essential for many people in the group, including myself. You further helped us by beautifully depositing Al on beautifully deposited nanowires. Thank you for all this and for all rich scientific discussions. **Sebastian H.**, **Marina** and **Francesco B.**, we were more than lucky to inherit from you such a powerful technique as the shadow-wall lithography that you developed. **Cristina**, I appreciate your warm personality and always sincere support. Thanks for useful inputs for the Ag deposition and your efforts to TEM our AlOx devices. **Mathilde** and **Jan Cornelis**, thank you for your help with the optimization and fabrication of our AlOx devices. **Alberto B.**, you jumped into the AlOx project a few times and gave tremendously precious help, thanks! It is amazing how you spread your overwhelming passion for research everywhere around yourself. Keep it up and be proud of it!

Besides the people from my group, I have also had pleasure to directly work with people from other research groups. **Alberto T.** and **Giordano**, the measurements of your clean Ge devices have been so reproducible that they revived my beliefs in scalable quantum technology. We got nice results within a few months of measuring, which doesn't happen often. During this short time we managed to develop super nice personal relations, which also doesn't happen so often. **Constantin**, it was my pleasure to host you together with Jie, Ji-Yin and Leo in Delft, and think together about our supercurrent parity-meter. **Hristo**, thank you for your efforts to develop the supercurrent model with Yuli. **Ghada**, **Saša**, **Roy** and **Erik**, thank you for your material support and interesting workshops in Delft and Eindhoven.

There are people who have been close to me over these years, but with whom I did not work directly. **Di**, your art-lover side has always resonated with me, and I have always enjoyed our conversations about art, travelling and life in general. **Marta**, it was nice to have you around for PhD- and physics-related chats, as well as for random everyday chats in-between our screens. **Arno**, thanks for being always friendly and willing to share useful ideas whenever our projects would intersect. Also, my greatest respect for the scientific output you and Marta made together. **Jaap**, we started our PhD runs at the same time and we are both now finishing... so matching - like tequilas and empanadas! Thank you for nice time and the gezellige party! **Lukas S.**, I have always admired your devotion to everything you would engage in. It went much beyond a working nanowire amplifier – to multiple activities you organized to make us all feel that we belong to our QuRe division. **Christian P.**, thank you for surfing through the arXiv and making sure we don't miss on any interesting fresh work! **Filip**, thanks for passionate discussions and bringing good music and order into the lab. **David**, dankjewel voor het corrigeren van mijn vertaling van de stellingen en samenvatting, en natuurlijk voor interessante wetenschappelijke discussies af en toe. **Francesco Z.**, fingers crossed for coupling many, many quantum dots and discovering new avenues of the Majorana field. **Tom**, your clear and deep thinking about physics would always help me clarify my own ideas and deepen my knowledge. **Willemijn**, thank you for nice conversations when I felt lost in the first year, for your tips for Colombia and for making me discover Taganga. **Jouri**, thank you for all your answers to my beginner's questions and for your patience in the cleanroom. **Michiel**, thanks for your interests in my projects, enriching physics-discussions and useful advice how to go through the PhD. I am also very thankful to many other people who also contributed to the group dynamics by their bright minds and unique personalities – **Damaz**, **Christian M.**, **Lukas G.**, **Daniel**, **Michael**, **Attila**, **Bas**, **Amrita**, **Robin**, **Peter**, **May An**, **Angela**, **Wolfgang**, **Gijs**, **Bernard**, **Fokko**, **James**, **Alex**, **Jasper**...

Srijit, it has been my pleasure to spend our after-work time with you, discuss physics and have fun with other QuRe people. Thank you for being always so approachable and trustworthy. **Qing**, chatting with you and sharing our experience and struggles would always be a relief before taking new steps. I can't wait to read your multi-probe paper! **Ivan**, thanks for inspiring conversations beyond physics - about the world politics and its complex laws. **Sebastian M.**, you are an incredibly and rarely cool person and I truly enjoyed every single moment we shared. **Figen**, your cheerfulness gives a special charm to our division. My sincere gratidues go to all the QuRe people – **Siddarth**, **Delphine**, **Anton**, **Chun-Xiao**, **Antonio**, **Mert**, **Hélène**, **Isidora**, **Taryn**, **Nataliia**, **Christian A.**... **Julien**, **Ajay** and everyone from True U, thank you for nice moments and activities we had together.

I want to thank the following people for their giant efforts to make our work possible. Even kijken... **Jenny**! Thank you for all kinds of help that you have provided through useful information and clear communication. En voor stukjes Nederlands die we met elkaar gesproken hebben. **Csilla**, thank you for nurturing the team spirit of QuRe and defending our interests in exhausting IP review processes. **Olaf**, **Jason** and **Raymond**, I cannot even imagine where we would have ended up without you. Your pro-active approach to constantly improve our setups is essential for the whole QuTech. Next to this, you have always been very patient to explain us all tips and tricks and correct all misconceptions that we inherited from more senior PhDs and PostDocs. I am glad I could learn so many things from you.

Let me thank the following people for their signatures in my Delft chapter that they left by visiting me or being very close to me over the past years. **Milica**, you are the greatest treasure this PhD has brought to me. Our friendship has quickly reached trust and love that friends often build since their childhood. **Aleksandar**, we know you are truly mooi soul mate. **Ena**, we discovered the Netherlands together nine years ago and you have remained close to me during my adventure in this beautiful country. **Ben** and **Gavriel**, we have spent so many nice moments together, and I am happy we are soon continuing with our rituals in Leuven even more intensively. **Hugh** and **Steve**, thank you for your presence and support, and for all regular meet-ups and thematic dinners. **Filip**, thank you for your endless stories, spectacular places and art walks you guided us through Antwerp together with **Paul**. **Andrej** and **Nikola K.**, thank you for our friendship filled with power

jokes, guys! **Sonja** and **Bojan**, it was great to celebrate King's Day in Amsterdam and to see you settling down in Rotterdam. **Sofija** and **Nikola**, it was my pleasure to see you in a new context while enjoying Belgium. **Marina**, aaayy, your support has always been true, loud and cheerful. **Sonja S.**, your visit was short, but almost intense as your laughs and our friendship. **Tara**, thank you for five unforgettable days in the Netherlands that bonded us in a unique way. **Nikola M.** and **Miša**, thanks for attending my defence and closely showing your support.

I would also like to express my gratitude to all my friends from the periods of high school, bachelor and master studies, with whom I have kept strong bonds despite being physically far. **Janko**, **Đole**, **Jovana**, **Maša**, **Danica**, **Taša T.**, **Taša Z.**, **Dumbe**, **Ogi**, **Selena**, **Miona**, **Sanjica**, **Dimitrije**, **Rade**, **Jelena**, **Marija**, **Adriana**, **Jaco**, **Öncü**, **Asser** and many others, thank you for our friendships.

Muchas gracias a las familias maravillosas **Espinel** y **Ramirez** por toda su afecto y por todos los momentos que disfrutamos juntos!

Moja bezgranična zahvalnost pripada mojoj porodici, rodbini i kumovima - za višedecenijsko (da, višedecenijsko!) prisustvo i podršku na akademskom putu, za stvaranje uslova da na tom putu postižem uspehe i iskreno učešće u sreći koju bi oni doneli. Veliko hvala... mojoj majci **Tanji** za apsolutnu posvećenost, ocu **Goranu** za negovanje mašte, bratu **Vuku** za najčistiju ljubav, nani **Radi** – mom prvom i najuticajnijem akademskom mentoru, dedi **Ljubi** za pozorište u kući, dedi **Rajku** za buđenje istraživačko-avanturističkog duha i baki **Radi** u ime fizike kao životnog poziva. Najdublje sam zahvalan i plejadi fantastičnih pedagoga - učiteljici **Miri**, nastavnici **Milici**, profesorkama **Slavici** i **Jasmini**, svim predavačima Matematičke radionice mladih - koji su zajedno negovali moj talenat za matematiku i motivisali me da krenem ovim putem.

During a PhD it can be hard to draw a line where deeply personal qualities take over purely professional ones. My personality was crucially shaped during my childhood and teenage period while being in a theatre group in my hometown. **Slaja** and all my theatre friends - **Sonja**, **Milan**, **Nena**, **Đole M.**, **Đole N.**, **Arsa**, **Sara**, **Milenica**, **Tamara**... - thank you for helping me discover spaces of freedom on stage and create them in myself.

Finally, **David**, you have always been there to give the greatest support on my way. Thank you for this and, even more importantly, thank you for making these years so vivid, colourful and adventurous. I am proud that we managed to build something that is truer and more beautiful than any work of science or any piece of art.

CURRICULUM VITÆ

Vukan LEVAJAC

12-02-1993	Born in Kragujevac, Serbia.
2008–2012	First Grammar School of Kragujevac, Serbia
2012–2016	Bachelor of Science in Electrical Engineering School of Electrical Engineering University of Belgrade, Serbia
2016–2018	Master of Science in Nanoscience and Nanotechnology KU Leuven, Belgium (1styear) Chalmers University of Technology, Sweden (2ndyear) *Thesis:* Decoherence analysis of a coaxmon qubit *Supervisor:* Prof. dr. Per Delsing
2018–2023	PhD in Physics Delft University of Technology, The Netherlands *Thesis:* Quantum transport in hybrid semiconductor-superconductor nanostructures *Supervisor:* Prof. dr. ir. Leo P. Kouwenhoven

List of Publications

1

Papers and preprints

9. **V. Levajac**, H. Barakov, G. P. Mazur, N. van Loo, L. P. Kouwenhoven, Y. V. Nazarov and J.-Y. Wang
   Supercurrent in the presence of direct transmission and a resonant localized state
   arXiv:2310.03296 (2023)

8. **V. Levajac** [1], J.-Y. Wang [1], C. Sfiligoj, M. Lemang, J. C. Wolff, A. Bordin, G. Badawy, S. Gazibegović, E. P. A. M. Bakkers and L. P. Kouwenhoven
   Subgap spectroscopy along hybrid nanowires by nm-thick tunnel barriers
   Nature Communications 14, 6647 (2023)

7. **V. Levajac**, G. P. Mazur, N. van Loo, F. Borsoi, G. Badawy, s. Gazibegović, E. P. A. M. Bakkers, S. Heedt, L. P. Kouwenhoven and J.-Y. Wang
   Impact of junction length on supercurrent resilience against magnetic field in InSb-Al nanowire Josephson junctions
   Nano Letters 23, 11, 4716-4722 (2023)

6. A. Tosato, **V. Levajac**, J.-Y. Wang, C. J. Boor, F. Borsoi, M. Botifoll, C. N. Borja, S. Marti-Sánchez, J. Arbiol, A. Sammak, M. Veldhorst and G. Scappucci
   Hard superconducting gap in germanium
   Communications Materials 4, 23 (2023)

5. J.-Y. Wang, N. van Loo, G. P. Mazur, **V. Levajac**, F. K. Malinowski, M. Lemang, F. Borsoi, G. Badawy, S. Gazibegović, E. P. A. M. Bakkers, M. Quintero-Pérez, S. Heedt and L. P. Kouwenhoven
   Parametric exploration of zero-eeergy modes in three-terminal InSb-Al nanowire devices
   Physical Review B 106, 075306 (2022)

4. J.-Y. Wang [1], C. Schrade [1], **V. Levajac**, D. van Driel, K. Li, S. Gazibegović, G. Badawy, R. L. M. Op het Veld, J. S. Lee, M. Pendharkar, C. P. Dempsey, C. J. Palmstrøm, E. P. A. M. Bakkers, L. Fu, L. P. Kouwenhoven and J. Shen
   Supercurrent parity meter in a nanowire Cooper pair transistor
   Science Advances 8 (16), eabm9896 (2022)

3. F. Borsoi, G. P. Mazur, N. van Loo, M. P. Nowak, L. Bourdet, K. Li, S. Korneychuk, A. Fursina, J.-Y. Wang, **V. Levajac**, E. Memisevic, G. Badawy, S. Gazibegović, K. van Hoogdalem, E. P. A. M. Bakkers, L. P. Kouwenhoven, S. Heedt and M. Quintero-Pérez
   Single-shot fabrication of semiconducting-superconducting nanowire devices
   Advanced Functional Materials, 31 (34), 2102388 (2021)

[1] These authors contributed equally to this work

2. J. Shen, G. W. Winkler, F. Borsoi, S. Heedt, **V. Levajac**, J.-Y. Wang, D. van Driel, D. Bouman, S. Gazibegović, R. L. M. Op het Veld, D. Car, J. A. Logan, M. Pendharkar, C. J. Palmstrøm, E. P. A. M. Bakkers, L. P. Kouwenhoven and B. van Heck
   Full parity phase diagram of a proximitized nanowire island
   Physical Review B 104, 045422 (2021)

1. A. Totović, **V. Levajac** and D. Gvozdić
   Electro-optical modulation bandwidth analysis for traveling-wave and reflective semiconductor optical amplifiers in transparency operating regime
   Optical and Quantum Electronics 48 (4), 262 (2016)

Patent

1. J.-Y. Wang, **V. Levajac**, M. Lemang and L. P. Kouwenhoven
   Semiconductor-superconductor hybrid devices having a tunnel barrier
   WO2023030626A1 World Intellectual Property Organization (2023)